ASME
SETTING THE STANDARD

Journal of Fluids Engineering

Published Monthly by ASME

VOLUME 129 • NUMBER 2 • FEBRUARY 2007

Transactions of the ASME, Journal of Fluids Engineering (ISSN 0098-2202) is published monthly by The American Society of Mechanical Engineers, Three Park Avenue, New York, NY 10016. Periodicals postage paid at New York, NY and additional mailing offices.
POSTMASTER: Send address changes to Transactions of the ASME, Journal of Fluids Engineering, c/o THE AMERICAN SOCIETY OF MECHANICAL ENGINEERS, 22 Law Drive, Box 2300, Fairfield, NJ 07007-2300.
CHANGES OF ADDRESS must be received at Society headquarters seven weeks before they are to be effective. Please send old label and new address.
STATEMENT from By-Laws. The Society shall not be responsible for statements or opinions advanced in papers or ... printed in its publications (B7.1, Par. 3).

TECHNICAL PAPERS

(Contents continued on inside back cover)

This journal is printed on acid-free paper, which exceeds the ANSI Z39.48-1992 specification for permanence of paper and library materials. ♾™
♻ 85% recycled content, including 10% post-consumer fibers.

(**Contents continued**)

Journal of Fluids Engineering **Volume 129, Number 2** **FEBRUARY 2007**

TECHNICAL BRIEF

The ASME Journal of Fluids Engineering is abstracted and indexed in the following:

Applied Science & Technology Index, Chemical Abstracts, Chemical Engineering and Biotechnology Abstracts (Electronic equivalent of Process and Chemical Engineering), Civil Engineering Abstracts, Computer & Information Systems Abstracts, Corrosion Abstracts, Current Contents, Ei EncompassLit, Electronics & Communications Abstracts, Engineered Materials Abstracts, Engineering Index, Environmental Engineering Abstracts, Environmental Science and Pollution Management, Excerpta Medica, Fluidex, Index to Scientific Reviews, INSPEC, International Building Services Abstracts, Mechanical & Transportation Engineering Abstracts, Mechanical Engineering Abstracts, METADEX (The electronic equivalent of Metals Abstracts and Alloys Index), Petroleum Abstracts, Process and Chemical Engineering, Referativnyi Zhurnal, Science Citation Index, SciSearch (The electronic equivalent of Science Citation Index), Shock and Vibration Digest, Solid State and Superconductivity Abstracts, Theoretical Chemical Engineering

Satoshi Watanabe
Associate Professor
Mem. ASME
Faculty of Engineering,
Kyushu University,
744 Motooka,
Nishi-ku, Fukuoka, 819-0395 Japan
e-mail: fmnabe@mech.kyushu-u.ac.jp

Tatsuya Hidaka
Graduate Student

Hironori Horiguchi
Associate Professor

Graduate School of Engineering Science,
Osaka University,
1-3 Machikaneyama,
Toyonaka, 560-8531 Japan

Akinori Furukawa
Professor
Faculty of Engineering,
Kyushu University,
744 Motooka,
Nishi-ku, Fukuoka, 819-0395 Japan

Yoshinobu Tsujimoto
Professor
Mem. ASME
Graduate School of Engineering Science,
Osaka University,
1-3 Machikaneyama,
Toyonaka, 560-8531 Japan

Steady Analysis of the Thermodynamic Effect of Partial Cavitation Using the Singularity Method

It is well known that the suction performance of turbopumps in cryogenic fluids is much better than that in cold water because of the thermodynamic effect of cavitation. In the present study, an analytical method to simulate partially cavitating flow with the thermodynamic effect in a cascade is proposed; heat transfer between the cavity and the ambient fluid is modeled by a one-dimensional unsteady heat conduction model under the slender body approximation and is coupled with a flow analysis using singularity methods. In this report, the steady analysis is performed and the results are compared with those of experiments to validate the model of the present analysis. This analysis can be easily extended into unsteady stability analysis for cavitation instabilities such as rotating cavitation and cavitation surge. [DOI: 10.1115/1.2409333]

Keywords: cavitation, thermodynamic effect, cascade, closed cavity model, singularity method

Introduction

Vapor production through cavitation extracts the latent heat of evaporation from the surrounding liquid, which decreases the local temperature, and hence the local vapor pressure in the vicinity of cavity. This is called the thermodynamic/thermal effect of cavitation. The thermodynamic effect of cavitation could be ignored for usual applications especially with water at ambient temperature, but is much more important for cryogenic fluids such as liquid oxygen and liquid hydrogen. For example, the suction performance of a turbopump inducer for a liquid propellant rocket engine is much better if operated with cryogenic fluids than in water; the development of the cavity is suppressed because of local vapor pressure depression due to the thermodynamic effect of cavitation.

Many studies have been done to clarify the thermodynamic effect of cavitation. The most important study might be Stepanoff's one [1], defining B-factor, to correlate the suction performance with the thermodynamic properties of working fluids with the idea of the latent heat exchange between vapor and liquid phases. Ruggeri and Moore [2] also derived an empirical formula to estimate the thermodynamic effect mainly for turbopump inducers of rocket engines. Fruman et al. [3] (and earlier Billet and Weir [4]) constructed the vapor entrainment theory to predict the thermodynamic effect based on the experimental correlation between the vapor flow rate and the gas flow rate in the ventilated cavity geometrically analogous to the natural cavity. Kato [5] proposed a simple model expressing the heat flow around the sheet cavity by a one-dimensional partial differential equation of unsteady heat conduction and Tokumasu et al. [6] investigated the thermodynamic effect on closed sheet cavities by combining Reynolds Averaged Navier-Stokes (RANS) simulation with Kato's model. Tani and Nagashima [7] simulated the cavitating flow around a hydrofoil with cryogenic fluids by the bubbly flow model based on the Rayleigh Plesset equation. Many numerical simulations are being developed. However, most of them are limited to the steady analysis and the impact of the thermodynamic effect on cavitation instabilities such as rotating cavitation and cavitation surge is still unclear.

We have developed a simple analysis of unsteady cavitating flow combining a free streamline theory and a singularity method and succeeded in simulating the cavitation instabilities of hydrofoil [8] as well as those of cascade [9] such as rotating cavitation and cavitation surge. The final goal of the present study is to construct a simple analytical method of the cavitation instabilities under the thermodynamic effect of cavitation by combining our singularity analysis and Kato's heat conduction model. As the first step, a steady flow analysis is performed in this report, and is

Contributed by the Fluids Engineering Division of ASME for publication in the JOURNAL OF FLUIDS ENGINEERING. Manuscript received October 20, 2005; final manuscript received July 3, 2006. Assoc. Editor: Georges L. Chahine. Paper presented at the 2005 ASME Fluids Engineering Division Summer Meeting and Exhibition (FEDSM2005), June 19–23, 2005, Houston, TX.

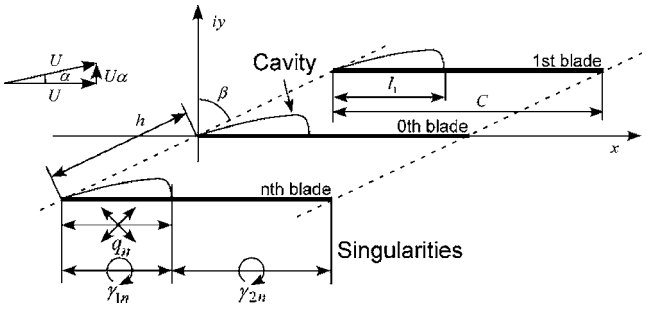

Fig. 1 Model for present analysis

validated through the comparison with the experiment by Franc et al. [10], who investigated the thermodynamic effect by Freon R-114 as a thermosensible working fluid.

Fundamental Flow Field

We consider a flat plate cascade with the chordlength C, spacing h, the stagger angle β, and the number of blade N as shown in Fig. 1. We assume the flow far upstream is uniform with the magnitude U and the angle of attack α. Each blades is represented by bound vortex distributions $\gamma_n(\xi)[n=0,1,\ldots,N-1]$ and the cavity with length l_n which develops on the suction surface of each blades is represented by source distributions $q_n(\xi)[n=0,1,\ldots,N-1]$. Then the complex conjugate velocity is expressed by the following equation:

$$\begin{aligned} w(z) &= u - iv \\ &= Ue^{-i\alpha} + \frac{1}{2\pi}\sum_{n=0}^{N-1}\left\{\int_0^{l_n} q_n(\xi)\cdot\left[f_n(z,\xi)+\frac{\pi}{Nh}e^{i\beta}\right]d\xi\right. \\ &\quad + i\int_0^{l_n}\gamma_{ln}(\xi)\cdot\left[f_n(z,\xi)+\frac{\pi}{Nh}e^{i\beta}\right]d\xi \\ &\quad \left. + i\int_{l_n}^{C}\gamma_{2n}(\xi)\cdot\left[f_n(z,\xi)+\frac{\pi}{Nh}e^{i\beta}\right]d\xi\right\} \end{aligned} \tag{1}$$

$$f_n(z,\xi) = \frac{\pi}{Nh}e^{-i\left(\frac{\pi}{2}-\beta\right)}\cdot\cot\left[\frac{\pi}{Nh}(z-\xi)e^{-i\left(\frac{\pi}{2}-\beta\right)} - \frac{n\pi}{N}\right] \tag{2}$$

We divide the velocity components into the uniform velocity U and the deviation (u_s, v_s), i.e.,

$$u = U + u_s, \quad v = U\alpha + v_s \tag{3}$$

In the present study, we linearize the equations under the assumptions of the small angle of attack $\alpha \ll 1$ and the small velocity deviations $|u_s|,|v_s| \ll U$.

Boundary and Complementary Conditions

We assume that the cavity is sufficiently thin so that all boundary conditions are applied on the blade suction surface. In the following sections, boundary and complementary conditions applied are described for nth blade.

Boundary Condition on Cavity Surface. We assume that the pressure on the cavity surface is equal to the vapor pressure. Under the presence of the thermodynamic effect of cavitation, the vapor pressure is locally different due to the temperature depression around the cavity surface. Here we apply the Clapeyron–Clausius equation for the relationship between the vapor pressure P_{Vn} and the temperature T_n on the cavity surface at a distance x from the leading edge as

$$P_{Vn}(x) - P_{V\infty} = \frac{dP_V}{dT}[T_n(x,0) - T_\infty] = \frac{L}{T_\infty}\frac{\rho_V\rho_L}{\rho_L - \rho_V}[T_n(x,0) - T_\infty] \tag{4}$$

where L denotes the latent heat of evaporation, and ρ_L and ρ_V denote the densities of liquid and vapor phases respectively. The subscript ∞ means the value at the upstream infinity. We assume that the temperature difference between on the cavity surface and far upstream ΔT_n is small, and express it as follows:

$$\Delta T_n = T_n(x,0) - T_\infty = \alpha T_\infty C_{Tn}(x,0) \tag{5}$$

Taking account of $\rho_V \ll \rho_L$, which is true for most real fluids, Eq. (4) can be rewritten as follows:

$$P_{Vn}(x) - P_{V\infty} = \rho_V L\alpha C_{Tn}(x,0) \tag{6}$$

Integrating the linearized momentum equation in the x-direction from far upstream and substituting Eq. (6) into it, we obtain the following equation:

$$\frac{u_{csn}(x)}{U\alpha} = \frac{\sigma}{2\alpha} - K_2 C_{Tn}(x,0) \tag{7}$$

where u_{csn} denotes the velocity deviation on the cavity surface. This equation can be regarded as the unsteady Bernoulli equation applied between the upstream infinity and the cavity surface. The cavitation number σ and the parameter K_2 are defined as

$$\sigma = (P_\infty - P_{V\infty})/(\rho_L U^2/2) \tag{8}$$

$$K_2 = \left(\frac{\rho_V}{\rho_L}\right)\frac{L}{U^2} \tag{9}$$

The boundary condition on the cavity surface can be obtained by equating u of Eq. (1) and u_{csn} of Eq. (7), i.e.,

$$\mathrm{Real}\lfloor w\{nhe^{-i(\pi/2-\beta)} + x + 0i\}\rfloor = U + u_{csn}(x) \tag{10}$$

Boundary Condition on Wetted Surface. We employ the following flow tangency condition on the wetted blade surfaces:

$$\begin{aligned} &\mathrm{Imag}[w\{nhe^{-i(\pi/2-\beta)} + x - 0i\}] = 0 \quad (0 < x < l_n) \\ &\mathrm{Imag}[w\{nhe^{-i(\pi/2-\beta)} + x \pm 0i\}] = 0 \quad (l_n < x < C) \end{aligned} \tag{11}$$

Kutta's Condition. We assume that the pressure difference across the blade vanishes at the trailing edge. This condition is simply expressed as follows:

$$\gamma_{2n}(l_n) = 0 \tag{12}$$

Cavity Closure Condition. We employ the closed cavity model for its simplicity. The cavity thickness η_n can be obtained by integrating the following kinematic boundary condition on the cavity surface

$$U\frac{d\eta_n}{dx} = q_n(x) \tag{13}$$

Imposing the zero cavity thickness at the trailing edge of cavity, we obtain the following cavity closure condition:

$$\eta_n(l_n) = \frac{1}{U}\int_0^{l_n} q_n(\xi)d\xi = 0 \tag{14}$$

Modeling of Thermodynamic Effect

In the previous section, we have described the kinematic and dynamic boundary conditions, assuming that the temperature distribution along the cavity surface is known. To close the problem, we need one more relation to obtain the temperature distribution. Here, we model the thermodynamic effect of cavitation, using the

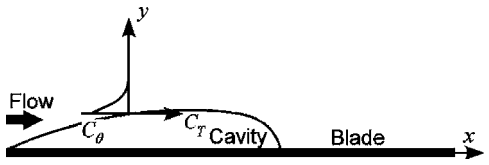

Fig. 2 Heat conduction model on cavity surface

following heat conduction model for the liquid flow around cavity and the evaporation model expressing the heat flux across the cavity surface due to evaporation.

Heat Conduction Model. Figure 2 shows the schematic view of the present heat conduction model. We assume that the heat conduction in the main flow direction (x) is negligibly small, compared to that in the direction (y) normal to the cavity surface. The temperature increase (decrease) due to the formation of thin cavity ΔT_n should satisfy the following linearized energy equation for inviscid flow

$$\frac{\partial \Delta T_n}{\partial t} + U\frac{\partial \Delta T_n}{\partial x} = \varepsilon a \frac{\partial^2 \Delta T_n}{\partial y^2} \tag{15}$$

where a denotes a thermal diffusivity. Kato [5] employed in his original model the turbulent diffusivity factor ε to take account of the enhancement of thermal diffusion due to the turbulent flow around the cavity. We also employ ε as a free parameter, which could be empirically determined. In the present study, we determine this value to obtain the qualitative agreement with the existing experiment in terms of cavity length and temperature depression as described later. Then, the other effects rather than turbulence diffusion might be included in the turbulent diffusivity factor.

For the present steady problem, Eq. (15) can be rewritten as follows using C_{Tn} introduced in Eq. (6)

$$U\frac{\partial C_{Tn}}{\partial x} = \varepsilon a \frac{\partial^2 C_{Tn}}{\partial y^2} \tag{16}$$

We can find that this equation is equivalent to a one-dimensional partial differential equation of unsteady heat conduction. Assuming no temperature depression at the leading edge of cavity ($x=0$), we can analytically integrate Eq. (16) using the normalized temperature increase along the cavity surface $C_{\theta n}(x)$

$$C_{Tn}(x,y) = \frac{y}{2\sqrt{\pi K_P}} \int_0^x C_{\theta n}(\xi) \frac{\exp\left(-\dfrac{y^2}{4K_P(x-\xi)}\right)}{(x-\xi)^{\frac{3}{2}}} d\xi \tag{17}$$

where K_p is defined here as $K_p = \varepsilon a / U$. Then, the temperature gradient normal to the cavity surface is derived as

$$\lim_{y\to 0} \frac{\partial C_{Tn}(x,y)}{\partial y} = -\frac{1}{\sqrt{\pi K_P}} \int_0^x \frac{dC_{\theta n}(\xi)}{d\xi} \frac{1}{(x-\xi)^{\frac{1}{2}}} d\xi \tag{18}$$

Evaporation Model. In the original model proposed by Kato [5], a parabolic velocity profile is assumed for the vapor flow inside the cavity. However, for simplicity, we herein assume that the velocity inside the cavity is uniform in the y-direction which equals to the liquid velocity $U+u_{csn}$ on the cavity surface, as shown in Fig. 3. The effect of velocity profile inside the cavity could be included in the thermal diffusivity factor ε. Considering the continuity relation in the small control volume inside the cavity, we obtain the following equation using the local evaporation velocity V_n of gas:

$$V_n dx = (U + u''_{csn})\eta''_n - (U + u'_{csn})\eta'_n = U d\eta_n \tag{19}$$

where we have made linearization under the assumption of small cavity thickness η_n. Then, we can relate the heat flux across the

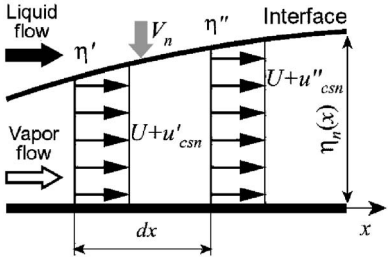

Fig. 3 Control volume for continuity equation

cavity surface q_{Tn} with the latent heat of evaporation as

$$q_{Tn} = -\rho_V L V_n = -\rho_V L U \frac{d\eta_n}{dx} \tag{20}$$

Using Eq. (13) and the normalized source strength $C_{qn} = q_n / U\alpha$ introduced later, Eq. (20) can be written as

$$q_{Tn} = -L\rho_V U \alpha C_{qn} \tag{21}$$

We can obtain the heat flux q_{Tn} also from Fourier's theorem using Eq. (18), using the temperature gradient normal to the cavity

$$q_{Tn} = -\varepsilon\lambda \left.\frac{\partial T_n}{\partial y}\right|_{y=0} = \frac{\varepsilon\lambda\alpha T_\infty}{\sqrt{\pi K_P}} \int_0^x \frac{dC_{\theta n}(\xi)}{d\xi} \frac{1}{(x-\xi)^{1/2}} d\xi \tag{22}$$

where λ denotes the thermal conductivity for the liquid phase. Then, we finally obtain the following equation, which relates the source strength with the temperature distribution along the cavity surface

$$\int_0^x \frac{dC_{\theta n}(\xi)/d\xi}{(x-\xi)^{1/2}} d\xi = -K_1 \sqrt{\frac{\pi}{C\varepsilon}} C_{qn} \tag{23}$$

Here, we have defined K_1 as

$$K_1 = \frac{L}{C_P T_\infty} \left(\frac{\rho_V}{\rho_L}\right) \sqrt{\frac{CU}{a}} \tag{24}$$

where C_p denotes the specific heat for the liquid phase.

From Eqs. (7) and (23), we can easily find that the thermodynamic effect of cavitation can be included through the following thermodynamic parameter Σ^*

$$\Sigma^* = K_1 \cdot K_2 = \frac{L^2}{C_P T_\infty} \left(\frac{\rho_V}{\rho_L}\right)^2 \sqrt{\frac{C}{aU^3}} \tag{25}$$

The parameter Σ^* is equivalent to Brennen's Σ^* [11]which is derived from the thermodynamics of a bubble flowing along the suction surface of a blade, and is also related to Stepanoff's B-factor [1]. We should note that the effect of the magnitude of the mainstream flow, i.e., the rotational speed of cascade, is included in the present analysis through the thermodynamic parameter Σ^*.

Analytical Method. Discretization of singularities distributed along the blades and cavities are made in the same manner as Horiguchi et al. [12], where nodes are distributed more densely near the leading and trailing edges of the blades and cavities. The temperatures along the cavity surface are evaluated at the midpoints between each node as well as at the leading edge. The control points, where boundary conditions are applied, are also placed at the midpoints between each node.

We define the normalized strength of singularities as follows:

$$C_{qn}(\xi) = q_n(\xi)/U\alpha$$

$$C_{\gamma 1n}(\xi) = \gamma_{1n}(\xi)/U\alpha$$

$$C_{\gamma 2n}(\xi) = \gamma_{2n}(\xi)/U\alpha \tag{26}$$

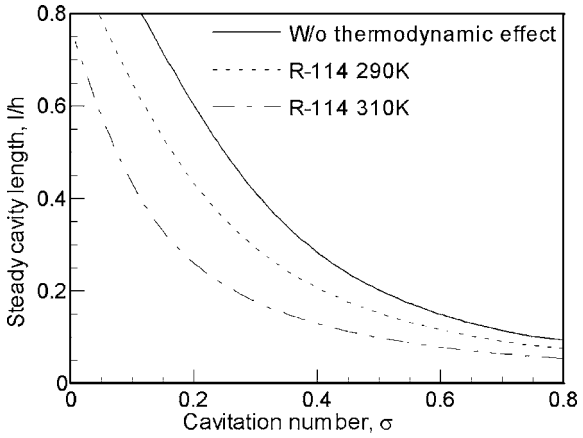

Fig. 4 Numerical results for steady cavity length in the case of R-114 C/h=2.0, β=78.8, α=4.32 deg, and ε=8000

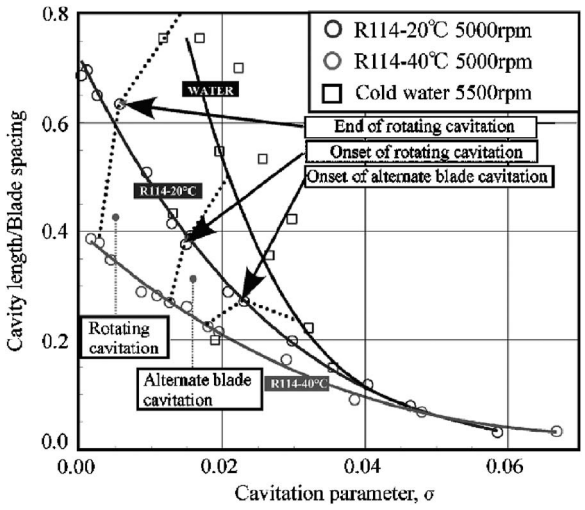

Fig. 5 Experimental results for cavity length in the case of R-114 and cold water (see Ref. [10])

Discretizing the boundary and complementary conditions Eqs. (7), (10)–(12), (14), and (23), we obtain a set of linear equations as follows:

$$[A(l_n)]\{Q\} = \{B\}$$

$$\{Q\} = \{C_{qn}(\xi), \ldots, C_{\gamma 1n}(\xi), \ldots, C_{\gamma 2n}(\xi), \ldots, C_{\theta n}(\xi), \ldots, \sigma/2\alpha\}^T \tag{27}$$

where $A(l_n)$ and B are a coefficient matrix and a constant vector, respectively.

In the analysis, we obtain the cavity length l_n, which satisfies Eq. (27) for the given values of $\sigma/2\alpha$, K_1, and K_2. Because the velocity deviation on the cavity surface u_{csn} is related directly with temperature distribution $C_{\theta n}$ through Eqs. (7) and (23), we can find from Eq. (27) that the cavity length l_n depends only on $\sigma_n/2\alpha$ and the thermodynamic parameter Σ^*.

In the present study, geometrical parameters of cascade are set such that the solidity is C/h=2.0 the stagger is β=78.8 deg and the number of blades is N=4. The angle of attack α=4.32 deg is used if needed. Numbers of nodes for discretization of singularity distributions are 37 both for cavity and wetted surfaces of each blade. It has been found that the present results coincide with those obtained with the number of nodes of 101 and that the errors among them are less than 1%.

Results and Discussions

The present analysis treats the cavity on each blade individually, so that it can be applied to the analysis of cavitating flow with different cavity shapes for each blade such as alternate blade cavitation, which is known to occur for inducers with even blade count [12]. However, in this paper, we concentrate on the cavitating flow with identical cavities for each blade; the results for alternate blade cavitation will be discussed in a future report.

Figures 4 and 5 show the cavity length plotted against the cavitation number obtained by the present analysis and the experiment by Franc et al. [10], respectively. These results are obtained for cold water and Freon R-114 with the temperature of 290 and 310 K. To specify the values of K_1 and K_2, the chordlength of C=0.203 m and U=34.0 m/s (5000 min^{-1}) are used. The turbulent diffusion factor ε is difficult to be estimated and chosen here to be ε=8000 so that the numerical results fit to the experimental results. Note that the value of ε=8000 is smaller than Kato's $\varepsilon = 10^5$, but it is still quite large for the turbulent diffusivity factor. Because, in the experiment, the cavity length is measured at the midspan of the blade, but plotted against the cavitation number defined at the tip, numerical results are also plotted against the cavitation number at the tip. The cavity length is normalized by the blade spacing h.

We can see from Fig. 4 that the cavity becomes shorter for higher temperature due to the thermodynamic effect of cavitation. This tendency coincides with the experimental results shown in Fig. 5. However, if we make a close comparison between Figs. 4 and 5 for lower cavitation number, we can find that the degree of increase of the cavity length against the decrease of the cavitation number is more remarkable for the present analysis. It can be also noticed that the range of cavitation number is very different between in Figs. 4 and 5 even in the case without thermodynamic effect of cavitation. The reason for this is not yet understood, but three-dimensional flow field, especially the flow induced by the leading edge swept of inducer possibly makes an important role, because it is known to be effective for cavitation performance; this cannot be included in 2D analyses like the present one.

In order to decrease the qualitative disagreement between the present analysis and the experiments, we think about the modification of the evaporation model. Figure 6 shows the normalized source distributions C_{qn} in the cases with σ=0.2 and 0.6 for Freon R-114 with the temperature of 290 K. As implied by Eq. (21), the heat flux normal to the cavity surface is proportional to C_{qn}, and for the positive (negative) values of C_{qn}, evaporation (condensation) occurs and the temperature there decreases (increases) due to

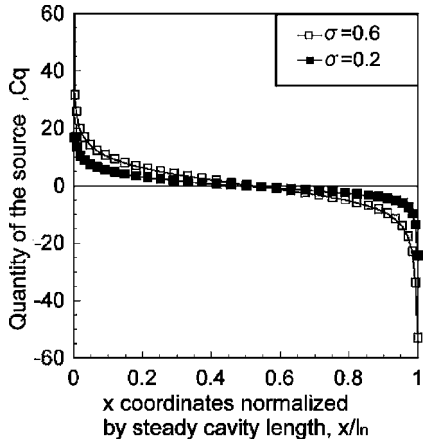

Fig. 6 Distribution of the quantity of the source along the cavity surface in the case of R-114, 290 K

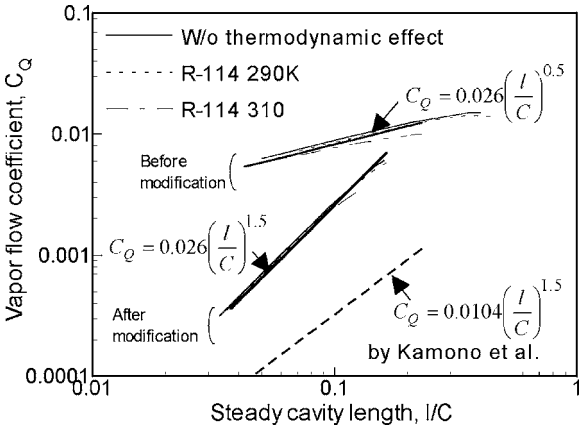

Fig. 7 Vapor flow coefficient required for formation for cavity

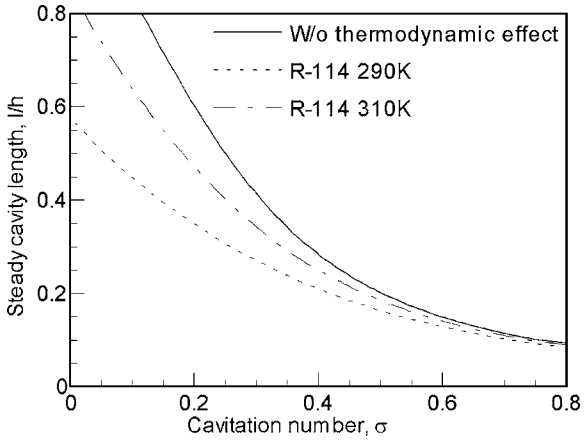

Fig. 8 Numerical results for steady cavity length in the case of R-114, C/h=2.0, β=78.8, α=4.32 deg, and ε=1000

the latent heat exchange between the cavity and the surrounding liquid. In the present closed cavity model, the cavity terminates with a rapid condensation near the trailing edge, but it is reasonable to imagine that some portion of vapor flows away forming a cloud cavitation and condensates far downstream of the cascade. Then, as an extreme case, we hereafter take account only of the heat flux due to evaporation and neglect that due to condensation near the trailing edge of cavity. This large amount of condensation comes from employing the closed cavity model with the linear assumptions of $|u_s|$, $|\nu_s| \ll U$, whereas we have large value of $\nu = U\alpha C_q$ on the cavity surface near the leading and trailing edges of cavity as shown in Fig. 6. This fact also encourages us to decide the neglect of recondensation. Nonlinear effects would be expected there and should be discovered in future studies.

Next, we derive an approximate relation between the evaporation flow coefficient C_Q and cavity length. We define C_Q here as a total amount of evaporation rate required to form the cavity as follows:

$$C_Q = \frac{1}{UC}\int_0^x (-V)d\xi = \frac{1}{UC}\int_0^x U\alpha C_{qn}(\xi)d\xi \tag{28}$$

where the integration is made in the region with $C_{qn} > 0$.

Figure 7 shows the evaporation flow coefficient C_Q obtained by the present analysis. Figure 7 also shows the following empirical relation, which is derived from Kamono et al.'s experiment [13] for ventilated cavitation on the isolated hydrofoil

$$C_Q = 0.0104(l_n/C)^{1.5} \tag{29}$$

We can find from the present analysis that C_Q is almost independent on the thermodynamic effect of cavitation. We can obtain the following approximate expression for C_Q by curve fitting of the results of the present analysis

$$C_Q = 0.026(l_n/C)^{0.5} \tag{30}$$

from which we can find that the present evaporation model leads the smaller exponent on l_n/C, which means the smaller effect of the cavity length on the evaporation flow coefficient for the present analysis. One of the possible explanations for this discrepancy is that the present analysis cannot simulate the cloud cavities shed from the trailing edge of the cavity, which is frequently observed for longer cavities in experiments; longer cavities might require more evaporation to compensate the cavity volume lost by the shedding of cloud cavity. Then, to take account of the effect of the cavity shedding virtually, we multiply the right hand-side of Eq. (23) by l_n/C.

Figure 8 shows the cavity length obtained from the present analysis with abovementioned modifications. The turbulent diffusion factor ε is rechosen to be ε=1000. We can see a good qualitative agreement between the present analysis and the Franc et al.'s experiment [10] shown in Fig. 5.

Franc et al. estimate the bulk temperature depression against the cavity length, defined as follows:

$$\frac{1}{2}\rho_L U^2(\sigma_c - \sigma) = \frac{dP}{dT}\Delta T \tag{31}$$

The bulk temperature depression ΔT is calculated from the cavitation number σ and that for cold water σ_c for the identical cavity length.

Figures 9 and 10 show the temperature depression ΔT obtained by the present modified analysis and Franc et al.'s experiment, respectively. We can find a good qualitative agreement between the present analysis and the experiment. The temperature depression is larger for longer cavities, higher main flow temperature, and larger main flow velocity (rotational speed of cascade.) It can be noticed that the amount of temperature depression is much larger in the present analysis than that in the experiment. The overestimation of the present analysis can be improved by choosing the other value of turbulent diffusivity factor ε, while no physical background can be found to do so. How to choose the

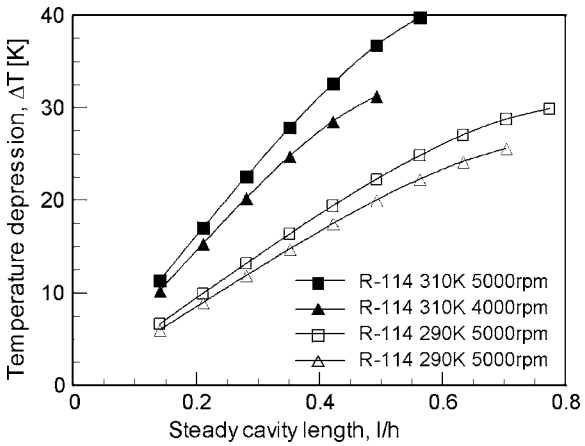

Fig. 9 Numerical results for temperature depression in the case of R-114, C/h=2.0, β=78.8, α=4.32 deg, and ε=1000

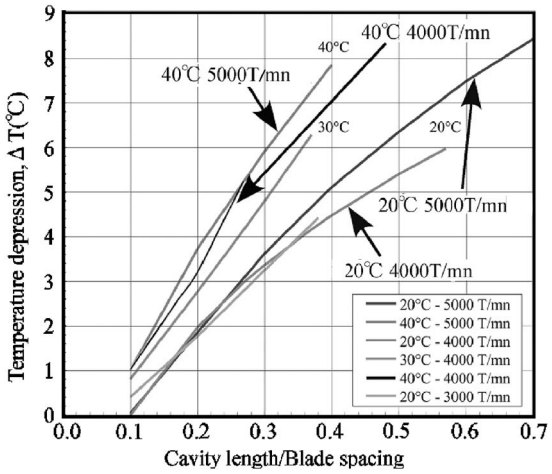

Fig. 10 Experimental results for temperature depression with R-114 (see Ref. [10])

appropriate value of the turbulent diffusivity factor remains unknown and is to be discovered in future studies.

Conclusions

In this paper, we made a simple steady analysis of partial cavitating flow with the thermodynamic effect of cavitation. The results are compared with those of the experiments by Franc et al. [10] for validation. The main results are summarized as follows.

(a) By combining the heat conduction model in the outer flow of cavity and the evaporation model expressing the heat flux across the cavity surface due to vaporization, it becomes possible to treat the local temperature on the cavity surface.

(b) We proposed a simple singularity analysis of partially cavitating flow with thermodynamic effect of cavitation by applying the local vapor pressure based on the local temperature for the cavity boundary condition.

(c) It is shown by a free streamline model that the thermodynamic effect can be included in the analysis only thorough one thermodynamic parameter Σ^*. Thus, for a given geometry of the cascade, the cavity length is a function of $\sigma/2\alpha$ and Σ^*.

(d) After the modifications considering the cloud cavity sledding, the present analysis agrees qualitatively with the experiment.

The present study analytically models the thermodynamic effect of cavitation, whereas some parts such as the determination of the turbulence diffusion factor ε and the inclusions of the effects of cloud cavity shedding rely on the experimental observations. The quantitative estimates of them are crucial to develop this analysis for more practical applications. Further experimental data with cryogenic fluids and sophistication of the model are needed for this purpose. The present analysis can be easily extended to unsteady stability analysis of cavitation instabilities such as rotating cavitation and cavitation surge. This would be made in the near future.

Acknowledgment

The authors would like to thank Daisuke Yumiba for his great help and many valuable discussions on the present study. This study is partly supported by the Grant-in-Aid for Scientific Research for the Ministry of Education, Science, Sports and Culture (No. 17360081).

Nomenclature

A = coefficient matrix in Eq. (27)
a = thermal diffusivity
B = constant vector in Eq. (27)
C = chordlength
C_q, $C_{\gamma 1}$, $C_{\gamma 2}$ = normalized strength of singularities
C_p = specific heat
C_Q = evaporation flow coefficient, defined by Eq. (28)
C_T, C_θ = normalized temperature increase
f = kernel function, defined by Eq. (2)
h = blade spacing
i = imaginary unit
K_1, K_2 = parameter defined by Eqs. (24) and (9)
K_P = $=\varepsilon a/U$
L = latent heat of evaporation
l = cavity length
N = number of blades
n = blade index
P_V = vapor pressure
Q = unknown vector in Eq. (27)
q = source representing cavity
q_T = heat flux on cavity surface
T = temperature
U = main flow velocity
V = local evaporation velocity
u, v = flow velocity components in x and y directions
u_{cs} = velocity deviation on cavity surface
u_s, v_s = velocity deviations in x and y directions
w = complex conjugate velocity
x, y = coordinates
z = complex coordinate, $=x+iy$
α = angle of attack
β = stagger angle
γ_1, γ_2 = bound vortices representing blade
ΔT = temperature depression
ε = turbulent diffusion factor
η = cavity thickness
λ = thermal conductivity
ρ_L, ρ_V = densities of liquid and vapor phases
Σ^* = thermodynamic parameters, defined by Eq. (25)
σ = cavitation number

Subscripts

n = blade index
∞ = upstream infinity

References

[1] Stepanoff, A. J., 1964, "Cavitation Properties of Liquids," ASME J. Eng. Power, **86**, pp. 195–200.
[2] Ruggeri, R. S., and Moore, R. D., 1969, "Method for Prediction of Pump Cavitation Performance for Various Liquids, Liquid Temperatures, Rotative Speeds," NASA TN D-5292.
[3] Fruman, D. H., Reboud, J.-L., and Stutz, B., 1999, "Estimation of Thermal Effects in Cavitation of Thermosensible Liquids," Int. J. Heat Mass Transfer, **42**, pp. 3195–3204.
[4] Billet, M. L., and Weir, D. S., 1975, "The Effect of Gas Diffusion on the Flow Coefficient for a Ventilated Cavity," ASME J. Fluids Eng., **97**(4), pp. 501–506.
[5] Kato, H., 1984, "Thermodynamic Effect on Incipient and Development of Sheet Cavitation," *Proc. of International Symposium on Cavitation Inception*, ASME FED, **16**, pp. 127–136.
[6] Tokumasu, T., Sekino, Y., and Kamijo, K., 2003, "A New Modeling of Sheet Cavitation Considering the Thermodynamic Effects," *CD-ROM Proc. 5th International Symposium on Cavitation*, Cav03-GS-16-003.
[7] Tani, N., and Nagashima, T., 2002, "Numerical Analysis of Cryogenic Cavitating Flow on Hydrofoil—Comparison Between Water and Cryogenic Fluids," *CD-ROM Proc. 4th Int. Conf. Launcher Technology*.
[8] Watanabe, S., Tsujimoto, Y., and Furukawa, A., 2001, "Theoretical Analysis of Transitional and Partial Cavity Instabilities," ASME J. Fluids Eng., **123**(3), pp. 692–697.

[9] Watanabe, S., Sato, K., Tsujimoto, Y., and Kamijo, K., 1999, "Analysis of Rotating Cavitation in a Finite Pitch Cascade Using a Closed Cavity Model and a Singularity Method," ASME J. Fluids Eng., **121**(4), pp. 834–840.
[10] Franc, J.-P., Rebattet, C., and Coukon, A., 2004, "An Experimental Investigation of Thermal Effects in a Cavitating Inducer," ASME J. Fluids Eng., **126**(5), pp. 716–723.
[11] Brennen, C. E., 1995, *Hydrodynamics of Pumps*, Concepts ETI, Inc. and Oxford University Press, New York.
[12] Horiguchi, H., Watanabe, S., Tsujimoto, Y., and Aoki, M., 2000, "A Theoretical Analysis of Alternate Blade Cavitation in Inducers," ASME J. Fluids Eng., **122**(1), pp. 156–163.
[13] Kamono, H., Kato, H., Yanaguchi, H., and Miyagawa, M., 1993, "Simulation of Cavity Flow by Ventilated Cavitation on a Foil Section," *Proc. of Cavitation and Multiphase Flow Forum*, ASME FED, **153**, pp. 183–189.

Numerical Model to Predict Unsteady Cavitating Flow Behavior in Inducer Blade Cascades

R. Fortes-Patella[1]
e-mail: fortes@hmg.inpg.fr

O. Coutier-Delgosha[2]

J. Perrin

J. L. Reboud[3]

Laboratoire des Ecoulements Géophysiques et Industriels,
LEGI–INPG,
BP 53, 38041 Grenoble cedex 9, France

The cavitation behavior of a four-blade rocket engine turbopump inducer is simulated. A two-dimensional numerical model of unsteady cavitation was applied to a blade cascade drawn from an inducer geometry. The physical model is based on a homogeneous approach of cavitation, coupled with a barotropic state law for the liquid/vapor mixture. The numerical resolution uses a pressure-correction method derived from the SIMPLE algorithm and a finite volume discretization. Unsteady behavior of sheet cavities attached to the blade suction side depends on the flow rate and cavitation number. Two different unstable configurations of cavitation are identified. The mechanisms that are responsible for these unstable behaviors are discussed, and the stress fluctuations induced on the blade by cavitation instabilities are estimated. [DOI: 10.1115/1.2409320]

Introduction

To achieve operation at high rotational speed and low inlet pressure, rocket engine turbopumps are generally equipped with an axial inducer stage. Under such operating conditions, cavitation develops on the suction side of the blades and at inducer periphery near the tip. When pressure is decreased from cavitation inception, vapor develops more and more and, finally, leads to the inducer performance breakdown (Fig. 1).

Between low-cavitation conditions and the performance drop, for some particular range of the cavitation number, unsteady phenomena may appear, associated with different blade cavitation patterns. Figure 2 illustrates successive flow patterns observed experimentally in the case of a H2 inducer for different values of the cavitation parameter τ' [1].

At cavitation inception, a steady and balanced flow pattern with one short attached cavity on each blade is observed from flow visualizations (Fig. 2(1)). When the cavitation parameter is slightly decreased, a steady and alternate cavitating configuration appears (only on four-blade inducers) with alternatively one short and one long cavity (Fig. 2(2)). Then flow visualizations achieve to identify an unsteady flow pattern (Fig. 2(3)): rotating cavitation appears at low cavitation parameter [2] just above breakdown. Unbalanced attached cavities are observed in the different channels, their distribution rotating faster than the inducer [1,3] and leading to large radials loads on the shaft [4]. Finally, near the breakdown of the inducer, a steady and balanced flow pattern with fully developed cavitation is observed (Fig. 2(5)).

Over the last few years, numerical models have been developed to predict the cavitation instability in inducers [5]. These models are based on stability analyses and linear approach, taking into account the total flow-rate variations through a cavitating blade-to-blade channel [6–9], or calculating the flow around attached cavities [10–12].

To improve the understanding and the prediction capability of cavitation instabilities, numerical and experimental analyses are developed through collaborations between the LEGI, the Rocket Engine Division of Snecma and the French space agency CNES. In the present paper, the cavitation behavior of a four-blade inducer is simulated using a two-dimensional (2D) model of unsteady cavitating flow developed at LEGI [13–16].

The paper illustrates a qualitative study whose aims are better understanding the instability phenomena and to propose a methodology for further parametric study. In spite of the progress of CFD, 3D unsteady calculations in inducer geometries are very time consuming and 2D approach is still interesting (even if it cannot represent completely the original three-dimensional case).

1 Physical and Numerical Model

Numerical simulation of the cavitating flow in the inducer was performed with the objective to take into account the cavitation sheets attached to the blades and their unsteady behavior. The 2D numerical model of unsteady cavitating flow IZ, developed in previous studies with the support of the CNES-Centre National d'Etudes Spatiales [13–15], was adapted to 2D blade cascades [16]. The main features of the models are:

- The liquid-vapor mixture is described as a single fluid, whose density ρ rapidly varies between the pure liquid density ρ_l and the pure vapor one ρ_v when the static pressure in the flow field reaches the vapor pressure. The fluid density is managed by a barotropic state law $\rho(p)$, as described in previous works. The barotropic law is given as a function of the maximum slope $1/A^2_{min}$, where $A^2_{min}=\partial P/\partial\rho$.
- 2D unsteady Reynolds-averaged Navier-Stokes equations are applied to model the homogeneous mixture. The numerical resolution uses a pressure-correction method derived from the SIMPLE algorithm on 2D structured curvilinear-orthogonal meshes. It is based on a conservative finite volume formulation (HLPA nonoscillatory second-order convection scheme) and on an implicit method for the time discretization. The used turbulence model is the classical k-ε RNG model, associated with wall functions along solid boundaries.
- Other boundary conditions are (Fig. 5): imposed velocity at the mesh inlet (the flow velocity is deduced from the classical value $Q/\rho S_{flow}$), imposed static pressure at the outlet, and periodicity or connection conditions between the different channels of the blade cascade. These conditions are ap-

[1]Corresponding author.
[2]Now at LML/ENSAM Lille.
[3]Now at CNRS-LEMD, University of Grenoble, France.

Contributed by the Fluids Engineering Division of ASME for publication in the JOURNAL OF FLUIDS ENGINEERING. Manuscript received November 25, 2003; final manuscript received May 23, 2006. Review conducted by Joseph Katz.

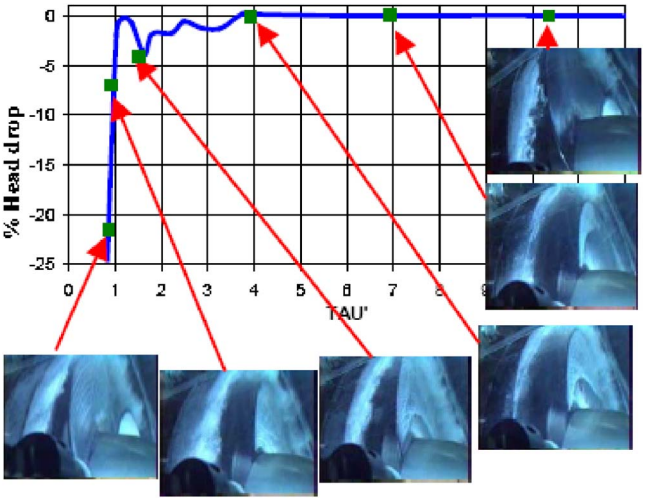

Fig. 1 Experimental performance chart for a H2 turbopump inducer (tests in cold water) [1]

plied along non-matching boundaries, through a special treatment developed in [16] to assure the best transfer of both mass and momentum fluxes.

The details of the numerical resolution were presented by [15] and [16]. A complete validation of the method was performed, and the influence of the numerical parameters was widely investigated. The results are reported in [15].

2 Geometry

The three-dimensional (3D) inducer geometry considered in the present study is illustrated by the Fig. 3. Even at nominal flowrate, the inducer is designed to operate with nonzero incidence angle. Nevertheless, in the range of running conditions, the angle of attack remains very small because of the variable thread and

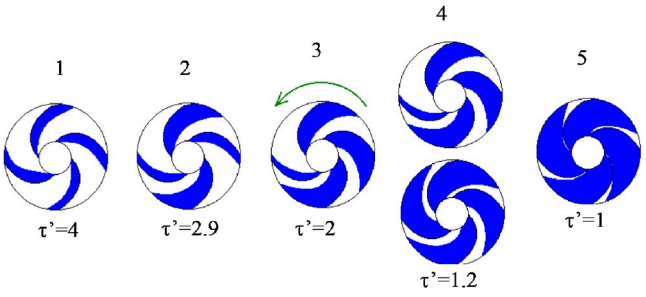

Fig. 2 Sketches of cavitation patterns for various cavitation parameters and their correspondence to the performance curve [1]

Fig. 3 3D inducer

the associated curvature of the blades. In these conditions, the inlet backflow is not relevant and a 2D geometry approach can be adopted for qualitative and parametric studies. It is important to note that tip clearance and backflow effects are neglected, and consequently, the applicability of the approach proposed in this paper might be limited to high inducer flow rates.

Hence, to study the unsteady behavior of the cavitating flow, some computations are performed in a four-blade cascade derived from an entire inducer. The transformation from the 3D geometry to the 2D blade cascade leads to neglect the peripheral cavitation in the inducer: only attached sheets of cavitation on the blades will be considered. To obtain the 2D geometry, the 3D inducer (Fig. 3) is cut at a constant radius R_c.

In the present paper we present results obtained for $R_c=70\%$ of the tip radius R. The resulting shape of the blade cut in the plane $(R_c \cdot \theta, Z)$ is given in Fig. 4.

We use a 195×40 structured mesh per channel, giving a total of 31,200 internal nodes when calculating the four-blade cascade. A special contraction of the mesh is applied close to the blades (Fig. 5) to ensure that the first cells remain in the logarithmic region of the turbulent boundary layer, and apply the k-ε RNG turbulence model with wall functions. The application of periodicity and connection boundary conditions needs also adequate meshes (small curvature and limited variation of cell sizes) in the connection zones between channels.

The calculations are done in the rotating frame. The imposed flow velocity **W** at the mesh inlet is given by

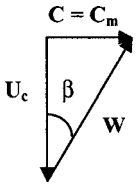

where

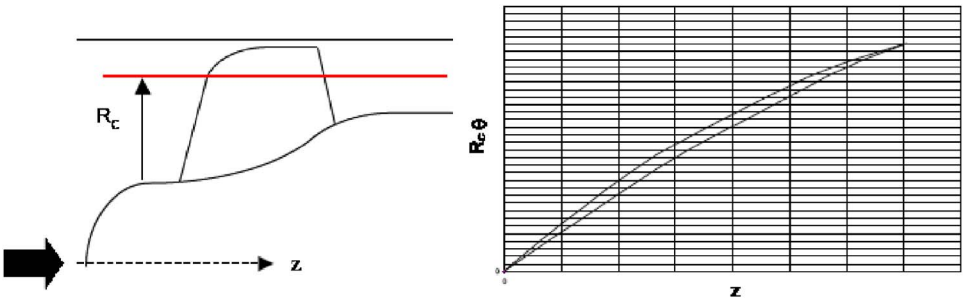

Fig. 4 Blade cut in the plane $(R_c.\theta, Z)$

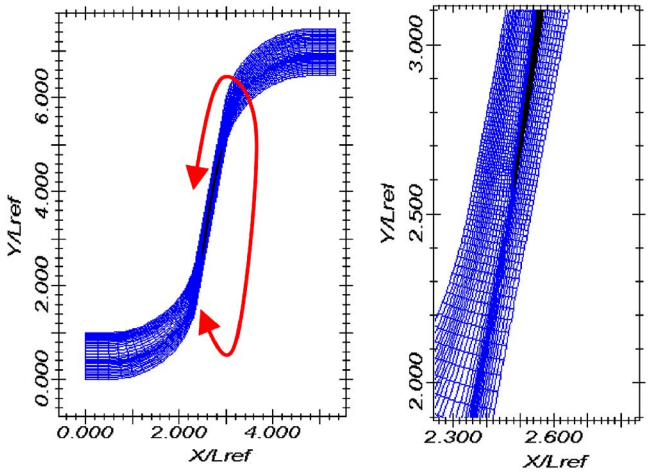

Fig. 5 Curvilinear, orthogonal mesh of a single channel (general view and zoom at the blade leading edge)

$$\phi = \tan\beta = \frac{C_m}{(\Omega R_C)} \tag{1}$$

The considered number Reynolds is equal to 10^6 and the barotropic law slope is given by $A_{\min}/V_{\text{ref}}=0.1$. The convergence criterion is given by a residue of 10^{-6} for the mass balance equation and a residue of 3.10^{-4} for momentum equations.

3 Results

Quasi-steady calculations are performed on the one-channel mesh and unsteady computations are performed on the four-blade mesh. The periodicity condition is then applied between the fourth and first channels, reflecting the true periodicity of the actual flow field. The time step, mesh, and turbulence model are chosen with the focus on capturing the low-frequency fluctuations of the attached cavity, rather than the local unsteadiness in the cavitation sheet wake (cloud shedding): the time step is fixed equal to 1% of the blade passage time T_{ref}. Successive time accurate computations are performed at fixed cavitation number and flow-rate coefficient.

3.1 Head Drop Chart. Several four-channel computations are performed at nominal flow rate, with a cavitation number σ varying from low-cavitation conditions down to the final performance drop. The corresponding head drop chart is drawn on Fig. 6. Some difference with the performance chart obtained with a single channel computation appears clearly, particularly for $0.6<\sigma<0.75$. This is due to the appearance, at these operating points, of unstable cavitating behaviors. We first present in Sec. 3.2 the results obtained in stable configurations ($\sigma>0.75$ or $\sigma<0.6$), and then the mechanisms of unstable configurations will be detailed in Sec. 3.3.

3.2 Stable Configurations. At nominal flow rate, stable configurations correspond to cavitation numbers higher than 0.75 or lower than 0.6. Between these two extrema, unstable conditions are obtained, which will be detailed in Sec. 3.3.

For $\sigma=0.8$, sheets of cavitation are small, as indicated on Fig. 7(*a*). The four cavities remain identical, even if the calculation is continued for a long time, or if perturbations are simulated to enhance a possible instability. The time evolution of the cavity in the first channel, reported in Fig. 7(*b*), confirms that sheets of cavitation are completely stable after the initial transient. For these flow conditions, the performance of the inducer is only slightly affected by the presence of vapor, since its decrease does not exceed 5%.

A similar configuration is obtained for a cavitation number equal to 0.6 (i.e., the inferior limit value). The sheets of cavitation are much more developed and responsible for the important performance drop that is observed at this operating point: the obstruction due to the cavities modifies the velocity fields on the blades, which leads to the head drop.

3.3 Unstable Configurations. For some particular values of the cavitation number, nonsymmetrical configurations of sheets of cavitation on the four blades are obtained. These configurations are periodical and involve physical fluctuations of almost constant magnitude in the flow field, after the initial transient period. Two main configurations were observed.

3.3.1 First Configuration for $\sigma=0.7$ (Nominal Flow Rate). At this operating point, mass flow rates in the four blade-to-blade channels become different. Their evolution is reported in Fig. 8. It appears that at a given time, the mass flow rate in channels 1 and 3 is very different from the mass flow rate in channels 2 and 4. All evolutions are periodical and suggest a coupling between, respectively, channels 1 and 3, and channels 2 and 4. The corresponding evolution of the four sheets of cavitation between $T/T_{\text{ref}}=115$ and $T/T_{\text{ref}}=135$ is represented in Fig. 9.

It is clear in Fig. 9 that mass flow-rate variations in the different channels are strongly correlated with the size evolution of the

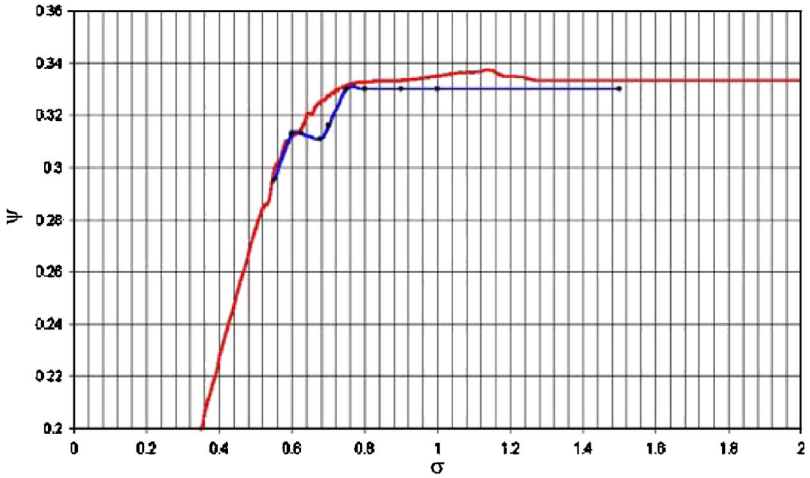

Fig. 6 Comparison between the performance charts obtained with four-blade computations (—•—) and with single blade computations (———) at nominal flow rate

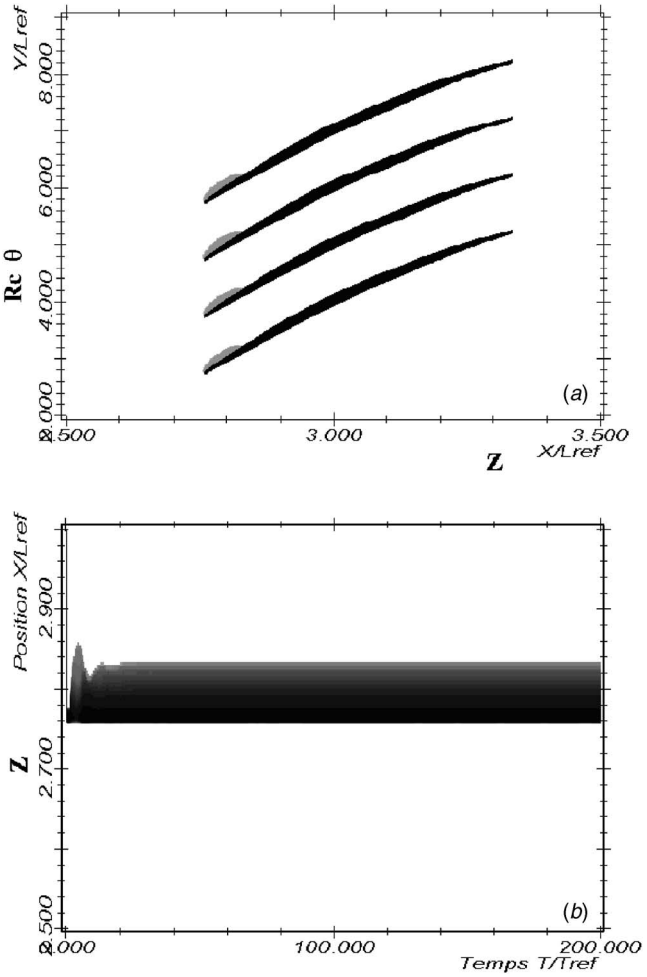

Fig. 7 Cavitation development for $\sigma=0.8$ and $Q=Q_n$: (*a*) Density fields: white corresponds to pure liquid, and black to pure vapor (scale ratio $x/y\approx10$). (*b*) Time evolution of the cavity in the first channel. The time is reported in abscissa, and the *Z* position on the blade is graduated in ordinate. The colors (shading) represent the density values. At a given point in time and position, the color (shading) indicates the minimum density in the corresponding cross section of the channel.

sheets of cavitation. This continuous variation of cavities in channels 1 and 3 is the opposite of the one in channels 2 and 4, as for the mass flow rate in Fig. 8. In the first two configurations of Fig. 9, for example, sheets of cavitation are growing in channels 1 and

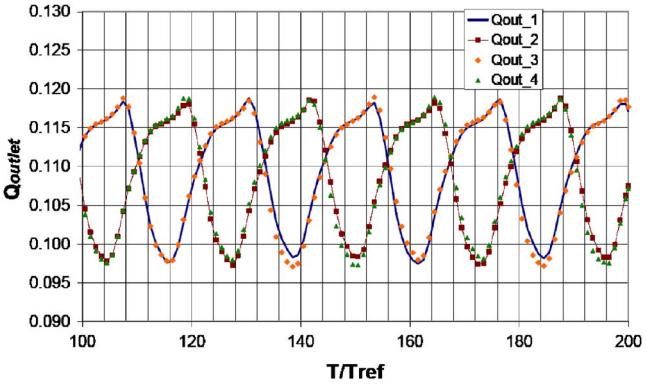

Fig. 8 Time evolution of the nondimension mass flow rate in the four channels ($\sigma=0.7$ and $Q=Q_n$)

3, whereas they decrease in channels 2 and 4; at the same time, mass flow rate is decreasing in channels 1 and 3, and increasing in channels 2 and 4. This is due to the obstruction generated by the biggest cavities, which leads to a deviation of the flow toward free channels (i.e., channels in which cavities are small). This mechanism is amplified by the increase of the void ratio in the cavitation sheets during the step of growth: the vapor makes the flow to curve round the leading edge of the corresponding blades, and a part of the flow rate passes in the upper channel. This is illustrated by Fig. 10, which shows (inside the circle) the deviation imposed by the biggest cavities to the flow.

A spectral analysis of the mass flow-rate evolution downstream from the blades is proposed in Fig. 11(*a*). The frequencies are indicated in the rotating frame. A characteristic frequency $f_c=0.16\ f_0$ (f_0 is the rotating frequency of the inducer) is obtained, which is consistent with the periodical mass flow-rate evolutions reported previously in Fig. 8. Indeed, f_c corresponds to the evolution of the sheets of cavitation on the blades. This phenomenon also appears on the spectral analysis in the absolute frame of the static pressure far upstream from the blades, drawn in Fig. 11(*b*): the frequency $f_{ca}=0.32\ f_0$ is predominant. $f_{ca}=2\times f_c$, the factor 2 being due to the alternate cavitation pattern on the blades. We can observe also other frequencies of about $4f_c$, $6f_c$, and $8f_c$.

In order to deepen the frequency study, we have plotted also the spectral analysis of the total pressure signal near to the leading edge of the blade cascade in the absolute frame (Fig. 12). These results indicate two characteristic frequencies of $(2f_0+f_c)$ and $(2f_0-f_c)$. The combination of these frequencies reproduces mass flow fluctuation with the frequency of f_c in the rotating frame shown in the Fig. 11(*a*). Moreover, the combination of these frequencies seems to be also related to the frequencies $2f_c$, $4f_c$, $6f_c$, and $8f_c$ observed in Fig. 11(*b*).

We will name this configuration "unstable alternate cavitation." This special configuration was found only for the values ($\sigma=0.7$, Q_n) and ($A_{\min}/V_{\text{ref}}=0.1$, $\text{Re}_y=10^6$, $10<y^+<60$). To deepen the analysis of this configuration, we have performed numerical tests with different meshes, Reynolds numbers, y^+ and time-step values. According to our numerical tests, for a different mesh (390×60; $10<y^+<20$; $A_{\min}/V_{\text{ref}}=0.1$, $\text{Re}y=10^6$), the simulations give a regular super synchronous cavitation instead of unsteady alternate cavitation.

For this operating point ($\sigma=0.7$, Q_n) and 195×40 mesh, the numerical tests pointed out also the influence of the following:

- The celerity value: for $A_{\min}/V_{\text{ref}}=0.04$ ($\text{Re}y=10^6$, $10<y^+<60$), we observe a regular supersynchronous cavitation with a characteristic frequency of $1.6\ f_0$. As a matter of fact, for smaller $A_{\min}$ values, the cavitation length and thickness change and the unsteady cavitation behavior is also modified.
- The Reynolds number: for $\text{Re}y=3.10^6$ (corresponding to a range of $20<y^+<100$ in the case of 195×40 mesh), the unsteady alternate cavitation becomes very irregular and changes to a supersynchronous configuration. Indeed, the trigger mechanism of the instabilities seems to be related to the friction in the boundary layer flow and, consequently, to the values of y^+ (calculated as a function of Reynolds number and mesh thickness).

It is interesting to note that a recent work [17], concerning the same geometry but based on a different numerical model and mesh ($20<y^+<100$), pointed out also an unsteady alternate cavitation configuration for $\sigma=0.7$ and $Q=Q_n$. In this same work, a steady alternate cavitation was observed for σ of ~0.77.

3.3.2 Second Configuration for $\sigma=0.625$ (Nominal Flow Rate). If the cavitation number is decreased down to a value between 0.6 and 0.65, another type of unstable behavior is obtained. It is characterised by four different sizes of the sheet of cavitation

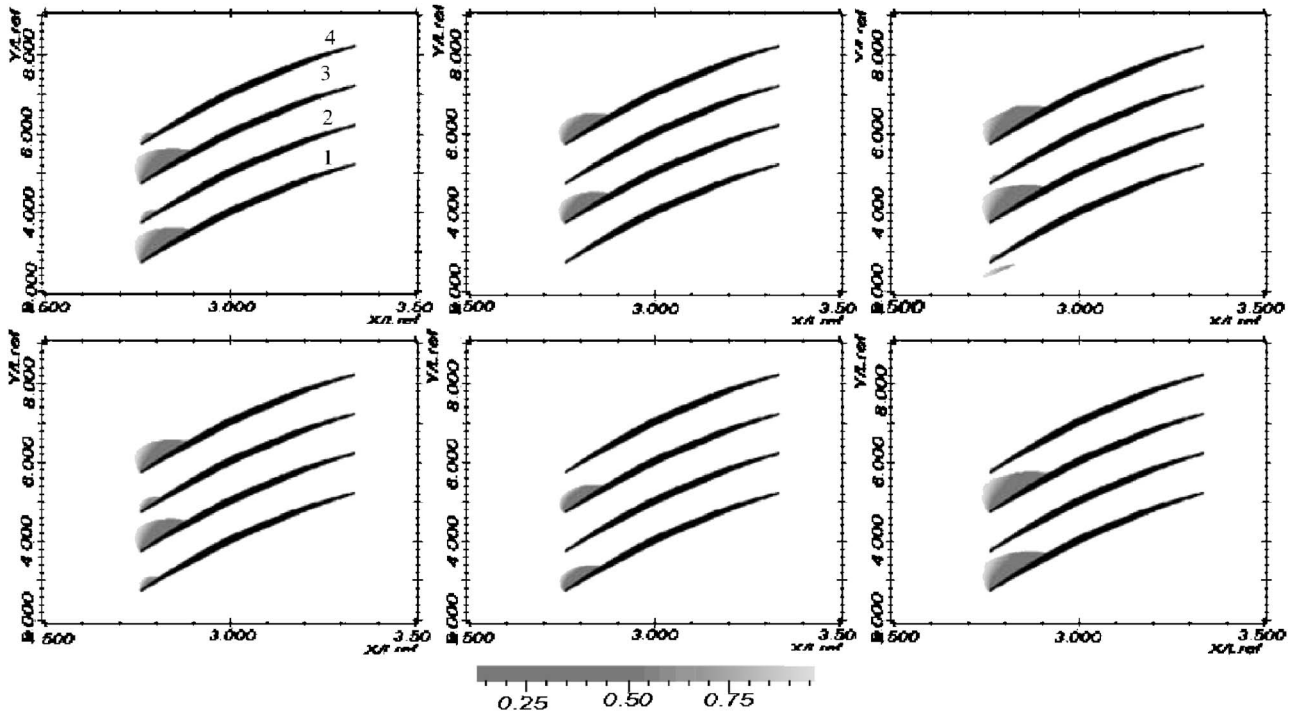

Fig. 9 Time evolution of the sheets of cavitation ($110 < T/T_{ref} < 135$)

in the four channels. No simple correlation between channels is detectable at any time, as can be seen in Fig. 13, in which the evolution during 155 T/T_{ref} of the four mass flow rates in the four channels is reported. As previously, the instability is periodical after the initial transient period, with mass flow rate fluctuations of constant magnitude in all channels. Nevertheless, the mechanisms that govern the cavity evolution in each channel are much more complicated than in the first unstable configuration, since all cavities interact.

The spectral analysis of the mass flow rate downstream from the blade is proposed in Fig. 14(*a*). A characteristic frequency $f_c = 0.38\ f_0$ clearly appears in the rotating frame, with two harmonic frequencies. It corresponds to the evolution of the mass flow rates in the four channels, and this phenomenon in the absolute frame has a higher frequency than the inducer rotation. The main characteristic frequency $f_c = 1.38$ in the absolute frame is observed, from the spectral analysis of the upstream static pressure evolution drawn in Fig. 14(*b*). This is the reason why such unstable configuration is called supersynchronous rotating cavitation. It means that the configuration in the inducer at a given time (the four different sizes of the cavities) rotates faster than the inducer

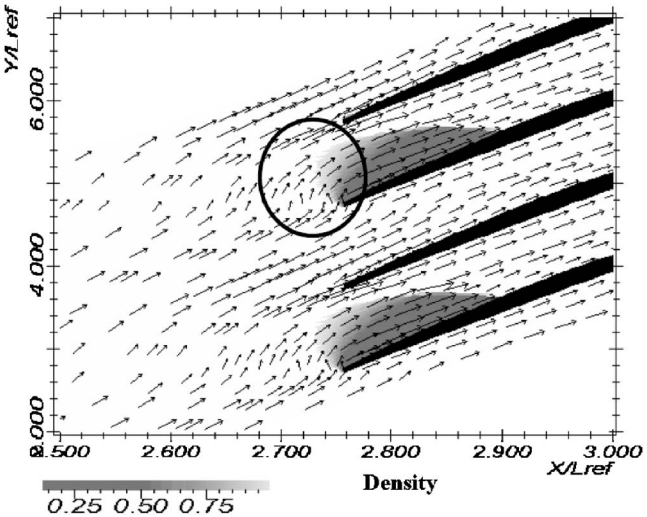

Fig. 10 Deviation of velocities due to high void ratio ($T = 110\ T_{ref}$)

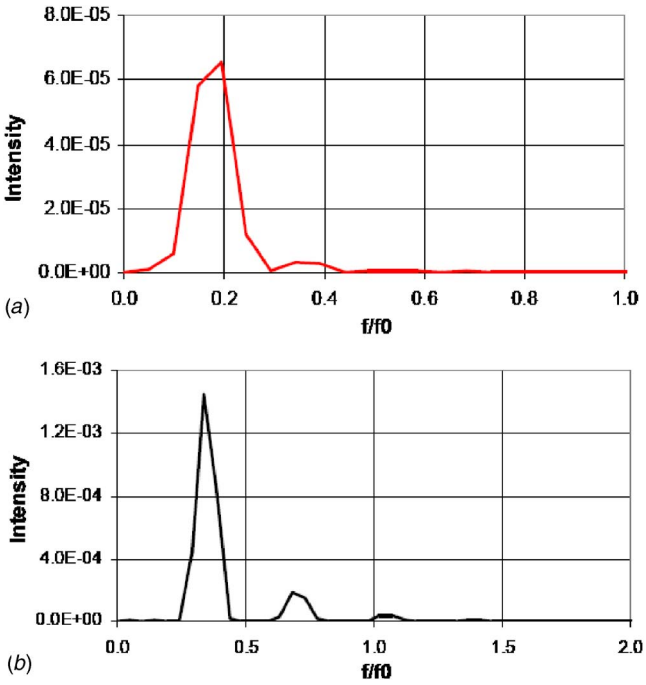

Fig. 11 Spectral analysis ($\sigma = 0.7$, $Q = Q_n$): (*a*) Mass flow rate downstream from the blades, in the rotating frame and (*b*) static pressure far upstream from the blades, in the absolute frame (results concerning a calculation time of about 30 rotation periods of the inducer)

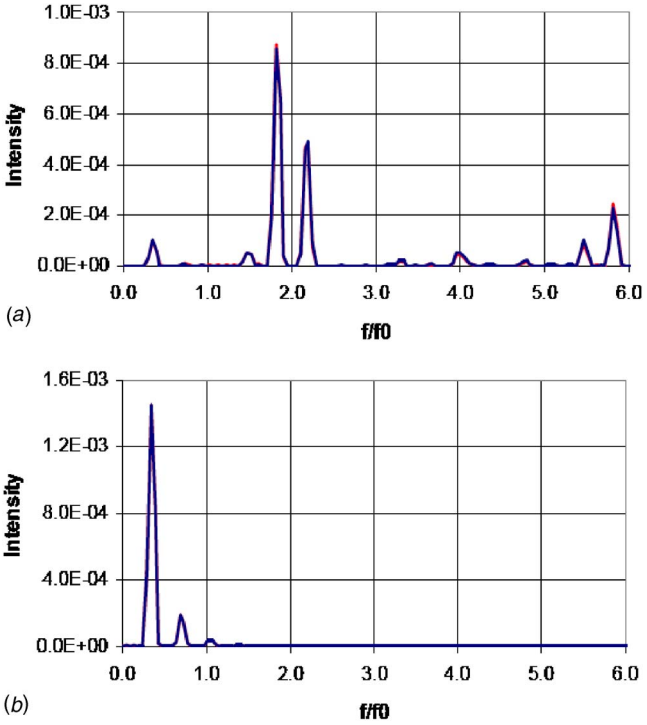

Fig. 12 Spectral analysis (σ=0.7, $Q=Q_n$): (*a*) Total pressure near to the leading edge, in the absolute frame and (*b*) total pressure far upstream from the blades, in the absolute frame (results concerning a calculation time of ~30 rotation periods of the inducer)

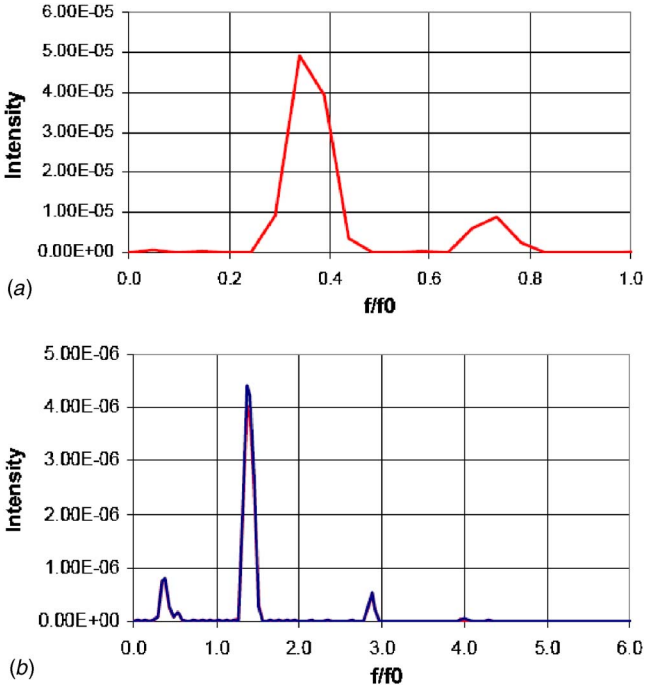

Fig. 14 Spectral analysis (σ=0.625, $Q=Q_n$): (*a*) Mass flow rate downstream from the blades, in the rotating frame and (*b*) static pressure far upstream from the blades, in the absolute frame (results concerning a calculation time of ~30 rotation periods of the inducer)

itself.

All frequency analyses performed in the present study have been carried out from calculations whose duration was at least 25 periods of inducer rotation. The whole of performed unsteady cavitating simulations represent a great effort in terms of computation time, and, at present, these kinds of frequency analyses cannot be done from 3D calculations. It is worth noting that the considered time step and time calculations do not allow us to detect very low frequencies (below 0.1 f_0).

3.4 Efforts on the Blade in Unstable Configurations.

3.4.1 Unstable Alternate Cavitation. To improve the understanding of the effects of cavitation instabilities on the blade and on the entire inducer, the fluctuations of the forces acting on the blades have been calculated and drawn in Fig. 15. The objective is to estimate the magnitude of the stress fluctuations. The stresses are calculated through the momentum conservation in a control volume surrounding one blade. Projecting this relation, respectively, onto the normal to the inlet boundary and onto the normal to the rotation axis gives the axial and the transverse components of the nondimensional hydrodynamic force, whose time evolution

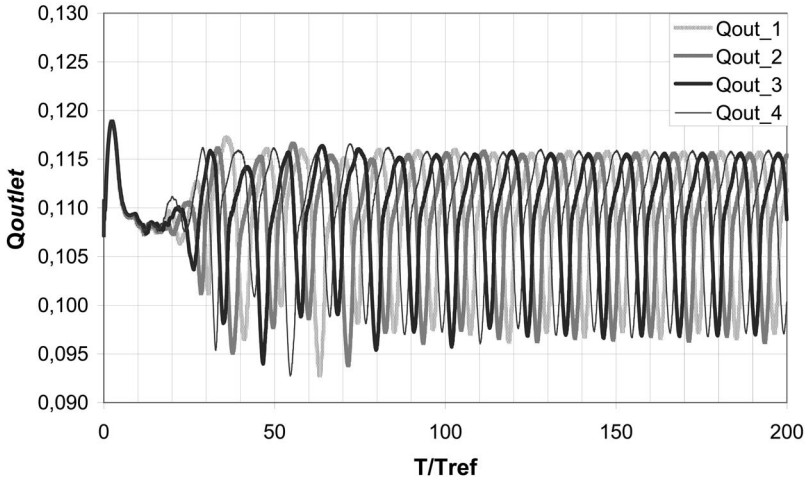

Fig. 13 Time evolution of the non dimension mass flow rates in the four channels (σ=0.625, $Q=Q_n$)

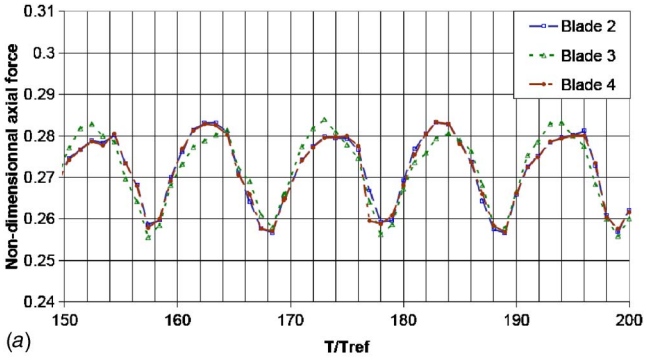

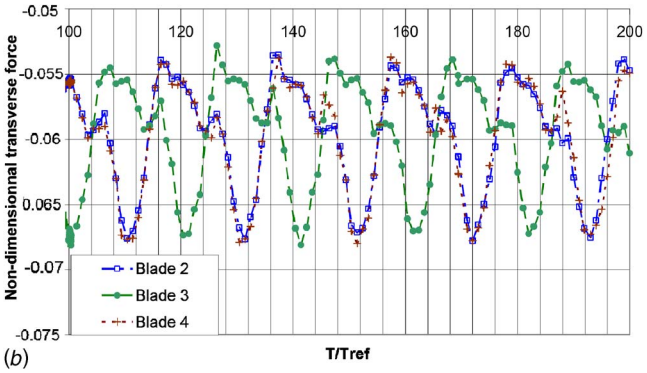

Fig. 15 Time distribution of the axial and transverse forces on the blades (σ=0.7 and $Q=Q_n$)

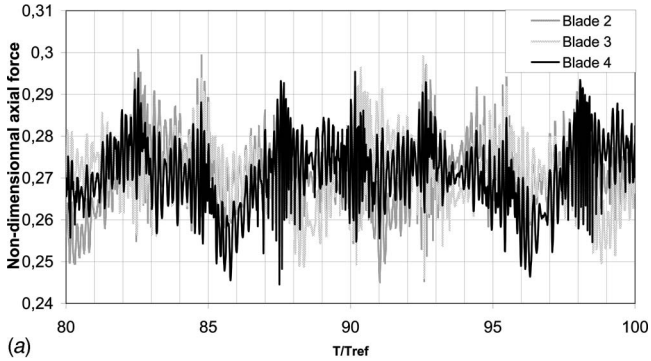

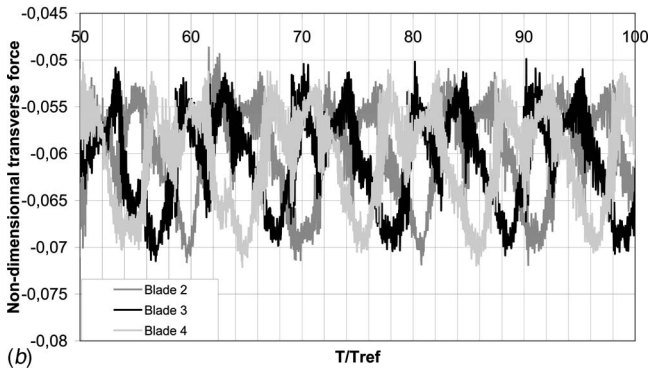

Fig. 16 Axial and transverse forces on the blades (σ=0.625 and $Q=Q_n$)

is then represented in Figs. 15(*a*) and 15(*b*) for three different blades. Stress fluctuations in these figures are generated by unsteady cavitation.

The mean nondimensional axial force $F_x/(\rho_{\text{ref}}V_{\text{ref}}^2L_{\text{ref}}^2)$ can be estimated to 0.27, whatever blade we consider, and the order of magnitude of the fluctuations is ~0.016. Thus, cavitation instabilities lead in the present case to fluctuations of the axial force equal to 6% of the mean force. In the case of the transverse force, the fluctuations reach 13% of the mean force.

3.4.2 Supersynchronous Configuration. The corresponding force evolutions are represented in Figs. 16(*a*) and 16(*b*). In the case of the second blade, for example, the mean axial force still equals 0.27, while the fluctuations magnitude is ~0.03: rotating cavitation is responsible, in this case, for fluctuations whose magnitude can be estimated to 10% of the mean effort. In the case of the transverse force, the fluctuations reach almost 20% of the mean force.

According to these first calculations, the simulated unstable alternate cavitation seems to be less critical for the inducer than with the calculated supersynchronous rotating cavitation. In this case, axial forces on the blades substantially increase and the periodical forces acting on the blades could be responsible for some damage to the inducer.

4 Conclusion

Computations were performed at different operating conditions by varying the mass flow rate and the cavitation number. The resulting performance charts of the blade cascade at the calculated mass flow rates are reported in Fig. 17. Stable and unstable cavitation configurations are also indicated, so that the limit of the rotating cavitation behavior can be identified. Results for mass flow rates $<0.9\ Q_n$ are not reported because of the numerical difficulties that we encountered at these flow conditions. Indeed, at partial flow rate, angle of attack of the flow at the blade leading edge and cavity thickness both increase. In case of rotating behavior, it can result in the complete obstruction of a channel, which induces serious numerical problems. Moreover, at partial flow rates, tip leakage and backflow influence cannot be neglected and a 2D approach would probably lead to high errors.

It can be seen (Fig. 17) that the cavitation parameter range of rotating cavitation increases when the flow-rate coefficient decreases. This result agrees with experimental observations [3,18]. At nominal flow rate Q_n, the experimental instability range is about $\Delta\sigma_{\text{exp.}}=0.15$, which is consistent with the results obtained previously by [16] in the case of a similar four-blade inducer geometry. The mass flow-rate limit for appearance of unstable configuration ($1.2\ Q_n$) is also identical to the one obtained in this previous study. Further work is now needed to assess the prediction capability of the model. Therefore, improvements of the analysis of 3D inlet flows and study of the influence of the cascade design by numerical simulations are in progress, in parallel to the development of a full 3D model [17,19].

Acknowledgment

The authors wish to thank Snecma (Rocket Engine Division) and the French space agency CNES for their support to the present work.

Nomenclature

$A_{\min}$ = slope of the barotropic state law: $A_{\min}^2=\partial P/\partial\rho$ (minimum speed of sound in the vapor/liquid mixture)

Q, Q_n = nondimensional mass flow rate, nominal mass flow rate

$\mathbf{C}(C_m, C_u)$ = velocity vector in fixed frame: $C_m=Q/(\rho S_{\text{flow}})$

L_{ref} = reference length $L_{\text{ref}}=\pi R_c/2$

p, P = static pressure, total pressure: $P=p+0.5\rho_l\mathbf{C}^2$

p_v = vapor pressure

R_c = cut radius for the passage from 3D to 2D

R, θ, Z = cylindrical coordinates

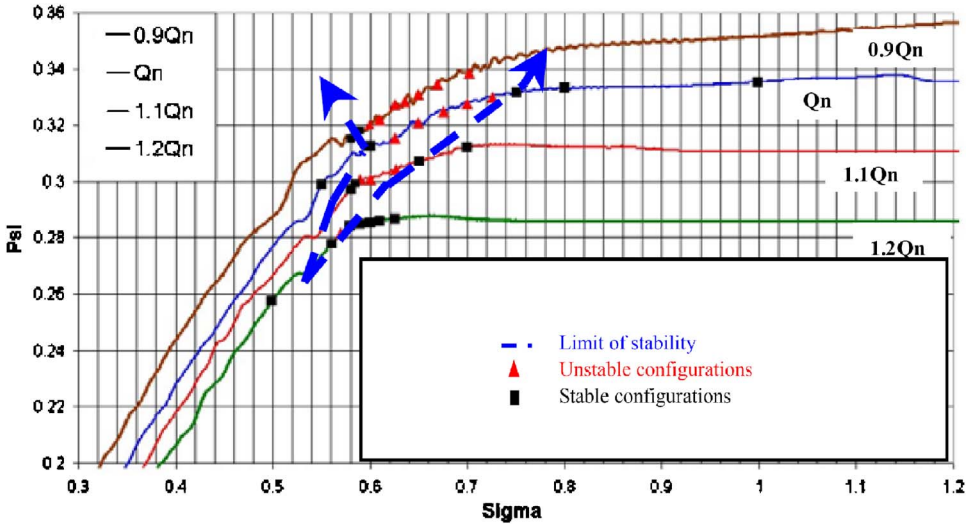

Fig. 17 Performance charts at several mass flow rates

T_{ref} = reference time: $T_{ref}=L_{ref}/V_{ref}$
V_{ref} = reference velocity: $V_{ref}=R_c\Omega$
$\mathbf{W}(W_m, W_u)$ = velocity vector in relative frame
y^+ = nondimensional distance to the boundary
Ω = angular rotation speed of the inducer (rad/s)
U = training velocity at inducer tip radius R_{tip}: $U=R_{tip}\Omega$
τ, τ' = cavitation parameter for inducers, $\tau'=\tau/\tau_c$
τ_c = critical value. $\tau=(P_{inlet}-p_v)/(0.5\rho_l R_{tip}^2\Omega^2)$
σ = cavitation nb (downstream): $\sigma=(P_{outlet}-p_v)/(0.5\rho_l V_{ref}^2)$
f, f_0 = frequency, inducer rotation frequency
Ψ = head coefficient $(P_{outlet}-P_{inlet})/(\rho_l R_{tip}^2\Omega^2)$
ρ_l, ρ_v, ρ = specific mass of the liquid, of the vapor, of the mixture
α = local void ratio: $\alpha=(\rho-\rho_l)/(\rho_v-\rho_l)$

References

[1] de Bernardi, J., Joussellin, F., and Von Kaenel, A., 1993, "Experimental Analysis of Instabilities Related to Cavitation in Turbopump Inducer," 1st Int. Symp. on Pump Noise and Vibrations, Paris, France, pp. 91–99.

[2] Kamijo, K., Shimura, T., and Watanabe, M., 1977, "An Experimental Investigation of Cavitating Inducer Instability," ASME Paper No. 77-WA/FW-14.

[3] Pagnier, P., Morel, P., Spettel, F., Henry, C., and Champagne, J.-Y., 1995, "Conception and Experimental Study of an Inducer," *Cav'95 Int. Symp.*, Deauville, France.

[4] Goirand, B., Mertz, A., Joussellin, F., and Rebattet, C., 1992, "Experimental Investigation of Radial Loads Induced by Partial Cavitation with Liquid Hydrogen Inducer," *3rd Int. Conf. on Cavitation, IMechE, C453/056*, Cambridge, England, pp. 263–269.

[5] Tsujimoto, Y., 2001, "Simple Rules for Cavitation Instabilities in Turbomachinery," *4th Int. Symp. on Cavitation*, Pasadena.

[6] Tsujimoto, Y., Kamijo, K., and Yoshida, Y., 1993, "A Theoretical Analysis of Rotating Cavitation Inducers," ASME J. Fluids Eng., **115**, pp. 135–141.

[7] Joussellin, F., and de Bernardi, J., 1994, "Analytical Modelling of Instabilities in a Cavitating Turbopump Inducer," *2nd Int. Symp. on Cavitation*, Tokyo, pp. 98–94.

[8] Horiguchi, H., Watanabe, S., Tsujimoto, Y., and Aoki, M., 2000, "Theoretical Analysis of Alternate Blade Cavitation in Inducers," ASME J. Fluids Eng., **122**(1), pp. 156–163.

[9] Horiguchi, H., Watanabe, S., and Tsujimoto, Y., 2000, "A Linear Stability Analysis of Cavitation in a Finite Blade Count Impeller," ASME J. Fluids Eng., **122**(4), pp. 798–805.

[10] Pilipenko, V., Semyonov, Y., and Kvasha, Y., 1995, "Theoretical and Experimental Computational Methods for Determining Volume of Cavities and Coefficients of Dynamic Equation of Cavitation Cavities," Tech. Report No. SEP TC/T 23227/96.

[11] Watanabe, S., Tsujimoto, Y., Franc, J.-P., and Michel, J.-M., 1998, "Linear Analyses of Cavitation Instabilities," *3rd Int. Symp. on Cavitation*, Grenoble, pp. 347–352.

[12] Watanabe, S., Sato, K., Tsujimoto, Y., and Kamijo, K., 1999, "Analysis of Rotating Cavitation in a Finite Pitch Cascade Using a Closed Cavity Model and a Singularity Method," ASME J. Fluids Eng., **121**(4), pp. 834–840.

[13] Delannoy, Y., and Kueny, J. L., 1990, "Two Phase Flow Approach in Unsteady Cavitation Modelling," *Cavitation and Multiphase Flow Forum*, ASME-FED Vol. 98, pp. 153–158.

[14] Reboud, J. L., and Delannoy, Y., 1994, "Two Phase Flow Modelling of Unsteady Cavitation," *2nd Int. Symp. on Cavitation*, Tokyo, pp. 39–44.

[15] Coutier-Delgosha, O., Reboud, J.-L., and Delannoy, Y., 2003, "Numerical Simulation of the Unsteady Behaviour of Cavitating Flows," Int. J. Numer. Methods Fluids, **42**, pp. 527–548.

[16] Coutier-Delgosha, O., Courtot, Y., Joussellin, F., and Reboud, J.L., 2004, "Numerical Simulation of the Unsteady Cavitation Behavior of an Inducer Blade Cascade," AIAA J., **42**(3), pp. 560–569.

[17] Pouffary, B., Fortes-Patella, R., and Reboud, J. L., 2005, "Numerical Analysis of Cavitation Instabilities in Inducer Blade Cascade," *5th Int. Symp. on Pumping Machinery*, ASME 2005 Summer Meeting, Houston.

[18] Yokata, K., Kurahara, K., Kataoka, D., Tsujimoto, Y., and Acosta, A. J., 1999, "A Study on Swirling Backflow and Vortex Structures at the Inlet of Inducer," JSME Int. J., Ser. B, **42–3**, pp. 451–459.

[19] Pouffary, B., Fortes-Patella, R., and Reboud, J. L., 2005, "Numerical Simulation of 3D Cavitating Flows: Analysis of Cavitation Head Drop in Turbomachinery," *5th Int. Symp. on Pumping Machinery*, ASME 2005 Summer Meeting, Houston.

Characterization of the Content of the Cavity Behind a High-Speed Supercavitating Body

Xiongjun Wu[1]
e-mail: wxj@dynaflow-inc.com

Georges L. Chahine
e-mail: glchahine@dynaflow-inc.com

Dynaflow Inc.,
10621-J Iron Bridge Road,
Jessup, MD 20794

A high speed/high flow test facility was designed and implemented to study experimentally the supercavitating flow behind a projectile nose in a controlled laboratory setting. The simulated projectile nose was held in position in the flow and the cavity interior was made visible by having the walls of the visualization facility "cut through" the supercavity. Direct visualization of the cavity interior and measurements of the properties of the cavity contents were made. Transducers were positioned in the test section within the supercavitation volume to enable measurement of the sound speed and attenuation as a function of the flow and geometry parameters. These characterized indirectly the content of the cavity. Photography, high speed videos, and acoustic measurements were used to investigate the contents of the cavity. A side sampling cell was also used to sample in real time the contents of the cavity and measure the properties. Calibration tests conducted in parallel in a vapor cell enabled confirmation that, in absence of air injection, the properties of the supercavity medium match those of a mixture of water vapor and water droplets. Such a mixture has a very high sound speed with strong sound attenuation. Injection of air was also found to significantly decrease sound speed and to increase transmission. [DOI: 10.1115/1.2409356]

1 Introduction

Cavitation on a given body takes many forms depending on the extent and intensity of cavitation characterized by the cavitation number, σ, defined as

$$\sigma = \frac{P_\infty - P_c}{\frac{1}{2}\rho V^2} \tag{1}$$

where P_∞ is the free stream or ambient static pressure, P_c is the cavity pressure, V is the flow velocity, and ρ is the liquid density. As σ becomes very low ($\sigma \ll 0.1$), the flow enters the supercavitation regime when the length of the continuous large cavity becomes greater than the body length [1–3]. In order to achieve a small σ such that the supercavitation can be maintained, either a high free stream velocity or a small pressure difference P_∞-P_c, or a combination of both is needed. The small pressure difference can be obtained by either decreasing the ambient pressure, P_∞ or increasing the cavity pressure, P_c, through cavity ventilation. Supercavitation with cavity ventilation is usually referred to as artificial or ventilated supercavitation compared to natural supercavitation in the absence of cavity ventilation [2,3]. Application of ventilation has simplified some research and expanded the application fields [2]. Gravitational effects may become important for artificial supercavitation, these effects are characterized by the Froude number, $\mathcal{F}_r$ [1], which is defined as

$$\mathcal{F}_r = V/\sqrt{gl} \tag{2}$$

where g is the gravitational acceleration and l is the characteristic length of the cavity.

Supercavitation has become a hot topic due to its potential to significantly enhance the speed of undersea weapons, projectiles, and vehicles by enabling them to travel inside a vaporous or gas fed cavity through significant reduction of viscous drag [4]. Several recent supercavitating body experiments and numerical simulations have improved our understanding of the physics of the phenomena [5,6]. Tests conducted on underwater high speed projectiles and self-propelled bodies have been able to characterize the cavity overall shape and behavior, and compared favorably with proper numerical simulations [7]. However, for underwater supercavitating projectiles, the measurements of the propagation of shock waves through the cavity showed significant differences from those obtained with tests preformed in an equivalent idealized static cavity. It was hypothesized that these differences are due to the contents of the cavity being different in the real situation from the idealized laboratory simulation.

This study aims at addressing this issue and at characterizing the contents of the cavity in a controlled laboratory setting. The investigations included visualization of the cavity, measurement of two properties of its acoustics: the speed of sound and the attenuation of an imposed perturbation, and measurement of some physical properties of the cavity contents. Such an investigation intends to contribute to enhancing our understanding of the physics of supercavitation.

2 Experimental Facility and Setup

The three dimensionality of a supercavity behind the projectile and the presence of a perturbed nonsmooth water/cavity interface renders the cavity opaque and makes it very difficult to have direct optical observations of the inside of the cavity and to conduct nonintrusive measurements of the physical properties of the cavity. In addition, generation of a natural supercavity requires a very low cavitation number, which requires either a very high velocity liquid flow or a very low ambient pressure in the test section.

To tackle these two challenges we adopted a test section design with a venturi-like profile sandwiched between two parallel transparent sidewalls to obtain a very low pressure in the test section without requiring reduction of the pressure everywhere in the test facility and to generate a cavity which is a slice through of the three-dimensional cavity (Fig. 1). This simplification of flow field is acceptable as long as the concerned cavities are such that velocities perpendicular to the flow direction are negligible and curvature effects have a negligible effect on the cavity characteristics.

[1]Corresponding author.

Contributed by the Fluids Engineering Division of ASME for publication in the JOURNAL OF FLUIDS ENGINEERING. Manuscript received January 4, 2006; final manuscript received July 14, 2006. Assoc. Editor: Theodore Heindel.

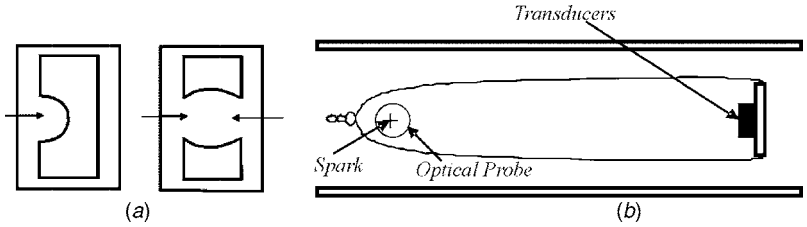

Fig. 1 Sketch of the experimental simulation of the supercavitation behind a projectile. On the left (*a*) two configurations for the simulated projectile head placement in the visualization facility are shown with the arrows indicating the viewing angle. On the right (*b*) a sketch of the developed cavity and the viewing angle and placement of measurement transducers are shown.

This simple design enabled us to construct a supercavitating-projectile facility that met the design requirements and that was able to use an existing 24.4 m (80 ft) wave tank as a very large water reservoir, where accumulation of air from the generated supercavity was not an issue. Through this facility we could also achieve very low ambient pressures over the cavity while keeping the outlet of the test section open directly to the atmosphere, which offers a major setup simplification. Since our objective is to quantify the cavity content and not the cavity shape and dynamics, effects neglected with this approximation are of little impact on the results of the study. Figure 1 shows sketches of two setups considered: in the first one, Fig. 1(*a*), curvature effects are included, while they are neglected in Fig. 1(*b*).

Figure 2 shows a sketch of the experimental setup. The flow is driven by an 11 kW (15 hp) Goulds pump model 3656, capable of 34.7 L/s (550 gpm) at a head of 172.4 kPa (25 PSI). The test section is made of acrylic and has multiple mounting locations to mount the projectile head in order to generate the desired supercavity. Since air ventilation has a large effect on the cavity characteristics, two air ports were machined in the test section, through which air can be injected into the cavity in order to generate a ventilated cavity. The flow rate of the air into the cavity is regulated by a set of valves. To facilitate the measurements inside the cavity, a series of measurement ports were arranged along the top and bottom sides of the test section, through which probes and sensors can be mounted.

A simplified sketch of the test section with dimensions (unit in cm) is shown in Fig. 3. The various mounting port positions are also shown in the figure. The projectile is mounted at port M. Air injection for ventilating the cavity is made possible through the two air injection ports A_1 and A_2. Devices for instrumentation can be mounted through the instrumentation mounting ports, S_1-S_4.

To write conservation equations at any point in the test loop of vertical position, h, we define Q as the liquid flow rate, and A as the considered section area. We also use subscripts p, b, and a to refer to the location of the pump, the projectile head, and the area open to the atmosphere, respectively

$$Q = VA \tag{3}$$

and

$$P = P_p - \frac{1}{2}\rho V^2 - \rho g(h - h_p) - P_{\text{loss}} \tag{4}$$

where P_{loss} is the unrecoverable pressure head loss due to viscous effects over the path from the pump to the given point in consideration. The test section comprises a constant pressure section in which the super cavity is formed. The cavity length, L_c, is related with the cavitation number and projectile diameter by the following approximate expression [8]:

$$L_c \simeq \frac{8b}{\pi} C_D \frac{1}{\sigma^2} \tag{5}$$

where b is the projectile diameter and C_D is the shape drag coefficient.

Behind the constant pressure section, the test section expands to allow a pressure rise from the very low pressure around the cavity to the atmospheric pressure. This is achieved through an expansion angle as large as possible without inducing flow separation. This is obtained by limiting the expansion angle to 7 deg. An additional constraint that we imposed was to minimize the overall length of the facility.

3 Flow Visualizations

3.1 Cavitation Number Effects. As the ambient pressure around the projectile head decreases with increasing flow rate, the flow evolves from a noncavitating flow to a cavitating flow then to a supercavitating flow. Flow visualization of the supercavity was achieved by high resolution digital photography as well as by high speed photography. The evolution of the cavitating flow from lim-

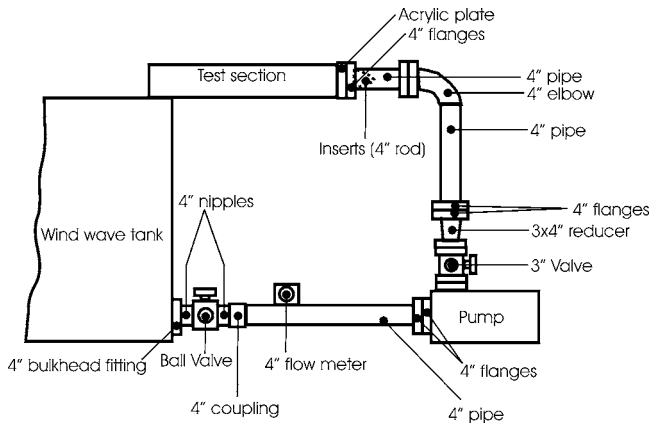

Fig. 2 Sketch of the experimental facility setup

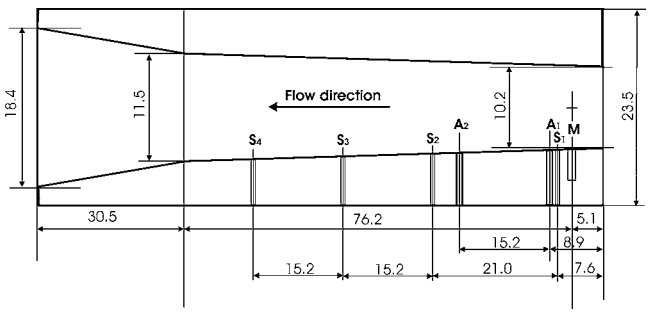

Fig. 3 Side view of the test section with dimensions in cm, A_1 and A_2 are air supply ports, S_1-S_4 are sensor mounting ports, and M is the projectile mounting port

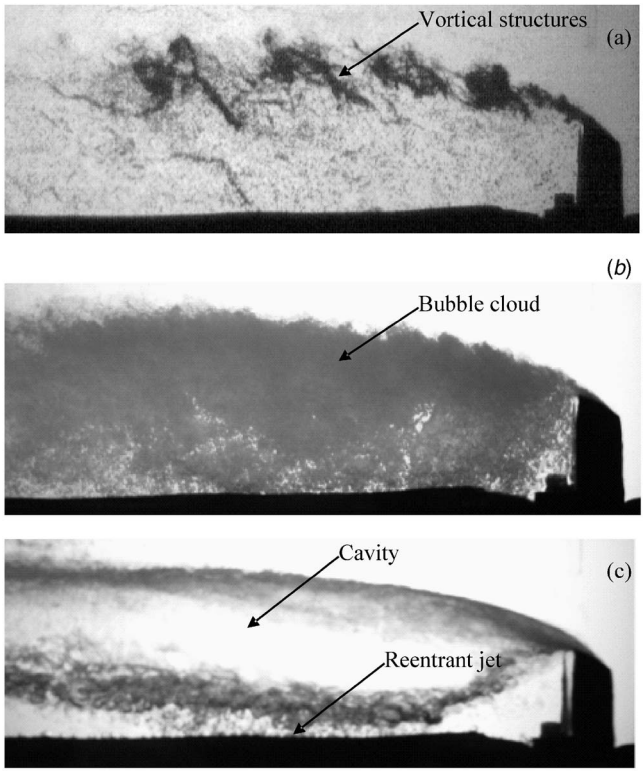

Fig. 4 Evolution of the cavitating flow with decreasing cavitation numbers (here increasing flow rates). (*a*) Q=15.8 L/s (250 gpm), $V\simeq$8 m/s, $\sigma\sim$0.13; (*b*) Q=22.1 L/s (350 gpm), $V\simeq$11 m/s, $\sigma\sim$0.07; (*c*) $Q\sim$34.7 L/s (550 gpm), $V\simeq$18 m/s, $\sigma\sim$0.02.

ited cavitation to supercavitation with an increasing flow rate for a projectile one inch high is shown in the pictures of Fig. 4. Figure 4(*a*) shows for $\sigma\sim0.13$ and a relatively low flow rate (Q =15.8 L/s (250 gpm), V=8 m/s) flow separation behind the projectile head and the resulting formation of shed cavitating vortices. Bubbles generated from the cavitation on the projectile head can be seen both as bubbles convect downstream and as bubbles "captured" in the separation area behind the projectile head. Figure 4(*b*) shows such a condition, for $\sigma\sim0.07$ (Q=22.1 L/s (350 gpm), $V\simeq$11 m/s). As seen in the picture, the bubbles generated from the intensified cavitation become so dense that the flow becomes a bubbly flow downstream of the projectile head and the shed vortices become more difficult to identify. The separated area becomes more and more filled with cavities with increasing flow rate; the cavities finally coalesce and form large cavity pockets. With further decrease in the cavitation number, $\sigma\sim0.02$ (Q $\sim$34.7 L/s (550 gpm), $V\simeq$18 m/s), a single cavity is formed and the flow becomes supercavitating as shown in Fig. 4(*c*). Once the cavity is formed, the cavity pressure remains very close to the vapor pressure in the range of 4000 Paand varies very little with further velocity increase.

3.2 Projectile Shape. The shape of the leading edge of the simulated projectile head affects the characteristics of the supercavity. Figure 5 illustrates the difference between the cavity interfaces when the leading edge is sharp versus an angled tip. The projectile heads in Figs. 5(*a*) and 5(*b*) are the same except they were mounted with opposite orientation. Although separation is initiated at the sharp edge of the projectile head in both cases, the disturbance of the cavity interface at the test section side wall is much less for a cavity formed from the projectile head without a transition slope (Fig. 5(*a*)) compared to that of the cavity formed from the projectile with a transition slope (Fig. 5(*b*)). The difference could be attributed to the fact that the shear layer between the cavity and the liquid is thinner and there is not much boundary layer development prior to the shear layer separation point in the case shown in Fig. 5(*a*), while a boundary layer develops on the projectile head and feeds the shear layer prior to separation in the case of Fig. 5(*b*). In this later case the shear layer is thicker and stronger entrainment of a two phase medium is seen at the interface.

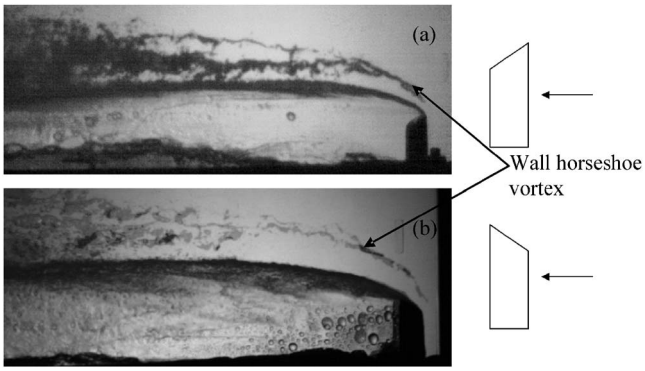

Fig. 5 Effects of the projectile shape on the cavity formation. $Q\sim$31.6 L/s (500 gpm), $V\simeq$16 m/s, $\sigma\sim$0.03. The vortices above the supercavity are the horseshoe vortices formed near the projectile.

3.3 Secondary Effects. Because the simulated projectile head is sandwiched between the two parallel sidewalls, the shape of the leading edge of the projectile that contacts the wall has a strong *secondary* effect on the flow pattern outside of the cavity. As shown in Fig. 5(*a*), there exists a strong horseshoe vortex above the supercavity if the leading edge of the projectile head contacting the wall is a 2D flat front face. As pointed out in Ref. [9], this strong horseshoe vortex around the 2D flat leading edge can be reduced or eliminated by adding a curved leading-edge section to the simulated projectile head shape, with either a filleted or an undercut shape, Fig. 6 shows a top view of different types of projectile leading edges that we have tested. The experimental results shown in Fig. 4 were conducted using a projectile head with a filleted leading-edge shape from which we can clearly see that the horseshoe vortex around the supercavity is greatly weakened, does not cavitate and thus is not apparent in the picture. However, in order to produce a clearer cavity for better inside-cavity observation and measurement, a simulated projectile head configuration as shown in Fig. 5(*a*) was used for most of the experiments reported here such that the disturbances at the intersection between the cavity interface and the side walls of the test section were minimal, even though the secondary vortex was present outside of the cavity.

3.4 Reentrant Jet. The range of values of σ that we were able to achieve while keeping the supercavity within the test section was $0.13\geqslant\sigma\geqslant0.02$. In this σ range, the supercavity had an

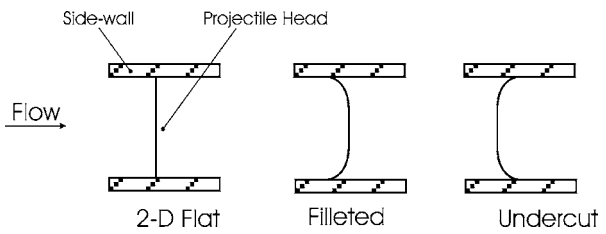

Fig. 6 Top view of different types of projectile shaped leading edge that were tested to minimize the secondary horseshoe vortex

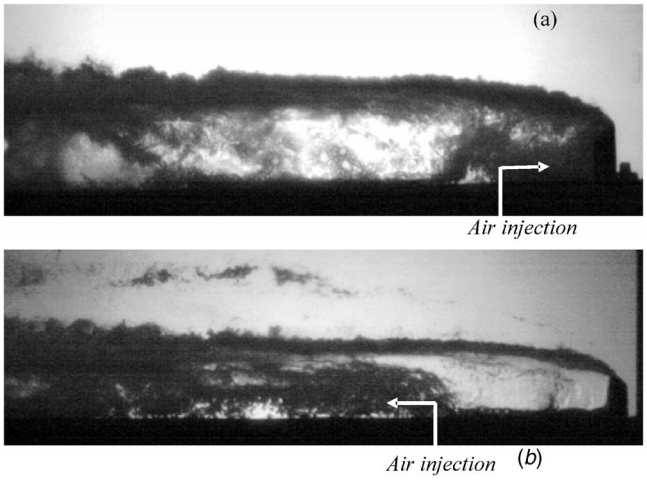

Fig. 7 Cavities with air ventilation. (*a*) Air injection towards upstream. (*b*) Air injection towards downstream. $Q \sim 31.6$ L/s (500 gpm), $V \simeq 16$ m/s. The vertical line and horizontal arrow indicates the approximate position of the injector and the direction of the injection, respectively.

oscillatory behavior. A reentrant jet, periodically appeared as a turbulent mass of liquid shooting upstream in the cavity toward the projectile head as seen in Fig. 4(*c*). The frequency of recurrence of the reentrant jet varied with the flow rate, the projectile head shape, and the degree of ventilation. Previous studies have shown that there is a critical Froude number $\mathcal{F}_{rc}$, below which the reentrant jet disappears, $\mathcal{F}_r < \mathcal{F}_{rc}$ [10]. Brennen's study gives a value of $\mathcal{F}_{rc} \sim 2.5$ [11]. In the present experiments the Froude number was between 4 and 8, i.e., in the range where a reentrant jet always existed. The frequency of recurrence, however, was relatively low, and a calm and clean supercavity free from the reentrant jet disturbances could be observed for a relatively long time for adequate measurements (a couple of seconds) between reoccurrences of successive reentrant jets.

3.5 Ventilation. Figure 7(*a*) shows a ventilated cavity with air injection towards upstream from an air injection port which is about 1.3 cm (0.5 in.) downstream from the projectile head, while Fig. 7(*b*) shows a ventilated cavity with air injection directed downstream from an air injection port which is about 16.5 cm (6.5 in.) away from the projectile head. Air injection raises the pressure in the cavity to the air injection pressure as expected. In our tests, the injector was bent to be parallel to the liquid flow to avoid direct jet impact on the cavity wall. However, even a very small air injection flow rate (P_{air} of 300 Pa) destroyed cavity stability and resulted in a very disturbed ventilated cavity as shown in Fig. 7. This is mainly due to the interaction of the air jet with the walls of the cavity. Probably, a careful design and extensive testing would result in conditions which avoid such an interaction, but such an effort was not pursued during this study.

3.6 Gravity Effects. All cavities shown above were obtained from experiments with the simulated projectile head mounted at the bottom of the test section, i.e., only half a cavity is produced with the flow occurring only above the top interface of the cavity which expands and then curves down from the maximum position to the closure. In such a configuration, a perfect symmetry is assumed between the top and the bottom part of the cavity. To study the effect of gravity and the imposed symmetry on the characteristics of the supercavities, experiments were also conducted with the 1/2 projectile head mounted at the top of the test section and a full projectile head mounted in the middle of the test section.

When the projectile head was mounted at the top of the test

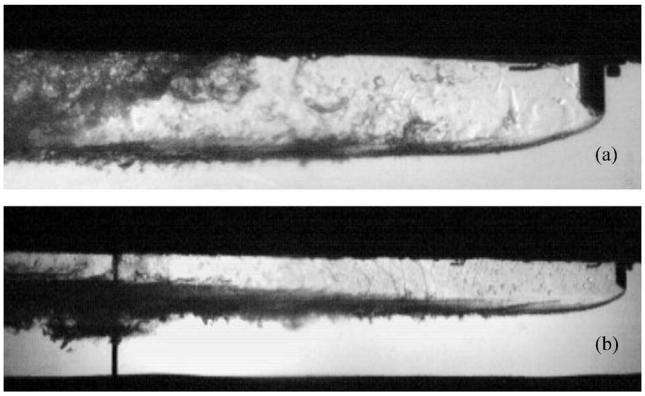

Fig. 8 Supercavity formed from a 1/2 projectile mounted on the top of the test section. (*a*) Formation of a reentrant jet, $Q \sim 31.6$ L/s (500 gpm), $V \simeq 16$ m/s, $\sigma \sim 0.03$. (*b*) Cavity vented to the atmosphere, $Q \sim 31.6$ L/s (500 gpm), $V \simeq 16$ m/s.

section, only the bottom interface of the cavity was simulated. Compared to the case where the supercavity is formed from the same projectile head mounted at the bottom of the test section, at the same flow rate, the supercavity formed at the top of the test section expands to a further downstream location before it curves up and closes. The observed cavity is then longer. Fig. 8(*a*) shows an example of such a cavity again with a strong reentrant jet. As the flow rate increases, the cavity formed at the top of the test section elongates further and further and finally reaches the exit section connected to the atmosphere. The test section cannot then accommodate further growth of the cavity, and the cavity can no longer close; instead the supercavity flow transforms into a free surface flow behind the projectile. Figure 8(*b*) shows an example of such a cavity that is open to the atmosphere.

When the projectile head is mounted in the middle of the test section, the flow can develop both above the top interface and below the bottom interface of the cavity and the cavity shape is affected by the effect of gravity. Figure 9 shows a supercavity formed from a 1.3 cm (0.5 in.) projectile head mounted in the middle of the test section, the cavity exhibits a nearly symmetric shape that tilts a little downward due to gravity. At the maximum flow rate that the pump can achieve, an end closed supercavity with reentrant jet is always maintained. However, the upstream distance that the jet can reach is reduced when a full projectile is used as the reentrant jet is no longer exactly symmetric and curves downward and hits the lower cavity wall before reaching the projectile head.

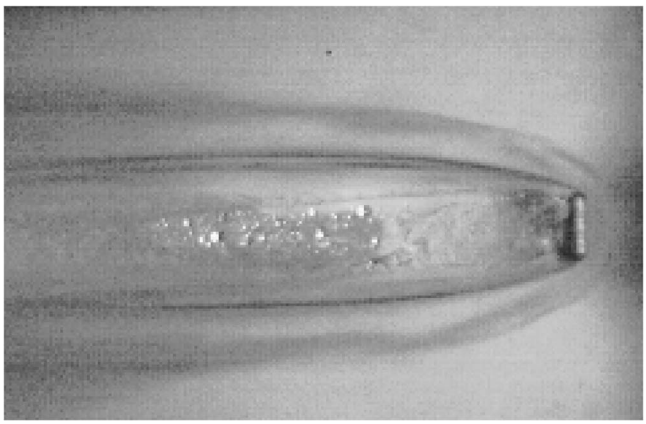

Fig. 9 Supercavity with reentrant jet formed from a full projectile mounted in the middle of the test section. $Q \sim 34.7$ L/s (550 gpm), $V \simeq 15$ m/s, $\sigma \sim 0.03$.

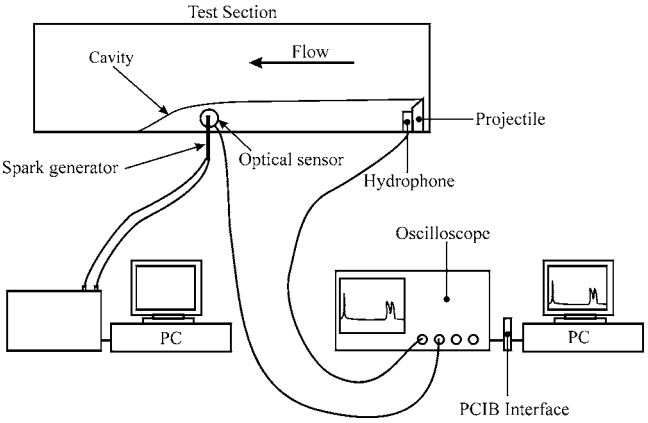

Fig. 10 Setup for direct sound speed measurement in the test section

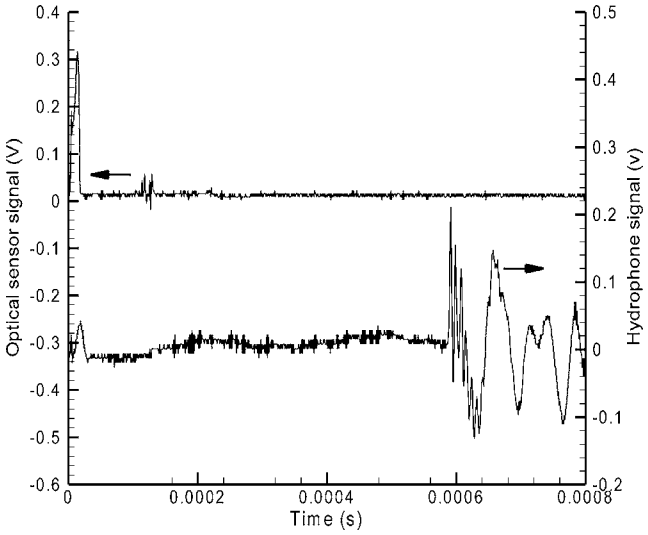

Fig. 11 Typical signals from optical sensor and hydrophone

4 Acoustic Properties of the Cavity Content

Sound speed and attenuation in the cavity fluid medium are direct indicators of the nature of the multiphase mixture in the supercavity. They can be used as indirect measurements of the properties of the medium. Technology developed for the ABS Acoustic Bubble Spectrometer® [12–15] was adapted to measure the acoustic properties of the cavity medium. Sound speed and attenuation measurements were conducted using a spark generator that is used for generating explosion-like bubbles [15] and a 1 in. square ABS hydrophone. The spark generator utilizes coaxial electrodes with the spark gap between the inner and the outer electrode filled with an insulating layer. A spark is generated by the very fast discharge of a high-voltage (up to 16,000 V) between the two electrodes [15]. The spark generator electrodes and the hydrophone were mounted at Port S_2 and S_1, respectively, as shown in Fig. 3 (also refer to Figs. 1 and 10).

Initially a second transducer was used, as in the ABS technique, as a sound signal generator, but the intensity turned out to be relatively weak and gave bad signal to noise ratios. In addition, use of two transducers required very small transducers or a very large supercavity to avoid interaction with the cavity walls. Compared to using another hydrophone as a projector, the spark generator provides a much stronger signal for time of flight measurements. The sensor element of the hydrophone used is made of piezoelectric material and has an operating frequency range from 20 to 250 kHz.

Figure 10 shows a sketch of the setup for direct sound speed and attenuation measurements inside of a supercavity. The hydrophone was located right behind the projectile where the supercavity initiated which ensured that it did not interact with the cavity and the spark electrodes were located downstream inside the supercavity and did not interfere with it. In most measurements, the distance between the electrodes and the transducer was 21 cm. A similar setup was also used for measurements in the side sampling cell and the vapor cell described later below. The data acquisition was handled by a digital oscilloscope, Gould 1604, which has a sampling rate of 20 MS/s and was connected to a personal computer through a general purpose interface bus board for data export. A Krohn–Hite 3103A filter was used between the hydrophone and the oscilloscope to filter out the low frequency electric noises below 1 kHz. An optical sensor located outside the cell and facing the spark was used to detect spark initiation and to trigger the data acquisition system when the spark was fired.

The hydrophone is used to detect the acoustic signal generated by the spark. The hydrophone and the spark generator are separated by a known distance, L. The spark generates an acoustic impulse very rich in high frequencies, which travels upwards and is detected by the transducer after a time of flight given by Δt, the sound speed can therefore be calculated from

$$c = L/\Delta t \tag{6}$$

Δt measures actually the time of arrival of the direct path from the electrodes to the hydrophone. This is followed by the arrival of other signals reflected by the facility side walls, from the supercavity, and from any other resonance of the air volume. Therefore, these are irrelevant for our problem here, where we are only interested in the direct path to measure c. This is illustrated in Fig. 11, which shows a typical signal received by the hydrophone. The signal strength is excellent and well above the noise level, and the arrival of the acoustic signal at the hydrophone can be unmistakably measured. Concerning the time of sparking, we initially thought that we could detect it through the electric noise generated in line at sparking, however, this signal turned out to not being well distinct under all conditions. For this reason, an optical sensor was used, which sensed the light generated at sparking and sent the signal to the data acquisition system to provide a synchronization of the timing of the event. This optically generated signal is also shown in Fig. 11, where one can clearly see distinct correspondence between the sharp optical signal and the weaker electric signal detected by the hydrophone at the time of sparking. The measurement of the time of flight was therefore quite accurate with signal to noise ratio being very high. After the distinct acoustic signal arrival, the hydrophone signal has some oscillations with decaying amplitude which are due to reflections, cavity oscillations, and transducer ringing. We did not consider this latter part of the signal for the present study.

In addition to the time of flight measurement, the amplitude of the received acoustic signal when compared to that measured in air under ambient conditions, provides the relative signal attenuation. In all test conditions, the spark was fired when the charge of the spark generator reaches 11,000 kV to maintain a consistent acoustic source for accurate attenuation measurements and all measurement were conducted under very similar room temperature of 25 °C.

To check the accuracy of the method, repeated tests were conducted in the dry test section (i.e., in air). The measured average sound speed was 347.5 m/s with a scatter lower than 0.8%. However, the measurement of the signal amplitude had much larger variations up to 18%.

For comparison purposes, sound speed measurements were conducted in the test section with and without the presence of a

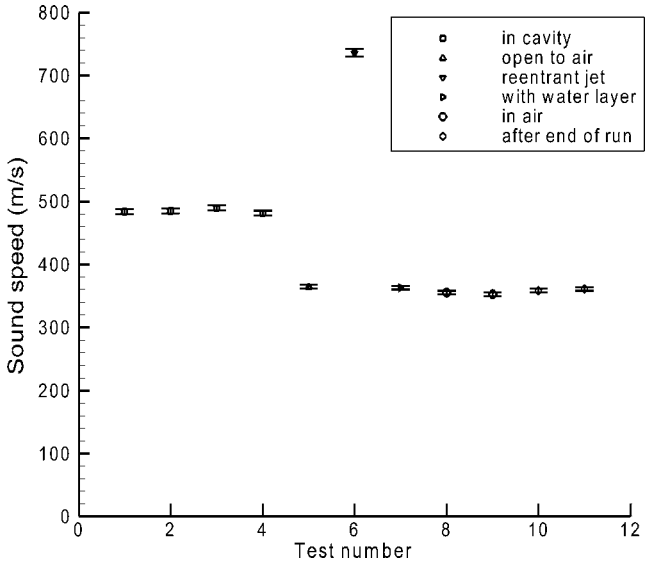

Fig. 12 Sound speed in the test section under various conditions as indicated on labels

supercavity. Figures 12 and 13 show the measurement results of the sound speed and the corresponding peak amplitudes of signals.

The sound speed was between 480 and 500 m/s when the measurements were conducted in a calm and clean cavity (labeled "*in cavity*"). However, when the measurement was conducted under conditions where occurrence of the reentrant jet was affecting the measurement (i.e., presence of water droplets in the cavity), the sound speed was significantly higher and varied in a wide range. In presence of the reentrant jet, the cavity content is a mixture of vapor and water. It is known that in a homogeneous mixture of gas and liquid, the sound speed could be much smaller than that of either of two constituents [10]. However our experiments consistently showed that the sound speed measurements taken between occurrences of two reentrant jets were much higher, and of the order of 750 m/s (labeled "*reentrant jet*").

Figure 12 also contains a data point where the measurement

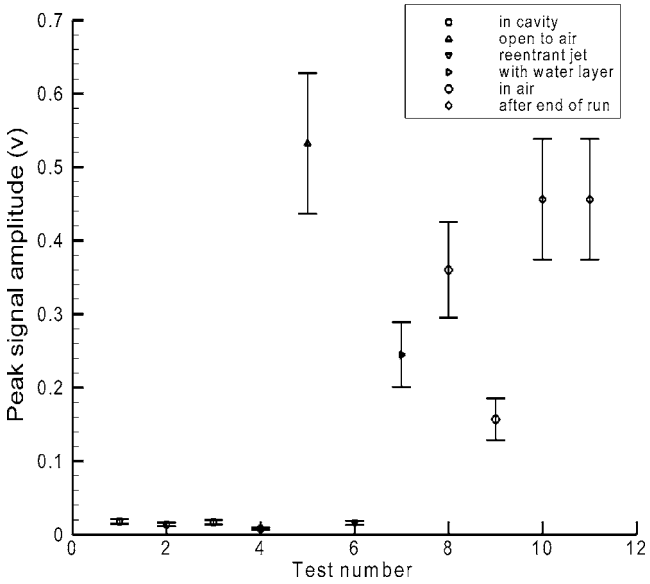

Fig. 13 Peak amplitude of signal in test section under various conditions as indicated on labels

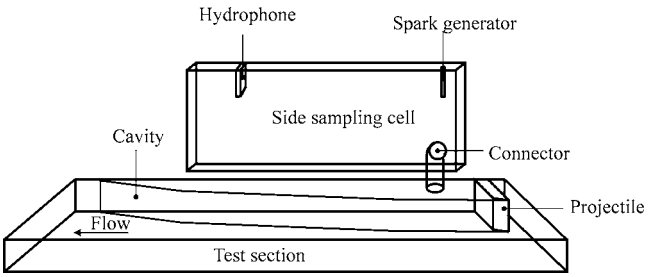

Fig. 14 Sketch of the setup for measurements in the side sampling cell

was conducted in a cavity which was formed from a projectile head mounted on the top of the test section and after the cavity vented to the ambient atmosphere (labeled "*open to air*"). As expected, the sound speed measured was about 360 m/s, only very slightly higher than the results obtained from measurements conducted before the run when the test section was dry. This provides a validation of the method. The sound speed measured with the same method in air was about 350 m/s (labeled "*in air*"), and was similar to the results obtained right after the run is stopped while there is a water layer in the test section (labeled "*with water layer*"). After the test loop was stopped following a run and while the test section was still wet, sound speed is seen to decrease further and become very close to the sound speed in air (labeled "*after end of run*"). The higher sound speeds can be attributed to the presence of droplets and to high moisture level in the measurement environment. The high sound speed measured in the cavity, as also evident from the measurements in the side sampling cell and the vapor cell discussed below, is attributed to the fact that the cavity is full of water vapor and droplets.

For measurements conducted inside a supercavity, the peak amplitudes of the signals received by the hydrophone, as seen in Fig. 13, were about an order of magnitude lower than those of the signals when the measurements were conducted when there was no cavity or when the cavity was open to the atmosphere. Therefore, the cavity contents significantly attenuate the acoustic signals.

5 Side Sampling Cell

Due to the nature of the turbulent environment inside the cavity, it was not easy to conduct direct measurements of the physical properties of the cavity contents. In order to overcome these difficulties, we took advantage of the fact that the pressure in the cavity is very low and attached a secondary cell to the test section of the main test facility. As shown in Fig. 14, the main test section was flipped over 90 deg and made horizontal and the side sampling cell was added and positioned vertically above the test section. The two cells were connected by a 1.9 cm (0.75 in.) diameter opening. Once a supercavity formed behind the projectile, the resulting low pressure in the cavity sucked out any liquid or gas in the side sampling cell which then filled with the contents of the supercavity. The geometrical location of the sample cell is such that the perturbations in the supercavity did not propagate inside the side sampling cell, and we could therefore always operate in this cell in a clean and quiet environment and obtain quality measurements, even when reentrant jet were impacting the projectile head or when we ventilated the supercavity.

Sound propagation experiments were then conducted in the side sampling cell for both natural and ventilated cavities, the distance between the electrodes of the spark generator and the hydrophone is the same as that used in the test section. While tests for ventilated cavities were impossible directly in the supercavity, they were easily conducted in the side sampling cell. The cavity pressure increased with the increase in air ventilation. The pressure in the cavity was therefore used as an indication of the amount of

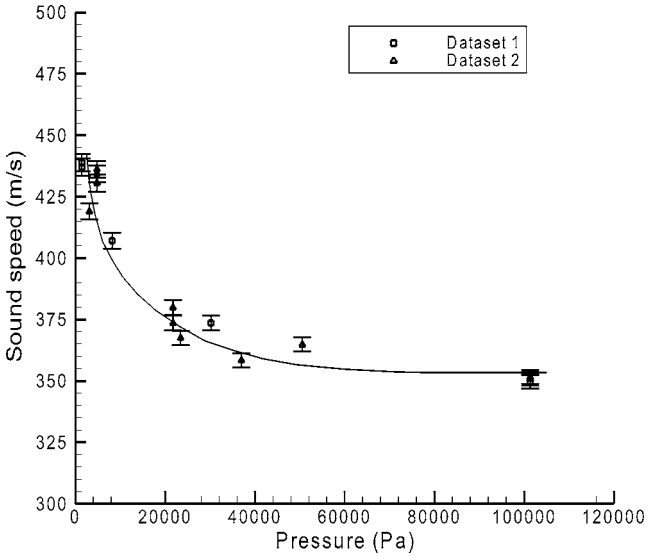

Fig. 15 Sound speed as measured in the side sampling cell for increasing amounts of ventilation or supercavity pressures, Dataset 1 and Dataset 2 were conducted at two different dates

ventilation. Figures 15 and 16 show the variations of sound speed with the pressure in the supercavity and sampling cell and the corresponding peak amplitudes of the signals. Both figures include datasets from experiments conducted at two different dates. As we can see, the variations in the sound speed measurement are much less than those in the attenuation measurement, this is due to the larger error in the spark energy repeatability.

As shown in Fig. 15, the sound speed measured is seen to decrease when the cavity pressure increases and thus when air is added to the ventilated cavity. From about 440 m/s, when no air was injected where the supercavity pressure stabilized at about 4000 Pa, it decreased to about 350 m/s when the injected amount of air was such that the pressure in the ventilated cavity became close to the atmospheric pressure. The trend is very clear and is as expected. Concerning the amplitudes, despite the scatter in the data, there is a trend for the peak amplitude of the received signal

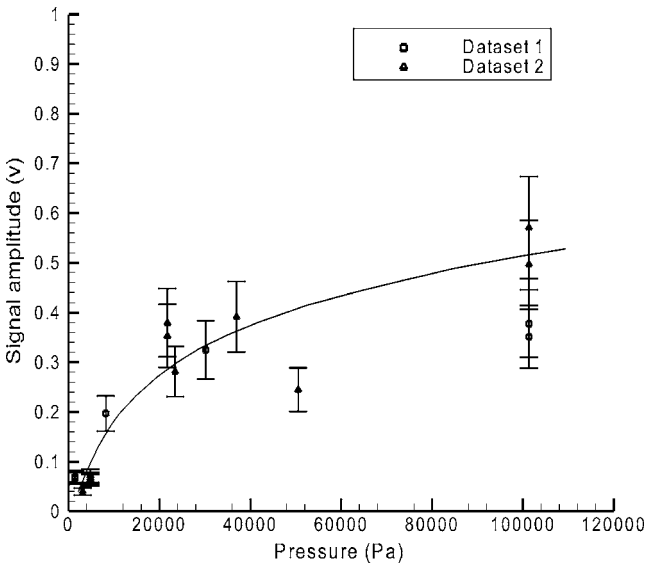

Fig. 16 Peak amplitude of signal measured in the side sampling cell for increasing amounts of ventilation or supercavity pressures, Dataset 1 and Dataset 2 were conducted at two different dates

to increase with increasing air and pressure in the cavity. In other words attenuation of the signal by the contents of the cavity decreased when the contents of the cavity had a larger portion of air. Since the sound speed is affected little by pressure, this presents further indication that the presence of vapor and droplets in the cavity is a strong attenuator to sound propagation in the supercavity.

6 Vapor Cell Tests

In order to interpret better the measurements conducted in the cavity and in the side sampling cell discussed above, we also conducted parallel measurements in a vapor cell where the air and vapor contents as well as the pressure were controlled to determine the air/vapor mixture proportions. Figure 17 sketches the operation of this cell. Vapor was generated by heating water and was injected in the vapor cell. Similarly ambient air was injected in the cell in a controlled fashion using metering valves. Once the saturated vapor entered the vapor cell, it condensed and produced droplets. By adjusting the amount of vapor and air into the cell, we could obtain an environment in equilibrium that has the desired composition of vapor, air, and droplets to simulate the contents of a supercavity.

Systematic measurements were also conducted in the vapor cell with and without air injection. When the cell was only filled with vapor (i.e., the air valve was closed), the temperature in the vapor cell stabilized at about 47°C (116°F) and the pressure equilibrated at about 9900 Pa. The measured temperature and pressure in the vapor cell then matched those of saturated vapor [16]. A steady vapor flow rate was maintained through the vapor cell with an incoming vapor flow rate of about 7600 cm^3/min and an outgoing vapor flow rate of about 1000 cm^3/min, the difference resulting from vapor condensation in the vapor cell. The corresponding water condensation rate was thus about 0.55 g/min. Therefore, the contents of the vapor cell consisted of a mixture of saturated water vapor and droplets. By varying the amount of air fed, a desired pressure in the vapor cell could be achieved. This provided us with a simulated environment of a *ventilated cavity*. Figure 18 shows the results of sound speed measurements. The trend is similar to that measured in the side sampling cell, i.e., the sound speed decreases from about 460 m/s in pure vapor to about 350 m/s in presence of air injection at a pressure close to the atmospheric pressure (this is also close to the sound speed in air at atmospheric pressure).

Figure 19 shows the corresponding peak amplitudes of the received signals. Again, the sound attenuation decreases with the reduction of the proportion of vapor in the mixture. Compared with those measured in the side sampling cell in Fig. 16, both shows the trend of decreased attenuation with increased pressure, however, the pattern of change are different, and the data scattering is much less and the attenuation is stronger in the vapor cell.

Both Figs. 18 and 19 include two datasets that were obtained from experiments conducted at two different dates. As before the sound speed measurements are much less scattered than the attenuation measurements. The two datasets show different attenuation slopes, which is again attributable to poor repeatability of the acoustic energy in the generated spark.

Since the cavity content is a mixture of vapor, air, and water droplets, a comparison of the sound speeds measured in different setups to the theoretical sound speed values in ideal environments of saturated vapor and air can provide some insight into the cavity content. Figure 20 compares the measured variations of sound speed with pressure obtained with the various methods described above, with the theoretical values for vapor and air. The figure thus includes the sound speed obtained theoretically at various pressures in air [16], in saturated water vapor [17,18], and in wet air at 304 K (86°F) [19], and sound speed obtained experimentally in the supercavity, in the side sampling cell, and in the vapor cell.

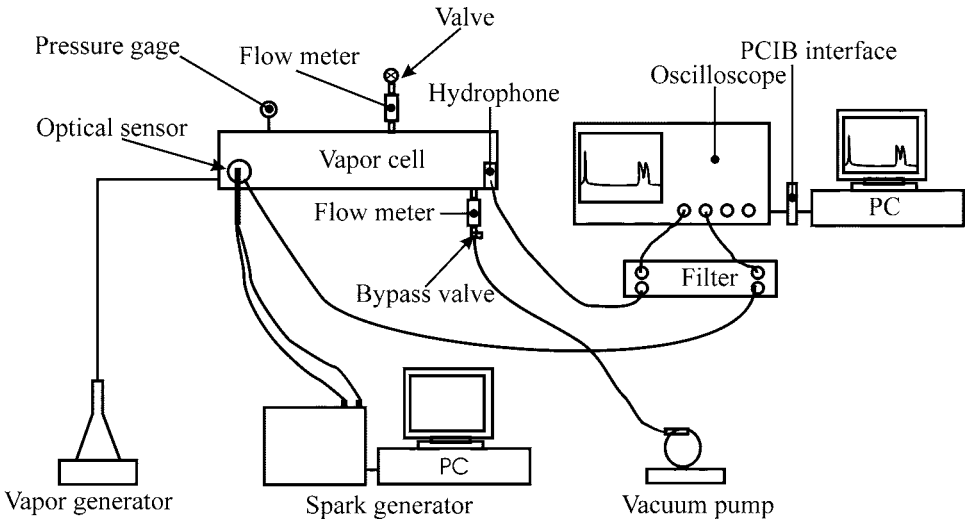

Fig. 17 A sketch of the setup for measurement in the vapor cell. Both contents of the cell (vapor and air) and pressure were controlled.

As seen in Fig. 20, for a supercavity without ventilation, the sound speed measured in the side sampling cell was very close to the sound speed in saturated water vapor. This indicates that the content of the supercavity as measured in the side sampling cell were principally saturated vapor. However, compared to the sound speed measured directly inside the supercavity, the sound speed measured in the side sampling cell is about 40–60 m/s (8–12%) lower. The reason for this difference can be attributed to the fact that in addition to saturated water vapor, there are fine water droplets scattered inside the cavity. The presence of droplets, which are not present in the quiet side sampling cell, increases the sound speed in the real supercavity. Although connected to the cavity, the passage from the cavity to the sampling cell may have partially blocked the entry of droplets to the sampling cell, which resulted in fewer droplets in the sampling cell.

As also shown in Fig. 20, the sound speed in the vapor cell without air ventilation is higher than the corresponding sound speed in saturated vapor; this can be attributed again to the presence of fine water droplets in the saturated vapor in the vapor cell due to condensation. The sound speed in the vapor cell was still lower than the sound speed directly measured in a natural cavity; therefore, the droplet concentration due to condensation in the vapor cell is less than that in the cavity.

For measurements at the higher pressures in the side sampling cell and in the vapor cell, high air ventilation was directed into the cavity. Measurements in both the side sampling cell and in the vapor cell with air ventilation show similar trends as those of wet air. The sound speed is shown to decrease as the air ventilation increases. Due to the injection of air into the cavity, the vapor droplets condensate and the gas content inside the cavity changes from mainly water vapor to a mixture of air and less and less water vapor and droplets. The larger the air injection rate, the lower was the measured sound speed until it became close to the sound speed in air when the pressure reached the atmospheric pressure.

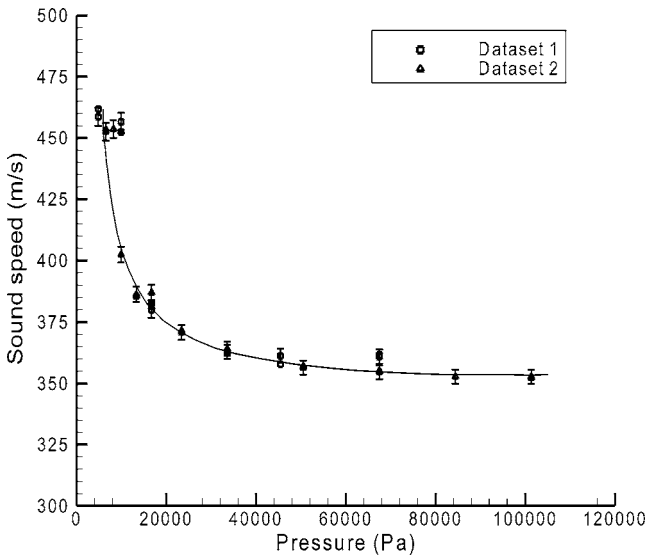

Fig. 18 Sound speed in the vapor cell for various cell pressures or amounts of air/vapor mixtures, Dataset 1 and Dataset 2 were conducted at two different dates

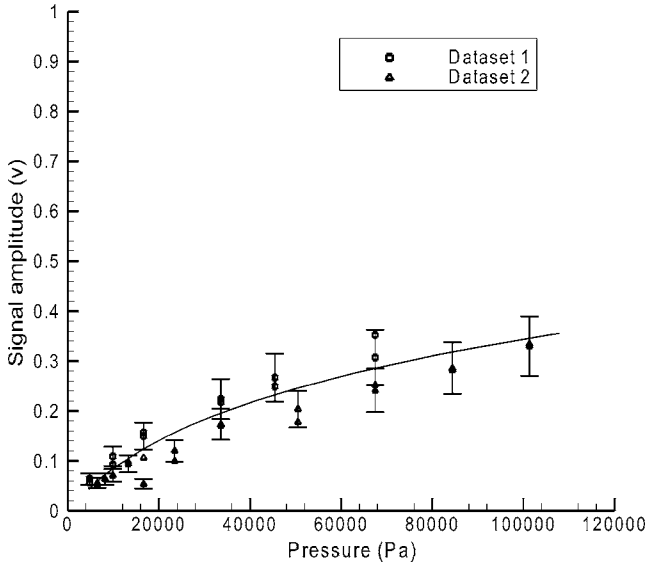

Fig. 19 Peak amplitude of signal in the vapor cell for various cell pressures or amounts of air/vapor mixtures, Dataset 1 and Dataset 2 were conducted at two different dates

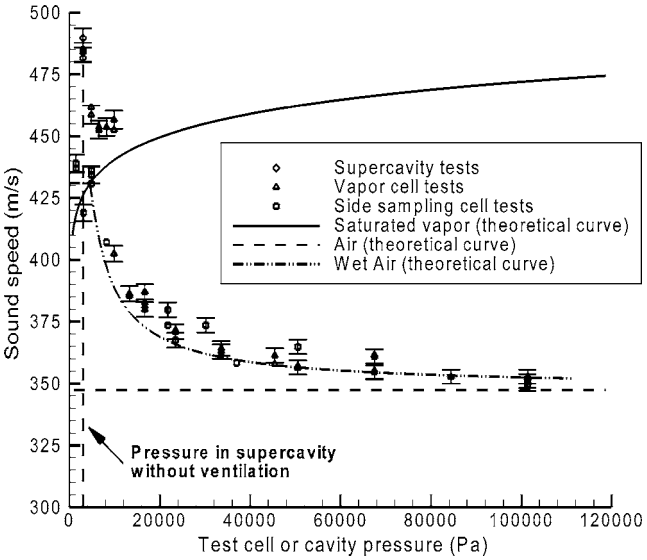

Fig. 20 Variation of sound speed with the pressure in the test cell or the cavity. Cavity and cell pressures increase are achieved by increasing air injection.

7 Conclusion

In this study, a supercavitation facility that allowed direct observations of supercavitation behind a simulated projectile head and enabled measurement of the properties of the fluid inside the supercavity was built and used to study the properties of the supercavity contents. This was achieved by utilizing transparent walls cutting through the cavity, and placing inside the cavity various instruments.

To overcome difficulties associated with the presence of unsteady reentrant jets which affected the instrumentation, a side sampling cell technique was developed. The side sampling cell was connected to the supercavity and was made to fill up with the supercavity content during the test. Sound measurements in this side sampling cell enabled repeatable collection of high signal to noise ratio data for both natural and ventilated cavities at various levels of ventilation. In order to be able to interpret the sound speed and attenuation measurements, calibration measurements were conducted in parallel in a vapor cell which enabled measurements in an environment where the amounts of vapor and gas were controlled.

Experiments have shown that the cavity/water interface or shear layer in the simulated conditions was strongly affected by the simulated projectile head shape and air ventilation. A projectile head with a sharp edge produces much less disturbance on the cavity interface than a projectile with a sloped transition. Sound speed and pressure attenuation measurements in a natural supercavity indicate very strongly that the cavity is full of water vapor and droplets which results in sound speeds as high as 440 m/s and in very strong shock attenuation. The sound speed and attenuation further increase in the presence of strong recurring reentrant jets, which saturate the cavity with droplets. Injection of air appears to reduce the effect of the vapor presence and significantly drops the sound speed in the cavity, while improving shock transmission.

In this study the sound speed was not studied as a function of the acoustic wave frequency and the values provided correspond actually to the fastest moving acoustic wave in the frequency rich source provided by a spark. Further study is therefore still needed to better characterize the cavity content in terms of droplet sizes and temperature effects.

Acknowledgment

This study was partially supported by Office of Naval Research Contract No. N00014-00-C-0344 monitored by Dr. Judah Goldwasser. We appreciate his support very much. We would like to thank Dr. Howard Steves from Advanced Technology and Research Corporation for closely following our work and making several useful suggestions. We also are very thankful for Gregory Harris from the Naval Surface Warfare Center, Indian Head Division for introducing us to the problem. Many colleagues at DYNAFLOW contributed to various degrees to this work. We thank most particularly Dr. Kenneth Kalumuck, Dr. Chao-Tsung Hsiao, and Dr. Jin-Keun Choi for various suggestions and comments, and Gary Frederick and Pat Aley for direct contributions to the experimental setup fabrication, and loop operation.

Nomenclature

c = sound speed
f = friction factor
g = gravitational acceleration
l = characteristic length
A = cross section area
D = hydraulic diameter
P = pressure
Q = flow rate
L = length
V = flow velocity
C_D = drag coefficient
$\mathcal{F}_r$ = Froude number, $\mathcal{F}_r = V/\sqrt{gl}$,
Δt = time of flight

Greek Symbols

ρ = density
σ = cavitation number, $\sigma = P - P_v/(1/2)\rho V^2$
σ_i = cavitation number at cavitation inception

Subscripts

c = cavity
p = pump
v = vapor
loss = friction loss

References

[1] Stinebring, D., Billet, M., Lindau, J., and Kunz, R., 2001, "Developed Cavitation—Cavity Dynamics," VKI Lecture Series.
[2] Savchenko, Y. N., 2001, "Supercavitation—Problems and Perspectives," *CAV2001, Proceedings of the Fourth International Symposium on Cavitation*, , Pasadena, CA.
[3] Wosnik, M., Schauer, T., and Arndt, R., 2003, "Experiment Study of a Ventilated Supercavitating Vehicle," *CAV2003, Proceedings of the Fifth International Symposium on Cavitation*, Osaka, Japan.
[4] Ashley, S., 2001, "Warp Driver Underwater," Sci. Am., **284**, pp. 70–79.
[5] Kirschner, I. N., et al., 2001, *Supercavitation Research and Development*, Undersea Defense Technologies, Waikiki, HI.
[6] Wang, G., Senocak, I., Shyy, W., Ikohagi, T., and Cao, S., 2001, "Dynamics of Attached Turbulent Cavitating Flows," Prog. Aerosp. Sci., **37**, pp. 551–581.
[7] Hrubes, J. D., 2001, "High-Speed Imaging of Supercavitating Underwater Projectiles," Exp. Fluids, **30**, pp. 57–64.
[8] Tulin, M. P., 1953, "Steady Two-Dimensional Cavity Flows About Slender Bodies," D.T.M.B. Report 834.
[9] Gatlin, G. M., Parker, P. A., and Owens, L. R., 2001, "Development of a Semi-Span Test Capability at the National Transonic Facility," 39th A1AA Aerospace Sciences Meeting & Exhibit.
[10] Brennen, C., 1995, *Cavitation and Bubble Dynamics*, Oxford University Press, Cambridge.
[11] Brennen, C., 1969, "The Dynamic Balances of Dissolved Air and Heat in Natural Cavity Flows," J. Fluid Mech., **37**, pp. 115–127.
[12] Chahine, G. L., and Kalumuck, K. M., 2003, "Development of a Near Real-Time Instrument for Nuclei Measurement: the ABS Acoustic Bubble Spectrometer®," Joint ASME/JSME Fluids Engineering Conference,

Honolulu, Hawaii.
[13] Duraiswami, R., Prabhukumar, S., and Chahine, G. L., 1998, "Bubble Counting Using an Inverse Acoustic Scattering Method," J. Acoust. Soc. Am., **104**, pp. 2699–2717.
[14] Prabhukumar, S., Duraiswami, R., and Chahine, G. L., 1996, "Acoustic Measurement of Bubble Size Distributions: Theory and Experiments," ASME Proceedings of the Fluids Engineering Summer Meeting, **1**, pp. 509–514.
[15] Chahine, G. L., Frederick, G. S., Lambrecht, C. J., Harris, G. S., and Mair, H. U., 1995, "Spark Generated Bubbles as Laboratory-Scale Models of Underwater Explosions and Their Use for Validation of Simulation Tools," 66th Shock and Vibration Symposium, Biloxi, MS, 2 pp. 265–276.
[16] Hilsenrath, J., 1995, "Tables of Thermal Properties of Gases," National Bureau of Standards Circular, 564.
[17] NIST, 2003, "Chemistry Webbook," NIST Standard Reference Database Number 69, http://webbook.nist.gov/chemistry/.
[18] Blevins, R. D., 1984, *Applied Fluid Dynamics Handbook*, Van Nostrand Reinhold, New York.
[19] Crammer, O., 1993, "The Variation of the Specific Heat Ratio and the Speed of Sound in Air With Temperature, Pressure, Humidity, and CO_2," J. Acoust. Soc. Am., **5**, pp. 2510–2516.

Gabriel Dan Ciocan
Research Associate
e-mail: gabrieldan.ciocan@orange.fr

Monica Sanda Iliescu
Doctoral Student
e-mail: msiliescu@yahoo.fr

Laboratory for Hydraulic Machines,
Ecole Polytechnique Fédérale de Lausanne
(EPFL),
Avenue de Cour 33bis,
CH-1007, Lausanne, Switzerland

Thi Cong Vu
Senior Developement Engineer
e-mail: thi.vu@ps.ge.com

Bernd Nennemann
Research Assistant
e-mail: bernd.nennemann@ps.ge.com

Hydropower Technology,
GE Energy,
795 George V,
Lachine, Quebec, H8S-4K8, Canada

François Avellan
Professor
Laboratory for Hydraulic Machines,
Ecole Polytechnique Fédérale de Lausanne
(EPFL),
Avenue de Cour 33bis,
CH-1007, Lausanne, Switzerland
e-mail: francois.avellan@epfl.ch

Experimental Study and Numerical Simulation of the FLINDT Draft Tube Rotating Vortex

The dynamics of the rotating vortex taking place in the discharge ring of a Francis turbine for partial flow rate operating conditions and cavitation free conditions is studied by carrying out both experimental flow survey and numerical simulations. 2D laser Doppler velocimetry, 3D particle image velocimetry, and unsteady wall pressure measurements are performs to investigate thoroughly the velocity and pressure fields in the discharge ring and to give access to the vortex dynamics. Unsteady RANS simulation are performed and compared to the experimental results. The computing flow domain includes the rotating runner and the elbow draft tube. The mesh size of 500,000 nodes for the 17 flow passages of the runner and 420,000 nodes for the draft tube is optimized to achieve reasonable CPU time for a good representation of the studied phenomena. The comparisons between the detailed experimental flow field and the CFD solution yield to a very good validation of the modeling of the draft tube rotating vortex and, then, validate the presented approach for industrial purpose applications.
[DOI: 10.1115/1.2409332]

1 Introduction

Hydropower is a clean form of power generation, which uses a renewable source of energy: water. Moreover, storage capability and flexible generation makes hydropower the quasi-ideal form of power generation to meet the variable demand of the electricity market, therefore it is not surprising that the turbines tend to be operated over an extended range, far from the optimum flow conditions. In particular, at part load operating conditions turbine fixed-pitch runners show a strong swirl at the runner outlet. As the incoming swirling flow is decelerating in the diffuser cone, a hydrodynamic instability arises under the form of a characteristic precession flow—see Jacob [1].

For the usual setting levels of the turbines, defined by the Thoma cavitation number σ, the static pressure is such that the cavitation development makes visible the core of the vortex and, therefore, the precession movement through a typical helical shape of the cavity in the draft tube cone. The cavitation vortex core of the swirling flow at the runner outlet is the so-called "rope." The development of cavitation introduces compliance in the turbine draft tube flow and, consequently, a natural frequency corresponding in a first approximation to the frequency of the free oscillation of the water plug in the draft tube against the compliant vapors volume of the rope. The coupling between this natural frequency and the precession frequency leads to the draft tube surge; see Nishi et al. [2], which can inhibit the operation of the whole hydropower plant.

Characterizations of the part load operating conditions have been carried out extensively; see Jacob [1], and the technology for overcoming the draft tube surge through active control has been established. However, any attempt of modeling the hydrodynamic phenomena leading to the development of the rope and its interaction with all the turbine and hydraulic system components needs further investigations.

Recent developments of experimental methods and numerical simulation techniques permit the detailed analysis of this flow. It is feasible presently to predict this operating regime, from the point of view of the theoretical background, the computational resources, and the existence of accurate experimental measurements to rely on.

The availability of advanced optical instrumentation, such as laser Doppler velocimetry (LDV) or particle image velocimetry (PIV) systems, gives the opportunity to perform flow surveys in turbomachinery and in particular to investigate the unsteady characteristics of the complex flow velocity fields in the case of, for instance, the rotor-stator interactions, the draft tube, or the spiral casing.

The progress of the numerical techniques in the prediction of the turbine characteristics for the operating ranges in the vicinity of the beam efficiency point (BEP) insure a good accuracy—see

Contributed by the Fluids Engineering Division of ASME for publication in the JOURNAL OF FLUIDS ENGINEERING. Manuscript received June 27, 2005; final manuscript received July 10, 2006. Review conducted by Joseph Katz.

Table 1 Bibliographical result of the CFD/experimental global values comparison

Comparison between experimental and numerical data	Ruprecht et al.[a]	Scherer et al.[b]	Miyagawa et al.[c]	Sick et al.[d]	This paper
CFD f_r/Experimental f_r	0.93	1 (low resolution)	Not available	1.12	1.13
CFD pressure pulsation amplitude/experimental pressure pulsation amplitude	0.7–1.3	1–1.4	Not available	0.83	1

[a]See Ref. [5].
[b]See Ref. [6].
[c]See Ref. [7].
[d]See Ref. [8].

Vu et al. [3]. The massively parallel computations development permits now the numerical simulation of the whole turbine—see Ruprecht et al. [4] or to detail the flow in a specific part of the turbine.

One of the new challenges for the numerical turbine simulation is to predict the partial or full flow rate operating regimes and the first simulations are promising. Ruprecht et al. [5] are focused on the influence of different turbulence models on the modeling of the draft tube vortex, carried out in a straight cone. Based on the length of the predicted vortex structure, certain turbulence models tend to have a damping effect and from this point of view, the most accurate, is found to be a two-scale model described by Hanjalic, reduced to a two equations set by a Very Large Eddy Simulation (VLES) approach. The validation of the numerical simulation is performed on a Francis turbine draft tube with three outlet channels. For a relatively coarse mesh—250,000 nodes—and the computed runner outlet velocity profile as inlet conditions, the vortex frequency is well predicted—93% of the measured vortex frequency, but an underestimation of the wall pressure fluctuation amplitudes is obvious. The given explanation turns towards the possible variation of the flow rate during operation at low flow rate.

Scherer et al. [6] reported the turbine design improvement for the draft tube operating at partial flow rate conditions by Computational Fluid Dynamics (CFD). An unsteady one-phase Reynold's Averaged Navier-Stokes (RANS) simulation of the draft tube vortex in a Francis turbine model is used to compare two draft tube configurations. By comparing the calculated performances of two model machines over the operating range, the second one is found to have better draft tube efficiency at low flow rate operation, justified by the obtained pressure pulsations improvement, the diminishing of the strong velocity gradients, and backflow zone in the cone. The comparison with wall pressure experimental data shows a good agreement for the vortex frequency and a systematic underestimation of the pressure fluctuation amplitudes.

Miyagawa et al. [7] performed an unsteady simulation of the draft tube vortex for a Francis pump turbine, consecutively for two different runners. The purpose was to analyze the influence of the velocity profile at the runner outlet on the flow instability in the draft tube. Two runner designs are tested for the same draft tube geometry—using a mesh of 620,000 nodes. The same vortex behavior changes are observed in CFD and experimentally by qualitative comparisons with the rope visualizations. The authors tested a one phase and a two-phase model as well, and found that it influences mainly the fluctuation amplitude and has no influence on the vortex frequency, but no further details are given. The void fraction in the vortex core is found to be similar compared to high-speed camera visualizations, but quantitative comparisons are not available.

In the last two papers, the inlet boundary conditions are taken as the result of the steady calculation of the runner and/or guide vanes—stay vanes. It provides, thus, the uniform axial and tangential velocity profile, circumferentially averaged. As outlet condition, a constant pressure value is considered.

Sick et al. [8] performed a numerical simulation of a pump turbine with a Reynolds stress turbulence model, already validated for near BEP operating conditions. Unlike other studies, the runner and the outlet domain were included in the computational domain with 1.5 million of cells for minimizing the steady inlet velocity profile effect and the uniform outlet pressure boundary condition effect. The comparison with experimental data shows an overestimation of the vortex frequency and a quite good agreement for the pressure fluctuations amplitude. The analysis of the forces and bending moments on the runner shaft due to the vortex gives the same characteristics like the pressure pulsations: a good agreement for the amplitude and an overestimation of the frequency.

These papers get to a fairly good agreement with the global characteristics of the flow—see Table 1, but a validation implies the validations of the partial flow rate vortex phenomenology and also comparisons of the detailed flow field.

In the frame of the FLINDT—flow investigations in draft tubes—project, Eureka No. 1625, the operation in low flow rate conditions of a Francis turbine is investigated, both experimentally and numerically.

The present paper describes:

— FLINDT phase 2 experimental LDV, PIV, and wall pressure measurements for the rotating vortex study in noncavitating regime in the cone of the draft tube. In this paper only the local measurements in the cone region will be presented;
— CFD methodology for the unsteady simulation of the rotating vortex;
— comparison of the numerical solution with experimental data.

2 Experimental Approach for the Draft Tube Rotating Vortex Measurement Scale Model of Francis Turbine

The investigated case corresponds to the scale model of the Francis turbines of high specific speed, $\nu=0.56$ ($n_q=92$) of a hydropower plant built in 1926, owned by ALCAN. The 4.1 m diameter runners of the machines were upgraded in the late 1980s. The original draft tube geometry is of Moody type. For the purpose of the FLINDT research project, an especially designed elbow draft tube with one pier replaces the original Moody draft tube. The scale model—$D_{1e}=0.4$ m—is installed on the third test rig of the EPFL Laboratory for Hydraulic Machines and the tests are carried out according to the IEC 60193 standards [9].

The energy-flow coefficients and efficiency characteristics of the scale model are represented on the hill chart in Fig. 1. According to the objective of the study, an operating point is selected at partial flow rate condition. The point of interest is selected for a specific energy coefficient of $\psi=1.18$ and a flow rate coefficient of $\varphi=0.26$, which corresponds to about 70% Q_{BEP} and a Re number of 6.3×10^6.

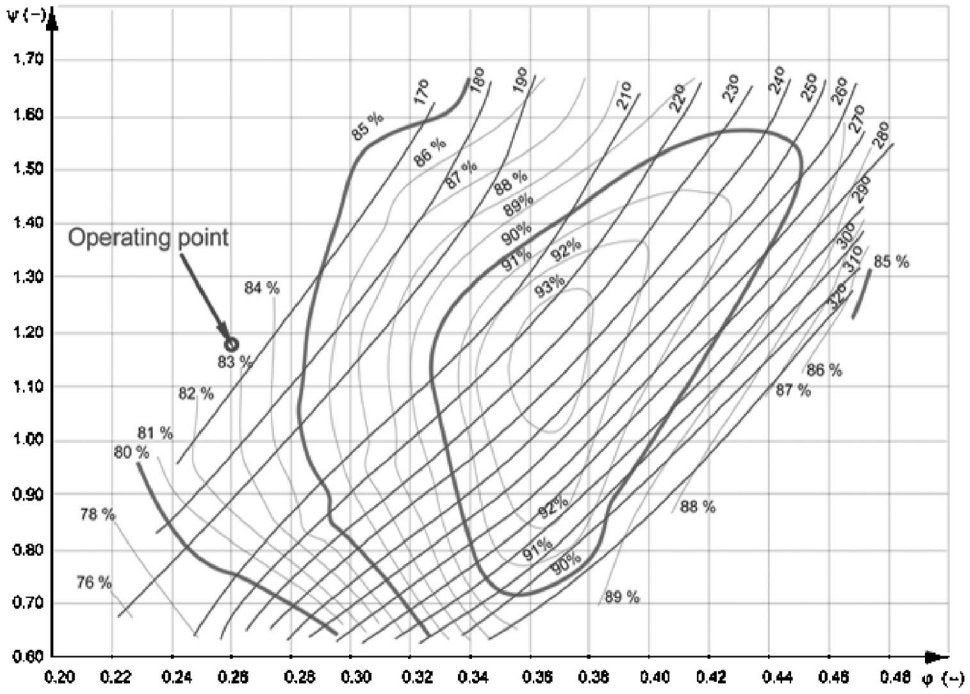

Fig. 1 Scale model hill chart and part load operating point

Three different measurement methods are used: 3D PIV, 2D LDV, and unsteady wall pressure. The investigated zones are presented in Fig. 2.

2.1 Particle Image Velocimetry Instrumentation. The 3D instantaneous velocity field in the cone is investigated with a Dantec M.T. 3D PIV system, which consists of a double-pulsed laser, two double-frame cameras, and a processor unit for the acquisition synchronization and the vectors detection by cross correlation.

The illuminating system is composed of two laser units with Neodynium-doped Yttrium Aluminium Garnet crystals (Nd:YAG), each delivering a short impulse of 10 ns and 60 mJ energy at 8 Hz frequency. Thus the time interval between two successive impulses can easily be adjusted within 1 μs–100 ms range, depending on the local flow characteristics or the phenomenon, which is to be captured. The output laser beam of 532 nm is guided through an optical arm, for accessibility, to a beam expander and transformed into a sheet of 4 mm width and 25 deg divergence.

Two Hi-Sense cameras with a resolution of 1280×1024 pixels are used for 200×150 mm^2 investigation area. The cameras are placed in a stereoscopic configuration, focused on the laser-sheet, synchronized with the two pulses. They capture the position of seeding particles of ~10 μm diameter by detecting their scattered light. In order to avoid possible reflections in the laser wavelength on the cameras, due to the optical interfaces or to residual bubbles in the flow, fluorescent particles of 580 nm emission wavelength are used, along with corresponding cutoff filters on the cameras.

For the optical access, the cone is manufactured in Polymethyl methacrylate (PPMA) with a refractive index of 1.4, equipped with a narrow window for the laser's access and two large symmetric windows for the cameras access, having a flat external surface for minimizing the optical distortions.

The corresponding two-dimensional vector maps, obtained from each camera by a fast Fourier transform-based algorithm, are combined in order to have the out-of-plane component, character-

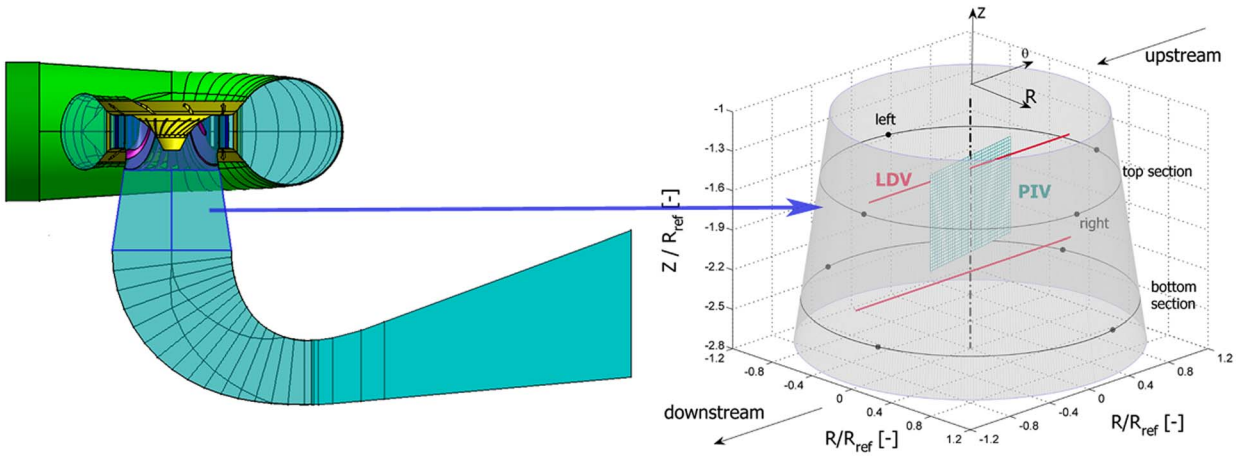

Fig. 2 Measurement zones in the cone of the FLINDT turbine

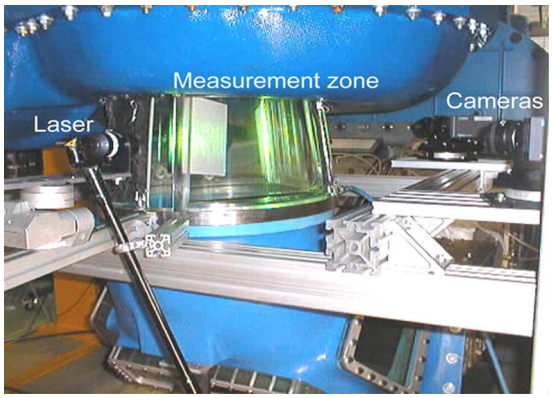

Fig. 3 Calibration setup for 3D PIV measurements

izing the displacement in the laser-sheet width.

The correlation between the local image coordinates and real space coordinates is realized through a third order optical transfer matrix, which includes the correction of distortions due to different refractive indices in the optical path and to the oblique position of the cameras. The calibration relation is obtained acquiring images of a plane target with equally spaced markers, moved in five transversal positions in order to have volume information, see Fig. 3. The target displacement in the measurement zone, with accuracy within the narrow limits of 0.01 mm in translation and 0.1 deg in rotation, insured a good calibration quality; see Iliescu et al. [10]. The overall uncertainty of the PIV 3D velocity fields is 3% of the mean velocity value.

2.2 Laser Doppler Velocitry Instrumentation. The 2D velocity profile survey is performed by the LDV measurement method—see Fig. 2, on two complete diameters, at the cone inlet and outlet.

The LDV system is a Dantec M.T. two components system, using backscattered light and transmission by optical fiber, with a laser of 5 W argon-ion source. An optical window with plane and parallel faces is used as interface. The geometrical reference position of the measurements is obtained by positioning the laser beams on the windows faces with accuracy better than 0.05 mm. Two components are measured: the tangential component of the velocity C_u and the axial one C_z, see Fig. 2. The uncertainties of the laser measurements are estimated to 2%—see Ciocan et al. [11].

2.3 Unsteady Wall Pressure Instrumentation. The unsteady wall pressure measurements—100 simultaneous acquisitions—permit to discriminate the rotating pressure field due to the vortex rotation and the synchronous pressure field at the same frequency—see Arpe. [12] In order to capture the phenomena of interest in low flow rate turbine operating conditions, all pressure signals are acquired simultaneously with a HP-VXI acquisition system using a sampling frequency of $16\times n$, $80\times n$ and 2^{14} samples. The spectral analysis does not show differences between the three sampling frequencies, thus for the analysis it was chosen the $16\times n$ acquisition rate. This setup allows recording 430 vortex passages, providing an acceptable number of segments for the averaging process and insuring an uncertainty of 3%.

The pressure field evolution, depending on the Thoma number, is obtained in the whole draft tube. Only eight pressure sensors in the cone will be presented in this paper, corresponding to the positions described in Fig. 2.

2.4 Data Post Processing. For periodic flows, the signal is reconstructed by synchronizing the acquisition with a reference signal at several time shifts τ—Fig. 4. The reference signal comes from a pressure sensor and the pressure drop corresponding to the vortex passage is used for triggering all acquisitions.

Thus the periodic signal can be decomposed according to

$$C_i(t) = \bar{C} + \tilde{C}(\tau) + C'(t) \tag{1}$$

The phase-locked component $\tilde{C}+\bar{C}$ is obtained by averaging the instantaneous values at the same τ value; see Eq. (3)

$$\bar{C} = \langle C_i \rangle = \lim_{N\to\infty} \frac{1}{N} \sum_{i=1}^{N} C_i(t) \tag{2}$$

$$\tilde{C}(\tau) = \lim_{N'\to\infty} \frac{1}{N'} \sum_{i=1}^{N} [C_i(\tau) - \bar{C}] \tag{3}$$

with

$$\bar{\tilde{C}} = 0$$
$$\langle C' \rangle = \lim_{N\to\infty} [C_i(t) - \bar{C} - \tilde{C}] = 0 \tag{4}$$

Fifteen phase values, equidistant in a vortex passage interval, T_r, are selected to complete the phase average. Thus the vortex synchronous flow is reconstituted.

The LDV acquisition is triggered with the wall pressure signal breakdown given by the vortex passage. The LDV data signal is not continuous, thus an additional reference signal is taken from an optical encoder mounted to the runner shaft. The resolution of the optical encoder is 0.04 deg of runner rotation. In this way we

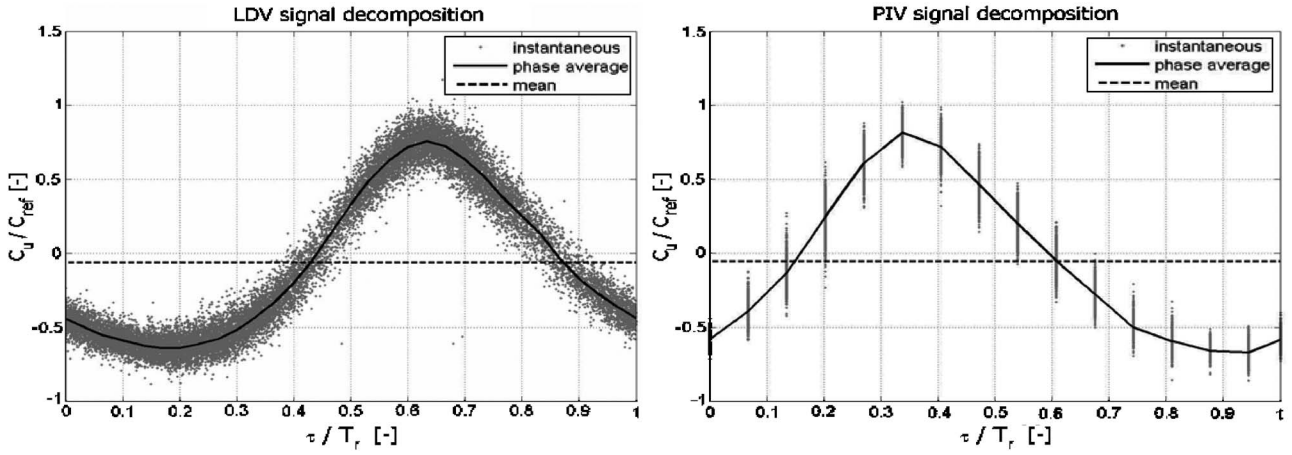

Fig. 4 Phase average calculation of the LDV and PIV velocity signal

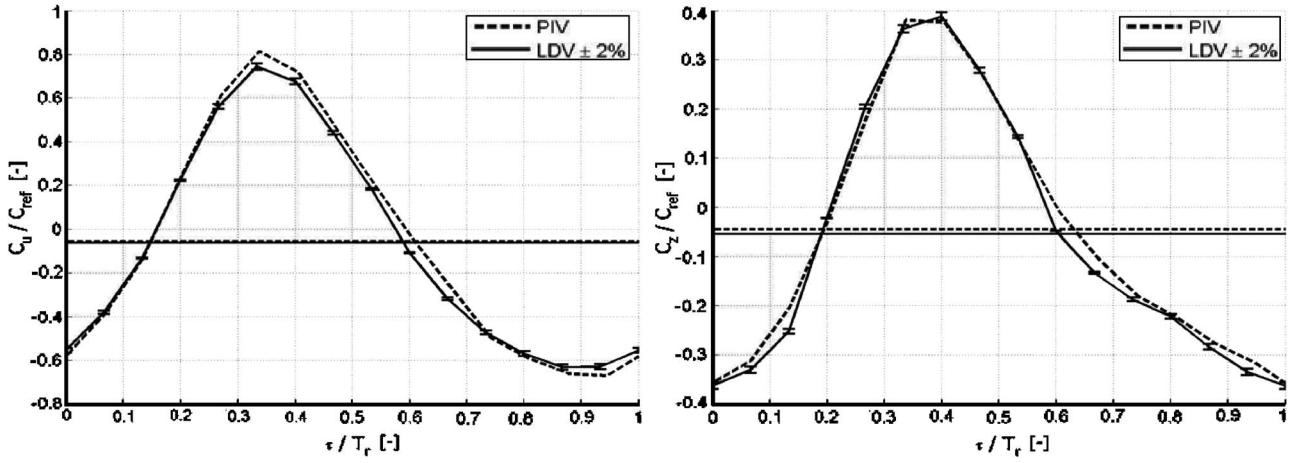

Fig. 5 LDV-PIV phase average comparison

have the relation between the runner spatial position and the vortex period. Thus each LDV acquisition is reported to the corresponding vortex period via the runner position—see Fig. 4. In this way the fluctuation of the vortex period is obtained at 3% of its mean value.

Subsequent to a mean convergence study, the number of acquired velocity values for each phase, τ value, has been between 1000 and 3000 instantaneous values, thus the mean velocity value $\bar{C}$ represents the statistic over 30,000 instantaneous velocity values.

For the PIV measurements, subsequent to a mean convergence study, the number of acquired vector maps for each phase, τ value, has been set to 1200, thus the mean velocity value $\bar{C}$ represents the statistic over 18,000 instantaneous velocity fields. The PIV acquisition is performed at constant τ value reported to the vortex trigger signal—see Fig. 4. The influence of the vortex period variation for this kind of phase average calculation is checked and fits within the same uncertainty range like the measurement method 3%—see Fig. 5.

The direct comparison between the mean velocity values, see Fig. 12, or phase average velocity values, see Fig. 5, obtained by LDV and PIV measurements in the upper part of the cone, shows an excellent agreement as well.

Concerning the phase average calculations for the unsteady pressure acquisition—at constant acquisition rate—and for the numerical results, they are performed by averaging the instantaneous values for each τ interval.

2.5 Description of the Study Case. The experimental inves-

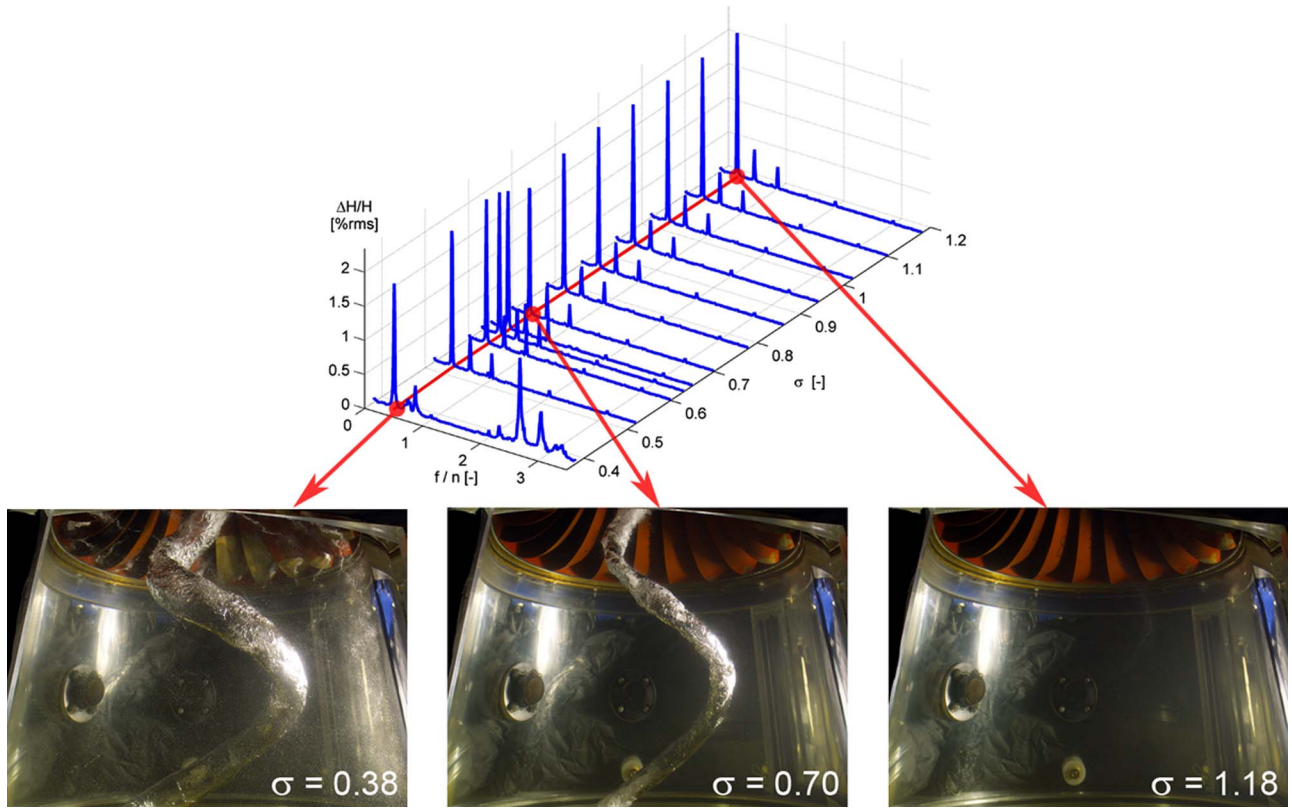

Fig. 6 Waterfall diagram and corresponding cavitation ropes

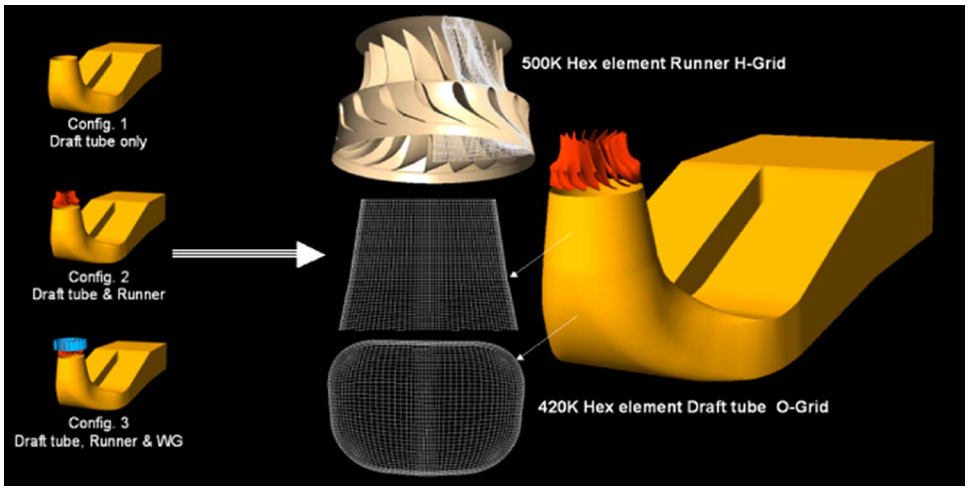

Fig. 7 Computation flow domain and mesh

tigation is carried out for a range of Thoma cavitation numbers varying from $\sigma=1.18$, cavitation free conditions, to $\sigma=0.38$, maximum rope volume. For a given operating point, same head and flow rate, the vortex frequency, pressure pulsation amplitude and volume of vapor in the vortex core are dependent of the σ value as shown on the waterfall diagram in Fig. 6.

Since, for the moment, the numerical simulation is performed for single-phase flow condition, the study case is limited to the cavitation free condition, $\sigma=1.18$. The present operating point corresponds to a flow coefficient $\varphi=0.26$ and a specific energy coefficient $\psi=1.18$.

3 Numerical Simulation of Unsteady Flow Behavior

3.1 CFD Methodology for the Unsteady Simulation of the Rotating Vortex. Nowadays it became common to predict flow behavior and energy loss in hydraulic turbine components by CFD application, using a Navier–Stokes flow solver closed with the *k*-epsilon turbulence model. When individual hydraulic components are optimized, then steady state stage flow analysis for combined hydraulic components is performed to establish the efficiency of the entire turbine—see Vu et al. [3]. For investigation of unsteady flow behavior in hydraulic turbine components, such as the rotating rope phenomena in draft tubes at partial flow rate condition or the interaction of flow between wicket gates and runner blades, unsteady flow computation is required. For the present application, ANSYS-CFX 5.6 version is used for the computation. Also the standard *k*-epsilon turbulence model is used for the flow simulation.

3.2 Choice of Computational Flow Domain. For the unsteady flow simulation of the rotating vortex rope, there are three possible configurations for the computational flow domain. The first configuration considers only the draft tube geometry. The second configuration includes runner and draft tube, and the third one includes wicket gates, runner, and draft tube geometries. The second configuration is selected here for the unsteady simulation as the best compromise between solution accuracy requirements and computer resources. The transient runner/draft tube simulation allows us to predict the true unsteady interaction of the flow between the upstream runner and the elbow draft tube. In this approach, the unsteady relative motion between the two components on each side of the general grid interface (GGI) connection is simulated. The interface position is updated for every time step, as the relative position of the grids on each side of the interface changes. Figure 7 represents the computational flow domain for the unsteady flow simulation and the multi block structured meshes generated for the runner and the draft tube. An O type 420,000 node mesh is used for the draft tube and an H mesh type with 500,000 nodes is generated for the 17 flow passages of the runner. Due to a foreseen requirement of very large Central Processing Unit (CPU) time for the computation, we prefer to keep a relatively coarse mesh size for the application.

3.3 Computational Procedure for Unsteady Flow Simulation. Two preliminary steady state calculations were performed, the first one for the spiral casing and the distributor, and the second one for the stay vane, guide vane, and runner assembly. The results of the first calculation were used as inlet conditions for the second calculation. In turn, the inlet conditions for the unsteady calculation—including turbulent kinetic energy and dissipation rate profiles—were extracted form the second steady state calculation. The average turbulence intensity at inlet to the unsteady calculation domain is about 3.5% while the average relative viscosity is 110. In this way, for the unsteady computational domain—runner and draft tube—the flow rate, flow direction, and the turbulence intensity obtained in the second steady preliminary calculation are specified as the inlet boundary conditions. The outlet condition is the zero gradient condition in the outflow direction is applied for all variables.

Since we are interested in simulating a periodic-in-time quasi-steady state, it is recommended to first obtain a steady state solu-

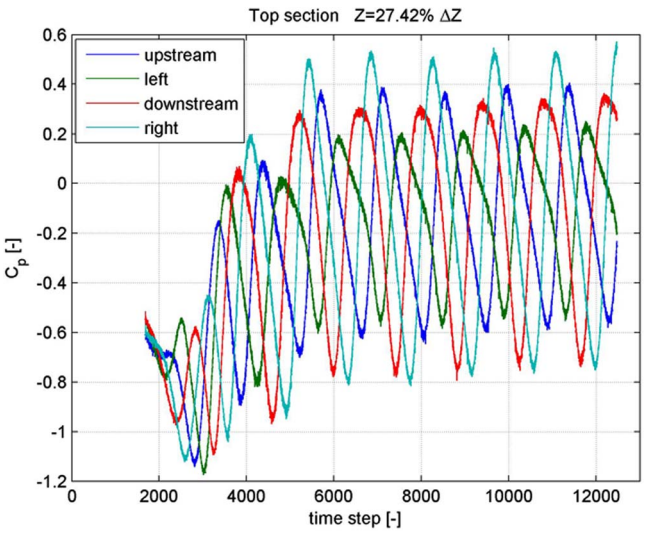

Fig. 8 Evolution of pressure monitoring in transient computation

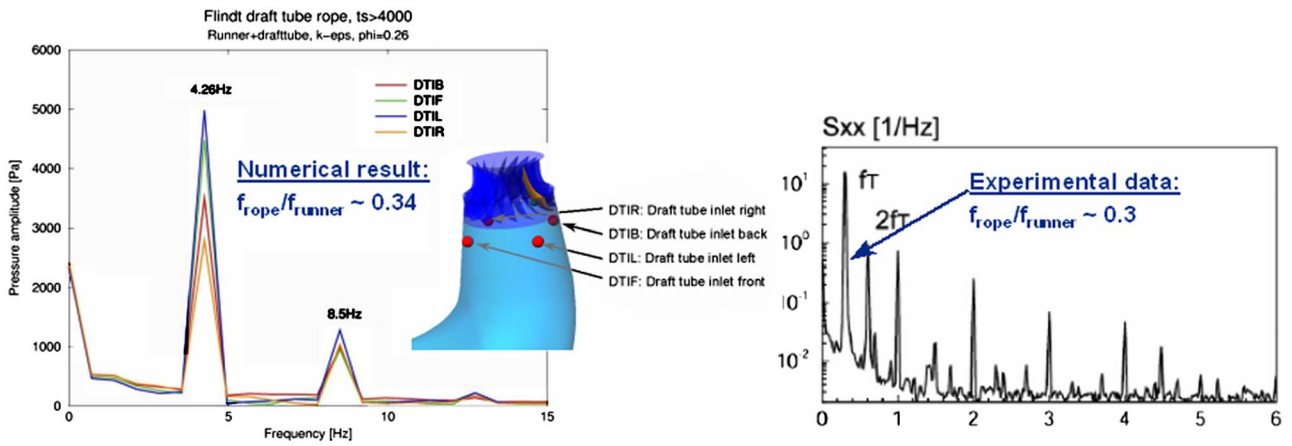

Fig. 9 Comparison of CFD and experimental frequency spectra

tion using the stage flow calculation and then using this steady state solution to start the unsteady runner/draft tube simulation. The transient solution should converge to the desired periodic behaviour after several runner revolutions. For hydraulic turbine machines, using time step of about 1 time step /deg of revolution is satisfactory. The rms convergence criterion of the residual for each time step is specified to 10^{-4}. Figure 8 shows the evolution of pressure monitoring in the draft tube cone during the transient computation. It takes about 1000 time steps to start the fluctuation from a steady state solution and another 3000 time steps to reach the periodic unsteady state. Then starting from that point, we obtain a periodic signal at the cone region as shown in Fig. 8. The numerical solution is considered to be well converged after 11,500 time steps or after 24 runner revolutions. The computation is carried out on a Beowulf Linux cluster. It takes about 25 CPU day time in parallel computing with 4 CPUs.

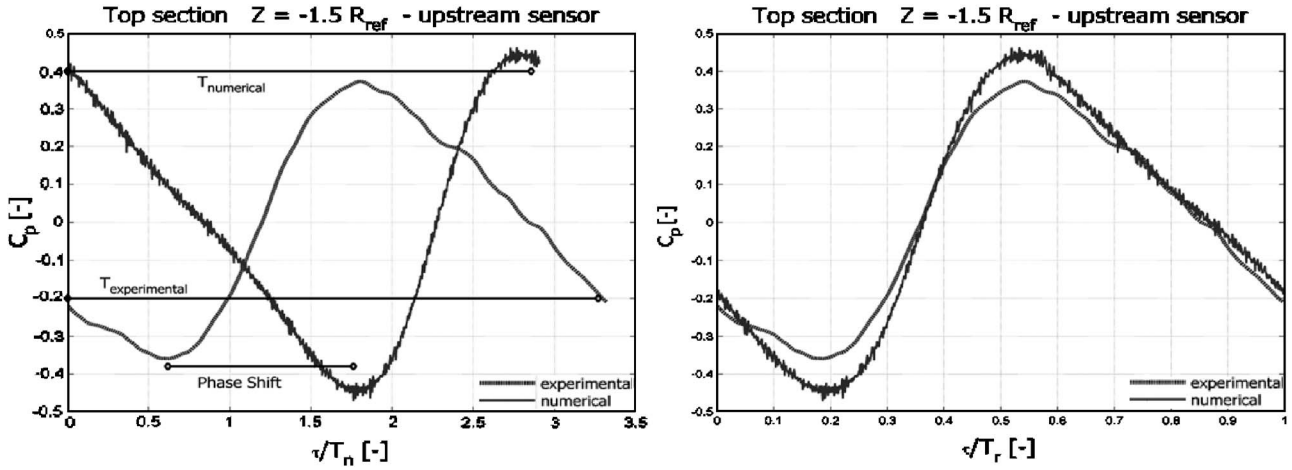

Fig. 10 Period adjustment and phase shift on the numerical data to compare with the experimental ones

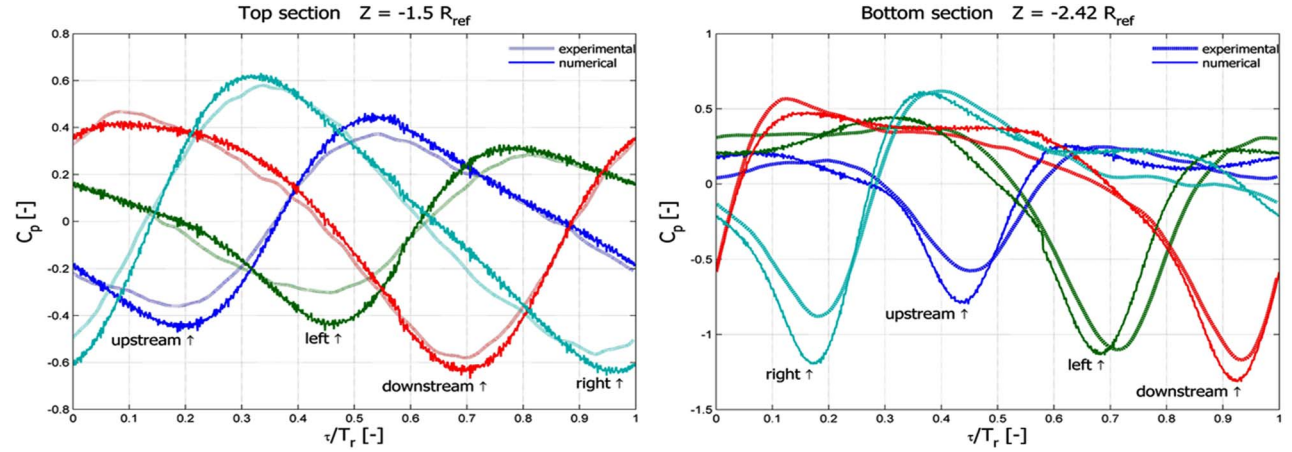

Fig. 11 Phase average wall pressure comparison

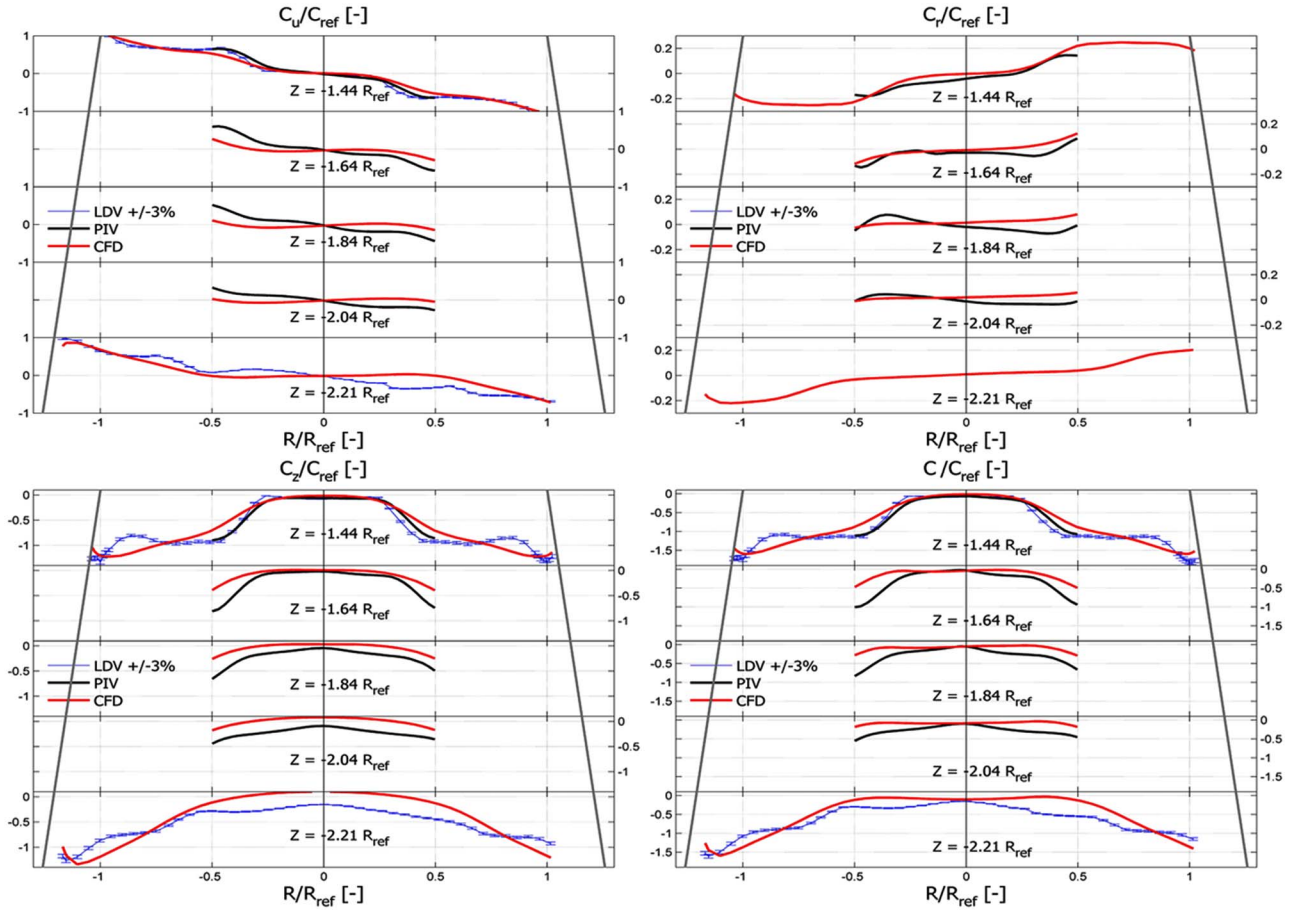

Fig. 12 Mean velocity profiles comparison in the cone

Unsteady flow computations generate tremendous amounts of data if one wants to write a transient solution for every single time step. It is preferable that monitoring points are specified at locations of interest during the preprocessing stage and only intermediary transient solutions are written at a certain interval time step. For the present application, during the last 2500 time steps, monitor points are specified for all locations at which pressure and velocity components (PIV) are measured for a total of about 1200 points. Also, transient solutions are written for every ten time steps.

4 Comparison of the Numerical Solution With Experimental Data

4.1 Validation With Global Quantities. For the partial flow rate operating points, the determining parameters for the interaction between the machine and the circuit are the vortex frequency and the associated pressure amplitude pulsations. The waterfall diagram, as shown in Fig. 6, gives a three-dimensional representation of the pressure fluctuation amplitude spectra in the frequency domain for each σ value. This frequency varies between 0.3 and 0.36 of the runner revolution frequency for the σ investigation range.

4.1.1 Vortex Frequency. For $\sigma=1.18$, the vortex frequency from the experimental data is 0.30 of the runner revolution. The numerical vortex frequency obtained by frequency spectrum analysis is 0.34 of the runner revolution frequency—see Fig. 9. Thus the numerical simulation vortex frequency is about 13% higher than the measured vortex frequency but it falls within the measured variation range for the σ values in these operating conditions.

4.1.2 Pressure Fluctuation Amplitude. For comparing the phase average pressure fluctuation resulting from the numerical calculation with the experimental results, the phase reference of the numerical simulation is adjusted in order to match the phase of the experimental signal. Therefore, the phase reference is chosen for an experimental sensor: all the others begin synchronized with this one. The numerical phase—without any physical significance—is adjusted on the position of the experimental sensor and all numerical phase averages are corrected with this phase shift (difference) $\delta\tau$—see Fig. 10.

To be coherent for the period representations, the experimental period was chosen like reference and the numerical period is stretched to a dimensionless vortex period as follows:

$$\tau = \tau_{\text{Numerical}} - \delta\tau$$

$$k_r = \frac{T_{r\text{Numerical}}}{T_{r\text{Experimental}}} \tag{5}$$

$$\tau = \tau_{\text{Experimental}} \cdot k_T$$

Figure 2 shows monitor points for static pressure at different section planes. Figure 11 shows the comparison of the numerical static pressure fluctuation with the experimental data for one period of the vortex. Both signals are normalized with their own vortex frequency. The correlation between the numerical simulation and the experimental data is excellent. The pressure fluctuation amplitude is well predicted not only at the runner outlet, but its evolution in the cone is in good agreement with the experimental data for all sensors angular positions, as well—see Fig. 2. The

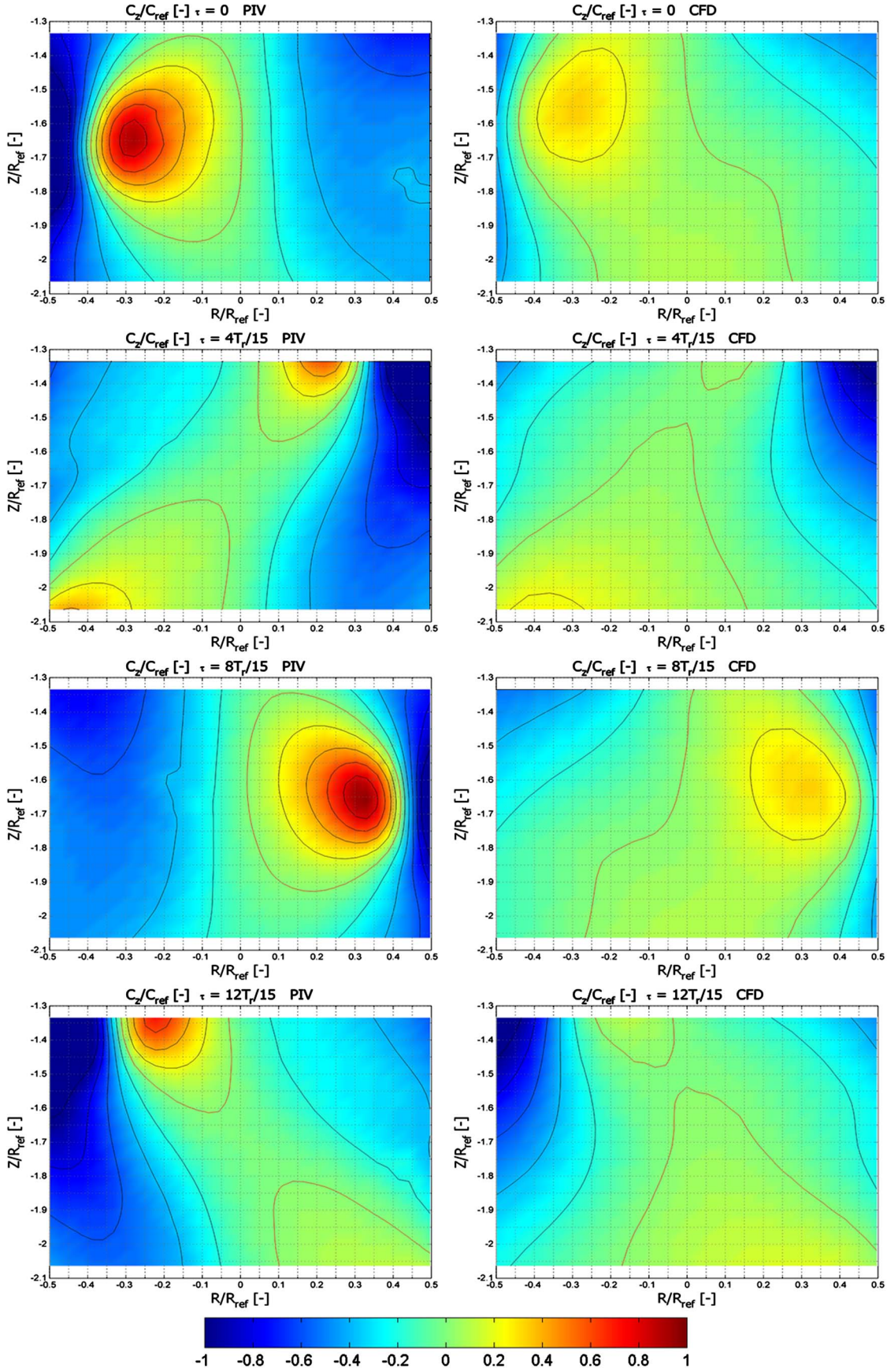

Fig. 13 C_z **phase average velocity profiles**

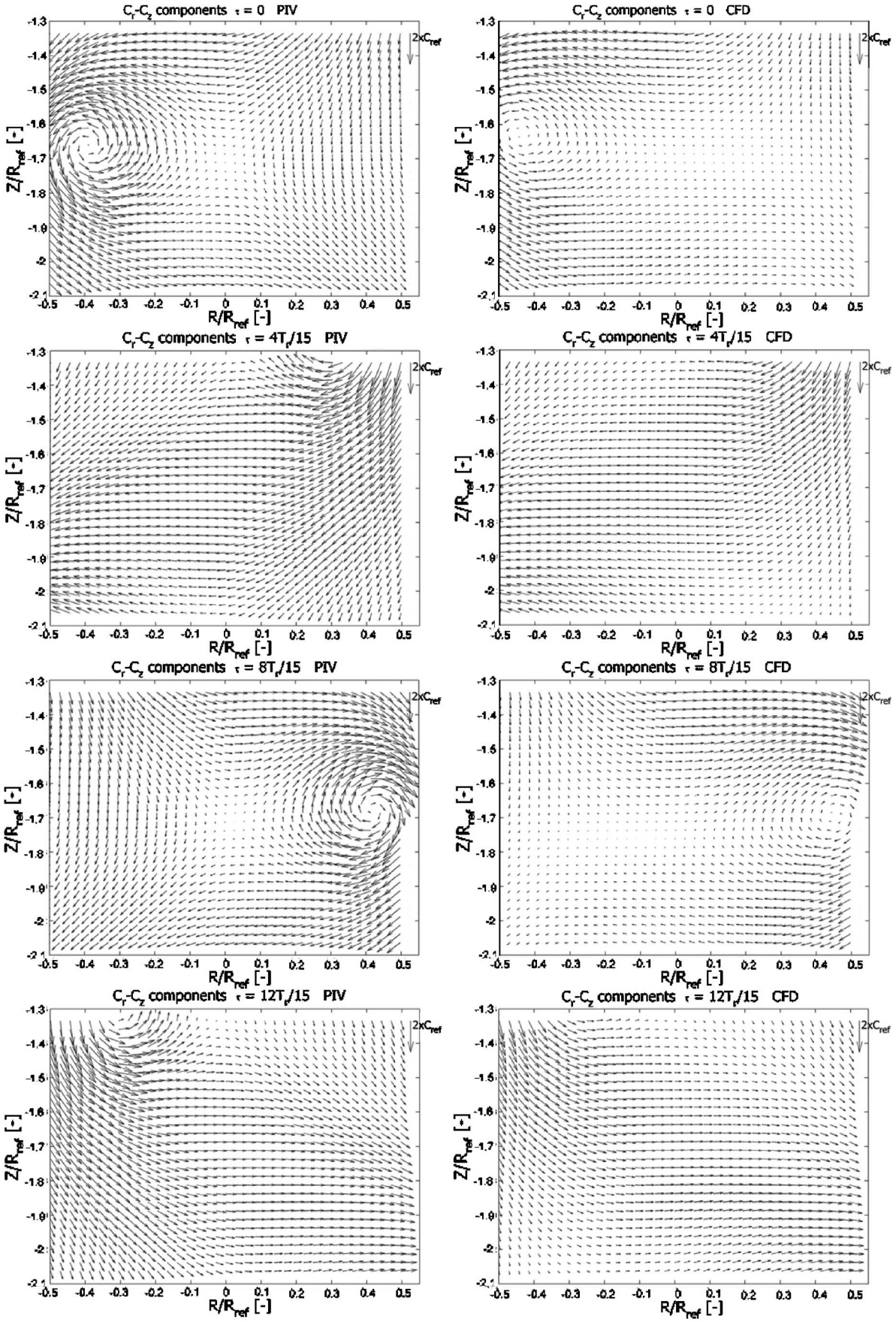

Fig. 14 C_r - C_z **phase average velocity profiles comparison in the cone**

difference between the experimental results and numerical ones reported to the mean pressure level is less than 2.5%, so in the same range as the measurement accuracy.

4.2 Validation with Local Flow Structure. For improving the turbines design it is necessary to predict the real flow structure and associated phenomenology throughout the entire analyzed domain.

4.2.1 Mean Velocity Profiles. The mean flow velocity shows the decelerated swirling flow that develops in a central stagnation zone—see Fig. 12. The vortex encloses this zone of average velocity near zero. The flow rate distribution is therefore restricted to the circular zone between the cone walls and the vortex conical supporting surface. The LDV measurements that complete the PIV measurements in the inlet and outlet cone cross sections show a higher velocity near the cone wall, for the axial and tangential velocity. The angle at which the stagnation region develops downstream is higher than the angle of the turbine cone.

For assessing the flow structure prediction, the numerical mean velocity field is compared with the LDV and PIV measurements. The comparison of the flow structure in the cone of the turbine shows a generally good agreement of the velocity mean values—see Fig. 12. A small difference is observed at the runner outlet in the strong velocity gradients zone—between $R/R_{out}=0.2$ to 0.35. The numerical results are smoother, and for this reason the zone of the mean near zero velocities, in the centre of the cone, is not the same.

4.2.2 Phase Average Velocity Field. For the comparison of LDV and PIV velocity measurements with the CFD results, the same procedure like for the pressure is considered: the numerical period is shifted onto the experimental one and the same phase shift $\delta\tau$ is applied for all numerical velocity signals.

The central stagnation zone, observed in the time averaged values, represents the zone closed by the vortex passage in phase average values. This region is a series of backflows, triggered by the vortex passage—see Fig. 13.

The phase average vector field representation shows the vortex position in the measurement section—see Fig. 14. The phase correspondence obtained by the pressure fitting is the same as for the phase velocity profiles. Qualitatively the vortex center position is placed on the same cone height. A small difference is observed in the radial position, in the numerical simulation, it is closer to the cone wall. This difference is in accordance with the mean velocity profile. The phase average flow structure of the numerical simulation is very similar to the experimental measurements one.

4.2.3 Vorticity Field. The calculation of the vorticity—see Eq. (6), for each phase averaged velocity field, permits to quantify the vortex evolution in the measurement zone.

$$\vec{\Omega} = \vec{\nabla} \times \vec{C} \tag{6}$$

As represented in Fig. 15, the vortex position is well predicted by the numerical calculations, with a difference of 5% of the radius between the predicted position and the measured one. The vorticity is smaller in numerical calculations with about 18%, but its position closer to the cone walls explains the fact that the same pressure fluctuation amplitude values are obtained at the wall.

4.2.4 Vortex Center. The vortex center position is estimated considering the vortex center as the maximum vorticity point in the cone section which corresponds to the stagnation point in the phase average flow field—see Fig. 16. The vortex position trace in the section is similar with the rope position visualization by the vapors zone in the section for the low sigma numbers—see Fig. 6. The comparison of the vortex center between experimental and numerical data is representative for the vortex phenomenology and the difference between the center position, as well as the vorticity intensity, could by explained by the relatively coarse mesh compared to the vortex size—see Fig. 17. The mesh size is chosen as the best compromise between the result quality and the required computational time.

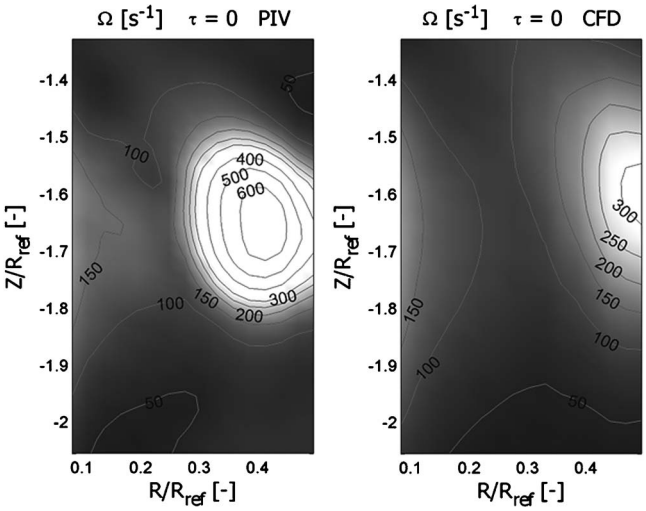

Fig. 15 Vorticity field in the cone

5 Concluding Remarks

This paper has presented a CFD methodology to study the unsteady rotating vortex in the FLINDT draft tube and associated experimental study of the flow phenomena.

A large experimental database is built in the frame of the FLINDT project for partial flow rate operating regime. 3D PIV, 2D LDV, unsteady wall pressure, and unsteady wall friction measurements are available for analysis, with certified accuracy.

The transient flow simulation is for single phase using a standard k-epsilon turbulence model. Although a relatively coarse mesh is used for the computational, an excellent agreement between numerical results and experimental data is obtained. The accuracy of the prediction for the vortex global quantities, pressure pulsation amplitude (3% error), and vortex frequency (13% error) is very good. For the first time the simulated vortex structure of the rotating vortex is assessed and compared with experimental measurements. The quantitative analyses in terms of mean velocity field, phase average velocity field, vorticity, and vortex center position also show a good agreement and validate the phenomenology of the vortex rope in numerical simulations. We can

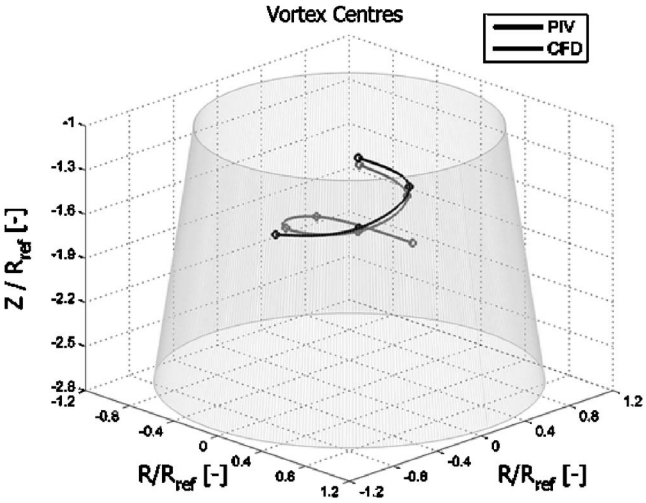

Fig. 16 Vortex center evolution in the cone

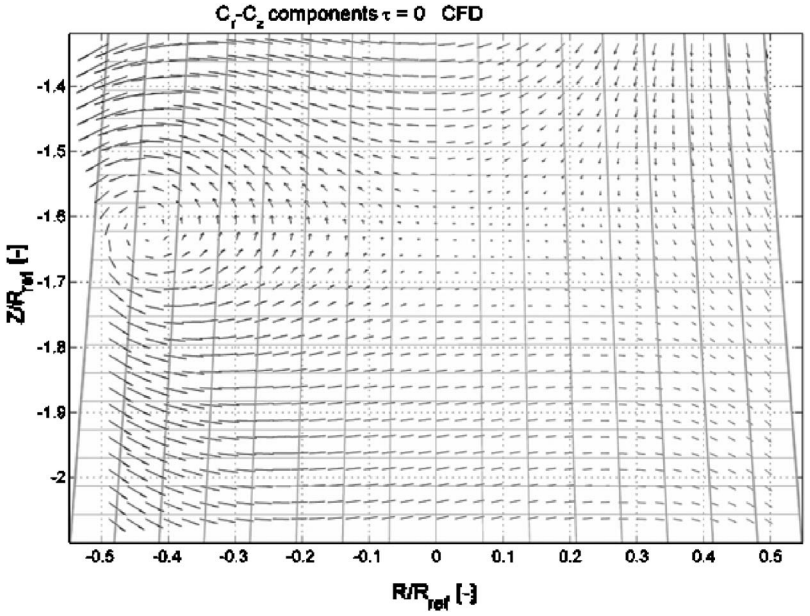

Fig. 17 Mesh size in the vortex center position

use with confidence this approach for design purpose application. Compared with a classical steady simulation, the unsteady CFD used for partial flow rate simulation provides important information for the machine design: the wall pressure unsteady fluctuations level and velocity field structure.

In the future the extension of this approach to two phase flows will permit to take into account another important parameter for the partial flow rate phenomenology: the cavitation and its compliance.

Acknowledgment

The authors take this opportunity to thank our FLINDT project—Eureka No. 1625—partners: Alstom Hydro, Electricité de France, VA Tech Escher Wyss Hydro, Voith Hydro, PSEL (Funds for Projects and Studies of the Swiss Electric Utilities), and the CTI (Commission for Technology and Innovation), for their financial support and the staff of the Laboratory for Hydraulic Machines for the technical support. We would also like to thank Jorge Arpe for the unsteady wall pressure measurements and Olivier Braun for the numerical results postprocessing. The automatic mesh generators used for runner and draft tube were developed under GMATH, a collaborative project between GE Energy and Ecole Polytechnique de Montreal, coordinated by Professor Francois Guibault.

Nomenclature

E = specific energy (J/kg)
Q = flow rate (m^3/s)
Q_{BEP} = flow rate at the best efficiency operating condition (m^3/s)
σ = cavitation number
$D_{\bar{1}e}$ = runner diameter (m)
C_i = instantaneous velocity (m/s)
$\tilde{C}$ = periodic fluctuating component (m/s)
$\bar{C}$ = time-averaged velocity value (m/s)
C' = random turbulent fluctuation (m/s)
C_u = tangential component (m/s)
C_z = axial component (m/s)
C_r = radial component (m/s)
C = absolute velocity (m/s)
C_{ref} = mean flow reference velocity $C_{ref}=Q/A$(m/s)
ψ = specific energy coefficient
φ = flow rate coefficient
C_p = pressure coefficient $C_p=(p-\bar{p})/1/2\rho c_{m\bar{1}}^2$
ω = rotational velocity (rad/s)
ΔZ = cone height (m)
Z = cone's current depth (m)
R = local cone radius (m)
R_{out} = cone outlet radius (m)
f_r = vortex rotation frequency (Hz)
n = runner rotation frequency (Hz)
τ = phase delay (s)
θ = angular position of the vortex $\theta=2\pi\tau f_r$ (rad)
T_n = runner rotation period (s)
T_r = vortex rotation period (s)
BEP = best efficiency operating point
Re = re number $\mathrm{Re}=UD/\nu=\pi ND^2/60\nu$

References

[1] Jacob, T., 1993, "Evaluation sur Modèle Réduit et Prédiction de la Stabilité de Fonctionnement des Turbines Francis," EPFL Thesis No. 1146, Lausanne, Switzerland.
[2] Nishi, M., Matsunaga, S., Kubota, T., and Senoo, Y., 1984, "Surging Characteristics of Conical and Elbow-Type Draft Tubes," in *Proceedings of the 12th IAHR Symposium*, pp. 272–283.
[3] Vu, T. C., and Retieb, S., 2002, "Accuracy Assessment of Current CFD Tools to Predict Hydraulic Turbine Efficiency Hill Chart," *Proceedings of the 21st IAHR Symposium on Hydraulic Machinery and Systems*, Lausanne, Switzerland, pp. 193–198.
[4] Ruprecht, A., Maihöfer, M., Heitele, M., and Helmrich, T., 2002, "Massively Parallel Computation of the Flow in Hydo Turbines," *Proceedings of the 21st IAHR Symposium on Hydraulic Machinery and Systems*, Lausanne, Switzerland, pp. 199–206.
[5] Ruprecht, A., Helmrich, T., Aschenbrenner, T., and Scherer, T., 2002, "Simulation of Vortex Rope in a Turbine Draft Tube," *Proceedings of the 21st IAHR Symposium on Hydraulic Machinery and Systems*, Lausanne, Switzerland, pp. 259–266.
[6] Scherer, T., Faigle, P., and Aschenbrenner, T., 2002, "Experimental Analysis and Numerical Calculation of the Rotating Vortex Rope in a Draft Tube Operating at Part Load," *Proceedings of the 21st IAHR Symposium on Hydraulic Machinery and Systems*, Lausanne, Switzerland, pp. 267–276.
[7] Miyagawa, K., Tsuji, K., Yahara, J., and Nombra, Y., 2002, "Flow Instability in an Elbow Draft Tube for a Francis Pump-Turbine," *Proceedings of the 21st IAHR Symposium on Hydraulic Machinery and Systems*, Lausanne, Switzerland, pp. 277–286.
[8] Sick, M., Dorfler, P., Michler, W., Salllaberger, M., and Lohmberg, A., 2004,

"Investigation of the Draft Tube Vortex in a Pump-Turbine," *Proceedings of the 22nd IAHR Symposium on Hydraulic Machinery and Systems*, Stockholm, Sweden.

[9] IEC 60193 Standard, 1999, "Hydraulic Turbines, Storage Pumps and Pump-Turbines-Model Acceptance Tests," International Electrotechnical Commission, Genève, Switzerland.

[10] Iliescu, M. S., Ciocan, G. D., and Avellan, F., 2002, "3D PIV and LDV Measurements at the Outlet of a Francis Turbine Draft Tube," Joint U.S. ASME—European Fluids Engineering Summer Conference, Montreal, Quebec, Canada, Paper No. FEDSM2002-31332.

[11] Ciocan, G. D., Avellan, F., and Kueny, J. L., 2000, "Optical Measurement Techniques for Experimental Analysis of Hydraulic Turbines Rotor-Stator Interaction," ASME Fluid Engineering Conference, Boston, Paper No. FEDSM2000-11056.

[12] Arpe, J. A., and Avellan, F., 2002, "Pressure Wall Measurements in the Whole Draft Tube: Steady and Unsteady Analysis," *Proceedings of the 21st IAHR Symposium on Hydraulic Machinery and Systems*, Lausanne, Switzerland.

Jingchun Wu
Ph.D.
Senior Research Scientist
LaunchPoint Technologies, Inc.,
Goleta, CA, USA
e-mail: jwu@launchpnt.com

Katsumasa Shimmei
Department Manager
Hitachi Ltd.,
Akihabara Dairu Building 18-13,
Soto-Kanda,
1-Chome, Chiyoda-ku,
Tokyo, Japan

Kiyohito Tani
Ph.D.
Senior Engineer

Kazuo Niikura
Chief Engineer

Hitachi Ltd.,
3-1-1 Saiwai-cho, Hitachi,
Ibaraki, Japan

Joushirou Sato
Ph.D.
Independent Consultant
Sato Consultants,
11-7 Namekawa, Honchou,
3-Chome, Hitachi,
Ibaraki, Japan

CFD-Based Design Optimization for Hydro Turbines

A computational fluid dynamics-based design system with the integration of three blade design approaches, automatic mesh generator and CFD codes enables a quick and efficient design optimization of turbine components. It is applied to a Francis turbine rehabilitation project with strict customer requirements to provide over 3% increase in peak efficiency, 13% upgrade in power, and improved cavitation characteristics. Extensive turbulent flow simulations are performed for both the existing and new turbines at design and off design conditions. In order to take into account the interactions between different components, particularly the effects between the rotating and stationary parts, coupling calculations based on the implicit coupling method under multiple frames of reference are carried out for the entire turbine model. As a result, the runner and guide vanes are optimized to the greatest extent, and the stay vanes are locally modified with a possible minimum cost under the geometrical constraints of the existing machine. The performance of the new design is verified by model tests, and exceeds required improvements.
[DOI: 10.1115/1.2409363]

Keywords: computational fluid dynamics (CFD), design optimization, hydro-turbines, cavitation

Introduction

Commissioned in 1950s and 1960s, many of the earliest hydropower stations in China contain very old Francis hydro turbine units. It is reported that the runners (rotors) in these turbines have suffered from serious cavitation damage. Frequent repairs of the cavitation damage destroyed regular flow passage, leading to drastic deterioration of turbine performance. As a result, these turbines do not generate their rated capacity. It is, therefore, strongly desired to rehabilitate the turbines with new runners using modern design methods to update the efficiency, raise the capacity and improve the cavitation characteristics. Runner replacement projects of this kind present a great challenge for hydraulic design because of the geometrical constraints of the existing machines.

The flow in a hydro-turbine runner is extremely complex, since it is generally turbulent, unsteady and highly three-dimensional (3D) in nature with strong effects from rotation and curvature. Recently, with the rapid development of computer technology and advanced CFD, it has become routine to directly simulate internal turbulent flow in individual or multiple components of a turbomachine [1–3]. Examples include sophisticated large eddy simulations (LES) in a Francis turbine [4] and in a centrifugal pump impeller at design and off-design conditions [5]. However, a robust and fully 3D inverse design approach, by which the required flow characteristics and parameters are specified as inputs and the corresponding blade geometry is computed and generated as output, is still not commonly performed [6,7]. Two primary factors have prevented the advancement and wide application of inverse design methods. One is that almost all the fundamental equations involved in the inverse design methods developed so far [6–10] are based on the assumption of inviscid flow, which is far different from the actual complex turbulent flow conditions in most turbomachinery. The other is that these inverse design equations require the input of either pressure loading or angular momentum distribution (rV_θ), which are heavily dependent on statistical and/or empirical data. Inverse design methods also require a 3D viscous CFD code to provide flow solutions to evaluate the design, with feedback from output solutions to modify the input of pressure loading or angular momentum distribution in an iterative optimization process. For all these reasons, conventional blade design approaches integrated with advanced CFD analysis have been revived in engineering practice and have become powerful and effective tools for design optimization of turbomachinery [11–13]. CFD-based design procedures of this type usually require several iterations of hydrodynamic design and direct CFD evaluations to meet design specifications or target functions [11,12].

Over a period of more than 2 decades, we have developed a CFD-based design optimization system that integrates internally developed blade design tools, automatic mesh generators, parameterized mathematical geometry models, and inviscid quasi-3D (Q3D) and 3D Euler codes with commercial 3D Navier–Stokes code like STAR-CD (CD-Adapco, London). Such a system per-

Contributed by the Fluids Engineering Division of ASME for publication in the JOURNAL OF FLUIDS ENGINEERING. Manuscript received August 11, 2005; final manuscript received July 6, 2006. Assoc. Editor: Akira Goto.

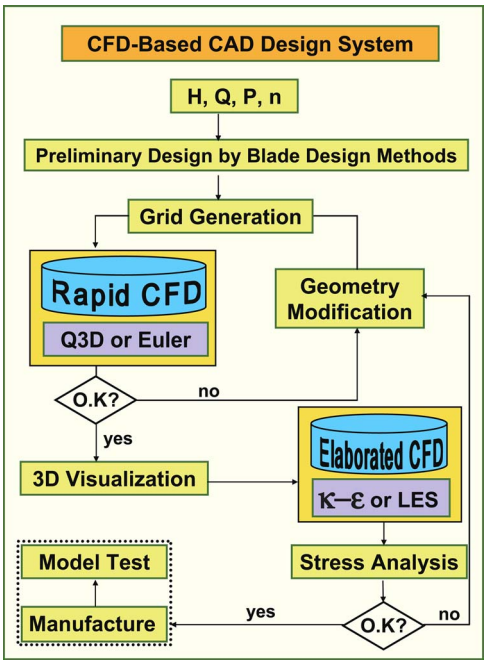

Fig. 1 CFD-based design system

mits designers to interactively generate, modify, and visualize the geometric model of a design. It offers an inexpensive and rapid means for a designer to acquire detailed flow field information and evaluate performance. The design process can be repeated until a fully optimized model with satisfactory performance is obtained. It offers a much more efficient means of optimization than traditional trial-and-error approaches. The basic concept of this CFD-based design system is outlined in the flow chart as shown in Fig. 1.

In this paper, the CFD-based design system is applied to the optimization of a Francis turbine runner and tandem cascade for a turbine rehabilitation project, which has a specific speed of 180 m kW with a 100 m class of head. A commercial Navier–Stokes code (STAR-CD) with standard κ-ε turbulence model, integrated into our CFD-based design system, is employed for turbulent flow simulation of the existing and new turbines. Special attention has been paid to flow matching between different components, particularly in regards to the effects between rotating and stationary parts, by using the steady-state flow solver based on the multiple frames of reference (MFR) with an implicit coupling method. The results of homologous model tests, conducted at Harbin Institute of Large Electric Machinery (China) for the verification of the characteristics of the new design, are also presented in the paper.

CFD-Based Design Optimization System

It is important to integrate a robust and flexible blade design tool in a CFD-based design optimization system to allow automatic or an expert-interfaced generation and modification of the design geometry. In the turbomachinery industry, tremendous advances have been made through the direct approach applying Q3D, Euler 3D, and viscous 3D Navier–Stokes methods to solve the flow fields for a given blade geometry [1–4]. However, a robust and cost-effective 3D inverse design approach is still not commonly available for the reasons as described above. The fundamental equation commonly used in the inverse design for the blade mean camber-line can be written as

$$d\theta = \frac{\omega r^2 - V_\theta r}{V_m r^2} dm \tag{1}$$

where θ is the wrap angle, and m denotes the meridional distance along the camber-line. In Eq. (1), as an approximation, the meridional velocity along the meridional streamlines can be computed by 1D or 2D potential flow theories; while the distribution of the angular momentum (rV_θ) or its derivative can be specified according to the pressure loading, as originally proposed by Jansen [10], and recently evolved by Zangeneh [8] and Goto [6]. Therefore, a 3D blade shape can be stacked together by integrating Eq. (1) along each streamline, provided that the blade thickness distribution is given. This method, under the assumption of axis-symmetric flow, is a simplified form of the inverse design method used in Refs. [6,7].

Equation (1) can be further simplified as

$$d\theta = \frac{1}{r \tan \beta} dm \tag{2}$$

According to Eq. (2), if the blade angle β distribution along a streamline is known, similarly the 3D blade geometry can be obtained. Compared to Eq. (1), the number of unknown variables in Eq. (2) for the blade is reduced to only one. According to the authors' experience, a blade design method by Eq. (2) is usually more flexible and efficient than by Eq. (1).

An alternative method to that of Eq. (2) is to directly and somewhat arbitrarily draw the camber-line in a conformal mapping plane (I-U), which is defined as

$$I = r_{\text{ref}} \int_{m_o}^{m} \frac{dm}{r} \tag{3}$$

$$L = \int_{\theta_o}^{\theta} r_{\text{ref}} d\theta \tag{4}$$

Then, according to Eq. (2), the local blade angles can be easily obtained by using

$$\tan \beta = \frac{dI}{dL} \tag{5}$$

Although the three basic blade design methods as described above are theoretically derived from the same equation or its deformation, it practically involves quite different techniques to adapt each into a flexible and robust design tool. The first method requires statistical or empirical data or a designer's experience in prescribing the distribution of angular momentum (rV_θ), or the distribution of its derivative. The second method requires the same in describing a blade angle distribution. The third method utilizes a designer's experience or intuition in drawing a camber-line in the conformal mapping plane. Each of these approaches, if integrated with the advanced 3D viscous CFD codes, can become a very practical and powerful tool in the design and optimization of turbomachinery. All three blade design methods have been adopted in our CFD-based design optimization system to allow a designer options in achieving a rapid optimization for the runner blades, guide vanes, and stay vanes of various types of hydroturbines. The three blade design approaches have also been incorporated into another CFD-based optimization system for the successful design and optimization of blood pumps [11]. The internally developed parameterized geometrical models based on B-spline curves and B-spline surfaces and other mathematical models [14] are also integrated into the system for other components such as spiral casing, draft tube, and meridional section as well. In the present investigations, the aforementioned second method is used for the design of runner blades, stay vanes, and guide vanes because it has been proven to be more flexible to use than the first and third methods according to our experiences. The leading and trailing edge blade angles are initially calculated by

Table 1 Specifications of existing and new turbines

	Existing	New
$Q_{11opt}=\frac{Q}{D_1^2\sqrt{H}}$ (m^3/s)	0.73	0.88
$N_{11opt}=\frac{ND_1}{\sqrt{H}}$ (rpm)	65	73.5
$Q_{11rat}=\frac{Q}{D_1^2\sqrt{H}}$ ($m^{1/2}/s$)	0.91	1.09
$N_{11rat}=\frac{ND_1}{\sqrt{H}}$ ($m^{1/2}/s$)	65	73.5
Rated power (MW)	81.3	91.9
Specific speed, N s (m kW)	180	205
Relative peak efficiency, η (%)	92	≧95

Eulerian velocity triangles, where the meridional velocity component is computed by the S_2 streamsurface solution of the Q3D. The blade angle distribution between the leading and trailing edge of the runner is then approximated by Bézier curves or *B*-spline curves with controllable parameters to adjust the curves slope and the shape, which in fact reflect the blade pressure loading. The blade angles are refined in the iterative optimization process until the runner can satisfy the hydrodynamic specifications.

Design Parameters and Considerations

The existing runner has a quite low efficiency and a very bad cavitation performance, particularly with a serious leading edge cavitation on the suction side near the band, even at the optimum operating point, possibly due to the inappropriate traditional design. According to the specifications of the customers, the turbine should be updated to provide over 3% increase in peak efficiency, 13% upgrade in power, and especially improved cavitation characteristics with the critical cavitation coefficient less than 0.095, under the strict constraints that the surrounding components of the runner should be retained except for the modification of the guide vane profiles. This presents a great challenge for the hydrodynamic design because, as known to us, the potential for cavitation damage will increase with the higher output of the new runner. It is very hard to establish the concrete target functions for these target parameters, because they are affected by so many geometric and dynamic parameters which also interactively affect themselves and each other. However, we generally know that, for example, the target efficiency is related to the Reynolds number, flow patterns, geometry of runner, stay vanes and guide vanes, incidence, and the flow match between the different components, particularly between the rotating and stationary parts, etc. The main objective of this study is to optimize the flow passages and the geometry of corresponding components to maximize the overall efficiency and power of the turbine, while maintaining a uniform pressure distribution on the runner surface with the lower pressure region as small as possible and the lowest pressure high enough to avoid cavitation. This objective can be more quickly and effectively reached by the current CFD-based design optimization than the traditional "trial-and-error" methods, with the iterations between the hydrodynamic design and direct CFD analyses under the experienced designer's evaluation and guidance.

The main specifications of the existing and new turbine are listed in Table 1, where the unit discharge, Q_{11_opt} and unit speed, N_{11_opt}, for the new design are parameters at an expected target optimum peak point.

CFD Method and Computational Details

The inviscid Q3D codes by means of both finite difference method [15] and finite element method [16] incorporated into our CFD-based design system are primarily employed in the preliminary optimization stages due to their rapid convergence rate and reliability. In particular, our Q3D codes can be used for the flow analysis of the combined computational domain with different components such as the runner, guide vanes, and stay vanes under the MFR. In the final optimization, a commercial Navier–Stokes code, STAR-CD (CD-Adapco, London), is used for the turbulent flow simulations to obtain physically more accurate solutions. STAR-CD is based on finite element-like finite volume method suitable for structured or unstructured mesh, with various available turbulence models, such as standard $\kappa-\varepsilon$ model and LES etc. Although it has been known that there is a deficiency in the performance of the $\kappa-\varepsilon$ turbulence model for problems involving rotation and curvature, the standard $\kappa-\varepsilon$ turbulence model is selected in this study for the steady-state turbulent flow calculations, due to its robustness in practical applications. In order to assure a high numerical accuracy, the second-order linear upwind differencing (LUD) [17] scheme is used in the present calculations.

Recently some attempts have been made to simulate turbulent flow in the entire turbine model including all through-flow components. However, this kind of computation has a huge requirement for CPU time and computer memory and sometimes it is hard to obtain a numerically grid-independent solution due to the generally used coarse meshes. In the present study, at the preliminary design stage, inviscid or viscous simulations are performed for individual components or their combinations. At the final de-

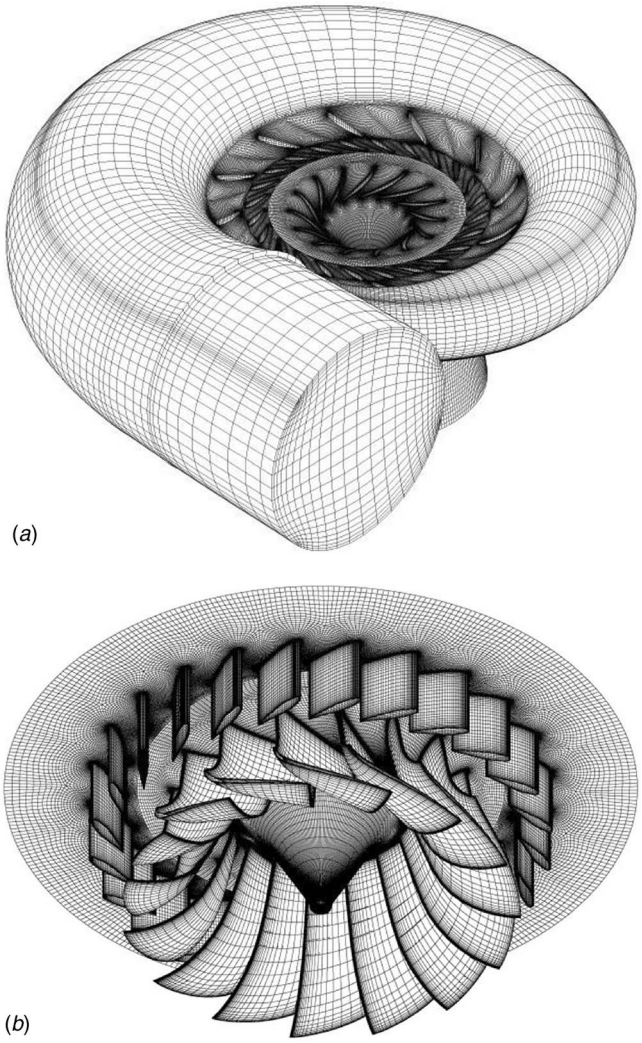

Fig. 2 Computational meshes: (*a*) surface grid of entire turbine model; and (*b*) surface grid of runner and guide vanes with the crown

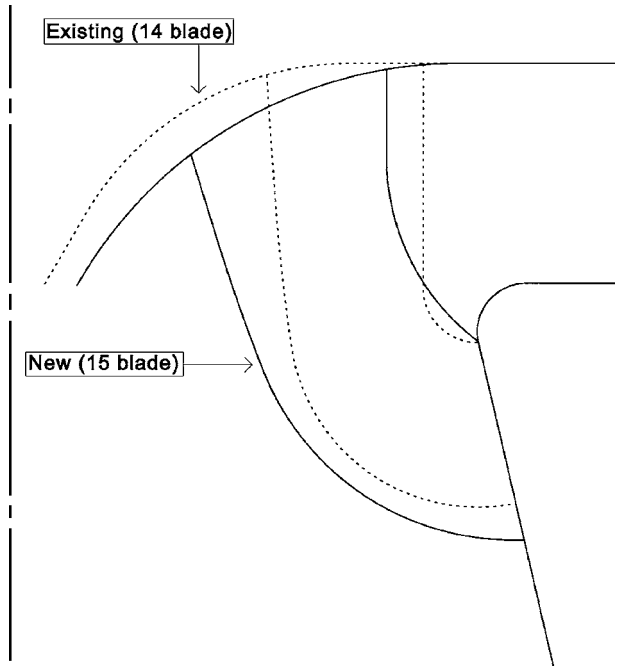

Fig. 3 Comparison of meridional sections between existing and optimized runners.

sign optimization stage, turbulent flow simulations are performed for the entire turbine model including the spiral casing, 12 stay vanes and 24 guide vanes, and the 14 (existing) or 15 blades (new) runners as shown in Figs. 2(*a*) and 2(*b*), to take into account the interactions between different components and to evaluate the asymmetry of the flow and the flow match between them. Whenever a Q3D flow analysis is performed, a pitch of computational region is used for the S_1-streamsurfaces with the implementation of periodic boundary conditions.

Mesh generation is one of the most important steps in the design and optimization of turbomachinery using the state-of-the-art CFD-based design optimization. Although some commercial CFD packages, like STAR-CD, FLUENT (Fluent Inc., Lebanon, USA), and CFX (ANSYS Inc, Canonsburg, USA), have automatic mesh generation capabilities, these packages usually require the boundary (surface) data in the form of output from a computer aided design (CAD) system. Furthermore these packages usually can only generate tetrahedral or hybrid cells and user manipulation of the grid is often needed. In the present study, the computational mesh consists of multiblock structured grids which are generated by our internally developed mesh generators based on the elliptic generation systems [18]. For all the turbulent simulations, the grid independency check is conducted to ensure a reasonable CPU time and appropriate density of grid cells. Because of the multiblock structured mesh, the grid of each block is easily refined by increasing the nodes in *i*, *j*, and *k* directions to ensure that the monitored variables such as pressure and velocity, at certain points of the two sets of meshes differ by less than 2%. For the entire turbine model, it totally contains an approximate number of 1.52 million high quality hexahedral cells, among which 62,000 cells are for spiral casing, 220,000 cells for stay vanes, 420,000 cells for guide vanes, and 820,000 for the runner. The mesh quality is assessed to satisfy the specified criteria either by the user-developed codes or by the STAR-CD, to avoid the distortion in terms of three factors: aspect ratio, skew angle, and warp angle. The computational domains in the tandem vanes and runner are discretized by the combination of clustering *O* grids around the blades and vanes, and with *H*-grids topology in upstream and downstream regions to accurately capture the steep velocity gradients near the blade and vane surfaces. In order to predict the

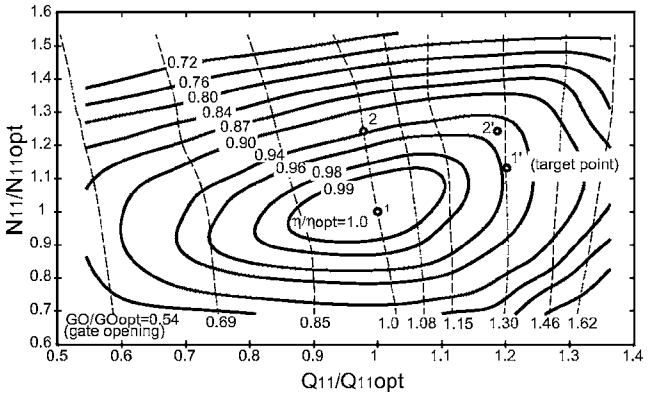

Fig. 4 Efficiency hill chart of existing turbine (Q_{11opt}=0.73, N_{11opt}=65, and η_{opt}=92%)

rotor–stator interaction flow, the coupled calculation is performed for runner and guide vanes with an implicit coupling method under MFR [19].

Optimization of the Meridional Section

The meridional section of a turbine has a significant effect on the turbine performance. The great challenge involved in the current optimization of the meridional shape is the constraint that the distributor height and the profile of the band should be retained exactly the same as those of the existing turbine. Under this constraint and the requirement of the specifications, the meridional shape is preliminarily generated by our parameterized geometry model, and then is further iteratively refined in the optimization design procedure. The finally optimized meridional shape is compared to that of the existing runner as shown in Fig. 3, where the new profile of the crown is shaped to converge more slightly than the current design. In order to improve the cavitation performance, the runner outlet is set slightly backward to increase the effective area of the blade, which is also dependent on the blade wrap angle. Great efforts have been made in shaping the leading edge of the runner and matching its angle with the incoming flow in the iterative optimization process to reach the desired design targets. Because the number of blades is intimately related to the blade geometry itself, such as the blade angle, the chord length, and the runner opening, it also has a considerable effect on both the hydraulic performance and the cavitation behavior of the runner. Usually the friction loss and the flow blockage increase with the number of blades although the overall pressure loading per blade may be reduced. However, with the decrease in the number of blades, the slip effect, due to the finite number of blades on the nonuniformity of the discharge flow, becomes more serious. Consequently, there is an important compromise that can be made in choosing the number of blades by the optimization evolution. It is found that the 15-balde design associated with the new meridional shape is reasonable for the new runner to assure the potential for higher efficiency and better cavitation characteristics.

Optimization of Spiral Casing and Tandem Cascade

Turbulent flow simulation is first performed with the entire turbine model for the existing design under the target operating point designated for the new designed runner, corresponding to point 1′ in Fig. 4, to examine the suitability of the existing stay vanes and guide vanes in providing the highest possible overall efficiency for the rehabilitation project. The predicted radial and circumferential velocity components at the outlet of spiral casing on the central plane are shown in Fig. 5. From this figure, it can be clearly observed that the calculation adroitly captures the interactive effects on the flow behavior between the spiral casing and stay vanes. Except for the area near the nose vane, the radial

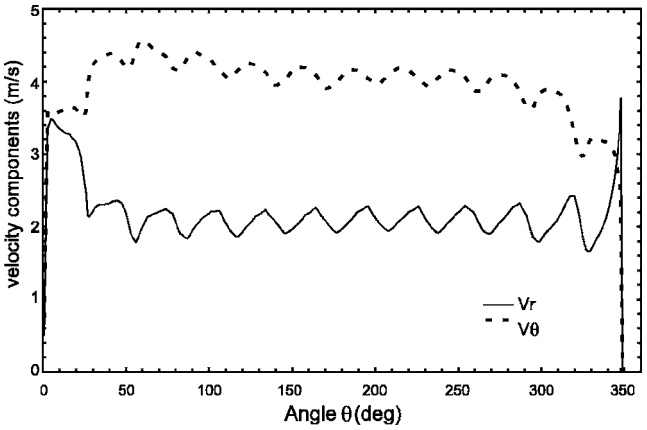

Fig. 5 Velocities at the outlet of spiral casing (central plane)

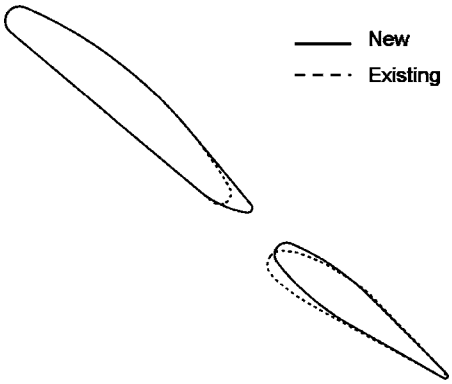

Fig. 7 Optimized guide vane and stay vane profiles

velocity component presents relatively uniform distribution, and the circumferential velocity component increases at several initial sections of the spiral casing and then periodically reduces gradually along the circular direction. This infers that the existing spiral casing is possibly adequate for the new design to distribute uniform flow into the stay vanes.

The calculated pressure distribution on the central plane of the existing spiral casing and tandem cascade under the target point operation is displayed in Fig. 6. As can be seen from this figure, the stagnation points, caused by stay vanes, coincide quite well with the symmetric points at the leading edge of stay vanes, indicating that the inflow angle matches well the leading edge angle of stay vanes. However, an inflow with a large positive attack angle occurs at the leading edge of the guide vanes, resulting in a severe pressure drop on the suction side near the leading edge. Consequently, the stagnation points are seen to deviate far from the symmetric points at the leading edge and shift to the pressure side. At operating points with larger flow rate than the target point, the inflow positive attack angle will become larger, leading to more serious hydraulic losses.

From the above discussions, it is realized that the leading and trailing edge angles, curvature, and geometrical profiles of both stay vanes and guide vanes should be optimized to assure the highest overall efficiency for the present rehabilitation. However, considerable modifications on stay vane profiles should be avoided to save the cost of replacement. Therefore, in order to match the flow between the stay vanes and guide vanes, special efforts are made on the optimization of guide vane geometry. The guide vane with a symmetric profile in combination with the original stay vane is investigated, and the turbulent simulation gives a much improved pressure distribution and flow pattern than the original results shown in Fig. 6. However, matching the flow pattern between stay vanes and guide vanes is still not satisfactory. It seems a guide vane with a negative curvature can meet the requirement of the flow match if the stay vane geometry remains unchanged. According to our experience, however, a guide vane with a negative curvature is inappropriate for a Francis turbine with a specific speed larger than 200 m kW.

Extensive studies on several proposals show that a local modification on the stay vane trailing edge is necessary to improve the flow pattern in tandem cascade. Based on the original stay vane shape, only the profile near the trailing edge is modified to protrude downstream to increase the vane trailing angles, as illustrated in Fig. 7. This slight modification can be conducted in the site operation by welding technology, and is easily peformed by the machine owners. The turbulent flow simulations are performed again under the target operation condition at the final stage of optimization for the entire model, including the existing spiral casing in combination with the slightly modified stay vanes and newly designed symmetric guide vanes (Fig. 7). Figure 8 shows the predicted pressure distribution on the central cut plane for this new design. As can be seen form this figure, the outflow from the stay vanes matches well the inflow toward guide vanes. The stagnation points caused by guide vanes are found to overlap the

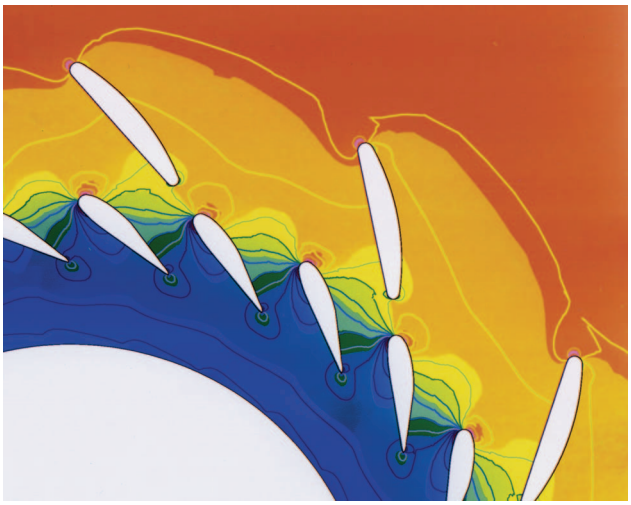

Fig. 6 Pressure contours on central plane of existing tandem cascade

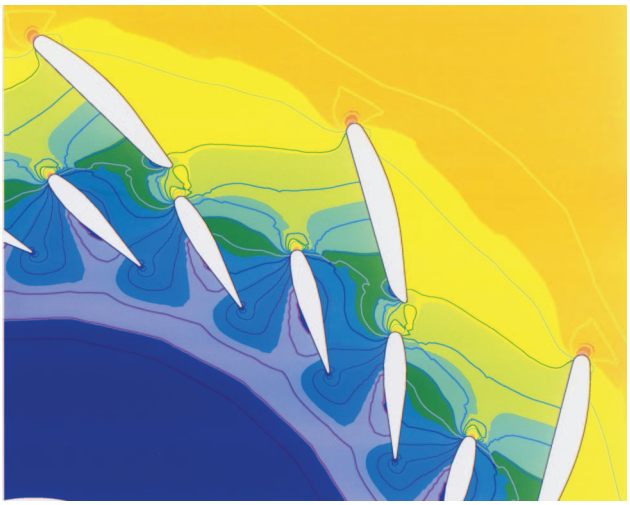

Fig. 8 Pressure contours on central plane of new tandem cascade

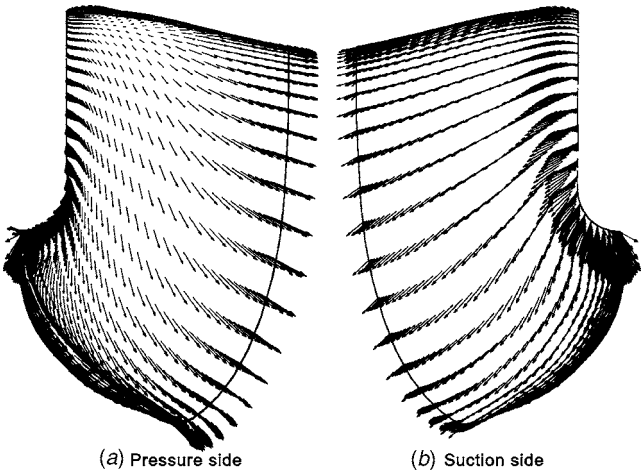

Fig. 9 Velocity vectors near blade surfaces of the existing runner at cell centers of the first layer grids: (*a*) pressure side, (*b*) suction side

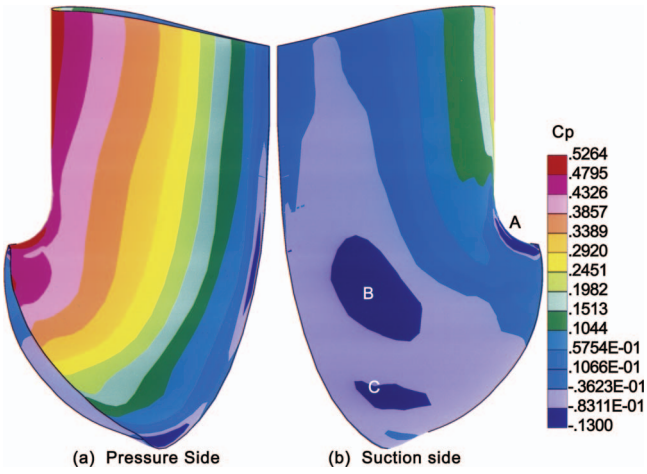

Fig. 10 Pressure contours on surface of existing runner blade: (*a*) pressure side; (*b*) suction side

leading edge of the symmetric points. As a result, the pressure drop on the suction side near the leading edge of the guide vanes is thoroughly improved in comparison with the original design. From Fig. 8, it can again be found that the existing spiral casing distributes periodically uniform flow with a very good match of the leading edge angles of the stay vanes. The predicted head loss through the spiral casing and tandem cascade for the new design is several percent lower than that of the original design, demonstrating the success of the present optimization.

Optimization of the Turbine Runner

For a turbine replacement project, it is very important to know the details of the existing runner before optimizing the new runner. A "diagnosis" program integrated into our CFD-based design system can help a designer to analyze the existing runner geometrically and hydrodynamically. The detected geometrical characteristics by the program are evaluated according to statistic data and previous experience. A flow analysis, including the efficiency evaluation, is then performed for the existing runner to provide the designers with useful information regarding the "strong point" and "weakness" of the old runner.

In the preliminary stage of a runner optimization, the inviscid Q3D and/or 3D Euler codes, integrated into our design system, are generally used in an iterative process to assist the designers in quickly approaching the desired target. In particular, Q3D, which takes into account the rotational effects and partial 3D geometrical effects, can give a very quick solution with relatively acceptable accuracy within minutes at neighboring points of design operation, where the viscous effects may not be predominant. At off design conditions, however, Q3D is usually poor in yielding an acceptable solution.

In the final stages of a runner modernization the commercial Navier–Stokes code STAR-CD, with several alternative turbulence models integrated into our design system, is employed for the turbulent flow simulation to supply designers with more accurate and realistic solutions. In particular, flow simulation at off design conditions and the head loss computations are especially important in assuring a satisfying performance of the runner optimization.

In the present study, turbulent flow simulations are performed for the entire turbine model at optimum operating point 1 and off design operating point 2 for the existing turbine, and at target point 1′ and off design operating point 2′ for the new optimization design as shown in Fig. 4.

CFD Results for the Existing Turbine Runner

The predicted relative velocity vectors near the blade surface at the first layer grid centers for the existing runner under operating point 1 are illustrated in Fig. 9. The velocity vectors are seen to be generally lined up well with the blade surface, indicating that no vortices occur near the blade surface under this operating condition. In the leading edge on the suction side near the band, however, the velocity vectors are not sufficiently tangential to the blade surface and the magnitudes of the velocities are quite large. This suggests that the incoming flow does not match the blade angle well even at the original optimum point.

The contours of pressure coefficient, C_p, on the surface of the existing runner are computed as shown in Fig. 10. The pressure distribution on the suction side of the existing runner displays an unsatisfactory uniformity, with three low pressure zones *A*, *B*, and *C* as displayed in Fig. 10(*b*). The low pressure zone *A*, near the leading edge of the band, is known to be typically responsible for the chronic cavitation damage in this area of most Francis runners. It is reported that serious cavitation occurs at zone *A* with the existing runner under almost all operation conditions, possibly due to the inappropriate conventional design, which was semi-empirically based on the 1D flow theory.

The distribution of pressure coefficient C_p along the hydrofoil of the existing blade at crown, midspan, and band sections is

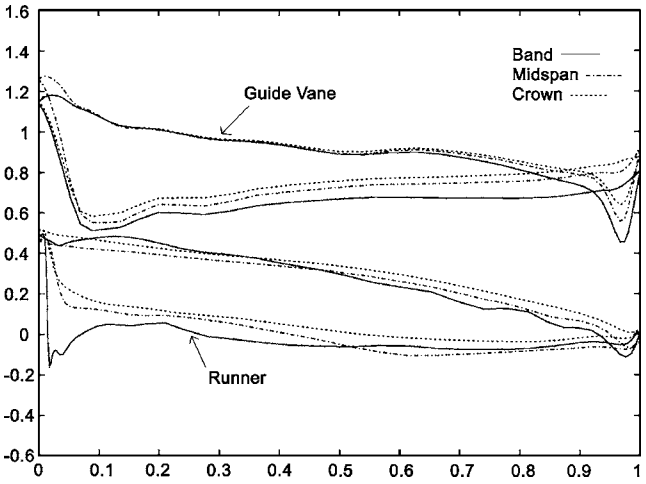

Fig. 11 Pressure distribution on different hydrofoil sections of existing runner and guide vane

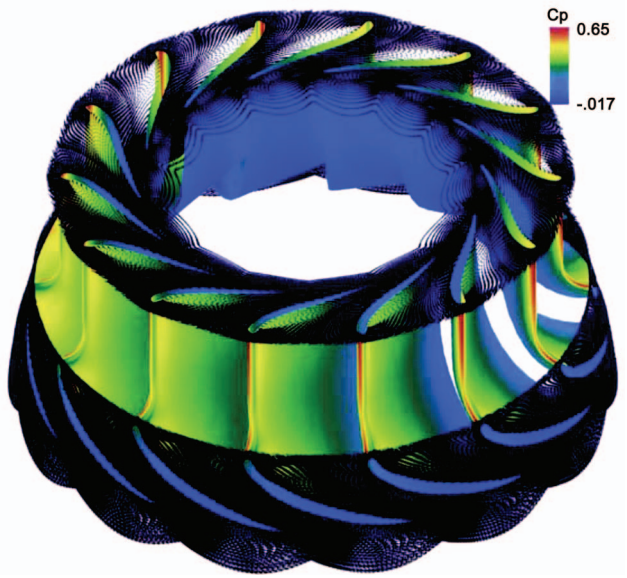

Fig. 12 Pressure distribution on runner surfaces and velocity vectors near crown and band for the existing runner at H_{min} operation

demonstrated in Fig. 11, where the pressure distribution on the same sections of the existing stay vanes is also superimposed. Again, the lowest pressure zone with blade loading concentration near the leading edge on the suction side beside the band is clearly observed. As explained earlier, due to the mismatch of the outflow of the stay vanes with the leading edge angles of the guide vanes, the stagnation points induced by the guide vanes deviate from the symmetric points at the leading edge and shift to the pressure side, leading to a low pressure zone on the suction side near the leading edge, as can be seen from Fig. 11. It can be inferred from this figure that the pressure on the whole suction side of the guide vanes presents an improper distribution.

The performance of the existing runner at off design conditions is also evaluated. Figure 12 illustrates the pressure distribution on the runner and the relative velocity vectors on the sections near the crown and band under the operation point 2, corresponding to the H_{min} operating condition. Because of the lower head condition, an inflow with a negative attack angle flows into the runner, causing a pressure drop on the pressure side of the blade near the

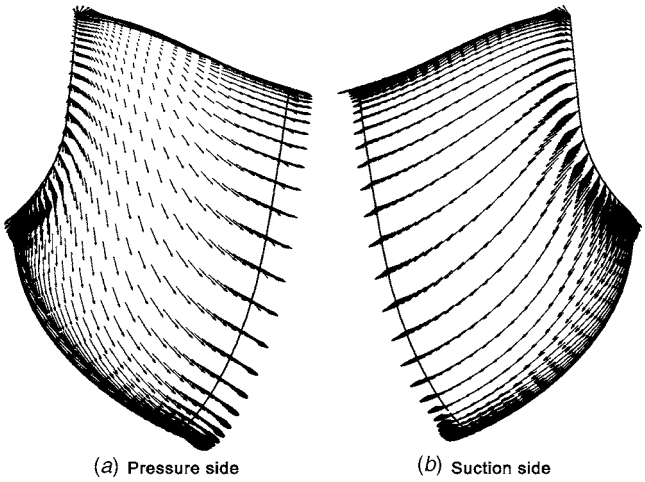

Fig. 13 Velocity vectors near blade surfaces of the new runner at cell centers of the first layer grids: (*a*) pressure side; (*b*) suction side

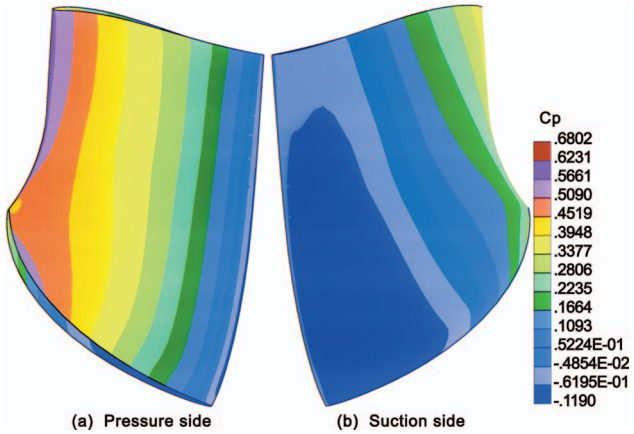

Fig. 14 Pressure contours on surfaces of new runner blade

leading edge. Therefore, a vortex may generate on that region from the crown and extend downstream toward the band, diminishing its strength into the draft tube This is generally observed from experiments at this operating condition. Unfortunately, in the present simulation, the vortex disappears on sections near the band. This prediction defect is possibly due to the weaknesses of the standard κ-ε model and wall functions in predicting swirling and separated flows.

CFD Results for the New Turbine Runner

Following the preliminary optimization of the new runner, turbulent flow simulations are performed for the entire turbine model to evaluate its performance at target point and off design conditions. Figure 13 illustrates the relative velocity vectors near the blade surfaces at the first layer grid centers under the target point operating condition. The velocity vectors are seen to be well lined up with the blade surface.

The computed contours of pressure coefficient C_p, on the blade surface of the new runner under the target point are demonstrated in Fig. 14. In comparison with the original runner, it can be clearly seen that the pressure exhibits a much more uniform distribution on both the pressure and suction sides of the new runner. The total pressure loading is balanced on the entire blade surface without a low pressure zone on the suction side near the blade leading edge of the band. This is attributed to our efforts made on matching the flow between the rotating and stationary parts through the optimi-

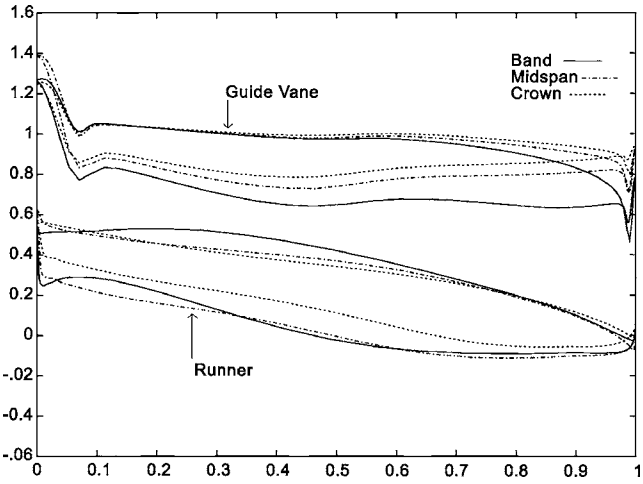

Fig. 15 Pressure distribution on different hydrofoil sections of new runner and guide vane

Fig. 16 Configuration of new runner design

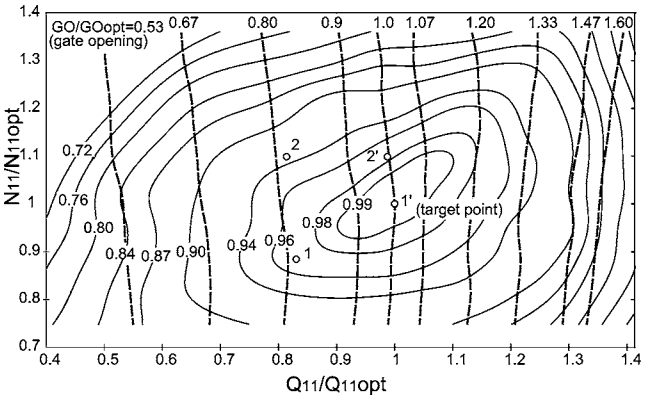

Fig. 17 Efficiency hill chart of new optimization design (Q_{11opt}=0.88, N_{11opt}=73.5, and η_{opt}=95.3%)

zation process. This type of pressure distribution can assure a higher efficiency over a wider range of operation conditions with a significant improvement of cavitation performance compared to the existing runner, as was proven by the model test results described later.

The pressure distribution along the blade profiles of both new runner and guide vanes at crown, midspan, and band sections are shown in Fig. 15. Again, the uniform pressure distribution on the new runner without a low pressure zone near the leading edge can be clearly observed. The uniformity of pressure on the blade surface can lead to thoroughly improved leading edge cavitation behavior as demonstrated by the model testing. Due to the optimization of the guide vane profiles, the outflow from the stay vanes matches closely the inflow into the guide vanes. This leads to a dominantly uniform pressure distribution along the complete guide vane surfaces along with the disappearance of the low pressure zone on the suction side of the vane leading edge.

The turbulent flow simulation is also conducted for the new runner at off design conditions. The obtained results at operating point 2′, H_{min} operation, show that pressure is still uniformly present over most areas of the blade except for the pressure side near the leading edge. Here a pressure drop, not as obvious as in the original runner, is found. A detailed computer 3D visualization of the results (not shown) indicates that no vortices occur at sections from crown to band. Therefore, the results obtained for the new runner at the H_{min} operating condition are omitted herein for this paper.

It should be noted that the existing draft tube has not been optimized due to the customer requirement that it must be retained unaltered in order to save on replacement costs.

Model Test Results

Through CFD-based design optimization, the new model runner is finally optimized and manufactured as shown in Fig. 16. Model tests are carried out to validate its performance in the high head test rig of Harbin Institute of Large Electric Machinery (China). The tests include the measurements of power, efficiency, cavitation coefficients, pressure pulsations, and runaway speed, etc. In order to verify our CFD analyses, the model is tested in two phases. In the first phase, the new model runner is installed in the test rig with the spiral casing, stay vanes, and guide vanes homologous to the existing prototypes. The testing results (omitted here) show that the new runner provides a guaranteed increase in power at conditions corresponding to the prototype rated head. The runner also shows excellent cavitation characteristics. Although it gives a 94.2% level of peak efficiency, about 2.2% higher than the existing model runner, it is still about 1% lower than the requirement of the customers.

In the second phase, the optimized guide vanes and locally modified stay vanes in the trailing edge are installed with the new model runner. The new performance test shows that the new design supplies approximately 100.0 MW of power, about a 23% upgrade from the existing runner at the rated condition, and even a 10% higher increase than guarantees. As anticipated, a peak prototype efficiency of 95.3% is gained with the new design, more than 3.3% higher than the original model. The peak efficiency for the prototype is transposed from that of model testing (93.3%) based on the code IEC 995 for an efficiency setup with an estimated $\Delta\eta$=2%. The efficiency hill chart for the new design is demonstrated in Fig. 17. As expected, the optimum point is perfectly positioned at the target point. A detailed comparison of the measured turbine performance between the existing and new models at the minimal (H_{min}), rated (H_r), and maximal (H_{max}) heads is illustrated in Fig. 18. From this figure, it can be clearly seen that the optimized model has a corresponding higher efficiency than the existing turbine at three different head values, especially at the minimum head operating range. A more detailed comparison at other operating points can be made by referring to Figs. 4 and 17. The predicted efficiencies at the target point 1′ for the new runner with the existing tandem cascade, and the entire new optimized design as well, are compared with the experimental data in Fig. 19. From this figure it can be found that the modified stay-vane profile and the optimized guide vanes yield about a 1.1% increase

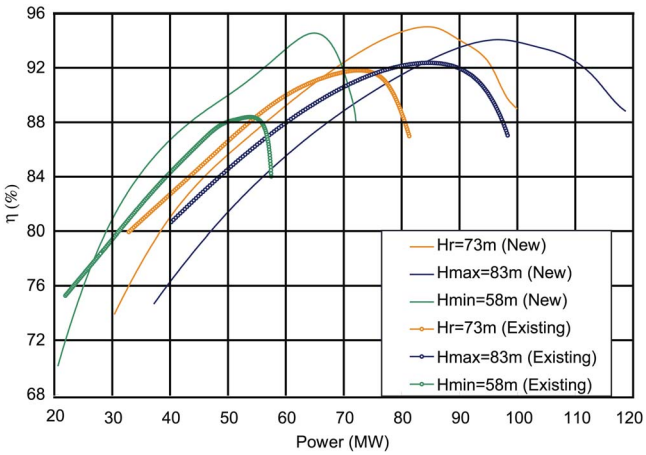

Fig. 18 Comparison of measured performance curves between existing and optimized turbines

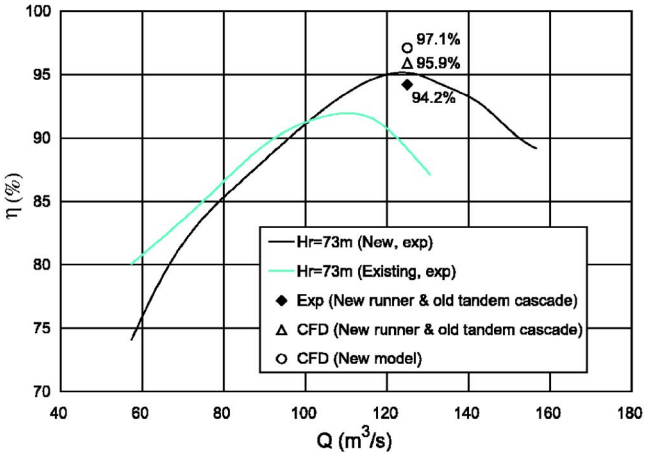

Fig. 19 Comparison between measured $\eta-Q$ curves and predicted efficiency at target operation point for the new runner with existing tandem cascade, and the entire new optimized design as well

in peak efficiency. It can be further noted that the CFD predicted efficiency generally agrees well with the experimental data but with a systematic overestimation, possibly due to the deficiency of the standard κ-ε model and the wall function for strong curvature and rotating flow. The model test results obtained in two phases indicate that optimization of each component neighboring the runner is important in assuring a high overall efficiency for a turbine rehabilitation project. Figure 20 shows the measured model critical cavitation coefficient σ, for both the existing and new models under rated head of 73 m. The cavitation coefficient for the new model is lower than that of the existing model and the plant σ over the whole flow range, demonstrating that the new runner has excellent cavitation characteristics, although the new model provides an approximately 23% increase in power.

Conclusions

A CFD-based design system, which integrates three blade design approaches, parameterized geometry models, automatic mesh generators, and CFD software, is presented in this paper. It allows a quick and efficient improvement and optimization of turbine components. The system has been applied to the optimization of a Francis turbine runner, guide vanes, and stay vanes for a turbine replacement project. Extensive turbulent flow simulations have been conducted for both the existing and new designs at the corresponding optimum and off design conditions. The coupled calculations are very efficient in guaranteeing a good flow match between different components. Numerical prediction, including the evaluation of the local flow and the global variables, of the turbine model at optimum and off design conditions is critical to ensure the satisfaction of the desired performance specifications. The performance of the new design has been verified by model tests carried out in two stages. The highly successful combination of the CFD-based design optimization with model testing has finally resulted in a new model which can provide about 23% increase in power and over 3% upgrade in peak efficiency. In addition the model provides for a thoroughly improved cavitation characteristic with extremely smooth performance over a much wider range of operations compared to the existing design.

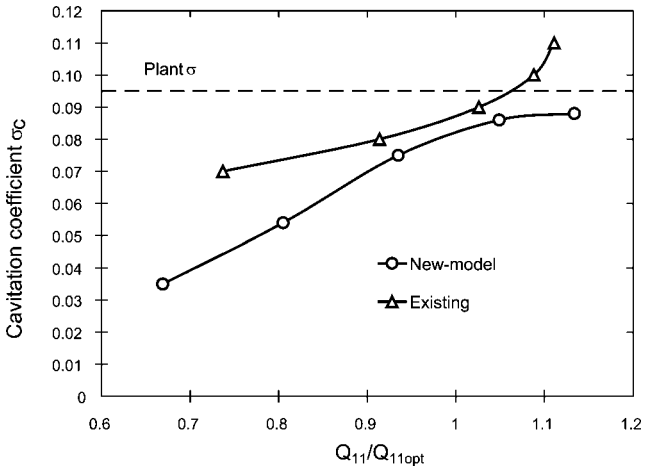

Fig. 20 Measured model critical cavitation coefficients at rated head of H_r=73 m (Q_{11opt}=0.73)

Acknowledgment

The authors wish to express their sincere gratitude to Mr. Xingming Tao, Chunlin Guo, and Yijie Liu of Harbin Research Institute of Large Electric Machinery, China, for conducting the model tests and providing us the experimental data.

Nomenclature

C_p = pressure coefficient $(p-p_{out})/0.5\rho V_{in}^2$
H = head, m
I,L = conformal coordinates
Q = volumetric flow rate
Q_{11} = unit discharge
N_{11} = unit speed
r = radius
V_r = absolute radial velocity component
V_θ = absolute angular velocity component
V_m = absolute meridional velocity component
m = meridional coordinate
β = blade angle
θ = angular coordinate
ω = runner angular speed
N = rotational speed, rpm
Ns = specific speed (SI units), $3.13N\sqrt{Q}/H^{3/4}$
p = static pressure
σ_c = critical or cavitation coefficient

Subscripts

θ = circumferential component
in = inlet of the spiral casing
m = meridional component
opt = optimum point or best efficiency point
out = outlet of the computational domain
rat = rated
ref = reference

References

[1] Vu, T. C., and Shyy, W., 1994, "Performance Prediction by Viscous Flow Analysis for Francis Turbine Runner," ASME J. Fluids Eng., **116**, pp. 116–120.
[2] Ruprecht, A., Heitele, M., Helmrich, T., Faigle, P., and Morser, W., 1998, "Numerical Modelling of Unsteady Flow in a Francis Turbine," Proceedings of XIX IAHR Symposium on Hydraulic Machinery and Cavitation, Singapore, pp. 202–209.
[3] Sabourin, M., Labrecque, Y., and Henau, V., 1996, "From Components to Complete Turbine Numerical Simulation," Proceedings of 18th IAHR Symposium on Hydraulic Machinery and Cavitation, Iberdrola, pp. 248–256.
[4] Song, C. C. S., Chen, X., Ikohagi, T., Sato, J., Shinmei, K., and Tani, K., 1996, "Simulation of Flow Through Francis Turbine By LES Method," Proceedings of 18th IAHR Symposium on Hydraulic Machinery and Cavitation, Iberdrola, pp. 267–276.
[5] Byskov, R. K., Jacobsen, C. B., and Pedersen, N., 2003, "Flow in a Centrifugal Pump Impeller at design and Off-Design Conditions-Part II: Large Eddy Simulations," ASME J. Fluids Eng., **125**(1), pp. 73–83.
[6] Goto, A., Nohmi, M., Sakurai, T., and Sogawa, Y., 2002, "Hydrodynamic Design System for Pumps Based on 3-D CAD, CFD, and Inverse Design Method," ASME J. Fluids Eng., **124**, pp. 329–335.

[7] Goto, Z., and Zangeneh, M., 2002, "Hydrodynamic Design of Pump Diffuser Using Inverse Design Method and CFD," ASME J. Fluids Eng., **124**(6), pp. 319–328.
[8] Zangeneh, M., 1991, "A Compressible Three Dimensional Blade Design Method for Radial and Mixed Flow Turbomachinery Blades," Int. J. Numer. Methods Fluids, **13**, pp. 599–624.
[9] Zangeneh, M., Schleer, M., Ploger, F., Hong, S., Roduner, C., Ribi, B., and Abhari, R. S., 2004, "Investigation of an Inversely Designed Centrifugal Compressor Stage- Part I: Design and Numerical Verification," ASME J. Turbomach., **126**(1), pp. 73–81.
[10] Jasen, W., and Kirschner, A. M., 1975, "Impeller Design Method for Centrifugal Compressor," NASA SP304, NASA, Washington, D.C.
[11] Wu, J., Antaki, J. F., Wagner, W., Snyder, T., Paden, B., and Borovetz, H., 2005, "Elimination of Adverse Leakage Flow in a Miniature Pediatric Centrifugal Blood Pump by Computational Fluid Dynamics-Based Design Optimization," ASAIO J., **51**, pp. 636–643.
[12] Bouchet, D. P., Tribes, C., Trépanier, J. Y., and Vu, T. C., 2004, "Hydrodynamic Optimization in Rehabilation Project," Proceedings of the 22nd IAHR Symposium on Hydraulic Machinery and Systems, Stockholm, Sweden.
[13] Schilling, R., Thum, S., Müller, N., Krämer, S., Riedel, N., and Moser, W., 2002, "Design Optimization of Hydraulic Machinery Bladings by Multi Level CFD-Technique," Proceedings of the 21st IAHR Symposium on Hydraulic Machinery and Systems, Lausanne, Switzerland.
[14] Rogers, D. F., 2001, *An Introduction to NURBS: With Historical Perspective*, Morgan Kaufmann, San Francisco.
[15] Tanabe, S., Toshima, M., Sato, J., Moriguchi, S., Mori, S., Kawamoto, K., and Yamabe, M., 1992, "Experience with Flow Analysis as Practical Design Tools," Proceedings 16th IAHR Symposium on Hydraulic Machinery and Cavitation, São Paulo, Brazil, pp. 271–280.
[16] Wu, J., Wu, Y., and Mei, Z., 1989, "Inviscid-Viscous Interaction for Internal Flow of a Francis Turbine Runner," Proceedings of the 3rd Japan-China Joint Conference on Fluid Machinery, Osaka, Japan, pp. 361–368.
[17] Shyy, W., Thakur, S., and Wright, J., 1992, "Second-Order Upwind and Central Difference Schemes for Recirculating Flow Computation," AIAA J., **30**, pp. 923–32.
[18] Thompson, J. F., Soni, B. K., and Weatherill, N. P., 1999, *Handbook of Grid Generation*, CRC Press, Boca Raton, FL.
[19] CD Adapco Group, 2001, STAR-CD Version 3.15, Methodology, Computational Dynamics Limited.

Curvature Law of the Wall for Swirling Axial Flows in Rotating Machinery

Jinxiang Xi
Department of Mechanical Engineering,
Virginia Commonwealth University,
Richmond, VA 23284

Xiuhua Si
Department of Mechanical Engineering and
Materials Science,
Rice University,
Houston, TX 77005

P. Worth Longest

Mohamed Gad-el-Hak[1]
e-mail: gadelhak@vcu.edu

Department of Mechanical Engineering,
Virginia Commonwealth University,
Richmond, VA 23284

A new law of the wall accounting for curvature effects in swirling axial flows is derived. The influence of the curvature on the turbulence mixing lengths in both axial and tangential directions is examined theoretically using the Reynolds stress transport equations. For equilibrium flows with weak curvature, identical mixing lengths are derived for the axial and tangential directions. Additionally, the effect of finite local curvature and shear stress ratio on the near-wall velocities is systematically explored. It is found that the curvature effect in swirling axial flows is suppressed by a factor of $1/(1+\sigma_w^2)$ *compared to that in curved channel flows, where* σ_w *is the ratio of the axial to swirl shear stress. For a given curvature radius, the maximum velocity deviation occurs when the axial-to-swirl shear stress ratio is zero. Finally, the performance of the new curvature law is evaluated by implementing it as a wall function in a well-established CFD code. The new wall function provides improved agreement for swirl velocity distributions inside labyrinth cavities in comparison with existing experimental laser Doppler anemometry measurements.* [DOI: 10.1115/1.2409360]

Keywords: dynamic modeling, curvature, law of the wall, swirling axial flow

1 Introduction

Swirling axial flow along curved solid walls is a fundamental phenomenon in rotating machinery. Curvature effects on both the mean flow and turbulence structures have been experimentally studied by Bradshaw [1,2], Patel et al. [3], Meroney et al. [4], So and Mellor [5,6], Hunt et al. [7], Gillis and Johnston [8], Muck et al. [9], Hoffmann et al. [10], Gibson et al. [11], and Barlow et al. [12]. As a result of their efforts, it is now generally acknowledged that (i) curvature influences both mean flow and turbulence structures; (ii) even small curvature could induce large changes in Reynolds stresses; and (iii) turbulent shear stresses are dampened on convex surfaces and amplified on concave surfaces.

Theoretical efforts to understand the effects of curvature on the law of the wall have been undertaken by Bradshaw [1,2,13], So [14–16], Moser and Moin [17], Patel and Sotiropoulos [18], among others. The analogy between the curvature effect and buoyancy was first recognized by Prandtl in 1929 and was later employed in a model by Bradshaw [1]. In this model, the curvature effect was described for two-dimensional flows by defining a dimensionless parameter known as the gradient Richardson number R_i. Patel [3] studied secondary flows in a curved channel and showed a similar effect between curvature and pressure gradients, with the influence of convex curvature being similar to that of an adverse pressure gradient. In contrast, the effect of concave curvature resembled that of a favorable pressure gradient. In a similar manner, permeable walls [19], heat flux [20], and fluid compressibility [21] can all similarly alter the near-wall velocity gradients, shifting the velocity profiles above the classical log-law on a wall with blowing or cooling (in liquids), while shifting the profile beneath the classical log-law on a wall with suction, heating (in liquids), or compressibility. This is schematically illustrated in Fig. 1.

Despite its inadequacies, the classical logarithmic law was still widely used for curved walls by both experimentalists and modelers with the qualification that its validity region is closer to the wall than that on a flat plate. Attempts to account for the curvature effects in turbulent modeling were performed by Wilcox and Chambers [22], who adjusted for curvature by adding extra source terms in the k-ω model equations. Rodi [23] investigated the curved shear layers using two-equation turbulence models and showed a considerable influence on the solution accuracy by employing a curvature wall function. Galperin and Kantha [24] used an algebraic Reynolds stress model to obtain a curvature law by assuming equilibrium and constant flux inside the boundary layer. Assuming a nonconstant-flux shear layer, Kind et al. [25] proposed a correction to the axial and tangential mixing length components based on the shear stress variations in the direction normal to the wall. However, their mixing length correction neglected the direct effect of curvature and assumed it had only an indirect effect on near-wall velocity distributions. This was improved later by Kim and Rhode [26] who proposed a curvature correction to the circumferential component of the mixing length using the local gradient Richardson number [1]. In Kim and Rhode's work, the streamline curvature effect was limited only to the circumferential direction. A curvature effect was not assumed in the axial direction, a fact which is not supported by experimental observations. The goal of this paper is to assess curvature effects in both the axial and circumferential directions by means of a theoretical analysis using the Reynolds stress model and to propose a generalized curvature law for swirling axial flows based on this analysis.

In this study, a new law of the wall accounting for curvature effects in swirling axial flows is derived. The curvature parameter that enters this problem is $y/(y+R)$, where y is the normal coordinate and R is the radius of curvature. The difficulty lies in the subtle way in which curvature influences the mean flow and the turbulence structures. Kind et al. [25] suggested that the near-wall flow was determined by wall shear stress and that curvature only indirectly affected the flow structure through its influence on the wall shear stress. Schwarz et al. [32] attempted to explain the curvature effects in terms of the centrifugal forces and the counteracting cross-stream pressure gradients. Experiments have shown large changes in Reynolds stresses even on small curva-

[1]Corresponding author.

Contributed by the Fluids Engineering Division of ASME for publication in the JOURNAL OF FLUIDS ENGINEERING. Manuscript received February 24, 2006; final manuscript received July 7, 2006. Assoc. Editor: Dimitris Drikakis.

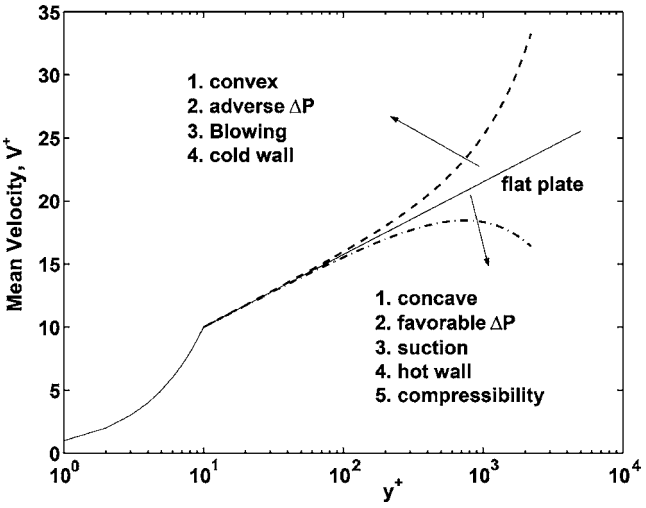

Fig. 1 Schematic illustration of the effects of various parameters on the law of the wall in turbulent boundary layers

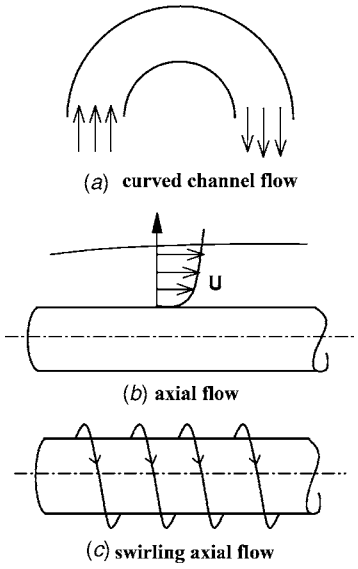

Fig. 2 Typical curvature flows in turbomachinery: (*a*) curved channel flow; (*b*) axial flow; (*c*) swirling axial flow

tures. However, these changes cannot be inferred from the relative magnitude of the curvature related terms $y/(y+R)$ in the mean-flow equations, which is often an order of magnitude less than the resultant shear stress variation. Bradshaw [2] attributed this apparent incapacity of the mean-flow equations to high-order fluctuating interaction terms such as pressure redistribution and turbulence diffusion. Because of this, Patel et al. [18] suggested that even the Reynolds stress model requires further development of the high-order interaction terms in order to capture the curvature effects.

The present study aims to better describe the near-wall behaviors of the turbulent swirling axial flows due to wall curvature in rotating scenarios. The goal is to improve the prediction accuracy of the swirl velocities in labyrinth seals by formulating a new curvature wall function. This is significant because the swirl variation along the rotor surface has a major influence on rotordynamic stabilities [27–31]. Specific objectives are:

(i) to determine how the wall curvature influences the near-wall velocity components in swirling axial flows
(ii) to derive a generalized curvature-sensitized law of the wall for both axial and circumferential directions
(iii) to study the effects of swirl intensity and curvature radius on the near-wall velocities
(iv) to evaluate the performance of the new curvature wall function against measurements inside a labyrinth seal.

2 Methods

2.1 Curvature Law Derivation. It is generally accepted that streamline curvature has a significant effect on flow properties in the near-wall region for 2D curved channel flows as illustrated in Fig. 2(*a*). These results, however, cannot be readily extended to a three-dimensional swirling axial flow model because of the additional degree of freedom, i.e., the axial direction. Specifically, the influence of the circumferential curvature on tangential shear stress in swirling axial flows was found to be different from that in curved channel flows [16,26]. Furthermore, behavior of the axial shear stresses under the influence of circumferential curvature has rarely received serious attention and remains ambiguous. This section theoretically examines whether circumferential curvature changes the shear stress in the axial direction, and how this change further alters the flow conditions in the circumferential direction.

We begin with the Reynolds stress transport equations. Based on the assumption of local equilibrium and small advection and diffusion, the Reynolds stress transport equation inside a turbulent boundary layer is formulated as follows [16]:

$$(\overline{u_i'u_k'}u_{j,k} + \overline{u_j'u_k'}u_{i,k}) = -\frac{q'}{3l_t}\left(\overline{u_i'u_j'} - \frac{1}{3}\delta_{ij}q'^2\right) - \frac{2}{3}\delta_{ij}\frac{q'^2}{\Lambda} \quad (1)$$

where $q' = (u_i'u_i')^{1/2}$, l_t is a turbulent length scale, and Λ is the Kolmogorov scale. The terms in Eq. (1) account for, respectively, production, energy redistribution, and dissipation. Only the turbulence return-to-isotropy term was retained in the redistribution term. The mean-strain rapid-distortion term was neglected because of its small effect in shear flows under small external body forces [33].

Expanding Eq. (1) in cylindrical coordinates, the turbulent shear stresses in both axial and circumferential directions were derived (see details in Appendix A)

$$\tau_{rx} \cong -\rho\overline{uv} = \rho l_{rx}^2\sqrt{\left(\frac{\partial u}{\partial r}\right)^2 + \left(\frac{\partial w}{\partial r} - \frac{w}{r}\right)^2}\left(\frac{\partial u}{\partial r}\right) \quad (2)$$

$$\tau_{r\theta} \cong -\rho\overline{vw} = \rho l_{r\theta}^2\sqrt{\left(\frac{\partial u}{\partial r}\right)^2 + \left(\frac{\partial w}{\partial r} - \frac{w}{r}\right)^2}\left(\frac{\partial w}{\partial r} - \frac{w}{r}\right) \quad (3)$$

where l_{rx} and $l_{r\theta}$ are the turbulent mixing lengths in the axial and tangential directions, respectively

$$l_{r\theta} = \kappa y\left[1 - \alpha R_i + \frac{3}{2}\alpha(\sigma R_i)^2\right]^{1/2} \quad (4)$$

$$\frac{l_{rx}}{l_{r\theta}} = \left(1 + \alpha R_i\frac{w/r}{\partial w/\partial r}\right)^{1/2} \quad (5)$$

In the above derivation, the only approximation introduced is the assumption that $w/r < \partial w/\partial r$, which is generally true for both weak curvatures (e.g., $\delta/R < 0.01$) and moderate curvatures (e.g., $\delta/R = 0.1$). So [16] had derived similar results except that this study did not explicitly give Eqs. (4) and (5). The associated algebra is very involved that to fully appreciate its details would be a formidable undertaking. Therefore, the repetitive part has been summarized and listed in Appendix A.

In Eqs. (4) and (5), α is a constant yet to be determined, σ is the ratio of axial-to-tangential local shear stress, and R_i is the local gradient Richardson number. Thus

$$\sigma = \frac{\partial u/\partial y}{\partial w/\partial y - w/r}; \quad R_i = \frac{w/r(\partial w/\partial r + w/r)}{(\partial u/\partial r)^2 + (\partial w/\partial r - w/r)^2} \tag{6}$$

Equation (5) gives the ratio of the axial turbulent mixing length to the tangential mixing length. In particular, if $w/r \ll \partial w/\partial r$, both R_i and (σR_i) will be much less than one. The mixing lengths in Eqs. (4) and (5) simplify to the Monin–Oboukhov formula

$$l_{r\theta} = l_{rx} = \kappa y(1 - \alpha R_i) \tag{7}$$

Based on a zero pressure gradient assumption, the expression for local shear stress can be deduced from the so-called "second-order equations" where terms of order (δ/R) are retained [18]

$$-\rho\overline{vw} = \tau_{r\theta} = \tau_{w\theta}(1 - 2y/r) \tag{8}$$

$$-\rho\overline{uv} = \tau_{rx} = \tau_{wx}(1 - y/r) \tag{9}$$

Therefore, the ratio of the axial-to-tangential local shear stress can be approximated as

$$\sigma = \sigma_w \sqrt{\frac{r - y}{r - 2y}} \tag{10}$$

The reference velocity scales are defined thus

$$u_\tau = \sqrt{\frac{\tau_{wx}}{\rho}}\sqrt{\frac{\tau_{wx}}{\tau_w}}, \quad w_\tau = \sqrt{\frac{\tau_{w\theta}}{\rho}}\sqrt{\frac{\tau_{w\theta}}{\tau_w}}, \quad q_\tau = \sqrt{\frac{\tau_w}{\rho}} \tag{11}$$

where $u_\tau^2 + w_\tau^2 = q_\tau^2$.

Based on the above velocity scales, the dimensionless wall variables are given by

$$u^+ = \frac{u}{u_\tau}, \quad w^+ = \frac{w}{w_\tau}, \quad y^+ = \frac{q_\tau y}{\nu}, \quad R^+ = \frac{q_\tau R}{\nu} \tag{12}$$

Substituting Eq. (12) into Eqs. (7), (8), and (10) and rearranging the terms

$$\frac{\sigma}{\sigma_w} = \frac{\partial u^+/\partial y^+}{\partial w^+/\partial y^+ - w^+/r^+} = \sqrt{\frac{r^+ - y^+}{r^+ - 2y^+}} \tag{13}$$

$$R_i = \frac{\dfrac{w^+}{r^+}\left[\dfrac{\partial w^+}{\partial y^+} + \dfrac{w^+}{r^+}\right]}{(1 + \sigma^2)\left[\dfrac{\partial w^+}{\partial y^+} - \dfrac{w^+}{r^+}\right]^2} \tag{14}$$

where $r^+ = y^+ \pm R^+$, with the positive and negative signs in front of R^+ corresponding to convex and concave curvature, respectively.

Further substitution of Eq. (7) into (9) and Eq. (12) into (2) and (3) yields

$$\left(\frac{\partial w^+}{\partial y^+} - \frac{w^+}{r^+}\right)(1 - \alpha R_i) = \sqrt{1 - 2\frac{y^+}{r^+}}\frac{1}{ky^+} \tag{15}$$

$$\frac{\partial u^+}{\partial r^+}(1 - \alpha R_i) = \sqrt{1 - \frac{y^+}{r^+}}\frac{1}{ky^+} \tag{16}$$

Equations (13)–(16) provide a generalized curvature law of the wall for swirling axial flows. To demonstrate the generality of these equations, we show in the three examples presented below that these equations are reduced to specific expressions for flat plates, curvature channels, and axial flows along a circular cylinder.

I. Axial Flow Along a Cylinder (Transverse Curvature): In this example (see Fig. 2(*b*)), the application of the generalized curvature law to flows under the influence of transverse curvatures, i.e., wall curvatures orthogonal to the main flow direction, is illustrated. For this case, $w^+ = 0$, $\sigma = \infty$, and $R_i = 0$. Thus, Eq. (16) reduces to (17), which is identical to the transverse curvature law given by Piquet and Patel [34]

$$\frac{\partial u^+}{\partial y^+} = \sqrt{1 - \frac{y^+}{r^+}}\frac{1}{ky^+} \tag{17}$$

II. Curved Channel (Longitudinal Curvature): For the curved channel (see Fig. 2(*a*)), only the longitudinal velocity (equivalent to circumferential velocity in the coordinate system of the present study) exists along the curved wall. Thus, $w^+ \neq 0$, $u^+ = 0$, and $\sigma = 0$. Substituting these values into Eqs. (14) and (15) and neglecting the small terms yields

$$R_i = \frac{w^+/r^+}{\partial w^+/\partial y^+ - w^+/r^+} \tag{18}$$

$$\frac{\partial w^+}{\partial y^+} - (\alpha + 1)\frac{w^+}{r^+} = \frac{1}{ky^+} \tag{19}$$

Equation (19) is a more precise form of the law of the wall proposed by Patel and Sotirpoulos [18] in which constant shear stress was assumed in the normal direction, and the coefficient in the second term is "α" in comparison to "$(\alpha+1)$" in Eq. (19).

III. Flat Plate $(r^+ = \infty)$: The law of the wall for a flat plate should be deduced from either Eq. (17), the transverse curvature law, or Eq. (19), the longitudinal curvature law, as the curvature radius approaches infinity. Applying $r^+ = \infty$ into Eqs. (17) and (19), one obtains

$$\frac{\partial u^+}{\partial y^+} = \sqrt{1 - \frac{y^+}{r^+}}\frac{1}{ky^+} \Rightarrow \frac{\partial u^+}{\partial y^+} = \frac{1}{ky^+} \tag{20}$$

and

$$\frac{\partial w^+}{\partial y^+} - (\alpha + 1)\frac{w^+}{r^+} = \frac{1}{ky^+} \Rightarrow \frac{\partial w^+}{\partial y^+} = \frac{1}{ky^+} \tag{21}$$

The right-hand sides of Eqs. (20) and (21) both represent the classical logarithmic law for flat plates.

2.2 Numerical Solution. Equations (13)–(16) are not solvable by direct analytical integrations because of their strong nonlinearities. Severe numerical instabilities were also encountered during numerical attempts to solve these stiff equations. The perturbation method proposed by Kim and Rhode [26] was followed here by taking the curvature function κy^+ (w^+/r^+) as the perturbation parameter ε. Note that u^+ does not appear in either Eq. (14) and (15). Therefore, w^+ and u^+ can be solved separately. Assume

$$f = \kappa y^+\frac{\partial w^+}{\partial y^+} \quad \text{and} \quad b = \sqrt{1 - 2\frac{y^+}{r^+}} \tag{22}$$

where f denotes the ratio of the swirl derivative to the u derivative for the flat plate. Substituting Eqs. (14) and (22) into (15), one obtains the governing equation for the law of the wall in the circumferential direction as

$$f^2(1 + \sigma^2) - f[b(1 + \sigma^2) + \varepsilon(2 + \alpha + 2\sigma^2)] + \varepsilon[b(1 + \sigma^2) + \varepsilon(1 - \alpha + \sigma^2)] = 0 \tag{23}$$

The function f and mean velocity w^+ can be expanded in terms of ε as

$$f = f_0 + \varepsilon f_1 + \varepsilon^2 f_2 + o(\varepsilon^3) \tag{24}$$

$$w^+ = w_0^+ + \varepsilon w_1^+ + \varepsilon^2 w_2^+ + o(\varepsilon^3) \tag{25}$$

Substituting Eq. (24) into (23) gives the algebraic relationship among f_i components as

$$\varepsilon^0: \quad f_0^2(1 + \sigma^2) - f_0 b(1 + \sigma^2) = 0 \tag{26}$$

$$\varepsilon^1: \quad 2f_0 f_1(1 + \sigma^2) - f_0(2 + \alpha + 2\sigma^2) - f_1 b(1 + \sigma^2) + b(1 + \sigma^2) = 0 \tag{27}$$

$$\varepsilon^2: \quad 2f_0f_2(1+\sigma^2) - f_1(2+\alpha+2\sigma^2) - f_1^2(1+\sigma^2) - f_2b(1+\sigma^2) + (1-\alpha+\sigma^2) = 0 \tag{28}$$

which results in

$$f_0 = b, \quad f_1 = 1 + \frac{\alpha}{1+\sigma^2}, \quad f_2 = \frac{2\alpha}{b(1+\sigma^2)} \tag{29}$$

Further, substituting Eqs. (24) and (25) into (22) yields

$$f_0 + \varepsilon f_1 + \varepsilon^2 f_2 + o(\varepsilon^3) = \kappa y^+ \left[\frac{\partial w_0^+}{\partial y^+} + \frac{\partial(\varepsilon w_1^+)}{\partial y^+} + \frac{\partial(\varepsilon^2 w_2^+)}{\partial y^+} \right] + o(\varepsilon^2) \tag{30}$$

It is noted that the curvature function ε involves both dependent and independent variables. Differentiating ε in the wall-normal direction gives

$$\frac{\partial \varepsilon}{\partial y^+} = \frac{\partial}{\partial y^+}\left[\kappa y^+ \left(\frac{w^+}{y^+ \pm R^+} + \Omega^+ \right) \right] = \frac{f_0}{y^+ \pm R^+} + \varepsilon \left[\frac{1}{y^+} + \frac{(f_1 - 1)}{y^+ \pm R^+} \right] + \varepsilon^2 \frac{f_2}{y^+ \pm R^+} \tag{31}$$

Substituting Eq. (30) into (31) and collecting the perturbed parameters f_0, f_1, and f_2, the relationships between f_i and w_i^+ are obtained as

$$f_0 = \kappa y^+ \frac{\partial w_0^+}{\partial y^+} + \kappa y^+ \frac{w_1^+}{y^+ \pm R^+} f_0 \tag{32}$$

$$f_1 = \kappa y^+ \frac{\partial w_1^+}{\partial y^+} + \kappa y^+ \frac{w_1^+}{r^+}(f_1 - 1) + 2\kappa y^+ \frac{w_2^+}{r^+} f_0 + \kappa w_1^+ \tag{33}$$

$$f_2 = \kappa y^+ \frac{\partial w_2^+}{\partial y^+} + \kappa y^+ \frac{w_1^+}{r^+} f_2 + 2\kappa y^+ \frac{w_2^+}{r^+}(f_1 - 1) + 2\kappa w_2^+ \tag{34}$$

Kim and Rhode [18] derived equations similar to (32)–(34) in their analysis of streamline curvatures. However, they omitted the first terms in the right-hand side of Eqs. (33) and (34) based on the augment that these two terms are negligible compared with the others. While this omission might not affect the results of their work, it would undermine computations in flow regimes with stronger curvatures.

The perturbation variables w_0^+, w_1^+, w_2^+, and ε were computed by simultaneously solving (32)–(34) using the fourth-order Runge–Kutta method. Then by substituting these variables into (25), the resultant value of w^+ was evaluated. Finally, u^+ was obtained by integrating Eq. (13).

Figure 3 shows the numerical results of the perturbation variables w_0^+, w_1^+, w_2^+, w^+, and ε as well as the resultant w^+ for $R^+ = 50{,}000$ and $\sigma_w = 0.2$. It is clear that the mean swirl velocity profile lies above the classical logarithmic law for a convex surface, and below it for a concave surface. This is because w^+ is reversely proportional to the wall shear stress, which is dampened on convex walls and amplified on concave walls.

Interestingly, the w_0^+ profile is almost identical to that of the classical log-law and the w_1^+, w_2^+ value can be considered as the perturbations due to the presence of wall curvature. The perturbation parameter ε in Fig. 3 is much less than 1 when $y^+ < 1000$, and increases rapidly for increasing y^+. It is suggested that this prediction can become unreliable when y^+ is large, e.g., $y^+ > 3000$, where the condition $\varepsilon \ll 1$ is no longer guaranteed.

Another interesting result is the trend of the velocity profile on a concave surface. From Fig. 3(*b*), one can see that the swirl velocity deviates from the log-law from $y^+ = 70$, reaches a dip (minimum) around $y^+ = 2000$, and then increases in magnitude after $y^+ = 2000$. This trend bears a very similar pattern to the measurements by So and Mellor [6] and Hoffmann et al. [10]. For the profile dip below the log-law, Hoffmann et al. [10] suggested that the Taylor–Görtler vortices near the concave wall enhance the turbulent mixing, which reduces the velocity differences between points at different distances from the surface.

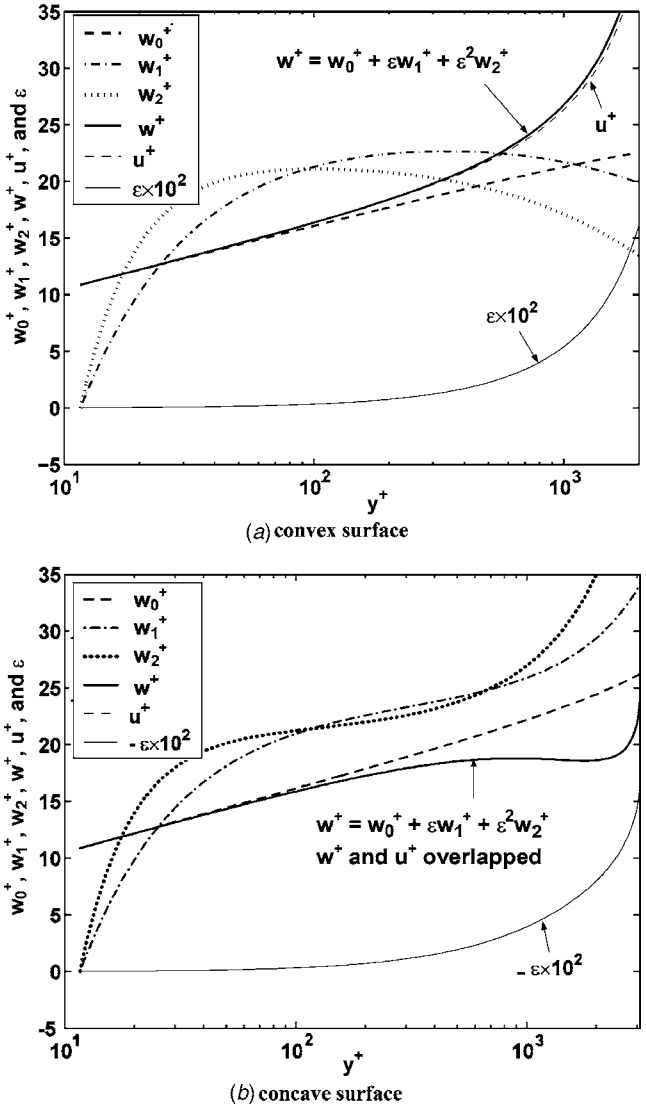

Fig. 3 Numerical results of the law of the wall in both axial (u^+) and circumferential (w^+) directions. The perturbation variables w_0^+, w_1^+, w_2^+ and ε are presented: (*a*) convex surface; (*b*) concave surface

Axial velocity u^+ was also plotted on Figs. 3(*a*) and 3(*b*). Almost no discernable difference was observed between u^+ and w^+.

2.3 Analytical Approximation. For weak curvatures where $y^+ \ll R^+$ and $\sigma = \sigma_w$, Eqs. (14)–(16) simplify as follows:

$$R_i = \frac{1}{(1+\sigma_w^2)} \frac{w^+/r^+}{\partial w^+/\partial y^+} \tag{35}$$

$$\frac{\partial w^+}{\partial y^+} - \lambda \frac{w^+}{y^+ \pm R^+} = \frac{1}{ky^+} \tag{36}$$

$$\frac{\partial u^+}{\partial y^+} = \left(\frac{\partial w^+}{\partial y^+} - \frac{w^+}{y^+ \pm R^+} \right) \tag{37}$$

where $\lambda = \alpha/(1+\sigma_w^2)$. Equations (36) and (37) can be integrated to obtain (see Appendix B)

$$w^+ = \exp\left(\lambda\frac{y^+}{r^+}\right)\left\{\frac{1}{\kappa}\ln y^+ + B - \frac{1}{\kappa}\left(\lambda\frac{y^+}{r^+}\right) + \frac{1}{\kappa}\frac{1}{2!}\left(\lambda\frac{y^+}{r^+}\right)^2 - \frac{1}{\kappa}\frac{1}{3!}\left(\lambda\frac{y^+}{r^+}\right)^3 + O\left(\lambda\frac{y^+}{r^+}\right)^4\right\} \tag{38}$$

$$u^+ = \exp\left(\lambda\frac{y^+}{r^+}\right)\left\{\frac{1}{\kappa}\ln y^+ + B - \frac{1}{\kappa}\left[(\lambda-1)\frac{y^+}{r^+}\right] + \frac{1}{\kappa}\frac{1}{2!}\left[(\lambda-1)\frac{y^+}{r^+}\right]^2 - \frac{1}{\kappa}\frac{1}{3!}\left[(\lambda-1)\frac{y^+}{r^+}\right]^3 + O\left[(\lambda-1)\frac{y^+}{r^+}\right]^4\right\} \tag{39}$$

Expanding the exponential, the above equations can be simplified as

$$w^+ = W_0^+ + \lambda\frac{y^+}{r^+}\left(W_0^+ - \frac{1}{\kappa}\right) + \frac{1}{2!}\left(\lambda\frac{y^+}{r^+}\right)^2\left(W_0^+ - \frac{3}{2\kappa}\right) + O\left(\lambda\frac{y^+}{r^+}\right)^3 \tag{40}$$

$$u^+ = U_0^+ + (\lambda-1)\frac{y^+}{r^+}\left(U_0^+ - \frac{1}{\kappa}\right) + \frac{1}{2!}\left[(\lambda-1)\frac{y^+}{r^+}\right]^2\left(W_0^+ - \frac{3}{2\kappa}\right) + O\left[(\lambda-1)\frac{y^+}{r^+}\right]^3 \tag{41}$$

where $W_0^+ = (1/\kappa)\ln y^+ + B_0$, $U_0^+ = (1/\kappa)\ln y^+ + B_0$ with $\kappa = 0.41$ and $B_0 = 4.9$.

Patel and Sotiropoulos [18] have studied the curvature law of the wall for curved channel flows and arrived at a similar expression as shown in Eq. (40). Their equation can be derived only if σ_w is specified as zero and the variable β reduces to α. It is concluded that the curvature effect on turbulent mixing length in swirling axial flows is suppressed by a factor of $1/(1+\sigma_w^2)$ compared to the curvature effect in curved channel flows. At a given curvature radius, the maximum velocity deviation occurs when the axial-to-swirl shear stress ratio is zero, i.e., swirling flows only.

On a convex curvature, close agreement between the analytical approximation and the numerical solution was achieved for moderate curvatures (i.e., $\delta/R < 0.1$), and for distances that are not large (i.e., $y^+ < 1000$). Increasing error was found beyond these conditions. This is not surprising because the analytical solution is based on a more limited assumption than the numerical solution. For a concave curvature, the same level of error occurs at a larger R^+ or a smaller y^+, indicating that the concave curvature is a more challenging case than the convex curvature.

3 Results and Discussion

3.1 Consistency. It is essential to identify the proper shear-velocity scale for each component direction, i.e., axial and tangential, of a swirling axial flow. The velocity scales, w_τ and u_τ, adopted in this study are different from the scales one might intuitively choose, such as

$$w_\tau^* = \sqrt{\tau_{w\theta}/\rho}, \quad u_\tau^* = \sqrt{\tau_{wx}/\rho} \tag{42}$$

The generality of the derived curvature law requires that the form of the velocity scale should be coordinate independent and be valid for any single plane of the flow. For example, the three scales given by Eq. (11) could be expressed by one general expression

$$\phi_\tau = \sqrt{\frac{\tau_{w\phi}}{\rho}}\sqrt{\frac{\tau_{w\phi}}{\tau_w}} \tag{43}$$

Here ϕ is a generic parameter denoting any plane direction in the flow. From Fig. 3, one can find that the resultant velocities derived from Eq. (43) follow the classical log-law at small y^+ for both axial and tangential components till departure begins as y^+ increases. However, derivations utilizing other velocity scales fail to give predictions that conform to the classical logarithmic law for small y^+ in both directions. Such a case can be observed in Fig. 4, which uses w_τ^* and u_τ^* in Eq. (42) as the velocity scales. One can see that the axial component u^+ begins to deviate from the logarithmic law beginning with $y^+ = 10$.

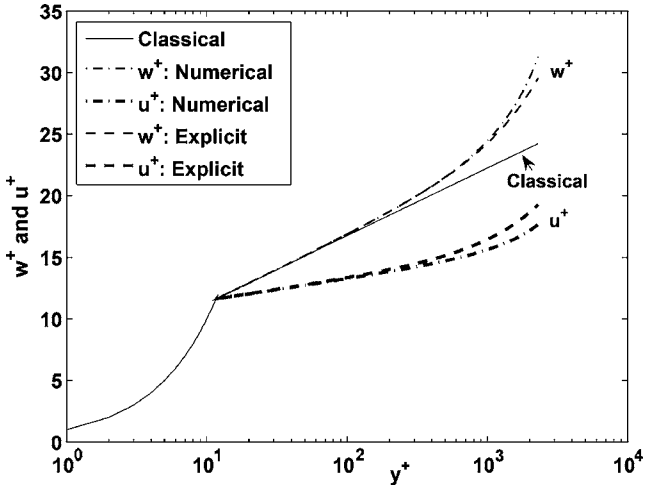

Fig. 4 Semi-logarithmic plots of near-wall velocities versus y^+ with w_τ^* and u_τ^* (Eq. (42)) as the velocity scales ($\sigma = 0.1$, $R^+ = 50{,}000$)

3.2 Curvature Radius. Figure 5 shows semi-logarithmic plots of the mean-swirl velocity w^+ versus y^+ for different curvature radii R^+ at a constant σ of 0.2. For both convex and concave curvatures, w^+ exhibits an earlier departure from the classical log-law for a smaller curvature radius, i.e., stronger curvature. For example, this departure becomes noticeable from $y^+ = 100$ for $R^+ = 50{,}000$ and from $y^+ = 800$ for $R^+ = 500{,}000$ on convex walls, as illustrated in Fig. 5(*a*). Furthermore, the profile dip in Fig. 5(*b*) occurs much earlier on a stronger curved wall, i.e., $R^+ = 5000$, than on a weaker one, i.e., $R^+ = 50{,}000$. This is consistent with the finding of Ellis and Joubert [35] that strong curvature substantially reduces the y^+ range over which the law of the wall can be applied. Compared to the convex curvature in Fig. 5(*a*), the effect of the concave curvature on the w^+ plots is opposite but not symmetric, indicating different influencing mechanisms [9,10].

3.3 Shear Stress Ratio. Figures 6(*a*) and 6(*b*) illustrate the effect of axial-to-swirl shear stress ratio σ on w^+ profiles for both convex and concave surfaces at a constant curvature radius R^+ of 50,000. For both cases, the departure from the classical log-law becomes progressively significant with decreasing shear stress ratio σ, i.e., increasing swirling intensity.

One important finding from Fig. 6 is that a w^+ profile envelope exists for flows with varying swirling intensities on curved walls of constant R^+. When σ approaches infinity, no swirl exists and the curvature effect is only noticeable for strong curvatures ($\delta^+/R^+ > 1$) [34]. When σ reduces to zero, the flow becomes a curved channel flow and the w^+ profile reaches its maximum derivation from the classical law of the wall for a given curvature radius. As deduced from Eq. (14) or (35), the curvature effect in swirling axial flows is reduced by a factor of $1/(1+\sigma_w^2)$ compared to that in curved channel flows.

In addition, comparison of the w^+ profiles in Figs. 5 and 6 reveals that R^+, and not σ, is the major factor determining the magnitude of w^+ in swirling axial flows.

3.4 Comparison With Measurements. The curvature law of the wall was compared with experimental data for convex curvatures [8] and concave curvatures [6,36]. This comparison is summarized in the following three items and the accompanying

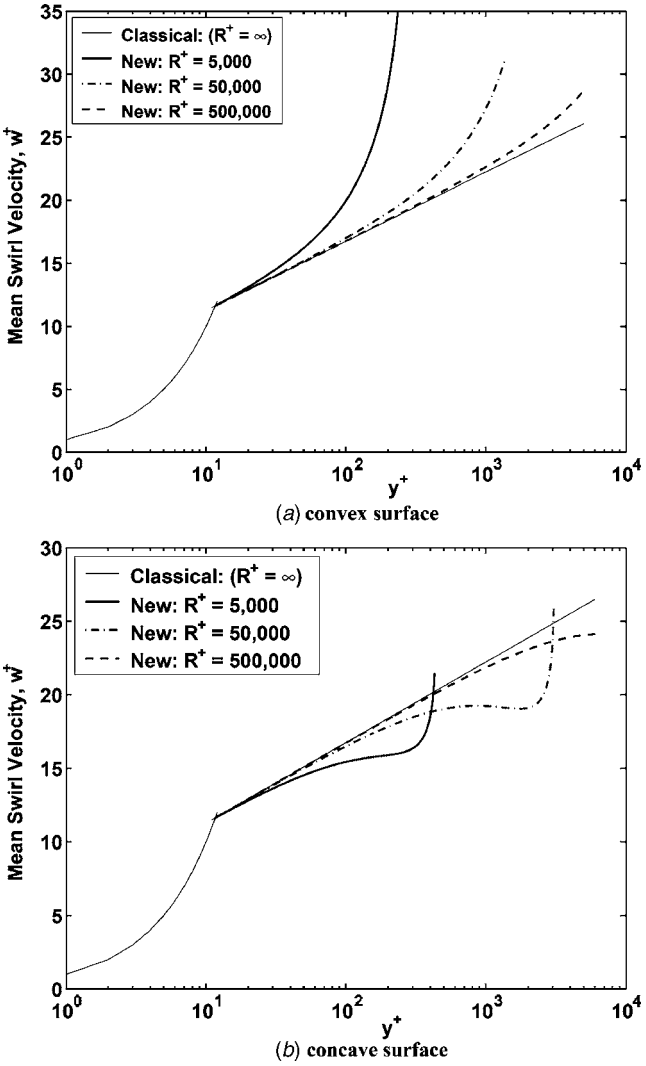

Fig. 5 Semi-logarithmic plots of near-wall swirl velocity w^+ versus y^+ for different curvature radii R^+: (*a*) convex surface; (*b*) concave surface

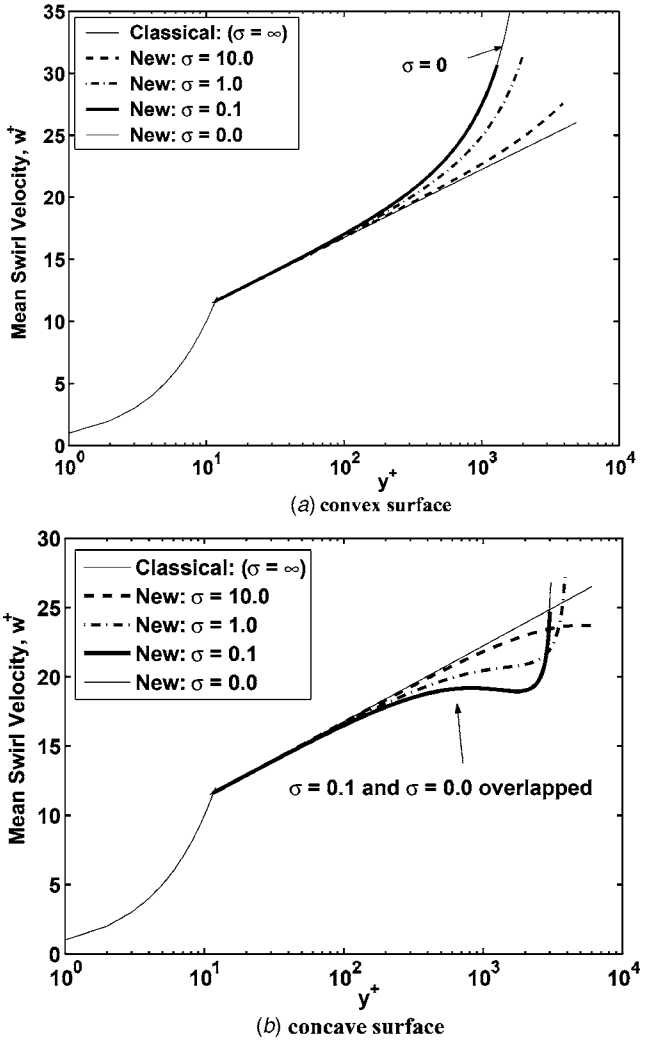

Fig. 6 Semi-logarithmic plots of near-wall swirl velocity w^+ versus y^+ for different axial-to-tangential shear stress ratios σ: (*a*) convex surface; (*b*) concave surface

figures.

I. Convex—Gillis and Johnston [8]: A very good agreement of the new curvature law with Gillis and Johnston's measurements [8] up to $y^+=800$ was obtained for a convex curvature as shown in Fig. 7. The curvature radius R^+ was 30,000 and the shear stress ratio σ was zero because only curved channel flow was present. Here $\alpha=9.0$ was found to give closer agreement with the measurement than $\alpha=7.5$ as recommended by Patel [18].

Figure 7 also shows that the experimental data exhibit a peak around $y^+=1000$ where it begins to deviate from the predictions. It is suggested that the dampening effect of a convex curvature on turbulent mixing length diminishes near the outer edge of the turbulent boundary layer and, hence, reduces the mean swirl velocity. Therefore, we suggest that the model is only valid for y^+ values less than 1000.

II. Concave—So and Mellor [6]: Figure 8 shows the comparison of the new curvature law with So and Mellor's measurements [6] for $R^+=25{,}000$ and $\sigma=0.0$. The numerical solutions agreed with the measurements up to $y^+=2000$. The curvature constant α was given a value of 4.5 as recommended by Patel [18]. Again, similarity was observed between the w^+ profile trends of the numerical prediction and the measurements.

III. Concave—Morrison et al. [36]: Figure 9 shows the comparison of the predicted swirl velocity near the stator of a laby-

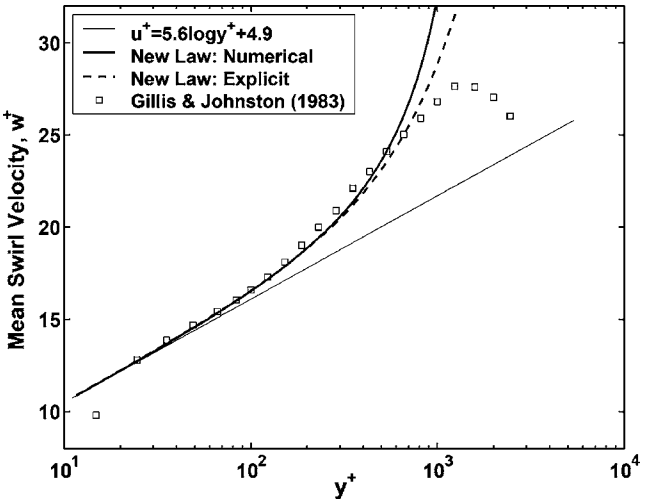

Fig. 7 Comparison of numerical results of the new wall law with measurements for convex curvature (see Ref. [8]); $R^+=30{,}000$, $\sigma=0$, $\alpha=4.5$

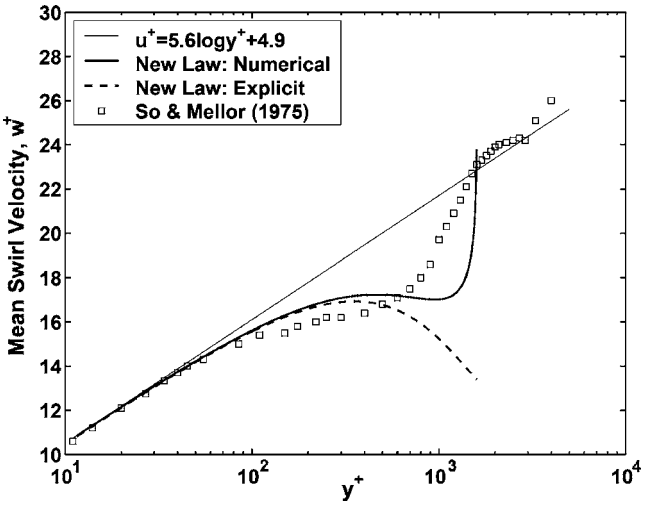

Fig. 8 Comparison of numerical results of the new wall law with measurements for concave curvature (see Ref. [6]); R^+ =25,000, σ=0, α=9.0

rinth seal with the laser Doppler anemometry (LDA) measurements by Morrison et al. [36] for Re=24,000, R^+=60,000, and σ=2.0. For this prediction α=4.5 was adopted. From Fig. 9, it is observed that the measurements were significantly different from the classical log-law because of the stator surface curvature effect. The new curvature law of the wall gave much better agreement with the measurements. Further, the numerically predicted swirl velocity profile exhibited resemblance to the measured profile.

4 Application

To evaluate the performance of the new curvature law for rotating machinery applications, it has been implemented in a well-established CFD code, and the results have been compared to the measurements of Morrison [37]. Further test cases such as inclined ellipsoids or swept wings are suggested for interested CFD practitioners. The system of interest in this study is a seven-cavity teeth-on-the-rotor labyrinth seal as illustrated in Fig. 10. The radial swirl velocity profiles were measured at the centerline of the third and fifth cavities using a LDA system [37].

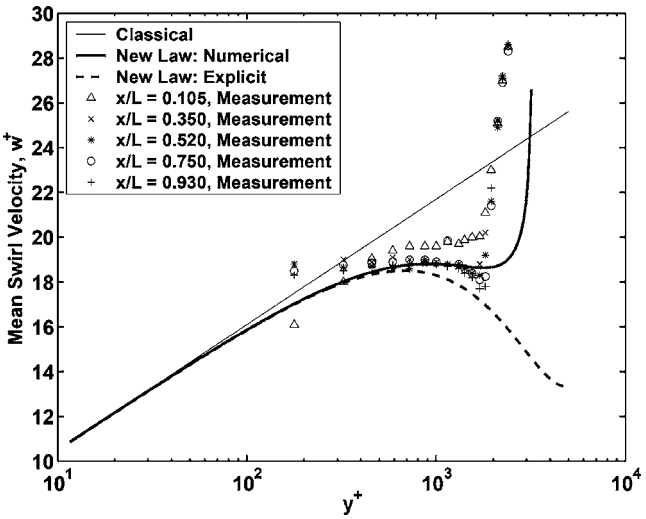

Fig. 9 Comparison of the new curvature law and classical log-law with measurements (see Ref. [36]) near the stator of a labyrinth seal (Re=24,000, R^+=60,000, and σ=2.0)

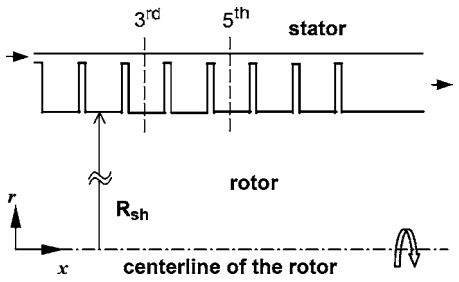

Fig. 10 Schematic configuration of the labyrinth seal in Morrison's (Ref. [37]) experimental apparatus

4.1 Curvature Wall Function Formulation. It is generally accepted that integrating the standard two-equation models through the near-wall region with the nonslip condition yields unsatisfactory results, at least for moderate- to high-Reynolds-number flows [38]. A way to overcome this deficiency is to introduce damping effects, which results in a low-Reynolds-number form of these models. As an alternative, the use of wall function is still widely employed to model the near-wall region parameters for the range of Reynolds numbers of interest herein. Wall functions express the longitudinal mean-velocity and turbulence quantities outside the viscous sublayer in terms of the distance from the wall and the wall shear stress. The wall functions can be used to provide near-wall boundary conditions for the momentum and turbulence transport equations, rather than boundary conditions at the wall itself. Hence, the viscous sublayer does not have to be resolved and the need for a very fine mesh is circumvented. As such, wall functions can be considered to be a numerically efficient alternative, which is a significant concern in most practical applications of significant size. Another important advantage of wall functions is that they allow inclusion of empirical information for special cases such as curvature, roughness, etc.

Based on the assumption of local equilibrium, Eqs. (11)–(13) could be reformulated as

$$y^+ = \frac{\rho c_\mu^{1/4} k^{1/2} y_p}{\mu}, \quad R^+ = \frac{\rho c_\mu^{1/4} k^{1/2} R}{\mu} \tag{44}$$

$$\sigma = \left(\frac{u_p}{w_p}\right)\left(\frac{w^+}{u^+}\right)\sqrt{\frac{r^+ - y^+}{r^+ - 2y^+}} \tag{45}$$

$$\tau_{rx} = \rho\left(\frac{u_p}{u^+}\right)c_\mu^{1/4} k^{1/2}, \quad \tau_{r\theta} = \rho\left(\frac{w_p}{w^+}\right)c_\mu^{1/4} k^{1/2} \tag{46}$$

where u_p and w_p are the computational results, and u^+ and w^+ are obtained from the axial-swirl law of the wall.

The standard k-ε turbulence model was used in combination with the SIMPLEC algorithm and the QUICK differencing scheme. The dissipation rate still has the form $\varepsilon_p = c_\mu k^2/\nu$. At near-wall grid points, the above wall functions are used during the iterative computing procedures. The k-ε turbulence model was chosen here because it is expected that this model will fail for confined curvature flows, and therefore will provide the worst-case scenario for improvement. Implementing the new curvature law into a more advanced turbulence model such as algebraic stress model or Reynolds stress model is believed to have a larger potential for improvement. Further, the k-ε model still finds wide application in turbomachinery community, and a substantial improvement with this model would best advocate the usage of the new curvature law.

4.2 Grid Independence Testing. Grid independence testing was performed utilizing three grids of 140×25 (coarse grid), 181×32 (mean grid), and 217×41 (fine grid) in the axial and radial directions, respectively. The root-mean-square deviations are shown in Table 1 for the swirl velocity at the centerlines of the

Table 1 Results of grid independence test

Grid NI×NJ	Third cavity			Fifth cavity		
	Convex wall y^+ max/min	Concave wall y^+ max/min	rms (%)	Convex wall y^+ max/min	Concave wall y^+ max/min	rms (%)
140×25	109/75	76/59	–	112/76	74/60	–
181×32	82/59	61/48	3.21	84/58	63/47	2.75
225×41	75/45	52/33	0.65	71/45	51/35	0.46

third and fifth cavities.

For both cavities, the coarse grid gave less than 3.2% discrepancy from the production grid, and the mean grid gave solutions with less than 0.8% discrepancy from the fine grid. Therefore, the mean grid was used for all reported simulations.

4.3 Comparison With Measurement. Two curvature law versions were tested to assess their performance. The axial-swirl law version developed in this study evaluates the near-wall velocities by applying curvature corrections in both axial and circumferential directions. The second version applies the curvature correction only in the circumferential direction while using the classical log-law in the axial direction as implemented by Kim and Rhode [26]. The second version, referred to as the "swirl-law-only," was considered because it represents the assumption that the effect of streamline curvature is limited to the circumferential direction. Thus, comparison of these two versions will give a indication of the need for a more realistic axial law of the wall in axial swirling flows.

Figure 11 shows the comparison with measurements for the swirl velocity profiles along the centerlines of the third and fifth seal cavities. The predicted radial swirl profiles both from the axial-swirl law version and the swirl-law-only version show acceptable agreement with LDA measurement at both cavities. The classical flat-plate log-law gave considerably worse agreement with measurements because of the lack of consideration of the curvature effect on turbulence. Furthermore, the benefit of having reasonable wall functions for the axial direction could be observed from the improved agreement with measurements from the axial-swirl law version than from the swirl-law-only version.

Slightly larger magnitudes of the swirl velocities were predicted from the axial-swirl law version than from the swirl-law-only version as shown in Fig. 11. It is suggested that this swirl increase resulted indirectly from the curvature effect in the axial direction. For a given y^+ value, the axial velocity near the stator, i.e., concave curvature, decreased in magnitude compared to that on a flat plate. This reduced the leakage rate for a seal with the teeth-on-the-rotor configuration, and accordingly increased the residence time of the fluid particles through the seal. Because the swirl velocity variation is mainly influenced by the fluid residence time, the mean flow has more time to adjust to the acceleration effect of the rotating teeth and rotor, and therefore raises the swirl velocity.

5 Concluding Remarks

A new law of the wall that accounts for curvature effects in both axial and circumferential directions for general swirling axial flows was derived starting from the Reynolds stress transport equations. The resultant curvature law of the wall was numerically evaluated for both convex and concave curvatures. Analytical solutions were also obtained for weak curvatures. Better insight was gained regarding the effect of the swirling intensity on the near-wall velocities. Improved agreement between predictions and ex-

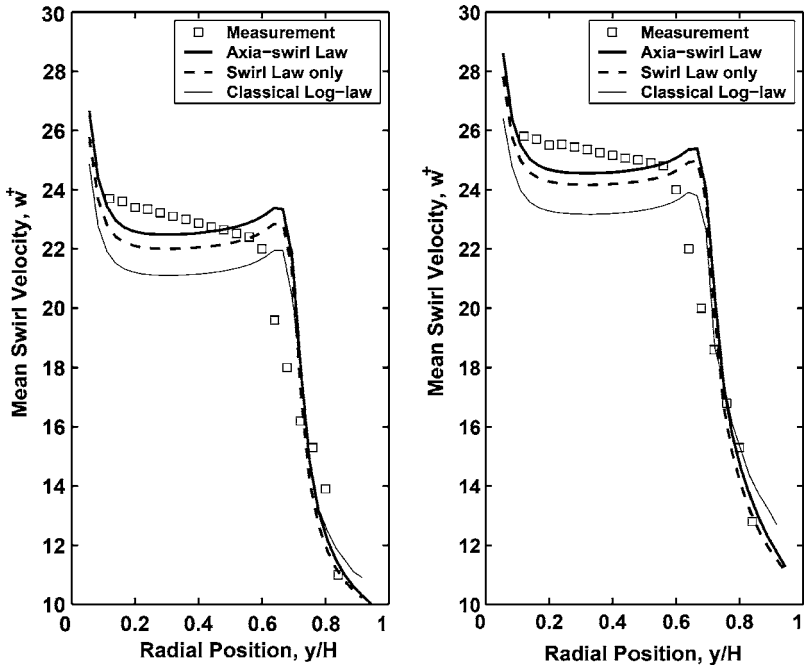

Fig. 11 Predicted swirl profile inside a labyrinth seal from the new wall function versus measurement by Morrison (Ref. [37])

perimental measurements [37] of the swirl velocity inside labyrinth cavities was obtained with the new wall function. The following findings are of specific interest:

(i) For equilibrium flows with weak curvature, the log-law in the axial direction is almost identical to that in the circumferential direction.
(ii) In support of generality, the new axial-swirl law of the wall could be readily reduced to: (a) the experimentally verified flat-plate law when the curvature radius approaches infinity; (b) the experimentally verified longitudinal curvature law [18] when the axial-to-swirl shear stress ratio reduces to zero; and (c) the experimentally verified transverse curvature law [34] as the axial-to-swirl shear stress ratio approaches infinity.
(iii) For a given curvature radius, the maximum velocity deviation occurs when the axial-to-swirl shear stress ratio is zero. The effect of curvature on the turbulence mixing length in swirling axial flows is suppressed by a factor of $1/(1+\sigma_w^2)$ compared to the curvature effect in curved channel flows.
(iv) For the empirical constant α in the Monin–Oboukhov formula, a value of 9.0 for the convex surface and 4.5 for the concave surface were found to give the best agreement with measurements. This is highly compatible with the empirical values of 7.0 and 4.5, which were recommended by Bradshaw [2] for convex and concave walls, respectively.
(v) Compared to that of the classical law of the wall, the derived wall function herein gives considerably improved agreement with experimental LDA measurements [37]. Furthermore, the improved accuracy of the new axial-swirl curvature law was demonstrated in comparison to the tangential curvature law.

Acknowledgment

The authors wish to thank Dr. David L. Rhode, Dr. Matthias Buschmann, and Dr. Xiang Fang for valuable discussions. This work was partially supported by the Texas ATP and the Supercomputer Center of Texas A&M University.

Nomenclature

k = turbulence kinetic energy
l_{rx} = turbulence mixing length in axial direction
$l_{r\theta}$ = turbulence mixing length in circumferential direction
P = kinetic energy production
q_τ = total wall shear velocity
r = coordinate in radial direction
R = radius of the wall curvature
R_e = Reynolds number ($=2u_{\text{in}}C_r/\nu$)
R_i = Richardson number
u = velocity in axial direction (m/s)
u_τ = wall shear velocity in axial direction (m/s)
w = velocity in circumferential direction (m/s)
u_τ = wall shear velocity in circumferential direction (m/s)
y = coordinate normal to the curved wall

Greek Symbols

α = empirical parameter in mixing length correction
δ = turbulent boundary layer thickness
δ_{ij} = Kronecker Delta
ε = kinetic energy dissipation rate
ε = perturbation parameter
κ = von Kármán constant
σ_w = axial-to-swirl wall shear stress ratio
ν = kinematic viscosity
τ = shear stress
φ = energy redistribution

Subscripts

r,θ,x = radial, circumferential, and axial directions in cylindrical coordinate system
w = wall

Superscripts

$'$ = fluctuating quantity
$+$ = dimensionless value in wall coordinates
f,c = fine and coarse grid system

Appendix A

For turbulent swirling axial flows, the Reynolds-stress transport equation is given by

$$\frac{D\overline{u_i'u_j'}}{Dt} + \left(\overline{u_i'u_k'}u_{j,k} + \overline{u_j'u_k'}u_{i,k}\right) = \varphi_{ij} + \varepsilon_{ij} + \overline{u_{i,k}'u_{j,k}'} + D_{ij} \quad \text{(A1)}$$

The terms, from left to right, are advection, production, energy redistribution (φ_{ij}), dissipation (ε_{ij}), turbulent diffusion, and pressure-viscous diffusion (D_{ij}).

Inside the turbulent boundary layer, it is assumed that (1) local equilibrium is satisfied, and (2) advection and diffusion terms are negligible. Thus the only two terms need to be modeled in Eq. (1) are energy redistribution and dissipation.

The energy redistribution term is typically modeled as the sum of a turbulent return-to-isotropy term and a mean-strain rapid distortion term. So and Peskin [33] studied the importance of the rapid-distortion term in modeling the turbulent shear flows and showed a negligible effect for shear flows under small external body forces. The turbulent return-to-isotropy term and the dissipation are formulated as follows [16]:

$$\varphi_{ij} = \frac{q'}{3l}\left(\overline{u_i'u_j'} - \frac{1}{3}g_{ij}q'^2\right) \quad \text{(A2)}$$

$$\varepsilon_{ij} = \frac{2}{3}g_{ij}\frac{q'^3}{\Lambda} \quad \text{(A3)}$$

Here $q' = (u_i'u_i')^{1/2}$, l is a turbulent length scale, and Λ is the Kolmogorov scale. Substituting Eqs. (A2) and (A3) into (A1) gives the Reynolds stress transport equation inside turbulent boundary layer as shown in Eq. (1).

Expanding Eq. (1) in cylindrical coordinates gives

$$-\frac{q'}{3l_1}\left(\overline{u'^2} - \frac{q'^2}{3}\right) - \frac{2}{3}\frac{q'^3}{\Lambda} - 2\overline{u'v'}\frac{\partial u}{\partial r} = 0 \quad \text{(A4)}$$

$$-\frac{q'}{3l_1}\left(\overline{v'^2} - \frac{q'^2}{3}\right) - \frac{2}{3}\frac{q'^3}{\Lambda} + 4\overline{v'w'}\frac{w}{r} = 0 \quad \text{(A5)}$$

$$-\frac{q'}{3l_1}\left(\overline{w'^2} - \frac{q'^2}{3}\right) - \frac{2}{3}\frac{q'^3}{\Lambda} - 2\overline{v'w'}\left(\frac{\partial w}{\partial r} + \frac{w}{r}\right) = 0 \quad \text{(A6)}$$

$$-\frac{q'}{3l_1}\overline{u'v'} - \overline{v'^2}\frac{\partial u}{\partial r} + 2\overline{u'w'}\frac{w}{r} = 0 \quad \text{(A7)}$$

$$-\frac{q'}{3l_1}\overline{v'w'} - \overline{v'^2}\left(\frac{\partial w}{\partial r} + \frac{w}{r}\right) + 2\overline{w'^2}\frac{w}{r} = 0 \quad \text{(A8)}$$

$$-\frac{q'}{3l_1}\overline{u'w'} - \overline{v'w'}\frac{\partial u}{\partial r} - \overline{u'v'}\left(\frac{\partial w}{\partial r} + \frac{w}{r}\right) = 0 \quad \text{(A9)}$$

The goal here is to solve the turbulent shear stresses in both direction components, i.e., $-\overline{u'v'}$ and $-\overline{v'w'}$. Rearranging Eqs. (A4)–(A9) without any additional approximation, one can obtain

$$l_{r\theta} = ky\left[\frac{Z^{3/2}}{Z+\beta R_i/2}\right]^{1/2} \tag{A10}$$

$$l_{rx} = ky\left[\frac{Z^{3/2}}{Z+\beta R_i/2}\right]^{1/2}\left[Z+\frac{\beta R_i}{2}+\gamma^2\left(Z+\frac{\beta R_i}{2}-1\right)\right]^{1/2} \tag{A11}$$

$$2Z = 1-\frac{5}{8}\beta Ri+\left[\left(1-\frac{3}{8}\beta Ri\right)^2+\frac{3}{2}\beta Ri^2\sigma^2\right] \tag{A12}$$

For curved walls ranging from weak curvature, i.e., $\delta/R=0.01$, to moderate curvature, i.e., $\delta/R=0.1$, the condition $w/r < \partial w/\partial r$ is generally satisfied in the near wall regions. From Eqs. (7) and (8), R_i and (σR_i) are both less than 1. Application of the above relation into Eqs. (A10)–(A12) yields the axial and tangential mixing lengths as shown in Eqs. (4) and (5).

Appendix B

$$\frac{\partial w^+}{\partial y^+}-\lambda\frac{w^+}{y^+\pm R^+}=\frac{1}{ky^+} \tag{B1}$$

Let $F(y^+)=\int(-\lambda 1/(y^+\pm R^+))dy^+=-\lambda\ln(y^+\pm R^+)$ be an antiderivative of $-\lambda(1/(y^+\pm R^+))$. Let $W(y^+)=w\exp[F(y^+)]$. Then differentiate $W(y^+)$, one can see that it satisfies

$$\frac{dW^+}{dy^+}=\exp[F(y^+)]\left(\frac{dw^+}{dy^+}-\lambda\frac{w^+}{y^+\pm R^+}\right)=\exp[F(y^+)]\frac{1}{\kappa y^+} \tag{B2}$$

Hence,

$$W^+=\int\exp[F(y^+)]\frac{1}{\kappa y^+}dy^++C \tag{B3}$$

$$W^+=\int\frac{1}{\kappa y^+(y^+\pm R^+)^\lambda}dy^++C \tag{B4}$$

Here C is an arbitrary constant. It follows the general solution, which has the form

$$w^+=\exp[F(y^+)]\left\{\int\frac{dy^+}{\kappa y^+(y^+\pm R^+)^\lambda}+C\right\} \tag{B5}$$

Remark. When λ is an integer, or even a rational number, the above integral can be explicitly evaluated. But when λ is irrational, no explicit expression beyond the above integral representation is available.

References

[1] Bradshaw, P., 1969, "The Analogy Between Streamline Curvature and Buoyancy in Turbulent Shear Flow," J. Fluid Mech., **36**, pp. 177–191.

[2] Bradshaw, P., 1973, "Effect of Streamline Curvature on Turbulent Flows," AGARDograph No. 169.

[3] Patel, V. C., 1969, "Measurements of Secondary Flow in the Boundary Layer of a 180 Degree Curved Channel," ARC CP No. 1043, Aeronautical Research Council, London.

[4] Meroney, R. N., and Bradshaw, P., 1975, "Turbulent Boundary-Layer Growth Over a Longitudinally Curved Surface," AIAA J., **13**, pp. 1448–1453.

[5] So, R. M. C., and Mellor, G. L., 1973, "Experiment on Convex Curvature Effects in Turbulent Boundary Layers," J. Fluid Mech., **60**, pp. 43–62.

[6] So, R. M. C., and Mellor, G. L., 1975, "Experiment on Turbulent Boundary Layers on a Concave Wall," Aeronaut. Q., **XXVI**, pp. 25–40.

[7] Hunt, I. A., and Joubert, P. N., 1979, "Effects of Small Streamline Curvature on Turbulent Duct Flow," J. Fluid Mech., **91**, pp. 633–659.

[8] Gillis, J. C., and Johnston, J. P., 1983, "Turbulent Boundary Layer Flow and Structure on a Convex Wall and Its Redevelopment on a Flat Fall," J. Fluid Mech., **135**, pp. 123–153.

[9] Muck, K. C., Hoffmann, P. H., and Bradshaw, P., 1985, "The Effects of Convex Curvature on Turbulent Boundary Layers," J. Fluid Mech., **161**, pp. 347–369.

[10] Hoffmann, P. H., Muck, K. C., and Bradshaw, P., 1985, "The Effects of Concave Surface Curvature on Turbulent Boundary Layers," J. Fluid Mech., **161**, pp. 371–403.

[11] Gibson, M. M., 1988, "Effects of Surface Curvature on the Law of the Wall," *Near Wall Turbulence*, S. J. Kline and N. H. Afgan, eds., Hemisphere, New York, pp. 157–171.

[12] Barlow, R. S., and Johnson, J. P., 1988, "Structure of a Turbulent Boundary Layer on a Concave Surface," J. Fluid Mech., **191**, pp. 137–176.

[13] Bradshaw, P., 1988, "Effects of Extra Rates of Strain–Review," *Near Wall Turbulence*, S. J. Kline and N. H. Afgan, eds., Hemisphere, New York.

[14] So, R. M. C., 1975, "A Turbulent Velocity Scales for Curved Shear Flows," J. Fluid Mech., **70**, pp. 37–57.

[15] So, R. M. C., 1975, "Effects of Streamline Curvature on the Law of Wall," *Proceedings of 12th Annual Meeting, Society of Engineering Science*, The University of Texas at Austin, Texas, pp. 787–796.

[16] So, R. M. C., 1977, "Turbulent Velocity Scales for Swirling Flows," *Turbulence in Internal Flows*, S. N. B. Murthy, ed., Hemisphere, Washington DC, pp. 347–368.

[17] Moser, R. D., and Moin, P., 1987, "The Effects of Curvature in Wall-bounded Turbulent Flows," J. Fluid Mech., **175**, pp. 479–510.

[18] Patel, V. C., and Sotiropoulos, F., 1997, "Longitudinal Curvature Effects in Turbulent Boundary Layers," Prog. Aerosp. Sci., **33**, pp. 1–70.

[19] Yamaguchi, H., 1992, "Analysis of Turbulent Boundary Layer Controls on Convex and Concave Curvature Surfaces With Suction or Injection," ASME Fluids Engineering Paper No. FED-133.

[20] White, F. M., 1991, *Viscous Fluid Flow*, 2nd ed. McGraw Hill, New York, pp. 546–549.

[21] Jayaram, M., Taylor, M. W., and Smits, A. J., 1987, "The Responses of a Compressible Turbulent Boundary Layer to Short Regions of Concave Surface Curvature," J. Fluid Mech., **175**, pp. 343–362.

[22] Wilcox, D. C., and Chambers, T. L., 1977, "Streamline Curvature Effects on Turbulent Boundary Layers," AIAA J., **15**, pp. 574–580.

[23] Rodi, W., and Scheuerer, G., 1983, "Calculation of Curved Shear Layers With Two-Equation Turbulence Models," Phys. Fluids, **26**, pp. 1422–1436.

[24] Galperin, B., and Kantha, L. H., 1989, "Turbulence Model for Rotating Flows," AIAA J., **27**, pp. 750–757.

[25] Kind, R. J., Yowakim, F. M., and Sjolander, S., 1989, "The Law of the Wall for Swirling Flow in Annular Ducts," ASME J. Fluids Eng., **111**, pp. 160–164.

[26] Kim, N., and Rhode, D. L., 1999, "Swirling Streamline-Curvature Law of the Wall From a Novel Perturbation Analysis," Numer. Heat Transfer, Part B, **36**, pp. 331–350.

[27] Childs, D. W., 1993, *Turbomachinery Rotordynamics: Phenomena, Modeling and Analysis*, Wiley, New York, pp. 290–354.

[28] Xi, J., and Rhode, D. L., 2006, "Rotordynamics of Impeller Eye Seals With Wear-Damaged Teeth in Centrifugal Compressors," Tribol. Trans., **49**, pp. 328–337.

[29] Xi, J., and Rhode, D. L., 2006, "Rotordynamics of Turbine Labyrinth Seals With Rotor Axial Shifting," Int. J. Rotating Mach., **2006**, pp. 1–11.

[30] Xi, J., and Rhode, D. L., 2006, "Seal-Inlet Disturbance Boundary Condition Correlations for Rotordynamics Models, Part 1: Correlation Development," Tribol. Trans., **49**, pp. 574–583.

[31] Xi, J., and Rhode, D. L., 2006, "Seal-Inlet Disturbance Boundary Condition Correlations for Rotordynamics Models, Part 2: Assessment," Tribol. Trans., **49**, pp. 584–591.

[32] Schwarz, S. G., Goldstein, R. J., and Eckert, E. R. G., 1991, "The Influence of Curvature on Film Cooling Performance," ASME J. Turbomach., **113**, pp. 472–478.

[33] So, R. M. C., and Peskin, R. L., 1980, "Comments on Extended Pressure-Strain Correlation Models," ZAMP, **31**, pp. 56–65.

[34] Piquet, J., and Patel, V. C., 1999, "Transverse Curvature Effects in Turbulent Boundary Layer," Prog. Aerosp. Sci., **35**, pp. 661–672.

[35] Ellis, L. B., and Joubert, P. N., 1974, "Turbulent Shear Flow in a Curved Duct," J. Fluid Mech., **62**, pp. 65–84.

[36] Morrison, G. L., Winslow, R. B., and Thames, H. D., 1995, "Phase Averaged Wall Shear Stress, Wall Pressure and Near Wall Velocity Field Measurement in a Whirling Annular Seal," ASME 95-GT-101.

[37] Morrison, G. L., Johnson, M. C., and Tatterson, G. B., 1988, "Experimental Verification of a Secondary Recirculation Zone in a Labyrinth Seal," AIAA Pap. 88-3692-CP.

[38] Launder, B. E., and Spalding, D. B., 1974, "The Numerical Computation of Turbulent Flow," Comput. Methods Appl. Mech. Eng., **3**, pp. 269–289.

Particle Image Velocimetry Evaluation of a Novel Oscillatory-Flow Flexible Chamber Mixer

Thomas N. Shipman

Ajay K. Prasad[1]
e-mail: prasad@udel.edu

Department of Mechanical Engineering,
University of Delaware,
Newark, DE 19711

Scott L. Davidson

Donald R. Cohee
e-mail: coheed@ilcdover.com

ILC Dover Inc.,
One Moonwalker Road,
Frederica, DE 19946

This paper describes a novel oscillatory-flow mixer consisting of a pair of flexible chambers connected by a perforated plate, or septum. During operation, the septum undergoes reciprocating motion such that the two chambers are alternately compressed and expanded. During compression, fluid is forced from one chamber to the other through the septum holes, creating an array of jets that drive the mixing process. Flow characterization within the mixer was conducted using particle image velocimetry. Tests were performed for Reynolds numbers ranging from 4 to 23,000, which encompass the creeping, laminar, and turbulent flow regimes. Results include mean and rms velocity maps, shear rate maps, vertical velocity profiles, and flow development data. The results suggest that the mixer is capable of gentle, continuous stirring (important for biological applications), as well as vigorous agitation. Finally, a comparison between this mixer and other existing mixing technologies is presented. [DOI: 10.1115/1.2409347]

Keywords: flexible-chamber mixer, oscillatory flow, perforated plate, PIV, particle image velocimetry, shear rate, jet, reciprocating

Introduction

The flexible chamber mixer (FCM) presented in this paper consists of two flexible chambers connected by a perforated septum plate. An artistic rendering of the setup (including a cutaway view) is shown in Fig. 1, and a full schematic is shown in Fig. 2. The mixing chambers used for the current experiments are made of simple plastic sheeting formed into cylinders. To induce mixing, the septum is oscillated vertically, alternately compressing one chamber and forcing the fluid into the second expanding chamber. Due to the septum motion, fluid issues in the form of jets from holes in the septum plate, driving the mixing process. A computer-controlled stepper motor supplies motive power, allowing for precise control over a wide range of septum oscillation configurations (combinations of multiple stroke lengths and frequencies within a single overall cycle), and septum speeds (3–300 mm/s). Additional details about the apparatus are provided in the procedure section.

Three key features of the mixer being studied here lend themselves to a wide variety of industrial, pharmaceutical, and biological applications. First, the mixer is designed so that all parts that contact the working fluid can be made disposable. The disposability feature eliminates the need for expensive cleaning processes required in current mixer designs, making the FCM ideal for applications involving biologically hazardous or toxic fluids, and applications requiring highly sterile conditions. The second advantage of the FCM design is the distribution of fluid jets throughout the entire mixing volume, as compared to an impeller mixer in which the high velocity/high shear region is limited to the immediate vicinity of the impeller. By controlling septum speed and perforation parameters, one can obtain very low shear rates while still thoroughly mixing the fluid. Alternatively, high shear can also be obtained by altering the aforementioned parameters. For example, extended-duration mixing at low shear rates is important in mixing applications involving live cells, whereas high shear rates are required for homogenization. Finally, mixer scaleup is possible by simply enlarging the diameter of the septum and mixing chambers, and/or by stacking multiple septa and mixing chambers in a vertical chain.

A broad base of knowledge already exists for many mixer configurations, including impeller driven mixers, oscillatory flow baffled column mixers, and reciprocating plate mixers. Because our research focuses entirely on oscillatory mixers, we will restrict our attention to previous work relating to oscillatory flow mixers with some brief comparisons to the other mixer classes.

An oscillatory flow baffled column reactor consists of a long cylindrical tube with multiple orifice plates. Fluid is placed in the tube, and an oscillatory flow profile is imparted to the fluid. Previous research in this area includes measurement of strain rate via particle image velocimetry (PIV) [1], study of heat/mass transfer in an oscillatory flow baffled column [2,3], and general flow and mixing characterization [4,5]. Dickens et al. [5] also studied optimal baffle placement, which is relevant to FCM scaleup using multiple septa. Previously studied reciprocating plate mixers (which are similar to the FCM presented here) consist of a *rigid* cylinder and a plate that is oscillated inside of the outer cylinder, driving the mixing process. Several different designs have been studied, including both nonperforated and perforated plates [6,7] and plates with "flapping blades" [8,9]. The aforementioned work included studies of flow profiles [6], heat transfer characteristics [7], mass transfer from soluble solid objects [8], mixing time [9], and mixer power consumption [10].

The major difference in the current research resides in the *flexible* nature of our mixing chambers in contrast with the rigid mixers studied previously. Thus, the FCM represents a new class of mixer and results provided in this paper are therefore new and interesting. We have applied a number of techniques to qualitatively and quantitatively measure the mixing performance of the FCM, such as laser induced fluorescence and PIV. However, we restrict ourselves to PIV results in this paper.

Primary goals of this research include analysis of flow fields, shear rates, and turbulence for Reynolds number values ranging

[1]Corresponding author.

Contributed by the Fluids Engineering Division of ASME for publication in the JOURNAL OF FLUIDS ENGINEERING. Manuscript received October 11, 2005; final manuscript received July 10, 2006. Assoc. Editor: Timothy J. O'Hern.

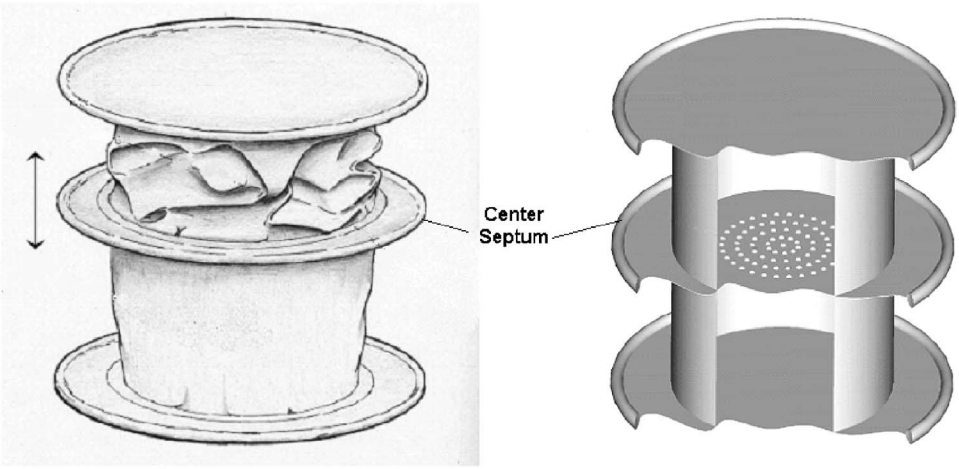

Fig. 1 Artistic rendering of mixer assembly

from 4 to 23,000, which encompass flow regimes ranging from creeping flow to turbulence. Study of a large Re range also allows analysis of mixing scenarios from gentle stirring to vigorous mixing and homogenization. Of additional interest is the potential impact of flexible chamber walls on mixing performance. Although the mixer is capable of complex oscillation configurations wherein multiple intermediate septum travel profiles can be incorporated within each overall repeating cycle, we will restrict ourselves in this study to the simplest case wherein the septum undergoes basic reciprocating motion at a prescribed frequency and stroke length. We used the same stroke length for all our experiments and varied the frequency (i.e., septum speed) to explore different flow regimes. Our data will help to evaluate the mixing effectiveness of the current design, suggest modifications for improved performance, and customize mixer parameters for different industrial applications.

Relevant Flow Parameters

As presented in the literature, such as Komoda et al. [6], Reynolds number is the key variable affecting flow characteristics. Komoda et al. [6] studied an oscillatory mixer with a solid disk, and proposed the following regimes: $\mathrm{Re}<20$, laminar creeping flow; $20<\mathrm{Re}<200$, formation of ring vortices behind the disk; and $\mathrm{Re}>200$, turbulent flow. Idelchik [11] proposed three distinct Re ranges for pressure drop for flow across a perforated plate: $\mathrm{Re}<10$, $10<\mathrm{Re}<30$, and $30<\mathrm{Re}<10^4$. These three ranges may be broadly classified as creeping flow, laminar flow, and turbulent flow, respectively.

In our case, the primary quantities of interest are the diameter of the septum (and the chambers as well) D_S, the working chamber length L_C, the stroke length L_S (we set $L_S \approx L_C$ in our experiments), the diameter of individual septum holes D_H, and their number N, which together determine the fractional area of the septum which is open A_O. All of these quantities were fixed for the experiments reported here. The septum speed $V_{S/L}$ was varied to create different flow regimes. The septum speed and septum-hole geometry determined the nominal fluid velocity through the septum hole (as seen by the septum) $V_{F\text{-NOM/}S}$. Using these variables, and the fluid kinematic viscosity ν, we define our Reynolds number as

$$\mathrm{Re} = \frac{V_{F\text{-NOM/}S} D_H}{\nu} \tag{1}$$

Jets issuing from the septum holes drive the mixing process and are therefore the most important flow feature of the FCM. Accordingly, we have used the jet orifice diameter (D_H) to define our Reynolds number. Similarly, Komoda et al. [6] used the orifice hydraulic diameter in their Reynolds number definition. To fully understand Eq. (1), a definition for $V_{F\text{-NOM/}S}$ is also required; mass

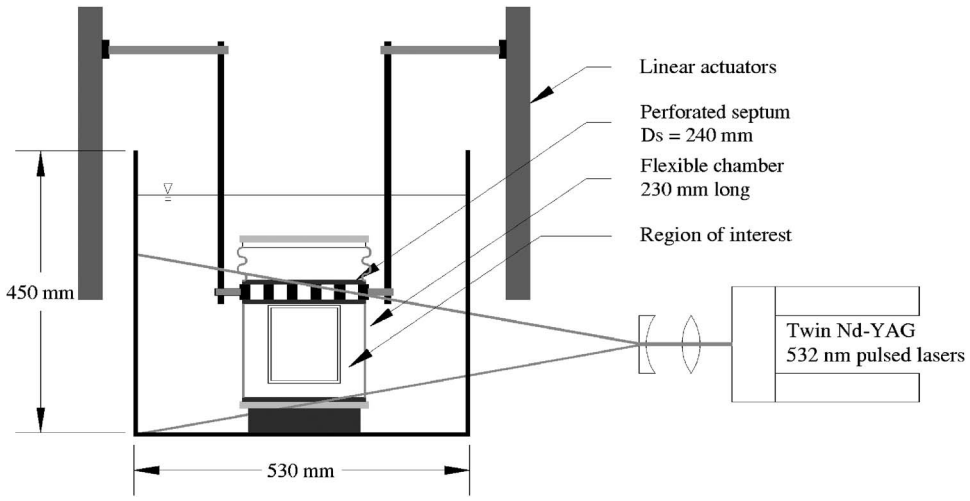

Fig. 2 Schematic of mixing apparatus

conservation gives $V_{F\text{-NOM}/S}=V_{S/L}/A_O$. From a stationary observer's viewpoint, the nominal through-hole velocity magnitude would then be $(V_{F\text{-NOM}/S}-V_{S/L})$. Note here that the subscripts $_{/S}$ and $_{/L}$ refer to the septum (moving) frame of reference, and the laboratory (stationary) frame of reference, respectively.

Next, the actual (as opposed to nominal) through-hole average velocity as seen by a stationary observer can be modeled as:

$$V_{F\text{-AVG}/L}=KV_{S/L}\left(\frac{1}{A_O}-1\right) \tag{2}$$

This expression differs from that for the nominal velocity by the introduction of the constant K, which accounts for deviations from the nominal velocity value caused by chamber folding characteristics; for example, when the chamber compresses, the chamber material sometimes will fold in a manner such that the outermost ring of holes is partially shaded. Consequently, the flow through the inner holes will speed up resulting in K values in excess of unity.

Finally, in the current design, the septum plate has a thickness of 76.2 mm, therefore, the flow through the hole may in fact develop to some extent depending on the Re under consideration. Such a thick septum was required to overcome visual obstruction caused by thick bag mounting rings, thus allowing clear optical access to both upper and lower septum edges. For small Re, the flow will emerge from the septum hole with a parabolic profile, for which $V_{F\text{-MAX}/S}=2V_{F\text{-AVG}/S}$. For large Re, the emerging flow should resemble a plug flow (due to reduced flow development), and $V_{F\text{-MAX}/S}\approx V_{F\text{-AVG}/S}$. To account for flow development, the following equations for $V_{F\text{-MAX}/S}$ and $V_{F\text{-MAX}/L}$ are proposed

$$V_{F\text{-MAX}/S}=CV_{F\text{-AVG}/S} \tag{3a}$$

$$V_{F\text{-MAX}/L}=CV_{F\text{-AVG}/L}+(C-1)V_{S/L} \tag{3b}$$

C is a measure of boundary layer development within the septum hole for a given flow profile. Fully developed laminar flow gives $C=2$, and fully developed turbulent flow gives $C\approx 1.23$ (for Re $=10^4$) [12]. To determine C experimentally, $V_{F\text{-AVG}/L}$ was computed by numerically integrating the vertical through-hole velocity through the central hole. Putting Eq. (2) and (3*b*) together, we arrive at the following relationship between $V_{F\text{-MAX}/L}$ and $V_{S/L}$

$$V_{F\text{-MAX}/L}=V_{S/L}\left[CK\left(\frac{1}{A_O}-1\right)+(C-1)\right] \tag{4}$$

A second key nondimensional parameter presented in the oscillatory-flow mixer literature [1] is the Strouhal number. Defining the Strouhal number as $\mathrm{St}=\omega D_H/V_{F\text{-AVG}/S}$ [12], where ω is the oscillation frequency, it is straightforward to show that $\mathrm{St}\sim D_H A_O/L_S$. Because this quantity does not vary in our experiments, the only parameter of interest hereafter will be the Reynolds number.

Another length scale witnessed in our work was jet penetration length. Jet penetration can be thought of simply as the jet length (as evidenced by the column of moving fluid) issuing from the septum hole. Using a simplified model, we can easily relate the nominal length of jet penetration (L_{JP}) to the septum speed $V_{S/L}$, fractional septum open area A_O, and septum travel time t

$$L_{\mathrm{JP}}=V_{S/L}\left(\frac{1}{A_O}-1\right)t \tag{5}$$

Note that $V_{S/L}$ remains essentially constant throughout the stroke. But the stroke length L_S is given by $V_{S/L}t$, which gives

$$L_{\mathrm{JP}}=L_S\left(\frac{1}{A_O}-1\right) \tag{6}$$

In our case, $A_O=0.46$, so L_{JP} is roughly equal to stroke length, which was 195 mm. For smaller A_O, it is possible that $L_{\mathrm{JP}}>L_S$ which simply means that the jet will travel through the chamber and eventually impact the lower boundary. If one accounts for the slowing of the jet fluid as it travels away from the septum hole, and the effect of $K\neq 1$, Eqs. (5) and (6) would become approximations.

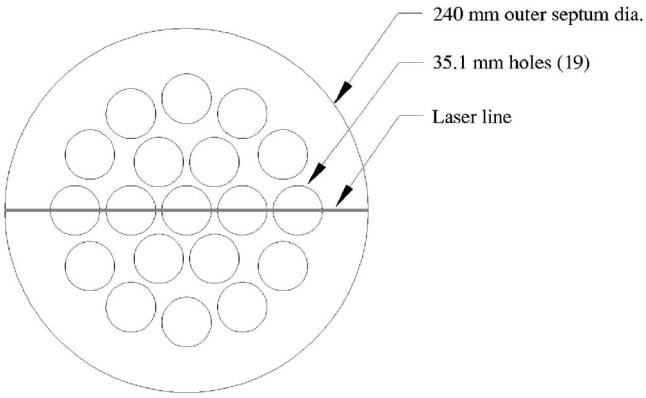

Fig. 3 Schematic of septum plate

Additional nondimensional parameters used in our data analysis include the nondimensional velocity ratio V^*, shear rate ε^*, and nondimensional length parameters r^* and z^* (radial and vertical locations). All nondimensional velocity values are measured with respect to the lab frame L

$$V^*=\frac{V_{F/L}}{V_{S/L}\left(\frac{1}{A_O}-1\right)},\quad \varepsilon^*=\frac{\varepsilon}{\varepsilon_{\mathrm{MAX\text{-}LAM}}},\quad \varepsilon_{\mathrm{MAX\text{-}LAM}}=\frac{8V_{F\text{-NOM}/S}}{D_H}$$

$$r^*=\frac{r}{D_S},\quad z^*=\frac{z}{D_S},\quad L^*_{\mathrm{JP}}=\frac{L_{\mathrm{JP}}}{D_S},\quad L^*_{\varepsilon P}=\frac{L_{\varepsilon P}}{D_S}$$

The fluid in the FCM experiences the highest shear rate as it transits the septum hole. A convenient shear rate scale is the maximum value attained for fully developed laminar flow through the septum hole denoted by $\varepsilon_{\mathrm{MAX\text{-}LAM}}$. Accordingly, we nondimensionalize shear rate with $\varepsilon_{\mathrm{MAX\text{-}LAM}}$. Also, by referring back to Eq. (2), it is seen that $V^*_{F\text{-AVG}/L}=K$.

Experimental Setup

All experiments were conducted using a prototype mixer design based on the FlexMixer, now marketed by ILC Dover LP and Wave Biotech LLC. An artistic rendering of the mixer is shown in Fig. 1 and a full schematic in Fig. 2. Twin 230-mm-long transparent bags (ILC No. BPC 16) along with a rigid septum were used. The bags were made out of highly flexible (but inelastic) transparent polyethylene, and were approximately 0.2 mm thick. Each cylindrical bag was constructed with a slight conical shape (with the largest diameter facing the septum) to allow more efficient bag folding during operation. The bag diameter at the septum end was approximately 240 mm, and the smaller diameter was 230 mm. Each bag was sealed to rigid fixed end plates and the oscillating septum using oversized hose clamps and O-rings. Ports were installed in each end chamber to allow for filling and draining of the mixer. Significant care was taken to minimize the presence of air bubbles inside of the mixer. The septum (see Fig. 3) consisted of a 76.2-mm-thick plastic plate with 19 holes of diameter 35.1 mm arrayed in a pattern shown in Fig. 3, with a resulting open area of 46%. As stated earlier, the unusually large septum thickness was dictated by the need for direct visual access to the upper and lower edges of the septum. In a field version of the mixer, septum thickness would range from a few millimeters to 10–20 mm. Effective stroke length was limited to about 195 mm due to safety requirements and the bag mounting system. During a typical stroke, the septum would approach within approximately 15 mm of the top and bottom end plates.

Table 1 Summary data for all trials (boldface numbers refer to cases plotted in Figs. 4–6)

Experimental variables			Results							
$V_{S/L}$ (mm/s)	$V_{F\text{-NOM}/L}$ (mm/s)	Re	$V^*_{F\text{-MAX}}$	$V^*_{F\text{-AVG}}$ K	C	L^*_{JP}	ε_{MAX} (1/s)	ε^*_{MAX}	$L^*_{\varepsilon P}$	$V^*_{RMS\text{-FF}}$
Low Re high viscosity runs (viscosity≈50 cP)										
2.9	**3.44**	**4**	**1.7**	**0.9**	**1.5**	**0.4**	**0.7**	**0.5**	**0.1**	**0.1**
6.1	7.17	9	2.0	1.0	1.6	0.4	1.5	0.5	0.1	0.1
10	11.7	15	2.3	1.1	1.6	0.4	2.7	0.5	0.1	0.1
50	**58.7**	**76**	**2.7**	**1.3**	**1.7**	**0.6**	**15**	**0.6**	**0.5**	**0.1**
300	352	460	1.9	1.3	1.3	0.6	111	0.7	0.5	0.3
High Re low viscosity runs (viscosity=1 cP)										
50	58.7	3800	1.8	1.5	1.2	0.6	23	0.9	0.3	0.3
150	176	11,400	1.8	1.4	1.2	0.6	59	0.8	0.2	0.3
300	**352**	**23,000**	**1.7**	**1.3**	**1.2**	**0.6**	**105**	**0.7**	**0.3**	**0.4**

Motive power for the apparatus was supplied by a pair of linear actuators and a computer-controlled stepper motor. A constant velocity profile was used, with acceleration/deceleration (also constant) being limited to the first and last 20 mm of septum travel. Thus, the septum traveled at a constant velocity during most of the 195 mm stroke length. Dwell time at the end of each stroke was on the order of 0.1 s, and was due to the computer control system. The control system allowed the user to program drive speed, acceleration profiles, and stroke length.

Experiments were conducted with water, and in some cases an aqueous solution of sodium carboxymethylcellulose (NaCMC) was used to increase fluid viscosity to approximately 50 cP. Using a lookup table and an electronic balance accurate to 0.1 g, an appropriate amount of CMC was added to achieve the desired viscosity. Although aqueous NaCMC solutions can display shear-thinning behavior, the dilute concentrations used here ensured that shear-thinning effects were minimal. Various Reynolds number regimes were considered, ranging from $4 < \mathrm{Re} < 23{,}000$. Table 1 lists the Reynolds numbers tested.

To improve viewing conditions, the entire bag assembly was fully submerged in a large square glass tank with a side dimension of 530 mm and a height of 450 mm. The tank was filled with water to a height sufficient to fully submerge both chambers. Additionally, a slight overpressure (about 150 mm of water) was applied to the mixing chamber to minimize optical distortions caused by folds in the bags. Perfect refractive index matching between the working fluid and the plastic chamber material was not essential as the chamber walls were thin (0.2 mm). It was, however, important that the fluid inside the mixing chamber have the same refractive index as the fluid in the outer square tank. Note that the addition of NaCMC to the water did not noticeably change the refractive index of the mixer fluid. The use of a square tank (allowing orthogonal viewing through a flat surface) eliminated the otherwise severe optical distortion that the camera would see through the curved bag surface.

Measurement Techniques

The PIV technique was used for data collection and analysis in this paper. As is shown in Fig. 2, all PIV measurements were taken in a region of interest (ROI) centered on the central septum hole, and extending downward to the bottom of the lower (expanded) chamber. Two specific ROIs were chosen: one spanning the central three septum holes and the second spanning the entire septum diameter. The smaller ROI (about 140 mm wide by 160 mm tall) was chosen to allow higher resolution data acquisition, especially important when determining strain rate values, while the larger ROI (about 250 mm wide by 150 mm tall) was used to investigate general circulation patterns. The ROI was illuminated with a pair of 532 nm Nd-YAG pulsed lasers (Continuum Surelite II) running at 10 Hz with a 6 ns pulse width. Output power was approximately 120 mJ/pulse. The laser sheet illuminated the mixer through the side, as shown in Fig. 2. The horizontal line in Fig. 3 represents the laser sheet. The presence of a drain port blocked some of the laser sheet from reaching the lowest part of the mixing chamber. (This region is blanked out in grey in the plots.) A LaVision Imager Intense (1376×1040 pixels) was used to acquire image pairs for PIV measurements. Camera magnification was varied using a Sigma 28–100 mm Aspherical Hyperzoom Macro lens. Additional cropping was performed during data analysis to remove extraneous effects due to the septum, bottom plate, and bag edges. Note that in the subsequent plots, only every other vector in the vertical direction is plotted to improve readability.

Camera triggering was accomplished with a LaVision PTU synchronization board, LaVision DaVis software, and a custom-designed optical triggering setup. Images were recorded upon triggering of an optical sensor during upstroke just before the septum reached top dead center (see below). Shot-to-shot septum jitter was limited to between 1 and 4 mm. Between 30 and 75 image pairs were recorded for time averaging of the velocity fields. For the lowest five Re tests, the septum was located approximately 165 mm from the bottom plate when the image was recorded. For the highest three Re values, the septum was located approximately 145 mm from the bottom plate. To ensure statistical independence of the data, only one image pair was recorded per stroke. Time separation between each image in a pair was optimized to maximize in-plane displacement (reducing random error) while limiting out-of-plane displacement (reducing the number of bad vectors). Time separation values ranged from 1 ms for the highest Re case to 0.1 s for the lowest Re. Cross correlation was used to complete the analysis, with a grid size of 32×32 pixels, and an overlap of 50%.

Fluorescent particles (20–40 μm) were used as tracers for PIV measurements. A long-wave filter was used to block scattered laser light, while allowing fluorescence to pass through to the camera. Use of this filter improved overall signal quality and protected the camera sensor from stray laser reflections from the apparatus.

Mean and rms velocity, and strain rate were computed in the usual manner. Nondimensional rms velocity in the far field ($V^*_{RMS\text{-FF}}$) was computed by averaging the rms velocity in a rectangular region near the lower left corner of the velocity fields. The lower right corner could not be considered in this calculation due to shading of the laser sheet. Strain and jet penetration depth ($L\varepsilon_P$ and L_{JP}) were determined by noting the distance at which the fluid shear rate or velocity dropped to less than $0.5\varepsilon^*_{MAX}$ or $0.5V^*_{F\text{-MAX}}$. Penetration depths were measured using data obtained from the jet issuing from the central hole.

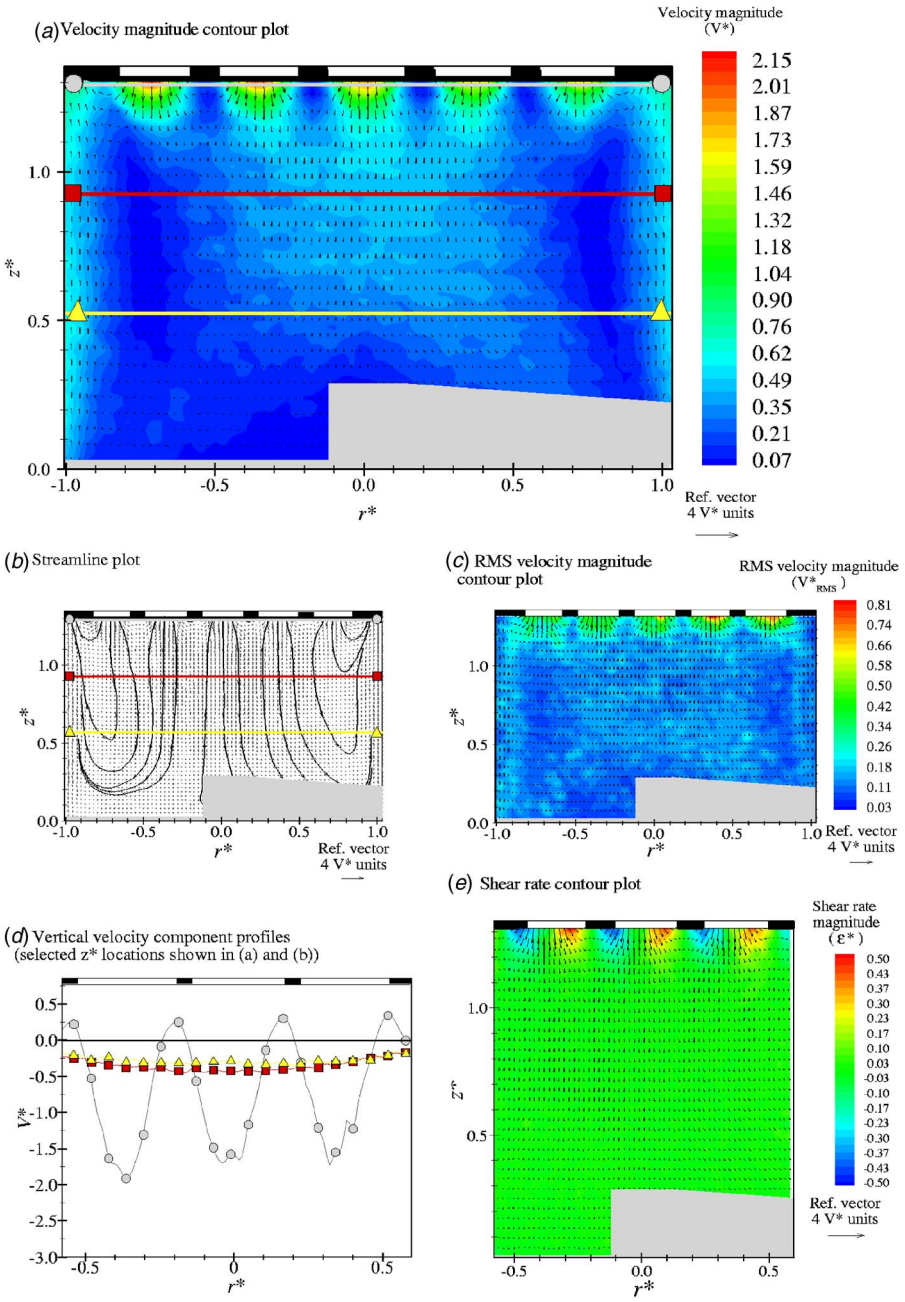

Fig. 4 Velocity magnitude, streamlines, rms velocity, vertical velocity profiles, and shear rate for Re=4

Experimental Uncertainty

Experimental uncertainty in the velocity measurements is primarily due to uncertainty in determining the location of the correlation peak to subpixel accuracy during PIV interrogation; the typically quoted value for this error is 0.1 pixel [13]. Typical peak pixel displacements at the jet centerline ranged from 4 to 8 pixels, resulting in a 1–3% velocity error at the centerline of each jet. To convert the data from pixel displacements to actual velocity values, a scale factor was used. The scale factor was accurate to within 2–3%. Table 1 contains summary data from all runs, and is accurate to about 10% of the stated value.

Additional sources of error include the aforementioned septum jitter, and the ability to line up the laser sheet with the center of each hole. These uncertainties would contribute small errors in jet width and velocity values. It is not expected that these uncertainties will significantly impact our findings.

Results and Discussion

Table 1 presents summary data for all Re values tested (boldface numbers represent the three cases that are plotted here). These three cases correspond to Re=4, 76, and 23,000. The lower two Re cases (Figs. 4 and 5) were conducted using aqueous NaCMC solutions as the working fluid, with an approximate viscosity of 50 cP. The high Re case presented in Fig. 6 was conducted using plain water. Five types of data are presented in each figure: (*a*) velocity fields; (*b*) streamline plots; (*c*) rms velocity

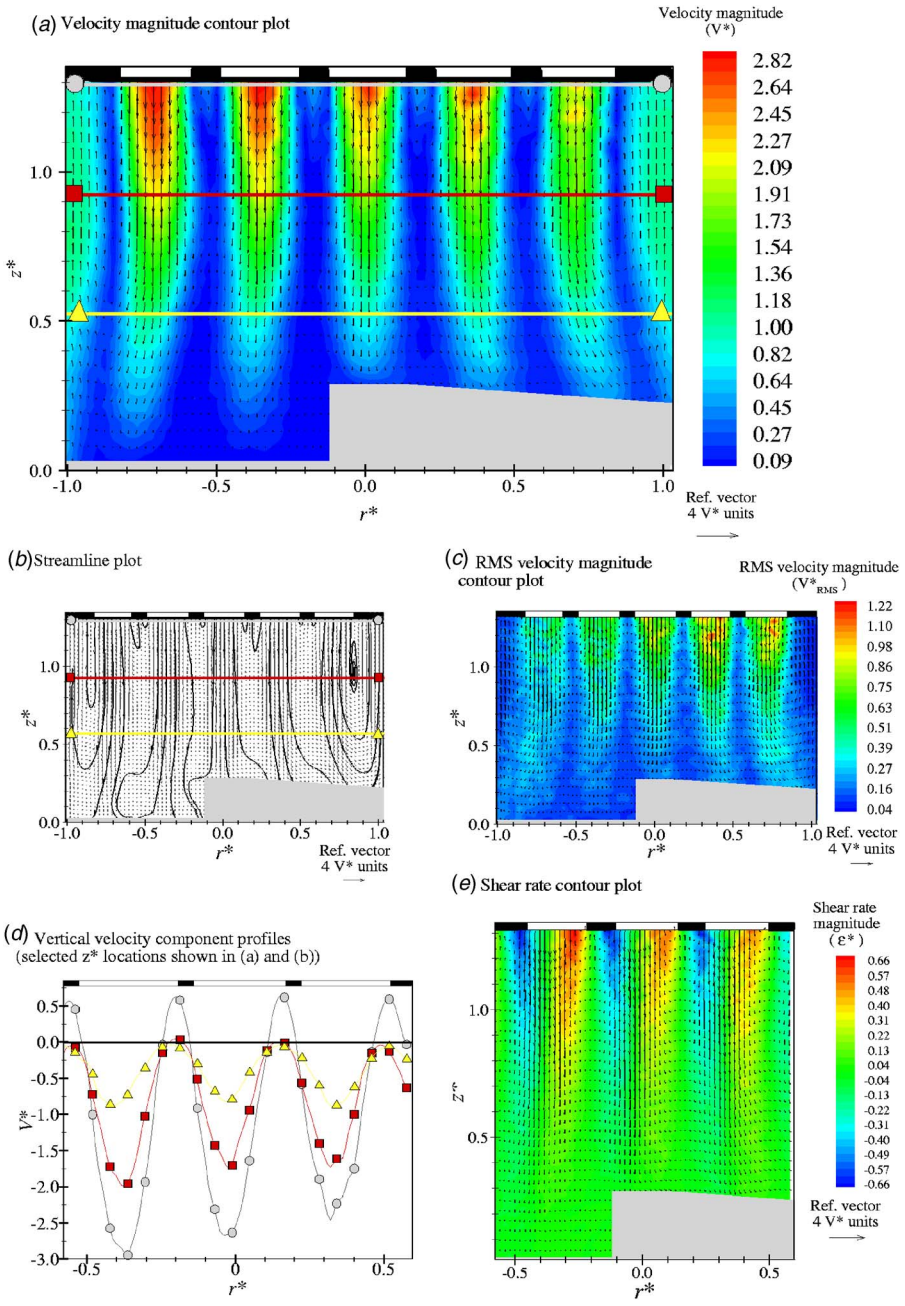

Fig. 5 Velocity magnitude, streamlines, rms velocity, vertical velocity profiles, and shear rate for Re=76

plots; (*d*) velocity profiles across the central three septum holes; and (*e*) shear rate contours. Figures 4–6 clearly illustrate the three flow regimes: creeping, laminar, and turbulent, respectively. The septum is located just above the upper edge of each plot. For convenience, a rough depiction of open and closed portions of the septum is provided at the top of each plot. The Re ranges presented here for the different flow regimes agree closely with those given by Komoda et al. [6] and to a lesser degree with those given by Idelchik [11]. It was also noted that, in general, peak velocity scaled well with septum speed, although there were important variations (discussed below). Shear rate values also scaled well with septum speed, although the high fluid viscosity cases (resulting in a lower Re) produced somewhat lower shear rate values as explained below. In all cases, the scaled shear values were less than unity, indicating that the measured shear was less than what would be predicted for laminar flow. This result can be explained by data smoothing and inadequate spatial resolution.

Creeping Flow: $4<\mathrm{Re}<15$. The creeping flow regime depicted in Fig. 4 is evidenced by several characteristics. As can be seen in Figs. 4(*a*) and 4(*e*) and as noted in Table 1, the jet penetration depth, measured by L^*_{JP} and $L^*_{\varepsilon_p}$ are very small. In the limit of true creeping flow, one would expect flow streamlines to be perfectly symmetric upstream and downstream of the septum. This would imply that the flow streamlines (see Fig. 4(*b*)) would converge rapidly as the fluid entered the septum hole, and diverge equally rapidly upon exiting the septum hole, leading to a rapid reduction of velocity away from the septum. The streamline plot depicted in Fig. 4(*b*), and the small velocity and strain penetration lengths shown in Figs. 4(*a*) and 4(*e*) suggest that the flow is indeed behaving in a manner that approaches creeping flow.

The vector field and vertical velocity profile plots (Figs. 4(*a*)

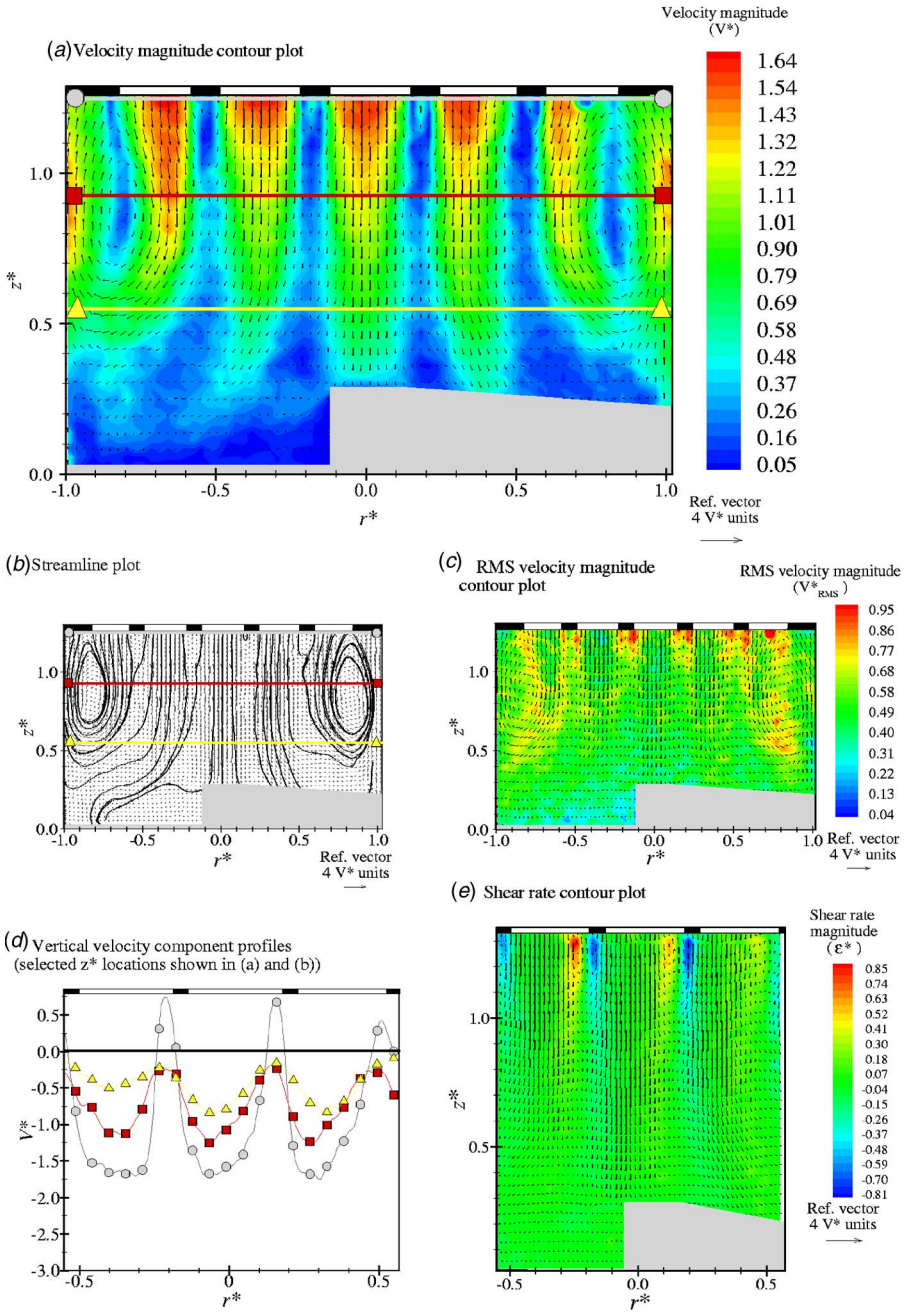

Fig. 6 Velocity magnitude, streamlines, rms velocity, vertical velocity profiles, and shear rate for Re=23,000

and 4(*d*)) indicate that the fluid emerging from the septum hole is surrounded by upward moving fluid. The upward movement is due to fluid being dragged upward by the closed portion of the septum. Additionally, a large volume of fluid was observed moving upward adjacent to the wall of the mixing chamber ($r^*=\pm 1$), as can be seen to some degree in Fig. 4(*a*). This is expected because the cylindrical wall of the mixing chamber is translating vertically during the upstroke and also because septum holes are absent at the septum circumference.

In the creeping flow case, ε^*_{MAX} should equal unity. However, strain rates depicted in Fig. 4(*e*) and in Table 1 were lower than expected for fully developed flow. It is suspected that lower than ideal spatial resolution, the presence of septum jitter, and the fact that the streamlines diverge rapidly downstream of the septum relaxing the velocity gradients will reduce the computed peak shear values. The low strain rates away from the septum (Fig. 4(*e*)) correlate with a lack of fluid movement in those regions, as can clearly be seen in Figs. 4(*a*) and 4(*d*).

Upon examination of $V^*_{F\text{-}MAX}$ and experimentally determined C values (a measure of fluid development, see Eq. (3*b*)) summarized in Table 1, one can see that the flow is indeed significantly developed ($C \approx 1.5$). Referring to well known correlations [12], the entrance length for our creeping flow cases should range from about 11 mm to 36 mm, all of which are less than the septum thickness. The reason C is not equal to 2.0 (the predicted value for fully developed laminar flow) in these cases lies in the rapid divergence of the streamlines away from the septum and a concomitant reduction in the maximum velocity. Due to experimental limitations, it was not possible to compute C based on velocity data

inside, or right at the edge of the septum.

Returning to Table 1, it is also apparent that, with the exception of the lowest Re case (Re=4) K is equal to or larger than unity as expected (see discussion following Eq. (2)). The discrepancy with Re=4 indicates that the average fluid velocity though the central hole is *less* than that predicted by mass conservation, and can be explained by asymmetric flow through the septum, which can be clearly seen in Fig. 4(*a*) by noting that the peak through-hole velocities are greater on the right side holes than the left. Asymmetry of the flow for this case may be due to bag folding. Additionally, shading effects are less pronounced in the true limit of creeping flow. Nonetheless, the deviation of K from unity is small.

A final characteristic of the creeping regime was the near absence of rms velocity away from the septum (Fig. 4(*c*)) and the low far-field strain values (Fig. 4(*e*)). Low $V^*_{\text{RMM-FF}}$ values are simply a consequence of the fact that the flow is highly repeatable in the creeping flow regime from cycle to cycle. High V^*_{RMS} values near the septum can be explained by the presence of septum jitter, which would result in local variations in the measured velocity near the septum. Were the septum jitter to be removed, it is expected that V^*_{RMS} near the septum would also be low.

Laminar Flow: Re=76. Between Re=15 and Re=76 several key changes take place. At Re=76, both the jet length L^*_{JP} and strain penetration length $L^*_{\varepsilon_p}$ (Figs. 5(*a*) and 5(*e*)) become significantly larger than that seen in the Re=4 results, as is also noted in Table 1. Additionally, the jets have significantly higher peak through-hole velocity ($V^*_{F\text{-MAX}}$=2.7), C, and $V^*_{F\text{-AVG}}$ (equal to K) values. In the Re=76 case, the entrance length for fully developed flow increases to roughly 160 mm, which would suggest that the flow should not be fully developed (resulting in $C<2$). As is noted in Table 1, C is nonetheless equal to 1.7, indicating significant development. Upon further examination of Figs. 5(*a*) and 5(*b*), one can see a lack of jet spread, strong upward fluid velocities directly adjacent to the downward jet, and a flow profile that is clearly parabolic. As was also seen in the creeping flow case, $\varepsilon^*_{\text{MAX}}$ remained lower than that predicted by laminar flow theory. The explanation for this is the same as that discussed in the creeping flow case.

Additionally, the value of $V^*_{F\text{-AVG}}$ (equal to K) reported in Table 1 clearly exceeds the expected value of unity. The explanation lies in the slight bulging of the lower bag, and folding of the flexible material that constitutes the walls of the upper bag. The former effect causes deviations from the ideal case wherein the mixing chamber is modeled as a cylinder that stretches axially while maintaining a constant diameter. Bulging of the lower bag during actual operation causes its cross-sectional area to increase and consequently, the amount of fluid required to pass through the septum holes also increases. Additionally, folding of the upper bag can shade the outermost ring of septum holes (for $r^* \rightarrow \pm 1$). Note that the outermost ring of holes contributes 63% of the total open area, therefore any shading effect there will significantly reduce the total open area and increase through-hole velocity further. During our experiments, uneven bag folding was observed on the right side, and is evidenced by reduced jet velocities on the right-hand side of each plot.

Although the V^*_{RMS} values near the septum increase significantly from the creeping flow case, $V^*_{\text{RMS-FF}}$ remains low. The high V^*_{RMS} near the septum can be explained by the septum jitter described in the experimental procedure section. It was also noted that most of the V^*_{RMS} comes from the vertical component. The horizontal rms component (not plotted here) remains very low throughout the view field.

Turbulent Flow: 460<Re<23,000. All four high Re cases revealed similar patterns for velocity, shear, jet penetration, and general flow behavior. PIV plots for Re=23,000 are shown in Fig. 6. Both strain and velocity (ε^*, $V^*_{F\text{-MAX}}$, and $V^*_{F\text{-AVG}}$) scale roughly linearly with increasing septum speed, as can be seen in Table 1. Additionally, L^*_{JP} and $L^*_{\varepsilon P}$ remained virtually constant throughout the entire regime, which is explained by Eq. (6) (penetration depth is not dependent on V_S). The transition from laminar to turbulent flow was clearly evidenced by a sharp increase in $V^*_{\text{RMS-FF}}$, which rose from negligible values to about 0.6, indicating significant fluid turbulence throughout the entire mixing volume. Additionally, the vertical velocity profile shows significant signs of blunting, as was expected for turbulent flow. This blunting can be seen by comparing Figs. 5(*b*) and 6(*b*), and by noting the lower C value (Table 1).

The flow showed evidence of development for the turbulent case, as can be seen in Figs. 6(*a*)–6(*d*), and by C values ranging from 1.3 for Re=460 down to 1.2 for the highest three Re (Table 1). As discussed previously, fully developed turbulent flow should yield a C value of about 1.23 [12]. The experimentally determined C values are somewhat high based on correlations for entrance length [12], which predict distances between 430 mm and 830 mm. We hypothesize that the high C values may be due to the interactions between adjacent jets in a jet array. We are conducting additional experiments to explore this issue. The impact of this anomaly is evidenced in lower than expected peak shear values, as discussed below.

Although the peak shear value $\varepsilon^*_{\text{MAX}}$ increased to between 0.7 and 0.9, it did not exceed unity as expected for turbulent flow. The reasons for this have been discussed earlier. The impacts of bag bulging and folding also evidenced themselves in the turbulent cases, as evidenced by higher than unity $V^*_{F\text{-AVG}}$ values shown in Table 1.

Comparison With Existing Mixing Technology

As discussed in the Introduction, there is a wide range of mixing tasks requiring different mixer characteristics. One key characteristic of a mixer is the ability to produce the desired shear rate values. Tatterson [14] provides several correlations for predicting shear rates in an impeller-driven mixer based on impeller speed, along with a plot relating shear levels to impeller speeds for various distances from the impeller for a particular test case. For the impeller-driven test case considered by Tatterson [14], a rotational speed of 100 rpm produces a shear rate of approximately 70 s^{-1} at the impeller tip. Increasing impeller speed to 400 rpm results in a shear rate of approximately 230 s^{-1}. However, as one moves away from the impeller, shear rates drop enormously. For example, at a distance of 2.5 mm from the impeller tip, the corresponding shear rates for 100 and 400 rpm are about 35 s^{-1} and 135 s^{-1}, respectively. High shear rates can either be desirable or detrimental depending on the mixing application. The results from cases presented in this paper show that the FCM can produce a wide range of shear rates from 0.7 s^{-1} to 111 s^{-1} (Table 1), although peak shear at the microscopic scale is likely higher. Ni et al.'s [1] shear rates for oscillatory baffled columns (0.7 s^{-1} for Re=251 and 21.4 s^{-1} for Re=4021) are in a similar range to ours. Even more extreme (low or high) shear rates can be attained in the FCM by changing the hole pattern, hole diameter, and percentage open area A_O. For example, a septum with a single large hole (comparable to the baffled column used by Ni et al. [1]) would increase A_O, and so reduce the peak fluid velocity and shear rate. In the case where high shear is desirable, decreasing A_O could produce tremendously higher fluid velocities, and proportionately higher shear rate levels. Importantly, it must be noted that the FCM produces high shear rates in an extended annular column downstream of *each* hole, implying that the high shear regions are more uniformly distributed throughout the mixing volume. In contrast, the impeller-driven mixer experiences high shear only in the immediate vicinity of the mixer. Likewise, for low shear mixing as well, the FCM ensures that the entire fluid volume is gently stirred due to the even distribution of septum holes and

the fact that the septum interacts with the full column of fluid during each oscillatory cycle.

Summary

A novel oscillatory flexible chamber mixer has been demonstrated in this study, and its flow characteristics have been investigated. The results presented here clearly demarcated three major flow regimes: creeping, laminar, and turbulent flow. For $4<\mathrm{Re}<15$, the flow exhibited creeping characteristics, with minimal flow activity away from the septum. This regime would be appropriate for continuous stirring at low shear levels, for example, in certain biological mixing applications. As the Reynolds number increased to Re=76, the flow became laminar and clear, strong jets issued from the septum plate, while the rms velocity away from the septum remained quite low. As the Reynolds number was increased beyond 460, the flow transitioned to turbulent, as evidenced by a marked increase in rms velocity throughout the mixing region. A model was also presented and verified relating the jet penetration length to septum speed for both laminar and turbulent regimes. Analysis of shear rates show the potential of the FCM to produce a wide range of shear values for different applications, and are comparable to shear rates produced by other designs [1,14]. The major difference between the current mixer and other impeller-driven mixers is that the entire fluid volume in the FCM is exposed to the desired shear level in contrast to the small region of high shear in the vicinity of the impeller in an impeller-driven mixer. Finally, recommendations for design refinement and customization for different mixing scenarios were presented.

Acknowledgment

This research was carried out with funding provided by ILC Dover LP.

Nomenclature

A_O = fractional open area of the perforated plate septum (-)
C = constant that accounts for flow development (-)
D_H = hole diameter (in the perforated septum) (mm)
D_S = septum diameter (mm)
K = constant that accounts for fluid velocity deviations from $V_{F\text{-NOM}/L}$ (-)
L_C = working chamber length (mm)
$L_{\varepsilon P}$ = strain penetration length (mm)
$L^*_{\varepsilon P}$ = nondimensionalized strain penetration length (-)
L_{JP} = jet penetration length (mm)
L^*_{JP} = nondimensionalized jet penetration length (-)
L_S = stroke length (mm)
N = number of holes in the septum (-)
Re = Reynolds number (-)
r = radial position (mm)
r^* = nondimensionalized radial position (-)
St = Strouhal number (-)
t = time (s)
V_F = fluid velocity (mm/s)
$V_{F\text{-AVG}/L}$ = average through-hole fluid velocity with respect to the lab frame L (mm/s)
V^*_{AVG} = nondimensionalized average through-hole velocity with respect to the lab frame L (-)
$V_{F\text{-AVG}/S}$ = average through-hole fluid velocity with respect to the septum S (mm/s)
$V_{F\text{-MAX}/L}$ = maximum through-hole fluid velocity with respect to the lab frame L (mm/s)
V^*_{MAX} = nondimensionalized maximum through-hole velocity with respect to the lab frame L (-)
$V_{F\text{-MAX}/S}$ = maximum through-hole fluid velocity with respect to the septum S (mm/s)
$V_{F\text{-NOM}/L}$ = nominal (predicted average) through-hole fluid velocity with respect to the lab frame L (mm/s)
$V_{F\text{-NOM}/S}$ = nominal (predicted average) through-hole fluid velocity with respect to the septum S (mm/s)
$V^*_{\mathrm{RMS\text{-}FF}}$ = non-dimensionalized far field rms velocity (-)
$V_{S/L}$ = velocity of the septum with respect to the lab frame L (mm/s)
V^* = nondimensionalized fluid velocity with respect to the lab frame (-)
z = vertical position (mm)
z^* = nondimensionalized vertical position (-)
ε = local shear rate (1/s)
ε^* = nondimensionalized shear (-)
$\varepsilon_{\mathrm{MAX\text{-}LAM}}$ = maximum laminar shear rate for laminar pipe flow (1/s)
$\varepsilon^{\mathrm{MAX}}_*$ = nondimensionalized maximum shear (-)
ν = kinematic viscosity (mm^2/s)
ω = oscillation frequency (1/s)

References

[1] Ni, X., Cosgrove, J. A., Arnott, A. D., Greated, A., and Cumming, R. H., 2000, "On the Measurement of Strain Rate in an Oscillatory Baffled Column Using Particle Image Velocimetry," Chem. Eng. Sci., **55**, pp. 3195–3208.
[2] Mackley, M. R., and Stonestreet, P., 1995, "Heat Transfer and Associated Energy Dissipation for Oscillatory Flow in Baffled Tubes," Chem. Eng. Sci., **50**, pp. 2211–2224.
[3] Ni, X., Mackley, M. R., Harvey, A. P., Stronestreet, P., Baird, M. H. I., and Rao, N. V. R., 2003, "Mixing Through Oscillations and Pulsations—A Guide to Achieving Process Enhancements in the Chemical and Process Industries," Chem. Eng. Sci., **81**(A), pp. 373–382.
[4] Dickens, A. W., Mackley, M. R., and Williams, H. R., 1989, "Experimental Residence Time Distribution Measurements for Unsteady Flow in Baffled Tubes," Chem. Eng. Sci., **44**, pp. 1471–1479.
[5] Brunold, C. R., Hunns, J. C. B., Mackley, M. R., and Thompson, J. W., 1989, "Experimental Observations on Flow Patterns and Energy Losses for Oscillatory Flow in Ducts Containing Sharp Edges," Chem. Eng. Sci., **44**, pp. 1227–1244.
[6] Komoda, Y., Inoue, Y., and Hirata, Y., 2001, "Characteristics of Laminar Flow Induced by Reciprocating Disk in Cylindrical Vessel," J. Chem. Eng. Jpn., **34**(7), pp. 919–928.
[7] Masiuk, S., 1996, "Heat Transfer Measurements in a Liquid Vessel That Is Mixed Using a Vibratory Agitator," Chem. Eng. J. and Biochem. Eng. J., **61**, pp. 107–112.
[8] Masiuk, S., 2001, "Dissolution of Solid Body in a Tubular Reactor with Reciprocating Plate Agitator," Chem. Eng. J., **83**, pp. 139–144.
[9] Masiuk, S., 2000, "Mixing Time for a Reciprocating Plate Agitator with Flapping Blades," Chem. Eng. J., **79**, pp. 23–30.
[10] Masiuk, S., 1999, "Power Consumption Measurements in a Liquid Vessel That Is Mixed Using a Vibratory Agitator," Chem. Eng. J., **75**, pp. 161–165.
[11] Idelchik, I. E., 1994, *Handbook of Hydraulic Resistance*, 3rd ed., CRC Press, Boca Raton, FL, Chap. 8, pp. 503–521.
[12] White, F. M., 1999, *Fluid Mechanics*, McGraw–Hill, Boston, Chap. 5, pp. 295–298.
[13] Prasad, A. K., 1999, "Particle Image Velocimetry," Curr. Sci., **79**, pp. 101–110.
[14] Tatterson, G. B., 1991, *Fluid Mixing and Gas Dispersion in Agitated Tanks*, McGraw–Hill, New York, Chap. 4, pp. 194–199.

A Functional Correlation for the Primary Breakup Processes of Liquid Sheets Emerging From Air-Assist Atomizers

V. Sivadas[1]
e-mail: vsdas@ntu.edu.sg

M. V. Heitor

Rui Fernandes

Laboratory of Thermofluids,
Combustion and Energy Systems,
Center for Innovation, Technology
and Policy Research, IN+,
Instituto Superior Técnico,
Technical University of Lisbon,
Avenue Rovisco Pais,
1049-001 Lisbon, Portugal

The study aims to highlight a general relationship between the characteristic variables of liquid sheet breakup and the principal forces of the flow domain. To accomplish this objective, an experimental investigation on air-assisted liquid sheets was carried out for a range of liquid-to-air velocities. The associated spray angle, breakup frequency, and breakup length were measured by exploiting high-speed imaging techniques. The results demonstrate that, when the stability variables are related to the liquid–air momentum flux ratio, a high correlation was attained for a range of flow conditions where capillary instability is insignificant. [DOI: 10.1115/1.2429701]

Keywords: liquid sheets, stability dynamics, shear waves, universal-correlation

1 Introduction

The demand for atomization arises due to the fact that most fuels employed in practical combustion systems are liquids, which must be atomized before being injected into the ignition zone. To efficiently meet this requirement, a high ratio of surface-to-mass liquid phase in the initial stages of injection is a prerequisite. One way to accomplish this is by utilizing thin liquid sheets of large aspect ratio, so that proper triggering of perturbations at the liquid sheet interface can promote rapid breakup of the fuel, and hence high turndown ratios for efficient combustion.

The liquid/air interface can be agitated in various ways, among which using the kinetic energy of the surrounding air stream in twin-fluid atomizers, as in air-assist or air-blast systems, offers enormous potential. The merits of these atomizers, such as minimum pollutant emissions due to enhanced mixing of air and fuel, have led to their installation in a wide variety of aircraft, marine, and industrial gas turbines. The two systems differ in terms of the quantity of air utilized and its respective velocity [1]. That is, air-assist atomizers are characterized by their use of relatively small amounts of very high velocity air. In contrast, the atomization quality of air-blast designs depends on the ratio of mass flow rates of air and liquid, with less reliance on velocity. Most systems use a prefilming technique, by which the fuel is spread out into a thin continuous sheet before being subjected to the atomizing action of the surrounding air.

Despite the enormous contribution of classical studies on interfacial instabilities [2–4] that dominate and control the primary breakup process of the liquid jet/sheet, the subject still poses new questions in the demanding practical domain. This is because in the modern era, atomizers need to satisfy the stringent requirements of a wide range of applications from pharmaceutical nebulizers to high-pressure combustion systems in rockets. Therefore, for specific applications, the design has to be carefully adjusted based on a better understanding of the fundamental processes of the initial breakup of liquid columns. Unfortunately, knowledge of twin-fluid atomization mechanisms is still incomplete owing to the complex interaction of various parameters, which include flow conditions inside the injector, turbulence level, and the interaction of liquid with the surrounding medium [5–7]. In other words, the dynamic state of the liquid and gaseous phase determines the departure from equilibrium, and the commencement of perturbations at the liquid sheet interface. Subsequently, the initial amplitude of disturbances and its growth rate may control the stability of the liquid column until the interface becomes unstable and breakup occurs.

The length of the continuous part of the liquid jet/sheet, denoted as the breakup length, is reckoned to be an indicator of stability of the liquid column. This has been the topic of many prior investigations; according to McCarthy and Molloy [8], the stability curve is given by the plot of the breakup length versus liquid velocity. The stability studies on liquid jets by Rayleigh [2] and later Weber [3] postulated that, as the perturbations propagate and grow along the liquid surface, breakup occurs at the wavelength of highest growth rate with the ensuing droplets having a diameter larger than the jet diameter. Even though the above analysis [2,3] did not take into account the influence of gravity and aerodynamic shear, their results are valid as long as laminar flow prevails in the liquid phase [9]. With increasing relative motion between the gas and the liquid, aerodynamic shear dominates, and the associated instabilities give rise to wind induced breakup that is characterized by droplets on the order of the jet diameter. Hence, the nondimensional Weber number based on the relative magnitude of inertial to surface tension forces distinguishes three principal breakup regimes: Rayleigh, wind induced, and atomization breakup [10,11].

The interaction of liquid with air results in oscillations at the interface, whose asymmetry increases with increasing velocity and turbulence of the air. In other words, a less stable sinusoidal mode dominates over dilation waves and the breakup is characterized by long thin ligaments and wide membranes, often referred to as "hook" shapes [12,13]. Theoretical analysis of liquid jet instability, specifically Kelvin–Helmholtz wave growth, is usually based on the notion that an initial disturbance propagates along the jet and increases in amplitude to a point of breakup and atomization, which is classified as convective or global instability [14]. Spatial instability analysis aims to predict the wavelength associated with the highest growth rate of perturbations in a given flow configuration. However, a further increase in the mean air velocity causes a sudden explosion of the liquid column, so that a

[1]Current address: Research Staff, Singapore Stanford Partnership, School of Civil & Environmental Engineering, Nanyang Technological University, 50 Nanyang Avenue, Singapore 639798, Republic of Singapore.

Contributed by the Fluids Engineering Division of ASME for publication in the JOURNAL OF FLUIDS ENGINEERING. Manuscript received September 21, 2004; final manuscript received August 29, 2006. Review conducted by Joseph Katz.

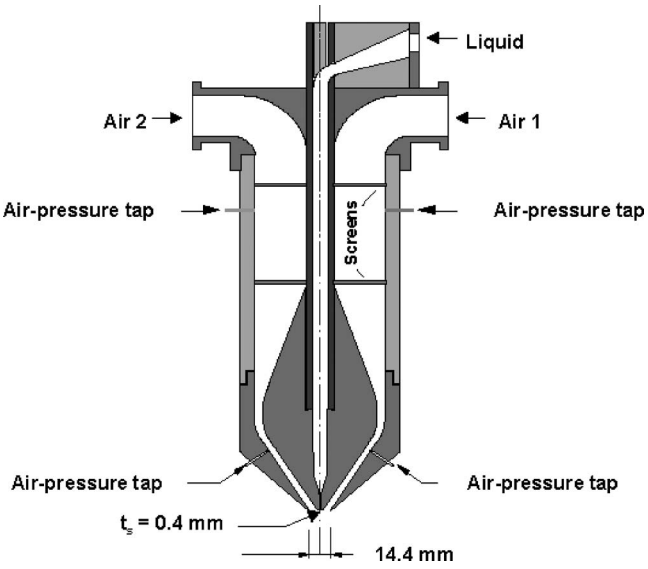

Fig. 1 Schematic diagram of liquid sheet generator

spectrum of structures will be generated in the breakup region. According to Huerre [15], this eruption can be attributed to the transition from convective to absolute instability; this is also substantiated by the studies of Li and Kelly [16]. The latter analysis proved that, as the surrounding air velocity increases, the variation in temporal growth rate is higher than the spatial growth rate. Liquid jets studies by O'Donnell et al. [17] show the likelihood of absolute instability for practically all Reynolds numbers. In addition to aerodynamic instability, for very low gas phase Weber numbers, which is less than the ratio of gas-to-liquid density, Li and Tankin [18] reported the existence of viscosity-enhanced instability for liquid sheets.

The above reviews provide an overview of possible scenarios of instabilities associated with liquid jets/sheets, and also highlight the notion that the primary breakup processes of the liquid will depend on the particular atomizer design. Therefore, a better understanding of the dominant forces that control the interacting flow field and its proper utilization may enable a universal relationship to be established for the stability of liquid columns, which may be useful in a wide range of flow configurations of practical importance. To accomplish this task, the present study focuses on the disintegration characteristics, such as breakup length, breakup frequency, and spray angle, of laminar liquid sheets under the influence of impinging airflows. The high Weber number ($\geqslant$0.4) flow domain is characterized by aerodynamic shear effects. This is the extension of an earlier work carried out by the first author [19] for low Weber number ($<$0.4), where gravitational effect dominates. The experimental investigation makes use of high-speed imaging techniques to delineate the flow features, for a range of air-to-liquid velocities, and for different air impingement angles.

2 Experimental Method and Measurement Techniques

Figure 1 shows a schematic layout of the atomizer. It comprises a two-dimensional unit to generate thin and flat liquid sheets of large aspect ratio, allowing adequate control and direct examination of the air–liquid interface. A pressurized supply of water eliminates fluctuations in the recirculating test liquid. The liquid emerges from a rectangular slit orifice of aspect ratio 200:1, with an exit thickness of 0.4 mm, and is "sandwiched" between two impinging air jets. The edge of the slit orifice is made sharp to prevent generation of flow disturbances and hence to ensure perfectly laminar conditions for the liquid sheet. In the present study, the liquid velocity varies from 0.7 m/s to 2.2 m/s; correspondingly the Reynolds numbers (Re_l) are 280 and 875, based on the film thickness. The range of test conditions is presented in Table 1. A calibrated rotameter continuously monitors the liquid flow rate. The atomizing air enters through the rectangular channels on either side of the liquid slot, and impinges on the liquid sheet at the nozzle outlet; convergence angles of 30 deg and 60 deg were utilized for the present investigation. The initial velocity of both air jets was kept identical with values varying from 10 m/s to 40 m/s, and the air-channel thickness at the exit port was 7 mm.

Table 1 Test conditions

α	We_a	U_l (m/s)	U_a (m/s)
60°	0.4 – 2.4	0.7 - 2.2	20
			25
			30
			35
			40
30°	1.5 – 7.5	0.7 - 2.2	20

Qualitative and quantitative analysis of the flow field was carried out by flow visualization techniques. The methodology applied in extracting the flow features will be given here, while the detailed description of the visualization setup is available elsewhere [20]. To enhance the image contrast, a white background illumination was utilized because of the transparent nature of the object plane. A high-speed digital charge coupled device (CCD) camera acquired images at an exposure time of 100 μs/frame. A temporal resolution of 100 μs was chosen based on the expected maximum frequency of the flow domain. In other words, the time scale is predetermined from the relation that connects the liquid sheet breakup length to the respective flow velocity. The relative velocity between the liquid and the surrounding air at the atomizer outlet gives the appropriate velocity scale; while the breakup length information is extracted from front-view images of the liquid sheet (see Fig. 2). That is, for the highest relative velocity of 39.3 m/s and the corresponding breakup length of 0.0055 m, the calculated frequency will be 7145 Hz. Therefore, the minimum time resolution (exposure time) required in the present investigation is about 140 μs. Hence the above resolution of 100 μs is sufficient to "freeze" the interfacial wave characteristics. The corresponding image acquisition rate was 2000 frames/ps, with a spatial resolution of 256$\times$120 pixels. Also, for qualitative analysis, a framing rate of 250 frames/ps was used, which boosted the image resolution to 512$\times$480 pixels. Throughout this study, recording was done with a 25 mm focal length lens.

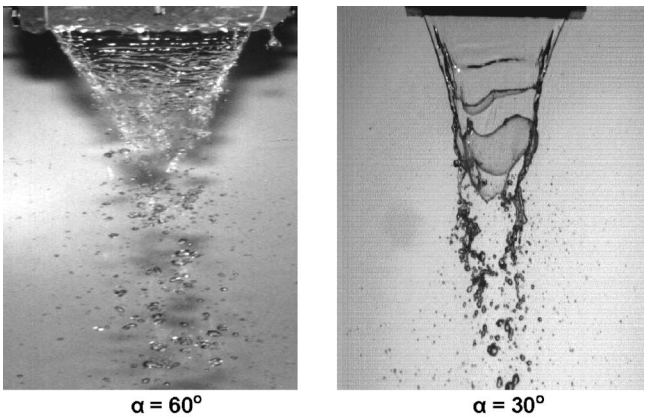

Fig. 2 Front-view images of liquid sheet for different impingement angles (Q_l=9.1 g/s)

The camera views the object plane normally, without distorting the image, in a way that allows the direct measurement of stability characteristics of the liquid sheet, such as the spatial growth of perturbations and the breakup length. The respective scale factor for the analysis was obtained interactively using the scale function: based on the known distance between two points in the object plane, the corresponding conversion factor was calculated. To acquire reliable data, the frame sampling was carried out in such a way that the procedure identifies the growth of large amplitude waves that attains the critical state of breakup. Thus, with reasonably low levels of measurement error, the associated spray angle, breakup length, and breakup frequency could be extracted from the image sequence. For high velocity conditions, the analysis utilized 7–8 frames in order to achieve a reasonably stable mean value.

The breakup length, L_b, is extracted from the front-view images of the liquid sheet (see Fig. 2), and is a measure of the axial distance from the nozzle outlet plane to the point where the central part of the sheet ceases to exist as a cohesive entity. Side-view images were utilized for the spray angle and breakup frequency measurements. The spray angle (θ) is defined by the angle between the locus of points of wave crests along the streamwise locations and the centerline of the injector. The distance between the liquid sheet centerline and the crest of the major disturbance gives the corresponding wave amplitude, and hence the peak value. The breakup frequency, f_b, is identified as the frequency at which bursting of the high-amplitude waves of the liquid sheet occurs, and is calculated based on the acquisition frame rate of the respective image sequence. That is, replay the recorded images until the identified high amplitude wave breaks down. The time associated with that particular frame can be extracted from the image acquisition rate and thus the breakup frequency. The maximum uncertainty for the averaged spray angle, breakup length, and breakup frequency are estimated to be ±19%, ±13% and ±17%, based on the repeatability of the measurements. In fact the ±19% uncertainty value corresponds to low relative velocity conditions for which fluctuations at the interface become minute, and is extremely difficult to delineate from the frames. This might have affected only the air velocity 20 m/s and liquid velocity greater than 1.6 m/s cases of the present investigation. The uncertainty corresponds to the variance of individual measurements from the averaged value. In other words, it is the standard deviation associated with individual data utilized to obtain the statistics of the requisite variables. The other source of uncertainty may be the enhanced activity at the liquid–air interface for high relative velocity conditions, which broadens the breakup frequency bandwidth as well as restricting the precise detection of boundaries from the image.

3 Results and Discussion

Figure 3 shows a qualitative overview of the liquid sheet breakup processes for air impingement angles (α) of 30 deg and 60 deg, respectively. The impingement angle is measured with respect to the major axis of the liquid sheet. That is, the surrounding air impinges on either side of the liquid sheet at an angle (α). The side-view images reveal that, with increasing α value, the radial dispersion of the liquid increases with relatively uniform droplet distribution downstream. This can be attributed to the increased physical interaction of the surrounding air with the liquid sheet, because of its larger angle of attack. Thus, effective energy transfer from the surrounding gas to the liquid column can sustain instability. In other words, large scale perturbation at the liquid–air interface can sufficiently overcome the initial liquid momentum and can instigate nonequilibrium conditions, which promote the rapid growth of disturbances until instability prevails at the liquid–air interface and breakup occurs.

Hence to achieve a universal correlation for the characteristic variables of instability, in differing flow configurations, necessitates the proper formulation of the initial momentum transfer occurring at the interface based on the relative magnitude of inertial-to-aerodynamic forces. This has been accomplished by considering Weber number classifications that correspond to the ratio of resultant liquid inertia-to-surface tension forces (We_l), and the ratio of aerodynamic shear-to-surface tension forces (We_a) independently [19]. Due to the inclined atomizing-air configuration, the normal air momentum can diminish the initial efflux of momentum of the liquid, while its tangential component supplements the aerodynamic shear at the interface. Consequently, We_l accounts for the resultant inertia force given by $\rho_l U_l^2 - \rho_a (U_a \sin\alpha)^2$, and the aerodynamic force associated with We_a becomes $\rho_a (U_a \cos\alpha - U_l)^2$. So, the ratio between We_l and We_a gives the nondimensional parameter of liquid-to-air momentum flux ratio, which is a measure of momentum transfer at the liquid–air interface. The effectiveness of the parameter We_l/We_a for attaining better correlation of the characteristic variables of liquid sheet disintegration is analyzed below.

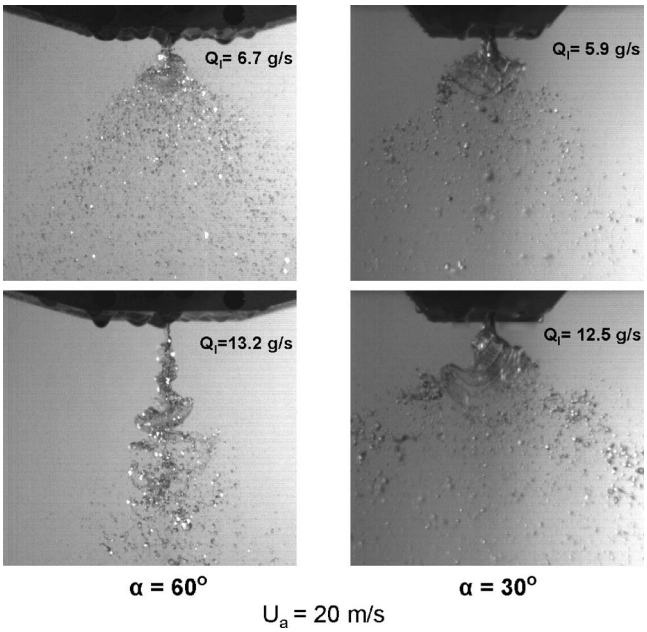

Fig. 3 Side-view images of liquid sheet disintegration for different impingement angles (Q_a=3 g/s)

Figure 4 shows the spray angle (θ) as a function of liquid velocity for a range of air velocities from 20 to 40 m/s. Since the criterion for measurement of the spray angle was to follow the crests of the major disturbances, the variable θ depends on the spatial growth of perturbations that ultimately leads to the liquid sheet breakup. In order to obtain the average spray angle, 4–8 images were utilized depending on the relative velocity between liquid sheet and surrounding air flow. The results exhibit an initial increase in spray angle followed by a decrease as the liquid velocity increases; also the spray angle follows distinct development with respect to air velocity. Independent evolution of spray angle for different air velocity conditions, and the initial increase in spray angle followed by a decrease as the liquid velocity increases, was also observed in the previous studies of Mansour and Chigier [21]. Now, the spray angle variation is analyzed by utilizing the parameter We_l/We_a (Fig. 5). This demonstrates that, unlike in Fig. 4, scatter of the data reduces and a functional relationship between spray angle and air velocities may exist. The initial rise in the spray angle, Fig. 5, can be attributed to the transition from adverse to favorable pressure at the injector outlet, as the liquid inertia increases. In other words, conditions are favorable to create deceleration of liquid sheet under low initial liquid veloci-

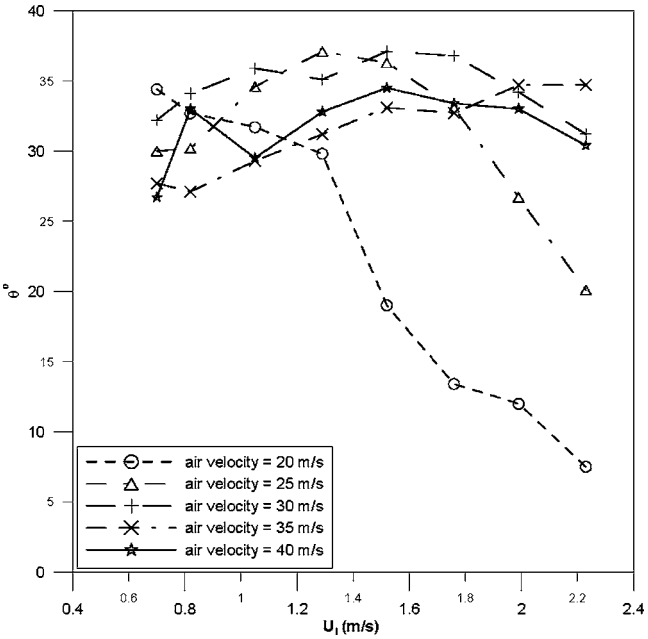

Fig. 4 Spray angle as a function of liquid and air velocities

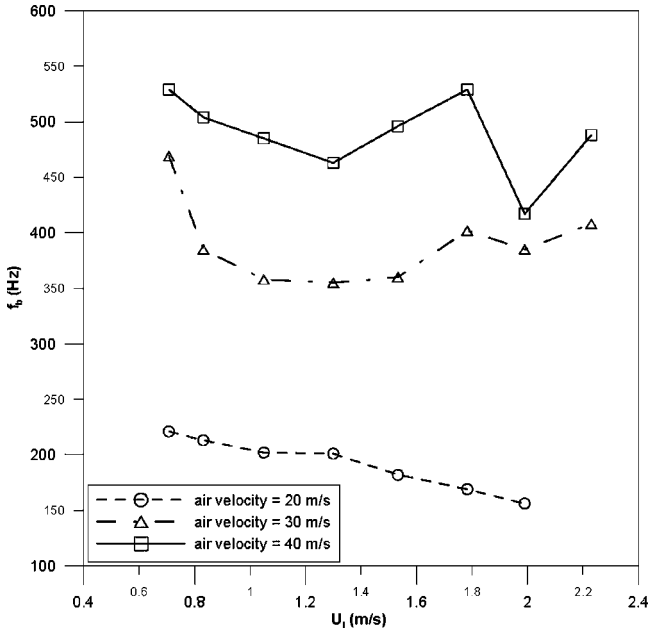

Fig. 6 Breakup frequency as a function of liquid and air velocities

ties. Because the normal air momentum acting on either side of the liquid sheet can effectively create a larger pressure at the atomizer outlet, this adverse condition in turn generates a backpressure at the exit port and the subsequent deceleration of liquid. However, with increasing liquid velocity, the surrounding air influence reduces and a changeover to positive or favorable pressure occurs; such changes in the initial flow conditions of the liquid sheet create perturbations of rapid growth rate. Consequently, the spray angle may increase in the transition zone. A further increase in liquid velocity reduces the relative velocity at the liquid–gas interface, which improves the stability of the liquid column, and so the spray angle starts to decrease monotonically.

In order to understand the intrinsic properties of instabilities associated with the preceding flow conditions, the breakup frequency (f_b) of the major disturbances is analyzed. Figure 6 depicts "f_b" as a function of liquid velocity for three different air velocities. The results demonstrate that individual functions exist for the respective air velocities, as well as appreciable escalation of breakup frequency with increasing air velocity. Now, following the same process of reasoning that achieved the correlation in spray angle, the nondimensional breakup frequency is plotted as a function of the parameter We_l/We_a (Fig. 7). f_b is nondimensionalized by the combination of initial liquid sheet thickness (t_s) and liquid velocity U_l. The liquid sheet thickness has been considered for nondimensionalization because the shorter side of the injector

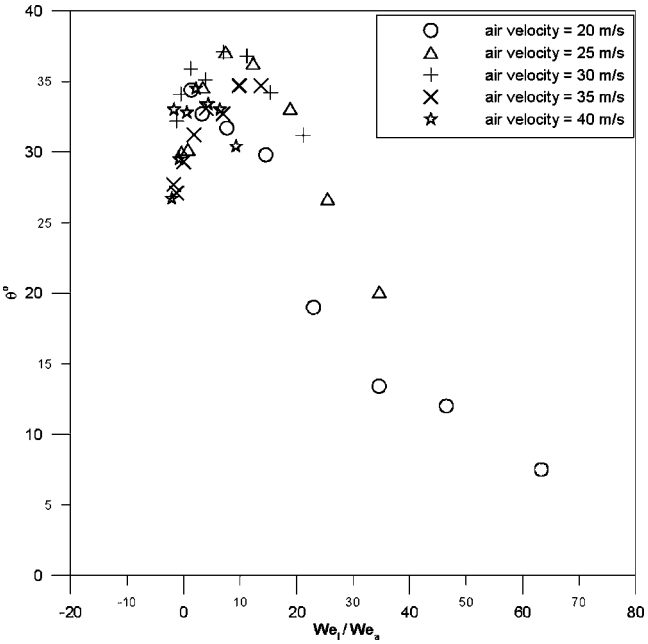

Fig. 5 Spray angle as a function of the ratio of inertial to aerodynamic forces

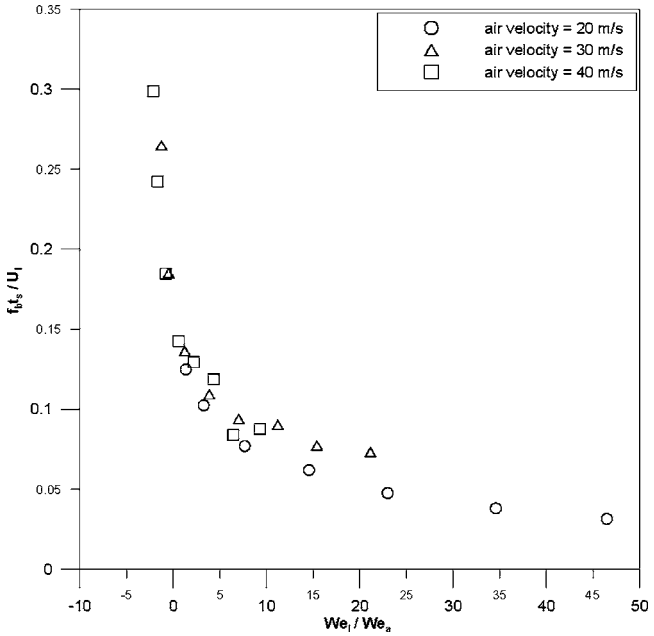

Fig. 7 Nondimensional breakup frequency as a function of the ratio of inertial to aerodynamic forces

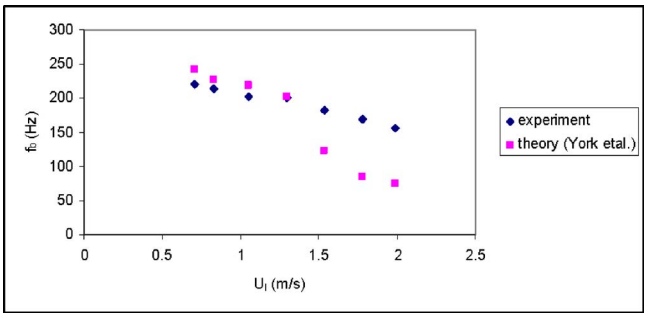

Fig. 8 Comparison of measured breakup frequency with theory (U_a=20 m/s)

limits the initial perturbation amplitude or energy. Figure 7 shows a better correlation of breakup frequency, with a single curve and less scatter of the data. It reveals that, for lower values of We_l/We_a, a drastic reduction in f_b occurs until the magnitude of liquid inertia force equals the aerodynamic shear force, and afterward the breakup frequency exhibits gradual variation. Analogous to the spray angle behavior, this trend might be expected due to the effect of pressure transition at the nozzle outlet that enhances instability and the associated breakup characteristics of the liquid sheet.

Figure 8 compares the present measurement of f_b with the preferred mode frequency determined from stability analysis [22]. The analysis considers an unstable interface with linear growth for the case of air velocity 20 m/s. The growth rate of the wave is extracted from spray angle measurements of the present study (see Fig. 4). The results indicate that as the relative velocity between liquid and surrounding gas decreases, perceptible deviation between theory and measurement can occur. In other words, under low Weber number flows, instability is controlled by surface tension and gravitational effects [19], so that application of the present stability analysis may not yield success for low velocities. It should be noted that for the present flow configuration both sides of the liquid sheet are subjected to the influence of impinging air jets, which is different from a liquid sheet influenced by parallel flowing air stream as investigated by York et al. [22]. Hence, the normal component of air momentum in the present flow domain enhances the breakup frequency which the theory may under estimate.

Citing the earlier work of McCarthy and Molloy [8] the breakup length, L_b, can be considered to be a measure of the stability of liquid column because it represents an integrated picture of perturbations that attains the critical state rapidly, and thus leads to the primary breakup processes of the liquid sheet. Figure 9 shows the liquid sheet breakup length (L_b) variation, for a range of air-to-liquid velocities. The results exhibit independent evolution of breakup length. However, when the L_b data are plotted with the parameter We_l/We_a (Fig. 10) a better collapse of data is achieved for the range of air velocities 20–40 m/s. L_b is nondimensionalized by the square root of the initial liquid sheet area. The sheet area was utilized for normalization because of the impinging air jet configuration of the present flow field. In other words, the normal component of air momentum on both sides of the liquid sheet can substantially influence the initial efflux momentum of the liquid. Hence, in spite of small liquid sheet thickness, the initial flow conditions at the outlet of the liquid sheet generator can be influenced by the surrounding air flow so that an initial perturbation may propagate over the entire cross-sectional area of the flow field, and its subsequent interaction in fact controls overall stability/breakup of the liquid column.

Careful examination of Fig. 10 reveals that the stability curve undergoes three stages of development. The initial region or zone *A* is characterized by a nonlinear trend, followed by a plateau (zone *B*), and thereafter the breakup length curve increases monotonically with We_l/We_a (zone *C*). Compatible with the preceding discussions on spray angle and breakup frequency, the nonlinear behavior in zone *A* can be attributed to the profound influence of pressure transition in the initial stages as the liquid velocity increases. The transition effect will continue until the magnitude of liquid inertia force equals the aerodynamic shear force, that is $We_l/We_a=1$ and then the flow field attains a dormant state, which is distinguished by a region of constant breakup length (zone *B*). Thereafter, due to the enhanced influence of liquid inertia, the breakup mode reaches stability, and hence L_b starts to increase linearly as depicted in zone *C*. It should be noted that the present correlation studies are valid for an aerodynamic shear dominated flow regime; that is, for We_a greater than or equal to 0.4. In other words, for $We_a<0.4$, the flow domain belongs to the Rayleigh

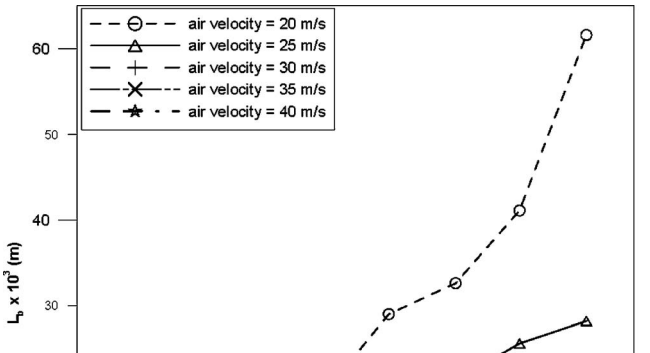

Fig. 9 Breakup length as a function of liquid and air velocities

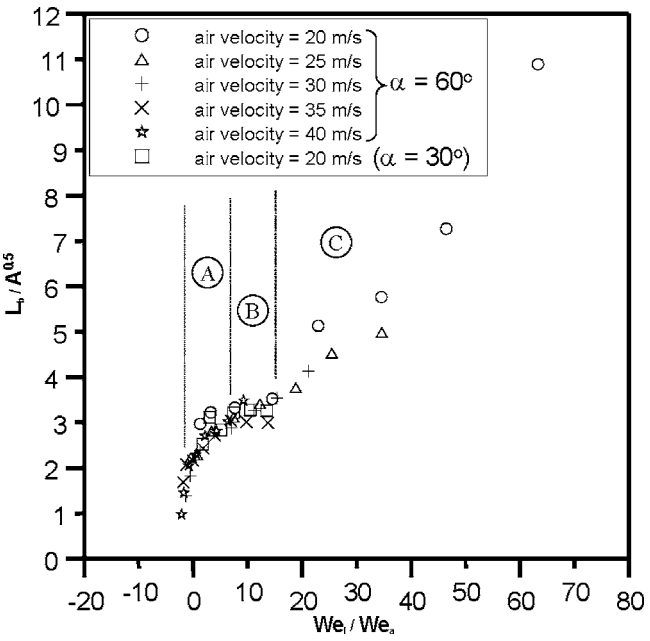

Fig. 10 Nondimensional breakup length as a function of the ratio of inertial to aerodynamic forces

regime where the perturbation growth and its breakup characteristics exhibit nonlinear behavior due to the supremacy of surface tension, as well as gravitational influence [11,19]. This may prevent the correlation of data for low Weber number flows.

4 Conclusions

The present studies on air-assisted liquid sheets for Weber numbers (We_a) above 0.4 reveal that the ratio of the primary forces of liquid inertia and aerodynamic shear can give rise to a high degree of correlation for the breakup variables. In other words, a universal relationship for stability parameters of the liquid column under different flow configurations is realized. This can be useful to predict the performance of practically relevant atomizers in the design stages, as well as a reliable source of primary breakup data that can generate the requisite input for the development of better analytical models of secondary atomization.

Acknowledgment

The authors acknowledge financial support from the Portuguese Science and Technology Foundation, Project No. 34586/99, and the EC funded project DIME, "Direct Injection Spray Engine Processes—Mechanisms to Improve Performance," DIME – ENK6-2000-00101. V. Sivadas is a post-doctoral research fellow at IST under the sponsorship of the Portuguese Science and Technology Foundation.

Nomenclature

A = area of the liquid sheet at the nozzle outlet
f_b = breakup frequency of the liquid sheet
L_b = breakup length of the liquid sheet
Q_a = air flow rate at the nozzle outlet
Q_l = liquid flow rate at the nozzle outlet
t_s = initial liquid sheet thickness
U_a = mean air velocity at the nozzle outlet
U_l = liquid velocity at the nozzle outlet
U_n = component of air velocity normal to the liquid sheet axis ($U_a \sin \alpha$)
U_r = relative velocity between air and liquid ($U_a \cos \alpha - U_l$)
We_a = Weber number based on aerodynamic shear ($\rho_a U_r^2 t_s / \sigma$)
We_l = Weber number based on liquid inertia [$(\rho_l U_l^2 - \rho_a U_n^2) t_s / \sigma$]
ρ_a = density of air
ρ_l = density of liquid
σ = surface tension of water at 20 °C
α = impingement angle of air with the liquid sheet
θ = spray angle

References

[1] Lefebvre, A. H., 1980, "Air-Blast Atomization," Prog. Energy Combust. Sci., **6**, pp. 233–261.
[2] Rayleigh, L., 1878, "On the Instability of Jets," Proc. London Math. Soc., **10**, pp. 4–13.
[3] Weber, C., 1931, "Disintegration of Liquid Jets," Z. Angew. Math. Mech., **11**, pp. 136–159.
[4] Taylor, G. I., 1963, "Generation of Ripples by Wind Blowing Over a Viscous Liquid," *The Scientific Papers of G.I. Taylor*, Cambridge University Press, Cambridge, UK, Vol. 3.
[5] Chigier, N., 1991, *Combustion Measurements*, Hemisphere, Washington, D.C.
[6] Lozano, A., and Barreras, F., 2001, "Experimental Study of the Gas Flow in an Air-Blasted Liquid Sheet," Exp. Fluids, **31**, pp. 367–376.
[7] Lozano, A., Barreras, F., Hauke, G., and Dopazo, C., 2001, "Longitudinal Instabilities in an Air-Blasted Liquid Sheet," J. Fluid Mech., **437**, pp. 143–173.
[8] McCarthy, M. J., and Molloy, N. A., 1974, "Review of Stability of Liquid Jets and the Influence of Nozzle Design," Chem. Eng. J., **7**, pp. 1–20.
[9] Lefebvre, A. H., 1989, *Atomization and Sprays*, Hemisphere, New York, pp. 201–267.
[10] Ranz, W. E., 1958, "Some Experiments on Orifice Sprays," Can. J. Chem. Eng., **36**, p. 175.
[11] Reitz, R. D., 1978, "Atomization and Other Break-up Regimes of a Liquid Jet," Ph.D. thesis, Princeton University, Princeton, NJ.
[12] Dombrowski, N., and Johns, W. R., 1963, "The Aerodynamic Instability and Disintegration of Viscous Liquid Sheets," Chem. Eng. Sci., **18**, pp. 203–214.
[13] Yang, H. Q., 1992, "Asymmetric Instability of a Liquid Jet," Phys. Fluids A, **4**, pp. 681–689.
[14] Weihs, D., 1978, "Stability of Thin, Radially Moving Liquid Sheets," J. Fluid Mech., **87**, pp. 289–298.
[15] Huerre, P., 1990, "Local and Global Instabilities in Spatially Developing Flows," Annu. Rev. Fluid Mech., **22**, pp. 473–537.
[16] Li, H. S., and Kelly, R. E., 1992, "The Instability of a Liquid Jet in a Compressible Air-stream," Phys. Fluids A, **4**, pp. 2162–2168.
[17] O'Donnell, B., Chen, J. N., and Lin, S. P., 2001, "Transition from Convective to Absolute Instability in a Liquid Jet," Phys. Fluids, **13**, pp. 2732–2734.
[18] Li, X., and Tankin, R. S., 1991, "On the Temporal Instability of a 2-D Viscous Liquid Sheet," J. Fluid Mech., **226**, pp. 425–443.
[19] Sivadas, V., and Moreira, A. L. N., 2006, "Surface Waves on Liquid Sheets Emerging from Air-Assist Atomizers," *Proceedings ICLASS-06*, Kyoto, Japan, Aug. 27 – Sept. 1, Paper ID-269.
[20] Santos, D., 1998, "Liquid Film Disintegration," M.Sc thesis, Technical University of Lisbon, Lisbon, Portugal (in Portuguese).
[21] Mansour, A., and Chigier, N., 1991, "Dynamic Behavior of Liquid Sheets," Phys. Fluids A, **3**, pp. 2971–2980.
[22] York, J. L., Stubbs, H. E., and Tek, M. R., 1953, "The Mechanism of Disintegration of Liquid Sheets," Trans. ASME, pp. 1279–1286.

Concentration Field Measurements Within Isolated Turbulent Puffs

E. Ghaem-Maghami
Graduate Student

H. Johari[1]
Professor
e-mail: hjohari@csun.edu

Mechanical Engineering Department,
Worcester Polytechnic Institute,
Worcester, MA 01609

The structure of passive scalar concentration field within isolated turbulent puffs was measured using the planar laser Mie scattering technique. Puffs were generated by injecting seeded air through a 5-mm-diameter nozzle into a chamber with a weak air co-flow. The injection time and volume was varied by the use of a fast-response solenoid valve. Puffs were examined in the range of 25–55 diameters downstream of the nozzle. The Reynolds number based on the average velocity and nozzle diameter was 5000. The results indicate that as the injection volume increases, puffs evolve from a spherical geometry to that with a tail. The half-width of radial concentration profiles through the puff center decrease as the injection volume increases. On the other hand, the puff length in the axial direction increases with the injection volume. The volume of ambient fluid entrained by the puff, and normalized by the injected volume, decreases with increasing injection volume. [DOI: 10.1115/1.2409348]

Introduction

Although entrainment and mixing in steady, reacting, and nonreacting jet flows has been investigated extensively in the past, little is known about mixing in unsteady or pulsatile jet flows. The latter are invariably involved in various flow control strategies being pursued currently. Moreover, pulsed combustion appears to have the potential to provide for rapid fuel/air mixing, compact and economical combustors, and reduced exhaust emissions [1]. Pulsed nonreacting incompressible jets have shown increased entrainment both in the near field and far field [2–4]. Fully modulated jets appear to have significantly increased entrainment even in the far field [3]. Work in our laboratory on reacting, fully modulated (pulsed) jets has indicated significantly reduced flame lengths when the injection times are short and a relatively long time exists between the subsequent pulses [5,6]. Under these conditions, the jet consists of a sequence of distinct, noninteracting turbulent puffs. These puffs react and burn rapidly, in comparison with the steady jet. It has been argued that the greater entrainment of turbulent puffs is responsible for the observed shorter flame lengths [5,6]. A puff may entrain ambient air over a relatively larger surface area as compared to a steady jet with lateral entrainment. Thus, the present investigation examined the passive scalar concentration field within isolated turbulent puffs. Literature on isolated turbulent puffs is reviewed below.

A puff refers to a distinct mass of turbulent fluid moving unsteadily through its surrounding and with which the puff mixes readily [7–9]. The puff structure has been considered similar to a turbulent vortex ring with the vorticity spread throughout the puff volume [10]. In fact, the scaling laws listed below for the width, penetration, and celerity of puffs are identical to those for turbulent vortex rings in the self-similar regime, except for the proportionality constants [7,8,10]

$$\delta \sim (x - x_0) \tag{1}$$

$$(x - x_0) \sim \left(\frac{I}{\rho}\right)^{1/4} (t - t_0)^{1/4} \tag{2}$$

$$\frac{dx}{dt} \sim \left(\frac{I}{\rho}\right)^{1/4} (t - t_0)^{-3/4} \sim \frac{I}{\rho}(x - x_0)^{-3} \tag{3}$$

The virtual origins in space and time, x_0 and t_0, depend on the apparatus generating the puff or vortex ring. The puff width increases linearly with the distance from the virtual origin (Eq. (1)), and the puff celerity decreases rapidly with the axial distance from the virtual origin (Eq. (3)). Note that the specific impulse, I/ρ, does not influence the puff width scaling law in Eq. (1). For compact puffs with nearly spherical geometry, the volume in the far field is expected to scale with the cube of puff width. Sangras et al. [11] measured the penetration and width of turbulent puffs in an aqueous media using video records of the puff visual outline at Reynolds numbers of 3000–12,000. It was found that the penetration and width of puffs follow the self-similar scaling for distances greater than 20–30 source diameters [11,12]. The proportionality constants in the puff scaling laws were also reported in Refs. [11,12]. Moreover, a virtual origin of 8.5 source diameters downstream of the nozzle was measured, independent of the injected volume and Reynolds number for the range of parameters in those experiments.

One method of generating puffs is to impulsively inject the source fluid through a nozzle. This technique creates a vortex ring if the stroke ratio, H/d, is small, say of order one. As the stroke ratio increases, the injected fluid rolls up into a compact puff. In the limit of very large stroke ratios, a starting jet is created. Past work has shown that the volume of an isolated puff increases with the axial distance to the third power, because the puff width increases linearly in the far field [13]. Volumetric arguments have been used to show that the bulk entrainment and mixing rates scale with the cube root of the injected volume [5]. To arrive at a nondimensional parameter capable of characterizing turbulent puffs with various initial conditions, the cube root of the injected volume was normalized with the nozzle diameter and was renamed the injection parameter P in Eq. (4). This parameter may be written in terms of the average injection velocity U_j and time τ as follows

$$P \equiv (4V_0/\pi d^3)^{1/3} = (U_j \tau/d)^{1/3} = (H/d)^{1/3} \tag{4}$$

Note that P is also the cube root of the stroke ratio. The parameter P has also been used to classify whether pulsed fuel injection results in compact burning puffs or elongated flame structures [6]. Puffs with low and high P values are shown schematically in Fig. 1: a compact puff with no tail signifying the low P case in Fig.

[1]Corresponding author.

Contributed by the Fluids Engineering Division of ASME for publication in the JOURNAL OF FLUIDS ENGINEERING. Manuscript received August 17, 2005; final manuscript received July 6, 2006. Assoc. Editor: Phillip M. Ligrani.

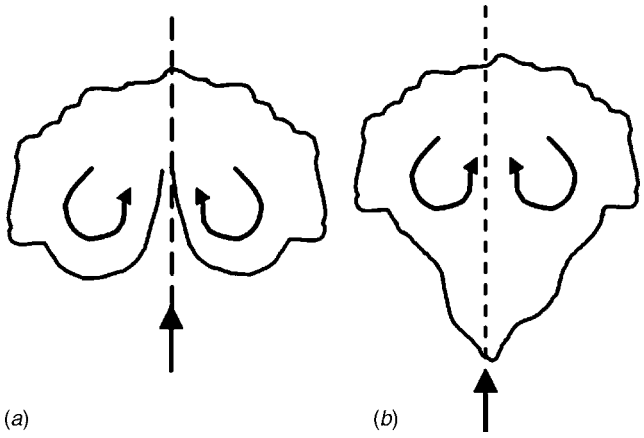

Fig. 1 Schematic of isolated turbulent puffs: (*a*) short injection time; and (*b*) long injection time. An elongated puff with a tail in (*b*) is distinguished from a compact puff in (*a*).

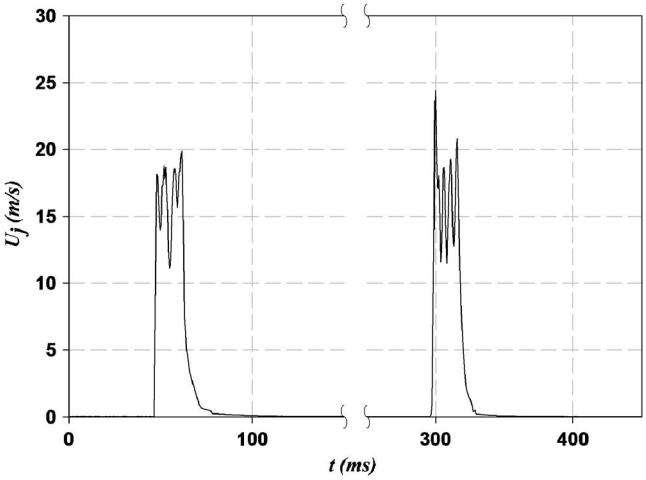

Fig. 3 Time trace of jet velocity for an injection time of 23 ms corresponding to $P=4$

1(*a*) and an elongated puff with a tail in Fig. 1(*b*).

The primary objective of the current study was to measure the passive scalar concentration field associated with the far field of isolated, nonreacting, turbulent puffs. The focus of this paper is on the effects of injection volume and P on the puff structure, entrained volume, and mixing efficiency. Moreover, the question of whether the distribution of a passive scalar within turbulent puffs resembles the same in turbulent vortex rings with $P \approx 1$ is addressed. Specifically, noninteracting puffs with $P \leq 8$ at a Reynolds number of 5000 and in the x/d range of 25–55 were studied.

Experimental Technique

The experimental apparatus consisted of a chamber with a square cross section of 30×30 cm^2, shown schematically in Fig. 2. Three sides of the chamber were made from glass to allow easy optical access. The injector consisted of a 5 mm i.d. stainless steel tube with a length of $40d$ upstream of the solenoid valve. The exit of the injector was in the center of the chamber, flush with the last flow straightening (honeycomb) element (see Fig. 2). A weak co-flow, with a mean velocity corresponding to 0.5% of the jet velocity, ventilated the chamber. The co-flow was used to reduce the confinement effects of the chamber walls on the puff development. The co-flow was sufficient to satisfy the entrainment requirement of a turbulent jet over the axial extent of interest, see Appendix B in Ref. [14]. Away from the intermediate vicinity of the nozzle, the co-flow was uniform. The jet and co-flow were at room temperature and the pressure in the chamber was atmospheric.

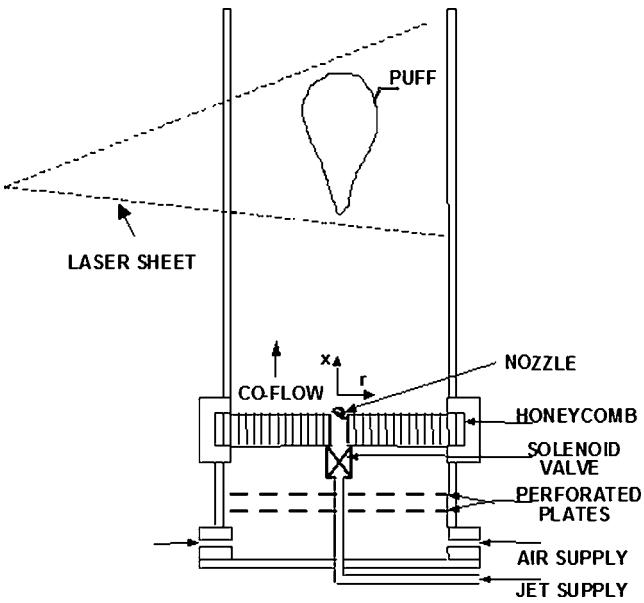

Fig. 2 Flow chamber schematic

The jet flow was controlled by the fast-response (approximately 500 μs) solenoid valve, actuated in an "on–off" (square wave) fashion by a control unit. A certain amount of velocity fluctuation was observed during each injection. To characterize the injection system, the jet velocity was measured by a hot-wire anemometer placed just downstream of the injector. A sample time trace of the injection velocity is shown in Fig. 3 for an injection time of 23 ms, corresponding to a $P=4$. Note that there is at least 230 ms between subsequent injections for the case depicted in Fig. 3. For all cases considered, the jet off time was at least ten times the injection time with the smallest off time shown in Fig. 3. The long off time ensured that each injection resulted in an isolated puff further downstream.

To define a precise value of injection time τ, the length of the time when the velocity was greater than 5% of the peak velocity was measured for each injection and averaged over the entire sample. Once the injection time was quantified in this way for each injection condition, the average jet velocity during the injection was computed and used for the calculation of the mean injected volume and P. The nominal values of injection time, based on the square-wave signal driving the solenoid valve, and the resulting nominal values of P are compared against the actual measured values in Table 1 for the range of parameters examined. The difference is primarily due to the hydraulic response of the injector, producing slight changes in the injection time and P.

The averaged jet velocity during injection was nearly constant for the cases listed in Table 1, and the Reynolds number based on this velocity and the injection tube diameter was 5000. Table 1 also provides the impulse for each puff and the specific impulse

Table 1 Puff injection characteristics

$\tau_{nominal}$ (ms)	$P_{nominal}$	τ_{actual} (ms)	P_{actual}	I (N s)	$I/(\rho U_j d^3)$
20	4	23	4.17	1.40E−04	57.1
39	5	38	4.95	2.30E−04	95.4
68	6	69	6.03	4.10E−04	172.6
161	8	170	8.13	1.01E−03	423.3

normalized by the jet velocity and diameter. The impulse increases by a factor of 8 as P goes from 4 to 8. It is possible to keep the impulse of the various puffs constant by reducing the injection velocity as P increases. However, the Reynolds number would be decreased to a value of about 675 if the impulse for all puffs were held at the same value as $P=4$. Thus, it was decided to retain the Reynolds number constant for all cases. It is worth noting that the impulse does not directly affect the puff spreading rate in Eq. (1).

The injected flow was seeded with ethylene glycol-based droplets produced by a fog generator. The generated droplets were mixed with the jet stream approximately $100d$ upstream of the injector. This ensured that the droplets were homogenously mixed at the injector exit. The droplets had an estimated diameter of 1 μm, and resulted in Mie scattering. To visualize the flow, the output from an argon ion laser was formed into a thin light sheet that illuminated the seeded flow. The elastic scattering from the droplets within the light sheet was imaged by a progressive scanning charge coupled device (CCD) camera with a 640 $\times$480-pixel resolution. The images were acquired by a frame grabber board at 60 frames/s. The images were then averaged and interrogated with image processing software. The images were corrected for background nonuniformity prior to averaging. The radial extent of the imaged area was $40d$ and the images covered the range of $25-55d$ in the axial direction. Puffs centered within this field of view should have achieved self-similarity according to Sangras et al. [11].

The in-plane resolution for this field of view was about 300 μm, and the out-of-plane resolution was dictated by the laser sheet thickness of $\approx$1.5 mm. These values are comparable to the estimated Kolmogorov length scale of $\sim$1 mm in the imaged area. The passive scalar distribution in the averaged images was examined as a function of the injection parameter P. Radial and axial concentration profiles through the maximum concentration location were extracted and compared among various flow conditions. The estimated average uncertainty of the concentration measurements is ±3%, based on the pixel count uncertainty, as well as the uncertainty of puff position and optical alignment. The average standard error of the mean concentration is about 1.4%.

Results

Puff Structure. Instantaneous images of $P=4$, 5, 6, and 8 puffs are shown in Fig. 4, with the background removed. For the lowest P, the puff appears similar to a buoyant thermal, with little or no fluid left behind in the wake. As the injection volume and P increase, the volume of seeded fluid in the wake of the puff increases. Closer inspection of the image sequences revealed a toroidal vortex-like structure within the puff head for the lower P cases in Figs. 4(a) and 4(b). For the case of $P=6$ and 8, the vortex structure was not discernible. Instead, the leading structure had an arrowhead shape. The "tail" region could be clearly distinguished from the leading structure. Arrows have been inserted in the images where the tail region connects with the leading structure. Except for the $P=4$ puff, the concentration is nearly uniform within the leading structure. It is noteworthy that none of the puff images reveal a structure similar to that seen in turbulent vortex rings, see Fig. 34 in Ref. [10]. Although the presence of a tail region is common among puffs and turbulent vortex rings, the vortex ring cores contain high concentrations when compared to the fluid moving with the core. For the puffs, no evidence of large concentrated regions within the seeded flow was observed.

The puffs evolve from a spherical geometry to an arrowhead shape with an attached tail as the injection volume increases. For the $P=4$ puffs, compact, spheroid structures without a tail were always observed. For puffs with $P\geqslant 5$, injected fluid was present in a tail region of varying size. The width of the tail was always smaller than the puff diameter. The axial extent of the tail increased for puffs with larger P. The other noteworthy feature in the images of Fig. 4 is the lower intensity for the $P=4$ puff as compared to the other puffs. This indicates an overall reduction in the dilution and mixing for the higher P cases at similar axial locations.

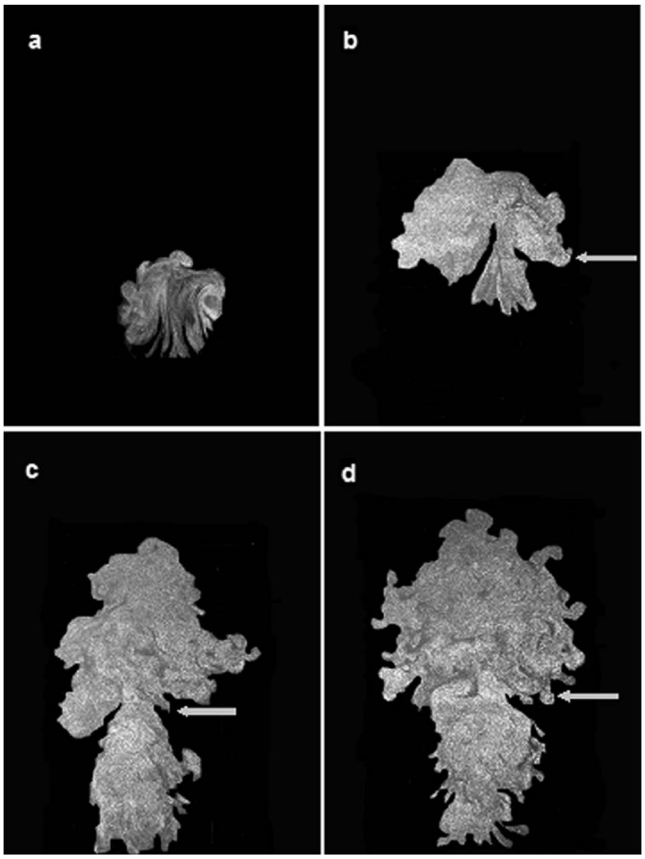

Fig. 4 Sample instantaneous images of individual puffs: (*a*) *P*=4; (*b*) *P*=5; (*c*) *P*=6; and (*d*) *P*=8. The arrows indicate the approximate location where the tail can be differentiated from the leading structure.

The passive scalar concentration field was computed from the averaged images and was normalized by the peak value in the puff center. Contours of the average concentration are shown in Fig. 5 for puffs with $P=4$ and 6. The nearly circular contours in Fig. 5(a), when contrasted against the instantaneous image in Fig. 4(a), are a result of the averaging process. The higher concentration contours are nearly circular for the $P=4$ case when compared to the same for the $P=6$ case. These contour plots clearly indicate that puffs elongate and become narrower as the injection volume and P increase. The average scalar field for the $P=8$ puff resembles that of $P=6$ in Fig. 5(b), whereas the $P=5$ puff is inbetween the $P=4$ and $P=6$ cases.

Radial Profiles. To quantify the radial extent of puffs and to contrast it against that of other turbulent jet flows, the radial concentration profile corresponding to the location of peak concentration within the puff was extracted from the averaged fields. The radial concentration profile through the puff center for $P=4$ and 6, corresponding to the contours in Fig. 5, is shown in Fig. 6. Gaussian curves fitted to the data are also shown in Fig. 6. Although the profiles for $P=4$ and 6 puffs exhibit some degree of asymmetry, the $P=6$ profile appears to be closer to the Gaussian fit than the $P=4$ puff. For the cases examined here, the Gaussian curves become a better fit as the injection volume and P increase.

The puff half-width, $\delta_{0.5}$, was defined as the radial extent where the concentration is one-half of the maximum value at the puff center, i.e., full width at halfheight in Fig. 6. The puff full width,

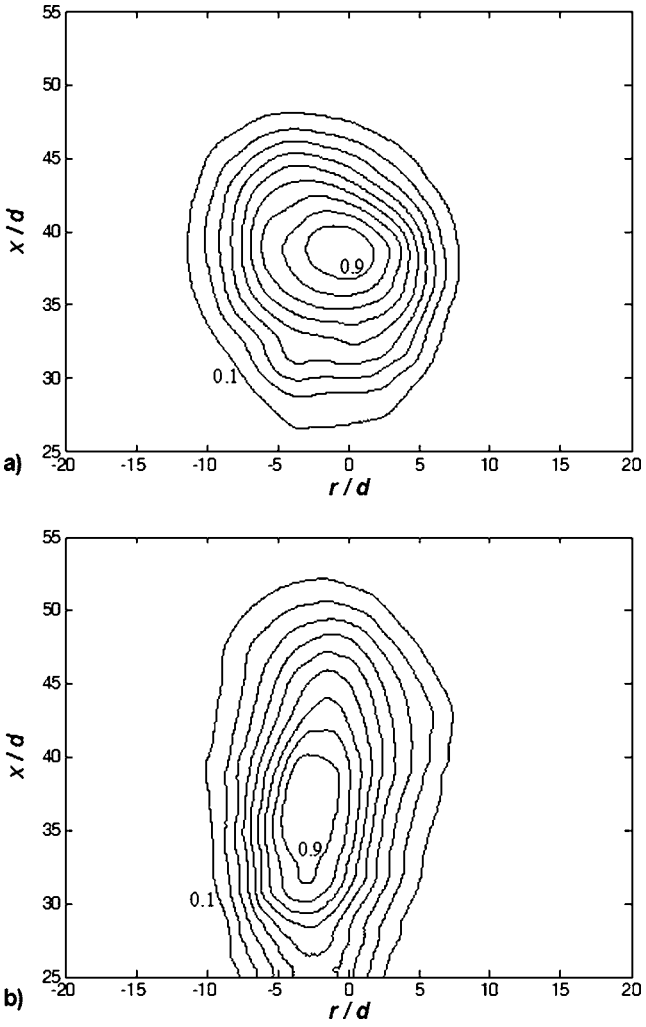

Fig. 5 Average passive scalar concentration field, normalized by the peak value, for isolated puffs: (*a*) *P*=4; and (*b*) *P*=6. The maximum contour has a relative concentration of 0.9 and the adjacent contours are spaced by 0.1.

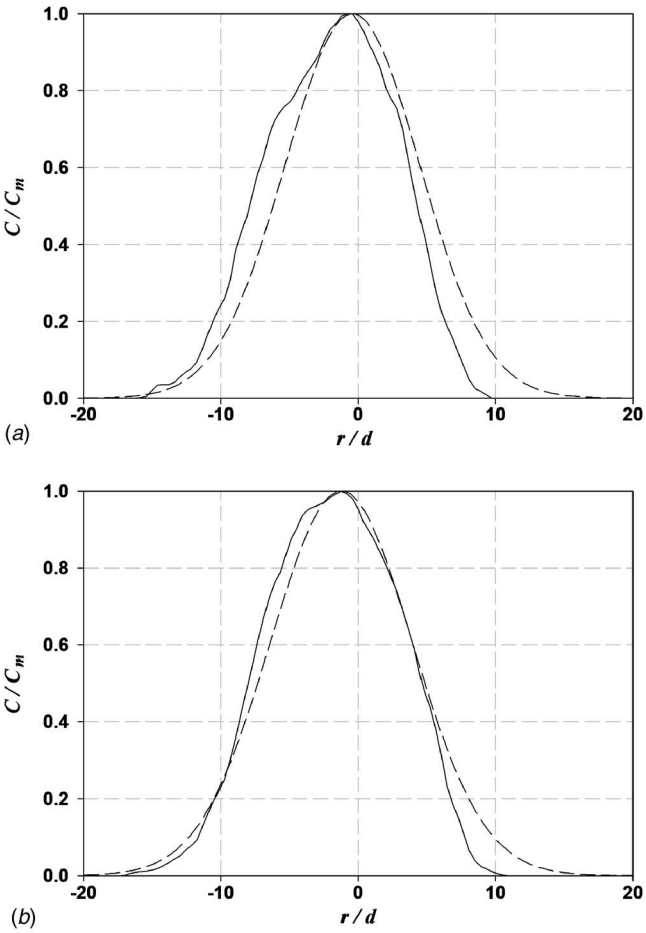

Fig. 6 Radial concentration profiles (solid line) through puff center: (*a*) *P*=4; and (*b*) *P*=6. Dashed curves represent Gaussian curve fits to the data.

$\delta_{0.1}$, was defined as the radial extent where the concentration is reduced to one-tenth of the maximum value at the puff center. The puff half and full widths normalized by the nozzle diameter, $\delta_{0.5}/d$ and $\delta_{0.1}/d$, are shown in Fig. 7. Both measures of puff width decrease with increasing P and injection volume. The decrease in the half-width is particularly noticeable for the half-width data in Fig. 7(*a*).

To compare the puff widths with that of a steady jet produced by the same apparatus and at the same Reynolds number, a set of experiments were performed where the flow was maintained for a sufficiently long time to establish a steady jet. The steady jet widths at the same axial location as the puff center are comparable to the $P=8$ puff width. On the other hand, the width of the $P=4$ puff is comparable to that of a buoyant puff (i.e., thermal) [13]. Thus, as P increases from 4 to 8, the puff width decreases from a value associated with buoyant thermals to a value close to the steady jet. The observation of puff widths at lower P values being comparable with that of thermals is consistent with the puff spreading rates measured by Sangras et al. [11].

Axial Profiles. The axial concentration profiles through the puff center are presented in Fig. 8 for $P=4$ and 6 puffs. These profiles correspond to the contours in Fig. 5. The scalar concentration drops rapidly away from the puff center for the $P=4$ puff when compared with the $P=6$ puff. The $P=5$ profile is inbetween $P=4$ and 6 cases. The $P=8$ puff has a similar axial profile to the $P=6$ puff in Fig. 8, and both $P=6$ and 8 puffs have a broader profile in contrast to $P=4$ and 5 profiles.

The puff length, $L_{0.5}$, was defined as the axial extent where the concentration is more than one-half of the maximum value in the puff center, i.e., full length at half height. The puff lengths were normalized with the nozzle diameter, $L_{0.5}/d$, and are plotted in Fig. 9. The data indicate that the puff length increases with the injection volume until about $P=6$, beyond which the length, as defined here, becomes nearly constant. The increasing length associated with the larger injection volumes is also discernible in the instantaneous images of Fig. 4. Furthermore, the length of the arrowhead structures for the $P=6$ and 8 in Fig. 4 are also comparable, corroborating the data in Fig. 9.

To estimate the elongation of puffs as the injection volume increases, the puff aspect ratio, defined as the ratio of half width to length, $\delta_{0.5}/L_{0.5}$, was computed and is shown in Fig. 10. A puff with a perfectly spherical core will have an aspect ratio of one, while elongated and flattened puffs will have aspect ratios smaller and greater than one, respectively. The data in Fig. 10 indicate that the aspect ratio decreases from about 1.1 to 0.33 as P increases from 4 to 8. This plot confirms that increasing the injection volume results in geometrically elongated puff structures.

Entrained Volume. To assess the volume entrained into the puff, the volume V enclosing the contour corresponding to the one-tenth of the maximum concentration was computed. The volume was determined by revolving this contour around the vertical axis. The volumes resulting from the left- and right-hand side

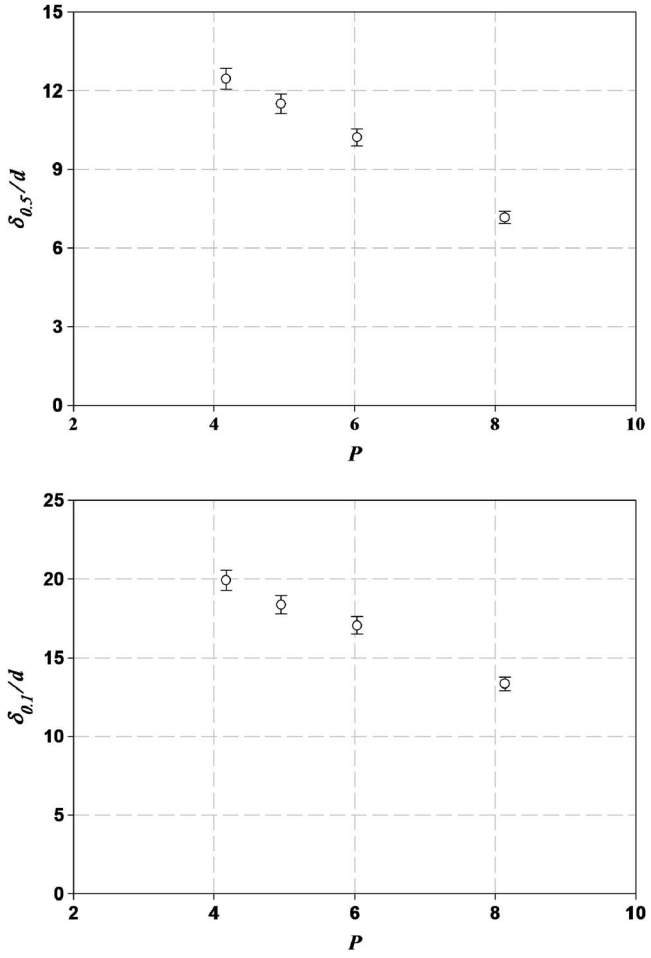

Fig. 7 Puff width as a function of *P*: (*a*) full width at half height; and (*b*) full width at 10% height

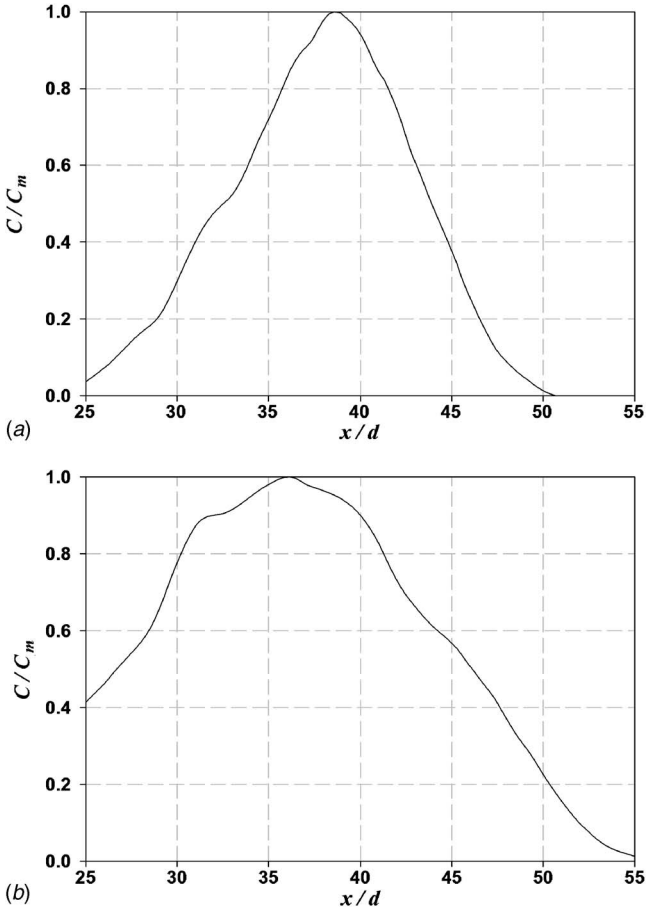

Fig. 8 Axial concentration profiles through puff center: (*a*) *P* =4; and (*b*) *P*=6

were averaged. This volume represents the total puff volume including the injected and entrained volumes. Because the length of puffs at the two larger P values extended beyond the imaged area, the data for these cases correspond to twice the volume obtained from the upper half of the puff. As the injection parameter P increases, the puff volume also increases. The entrained volume is computed by the difference between the puff volume and injection volume.

The entrained volume, normalized by the injection volume $((V-V_o)/V_o)$, is plotted Fig. 11. The data in Fig. 11 in effect illustrate the mixing of the injected fluid with the ambient air at the imaged location. The data indicate that the ratio of entrained volume to initial volume decreases as the injection volume increases. Although the puff volume increases with P, the initial volume is also larger. For example, going from $P=4$ to 8, the injection volume increases eightfold. Therefore, puffs with smaller injection volume mix more rapidly than those with a larger injection volume within the imaged region. This corroborates the higher intensities observed for the larger P cases in Fig. 4. Furthermore, the large difference in the dilution of $P=4$ and 8 puffs is consistent with the approximately threefold increase in the length of flame puffs at $P=4$ compared to $P=8$ in the earlier reacting puff studies [6].

Summary

An experimental study of passive scalar concentration field in isolated, turbulent puffs has been carried out using the laser Mie scattering technique. The principal findings of this work are as follows:

1. For injection volumes corresponding to $P \leqslant 8$, isolated puffs evolve from a spherical geometry at $P=4$ to an arrowhead structure with a tail as the injection parameter P increases. A considerable tail region is present for the case of $P=8$. The distribution of a passive scalar within turbulent puffs with $4 \leqslant P \leqslant 8$ is unlike that in turbulent vortex rings.
2. The measured half and full width, at the location of maximum concentration within the puff, decrease as the injection parameter P increases. The half width for a puff with $P=8$ is

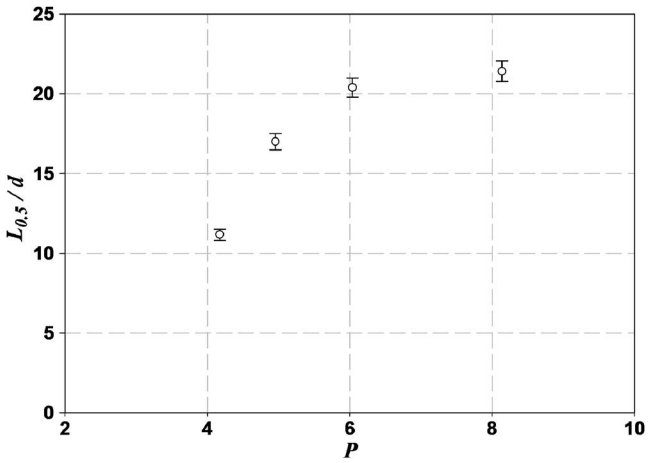

Fig. 9 Puff length as a function of *P*

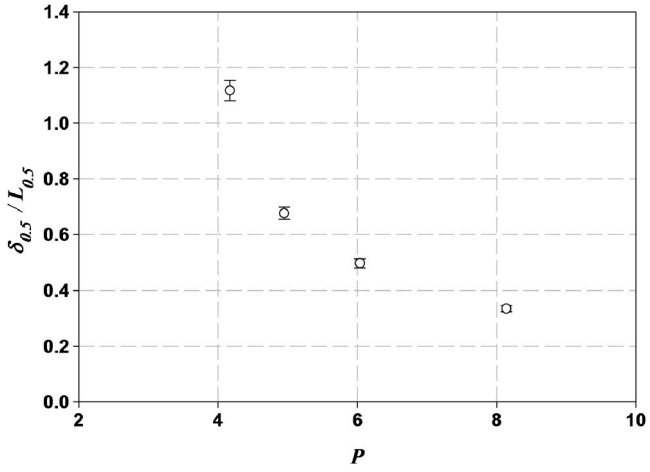

Fig. 10 Variation of puff aspect ratio with *P*

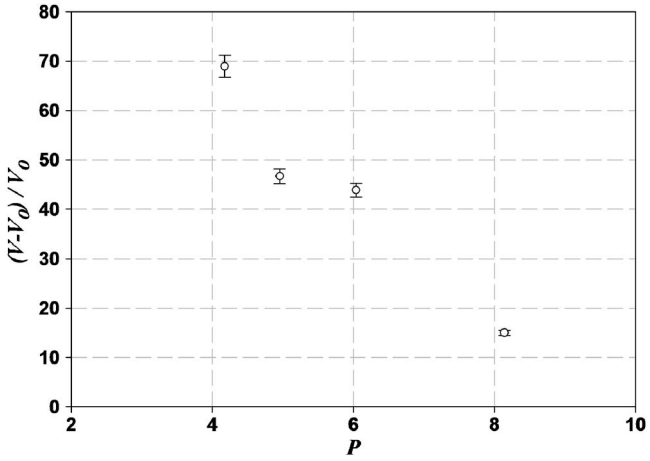

Fig. 11 Normalized entrained volume as a function of *P*

comparable to that of a steady jet at the same location. The mean radial profiles become more Gaussian like as P increases.

3. The axial length of puffs enlarges with increasing P for the range of parameters examined.
4. The puff volume within the imaged area increases with P; however, the ratio of entrained volume to injected volume decreases as P increases. The decreasing normalized entrained volume indicates that puffs with larger P are less efficient in entraining and mixing with the ambient fluid.

Acknowledgment

This work was supported by the National Aeronautics and Space Administration Grant No. NNC04GA61G.

Nomenclature

C = scalar concentration
C_m = maximum scalar concentration
d = nozzle diameter
H = stroke length, $4\ V_0/\pi d^2$
I = puff impulse
L = puff length
P = injection parameter in Eq. (4), $=(H/d)^{1/3}$
r = radial coordinate
U_j = average injection velocity
V = puff volume
V_0 = injected volume
x = axial coordinate
x_0 = virtual origin in space
t = time
t_0 = virtual origin in time
δ = puff width
ρ = density
τ = injection time

References

[1] Tang, Y. M., Waldherr, G., Jagoda, J. I., and Zinn, B. T., 1995, "Heat Release Timing in a Nonpremixed Helmholtz Pulse Combustor," Combust. Flame, **100**, pp. 251–261.
[2] Crow, S. C., and Champagne, F. H., 1971, "Orderly Structure in Jet Turbulence," J. Fluid Mech., **48**(3), pp. 547–591.
[3] Bremhorst, K., and Hollis, P. G., 1990, "Velocity Field of an Axisymmetric Pulsed, Subsonic Air Jet," AIAA J., **28**(12), pp. 2043–2049.
[4] Vermeulen, P. J., Ramesh, V., and Yu, W. K., 1986, "Measurement of Entrainment by Acoustically Pulsed Axisymmetric Air Jets," J. Eng. Gas Turbines Power, **108**, pp. 479–484.
[5] Johari, H., and Motevalli, V., 1993, "Flame Length Measurements of Burning Fuel Puffs," Combust. Sci. Technol., **94**(1–6), pp. 229–245.
[6] Hermanson, J. C., Dugnani, R., and Johari, H., 2000, "Structure and Flame Length of Fully-Modulated, Pulsed Diffusion Flames," Combust. Sci. Technol., **155**, pp. 203–225.
[7] Richards, J. M., 1965, "Puff Motions in Unstratified Surroundings," J. Fluid Mech., **21**(1), pp. 97–106.
[8] Kovasznay, L. S. G., Fujita, H., and Lee, R. L., 1974, "Unsteady Turbulent Puffs," *Advances in Geophysics*, Academic, New York, Vol. 18b, pp. 253–263.
[9] Oshima, K., Kovasznay, L. S. G., and Oshima, Y., 1977, "Sound Emission from Burning Puff," Lect. Notes Phys., **76**, pp. 219–230.
[10] Glezer, A., and Coles, D., 1990, "An Experiment Study of a Turbulent Vortex Ring," J. Fluid Mech., **211**, pp. 243–283.
[11] Sangras, R., Kwon, O. C., and Faeth, G. M., 2002, "Self-Preserving Properties of Unsteady Round Nonbuoyant Turbulent Starting Jets and Puffs in Still Fluids," ASME J. Heat Transfer, **124**, pp. 460–469.
[12] Diez, F. J., Sangras, R., Kwon, O. C., and Faeth, G. M., 2003, "Erratum: Self-Preserving Properties of Unsteady Round Nonbuoyant Turbulent Starting Jets and Puffs in Still Fluids," ASME J. Heat Transfer, **125**, pp. 204–205.
[13] Scorer, R. S., 1957, "Experiments on Convection of Isolated Masses of Buoyant Fluid," J. Fluid Mech., **2**, pp. 583–594.
[14] Hussein, H. J., Capp, S. P., and George, W. K., 1994, "Velocity Measurements in a High-Reynolds-Number, Momentum-Conserving, Axisymmetric, Turbulent Jet," J. Fluid Mech., **258**, pp. 31–75.

Mean and Fluctuating Velocity Characteristics of a Separated Shear Layer Past a Surface Mounted Block

Ü. Özkol
Department of Mechanical Engineering,
İzmir Yüksek Teknoloji Enstitüsü,
İzmir, Turkey
e-mail: unverozkol@iyte.edu.tr

C. Wark
Mechanical, Materials and Aerospace
Engineering Department,
Illinois Institute of Technology,
Chicago, IL 60616
e-mail: wark@iit.edu

D. Fabris
Mechanical Engineering Department,
Santa Clara University,
Santa Clara, CA 95053
e-mail: dfabris@scu.edu

The mean velocity, Reynolds stress, and mean vorticity regions of a separated shear layer over a surface mounted block are investigated by 2D Digital Particle Image Velocimetry (DPIV) for three Reynolds numbers (Re_a*=500, 1000, and 2500) and two channel-to-block height ratios (*H/a*=1.825 and 4.6). The recirculation region's height and length are determined for the separated shear layer by means of* $\bar{U}=0$ *contours. It is observed that the high Reynolds stress regions lay just outside of the* $\bar{U}=0$ *contours. The flow visualization and DPIV measurement of vorticity indicate that the differing normalized Reynolds stresses between* Re_a*=500 and 1000 are most probably due to the initiation of the vortex shedding between these two Reynolds numbers while, differences are minimal between* Re_a*=1000 and 2500. A sign change in the Reynolds shear stress distribution of the separated shear layer near the leading edge of the block was recognized for every Reynolds number and channel width.* [DOI: 10.1115/1.2409359]

1 Introduction

Separated flows from complex geometries are of interest in many engineering practices. For example, problems related to electronics cooling involve surface mounted components that are heat dissipating and are placed in a forced crossflow. Separated flows that are investigated in the literature are generally at high Reynolds numbers; whereas, low Reynolds number laminar, and transitional flows may be more representative of some of the industrial applications. Studies by Chu and Simons [1] and Incropera and Ramadhyani [2] report that coolant flows in electronic cooling applications experience Reynolds numbers based on channel height as low as 1000. Flows around complex geometries include flows through orifices, around prisms, backward facing steps, etc. In these complex geometries a natural flow feature is a separated region that affects the flow pressure drop, mixing, and local heat transfer. Based on the Reynolds number and local geometry the separated regions may be laminar, turbulent, or transitional, and steady or unsteady. Similarly, reattachment may occur in any of these regimes.

Usually separated regions involve coherent vortical structures originating near the separation point and convecting along the separation boundary. Occurrence and characteristics of these vortical structures depends on the Reynolds number and upstream conditions of the flow. The strength of the vortical structures will impact the mixing of the flow. To better understand the nature of the separated regions and the effectiveness of the unsteady mixing process, detailed full-field flow measurements are required.

Separated shear layer flows forming from the sharp cornered bluff bodies have been investigated by many researchers [3–8,16]. The previous research has focused on Reynolds stress magnitudes, thickness of the separated shear layers, the frequency of the resulting vortex shedding, and location of the reattachment points. Castro and Robins [3] studied the flow around surface mounted blocks at high Reynolds numbers (Re_a=30,000–100,000) for various sizes of blocks by means of an X-wire and surface oil visualizations. Castro and Robins found that the existence of the approach boundary layer has a significant effect on the pressure distribution and the magnitude of the Reynolds stresses around the bluff body. Cherry and Hillier [6] observed flow past a blunt-faced flat plate (a typical sharp cornered bluff body) at Re_a=32,000. Their simultaneous measurements of wall pressure and flow visualizations indicated that shed vortices correlate with a low local wall pressure. Besides these pressure fluctuations due to vortex shedding, they have also identified a low frequency fluctuation of the separated shear layer. Martinuzzi and Tropea [4] studied a flow around a surface mounted block in a fully developed channel flow by means of laser doppler anemometry. They argued that separation bubbles around a three dimensional obstacle were communicating with each other by means of vortex shedding. Hussein and Martinnuzi [5] showed that around a surface mounted cube the area of maximum turbulence production and the largest values for the turbulence quantities coincide with the regions of maximum vorticity along the shear layer enveloping the recirculation region. For the separation forming from the leading edge of the block, they concluded that turbulent diffusion and production terms are dominant in the thin shear layer while the convective term was only significant inside the recirculation region. They have also argued that viscous transport is only important in the regions close to the solid surfaces. The studies published in this area were usually performed in a fully developed channel flows [3,4,9] or in a uniform flow [7,16] in order to reduce the governing parameters of the flow. Again, it should be noted that these experiments considered high Reynolds numbers and mostly involved the measurement of statistical turbulence quantities.

It has also been determined that the separated regions affect the nature of the larger flow field. In a flow over an array of surface mounted blocks Martinuzzi and Tropea [4] found that as the aspect ratio of the block (height-to-span ratio) was increased, proportionally less fluid was channeled along the sides. As this occurred, a distinct, quasi-equidistant array of alternating node and saddle points appeared. Ota et al. [7] mentioned that the change in the reattachment length of the separated shear layer is to be related to the laminar to turbulent transition of this shear layer.

This study considers flow through a 2D channel with a rectangular 3D block mounted on one surface. This configuration is an idealized scenario for an electronic component cooling applica-

Contributed by the Fluids Engineering Division of ASME for publication in the JOURNAL OF FLUIDS ENGINEERING. Manuscript received January 2, 2006; final manuscript received August 5, 2006. Assoc. Editor: James A. Liburdy.

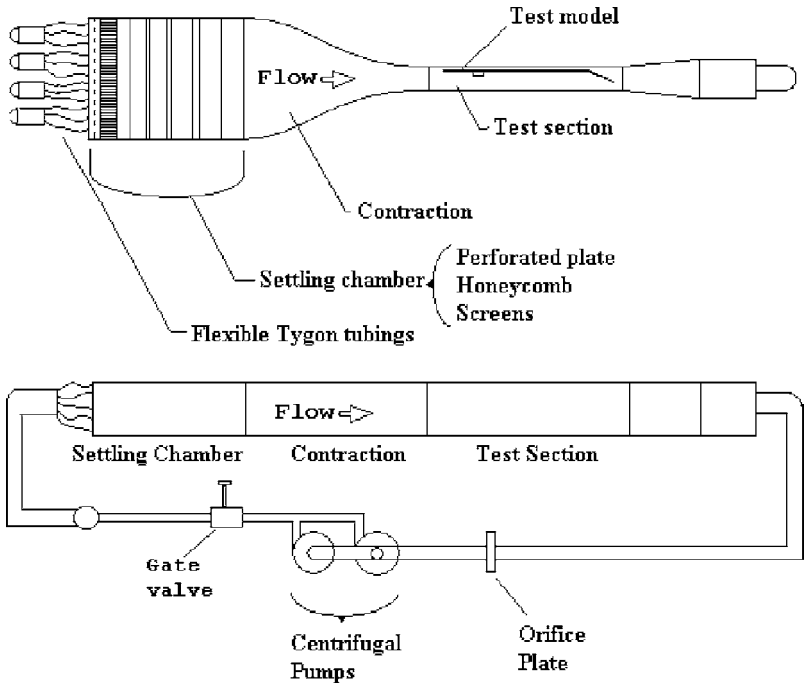

Fig. 1 Water flow facility, top view and side view

tion. The main characteristics of this geometry are the separated flows that originate not only from sharp edges of the block but also due to the adverse pressure field upstream of the block [10,11]. It is known that separated flows can decrease heat transfer from a surface since the flow is diverted away from the surface, resulting in a slow moving fluid region occur next to the surface; however, vortical structures in the separated shear layers may increase surface heat transfer due to increased mixing. This study investigates the flow features, such as size of the separation region, magnitude, and sign of the turbulent stresses in the separated shear layers, in the symmetry plane of the model in detail and at representative Reynolds numbers, Re=500–2500. Although much of the published work in this area is focused on the behavior of the reattachment distance with changing Reynolds number, there is little known about the height of the separated region and the Reynolds stress characteristics of the separated shear layer, especially for different Reynolds numbers and channel widths. The current investigation focuses only on the fluid dynamics problem in the symmetry plane of the top of the block region, leaving the heat transfer aspects to further studies.

2 Experimental Setup and Data Acquisition

Experiments were conducted in a closed-circuit water tunnel equipped with a standard free stream turbulence reduction system which consists of a settling chamber (perforated plate, honeycomb, and screens), and a contraction with a 12:1 reduction ratio (see Fig. 1). A 60.3 mm wide, 285.8 mm high, and 1270 mm long glass-walled test section was located downstream of the contraction. The total flow rate in the test section is adjusted with a gate valve which is located downstream of the circulation pumps of the water tunnel. The test model consisted of a flat plate, 6.35 mm thick, 610 mm long, and 285.8 mm wide, and a surface mounted block. The surface mounted block was mounted 88.9 mm downstream of the leading edge of the flat plate and was 25.4 mm by 25.4 mm in cross section and 10 mm high. The flat plate's leading edge was located 140 mm downstream of where the test section and the contraction meet (see Fig. 1). The flat plate's trailing edge was equipped with an adjustable streamlined tail in order to balance the flow rates on either side of the flat plate (see Fig. 2). This

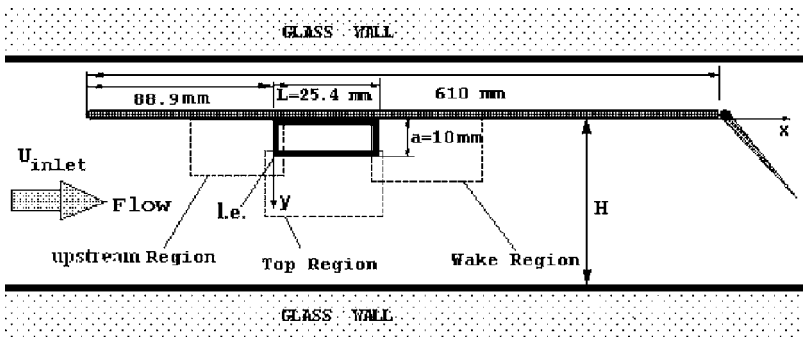

Fig. 2 Schematic of model geometry and measurement regions. The orientation of the coordinate system is based on the leading edge of the upper surface, indicated by l.e.

Table 1 Reynolds numbers and channel width to block height ratios investigated

	$\mathrm{Re}_a = U_{\mathrm{inlet}} a/\nu$	H/a
Case I	500, 1000, 2500	1.825
Case II	500, 1000, 2500	4,6

assured a symmetrical flow at the circular leading edge of the flat plate and prevented local separation at the leading edge.

Experiments were performed at three Reynolds numbers, based on block height, and two different channel spacings between the flat plate and the channel wall. Table 1 lists Reynolds numbers Re_a and channel width to block height ratios H/a investigated. The measurements presented will exclusively focus on the region identified as the top region in Fig. 2.

2D digital particle image velocimetry experiments were conducted using a pair of Nd-yttrium-aluminum-garnet lasers (532 nm) pulsed at 10 Hz each. The time difference, Δt, between the two laser pulses was adjusted by an SRS DG535 time delay generator and controlled by a function generator. The flow was seeded with silver coated hollow spheres with a 30 μm average diameter from Potters Industries. These particles have a density of 1.6 $\mathrm{g/cm^3}$. A laser sheet was obtained by passing the laser beam through a cylindrical lens. The seeding particles were illuminated in the symmetry plane (x-y plane) of the block. An ensemble of DPIV realizations were recorded on a personal computer using a Kodak 1.0ES charge coupled device (CCD) camera. The velocity measurements were not recorded consecutively and the data sets are reduced statistically.

A cross-correlation algorithm developed by Fabris [12] was used to interrogate the DPIV data. The bias errors due to the finite interrogation window size was minimized by a window-offsetting algorithm by which the effective displacement was kept to less than 0.5 pixels. Interrogation of each DPIV realization resulted in x and y components of the instantaneous velocity vectors (U,V). The spatial measurement resolution of the experiment was 0.21 mm $\times$ 0.21 mm. The mean velocity field $(\bar{U},\bar{V})$ and the Reynolds stress fields $(\overline{u'u'},\overline{v'v'},\overline{u'v'})$ were obtained by ensemble averaging the DPIV realizations. Most of the statistical results shown in this paper are based on the ensemble-average of 100 DPIV realizations. For the Re_a=1000, H/a=4.6 case, the statistical results presented in Fig. 3 were obtained from ensemble-averaging 1000 DPIV realizations.

Uncertainties in a DPIV measurement could result from (i) quantization errors which is a function of the resolution of each pixel of the camera's CCD array, (ii) the ratio of the particle image size to pixel size, (iii) the size of an interrogation window, (iv) local velocity gradients, (v) the number of particles in an interrogation window, and (vi) instrument and experiment setup imperfections. Westerweel [13] has shown that the theoretically optimum particle image to pixel size ratio is near 2. Second, the local velocity gradients cause a biasing effect towards smaller displacements but are mitigated by using a window shifting routine. Uncertainties resulting from the first three sources are estimated to be approximately ±0.15 pixels, which is very close to that found by Willert et al. [14]. Including magnification errors, the total error estimation, results in a mean velocity uncertainty of 0.5% of the inlet velocity for all of the Reynolds numbers investigated.

Determining uncertainties for Reynolds stresses is more difficult due to the magnitude of the uncertainty relative to the velocity fluctuation and possible correlation of the errors in each component. To the authors' knowledge, the only characterization of uncertainty for Reynolds stresses was by Weisgraber and Liepmann [15] using the same experimental technique. They estimated Reynolds stress uncertainties for a round jet between 3 and 20 percent of maximum fluctuations. Uncertainty estimates in each quantity are based on propagating the general uncertainty estimate

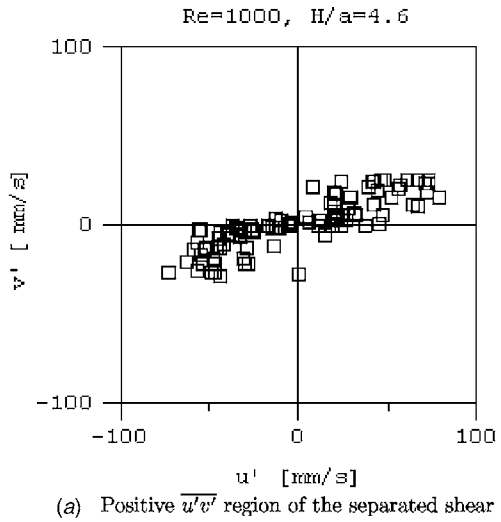

(*a*) Positive $\overline{u'v'}$ region of the separated shear layer, $(x/a, y/L) \approx (0.2, 0.04)$.

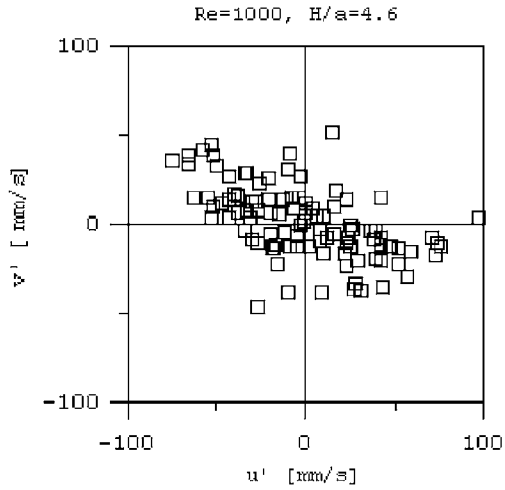

(*b*) Negative $\overline{u'v'}$ region of the separated shear layer, $(x/a, y/L) \approx (0.85, 0.08)$.

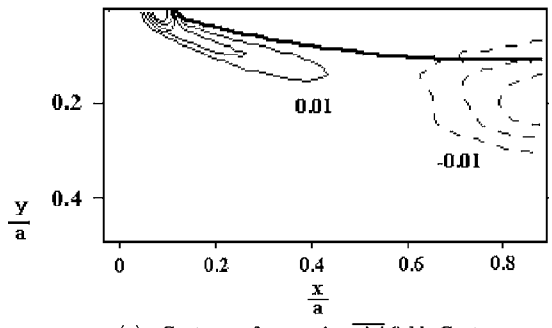

(*c*) Contours of respective $\overline{u'v'}$ field. Contour levels at 0.01.

Fig. 3 Joint histogram of U' and V' along with the normalized Reynolds shear stress contours, Re_a=1000, H/a = 4.6. The data for this figure result from the ensemble average of 1000 DPIV realizations.

in each velocity component multiplied by the mean value of the other velocity component with the uncertainties for each component correlating for $\overline{u'u'}$ and $\overline{v'v'}$. Estimated uncertainties in this study for $\overline{u'u'}$ are 2.6% of $\overline{u'u'}_{\max}$ for Re_a=2500 and 1000 and

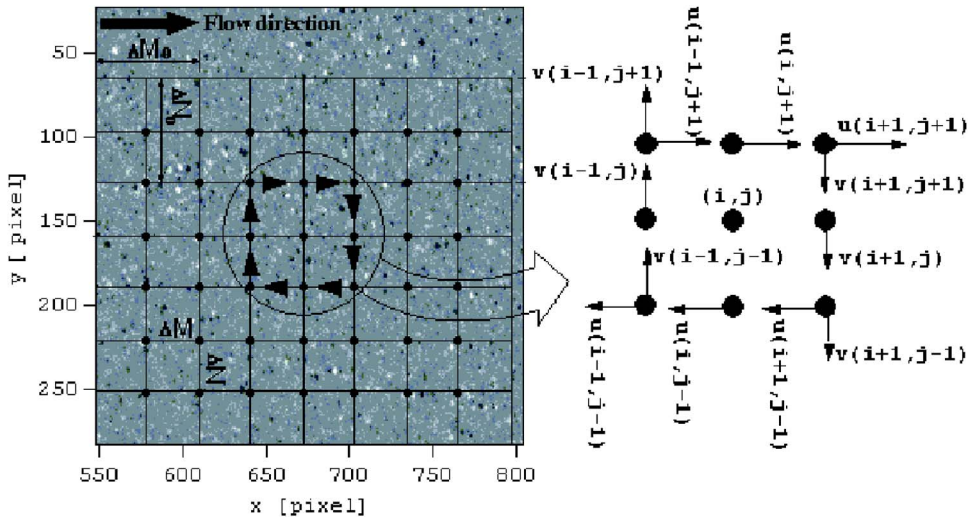

Fig. 4 Path used in the calculation of the circulation estimate

4.2% for $Re_a=500$. On the other hand, estimated uncertainties for $\overline{u'v'}$ are 4.5%, 9%, and 58% of $\overline{u'v'}_{max}$ for $Re_a=2500$, 1000, and 500, respectively. Uncertainties for $\overline{v'v'}$ are 14.1% of $\overline{v'v'}_{max}$ for $Re_a=500$. As it may seem from these uncertainty estimates that y fluctuations (v') are much smaller than the x fluctuations (u') and therefore result in larger uncertainties.

The relationship between circulation and vorticity was used for the vorticity calculations,

$$\Gamma = \oint \mathbf{U} \cdot d\mathbf{l} = \int \hat{\mathbf{n}} \cdot (\nabla \times \mathbf{U}) d\mathbf{S} = \int \hat{\mathbf{n}} \cdot \omega d\mathbf{S} \tag{1}$$

where Γ is the circulation on path $\mathbf{l}$ enclosing surface $\mathbf{S}$ and $\mathbf{n}$ is the unit vector normal to $\mathbf{S}$. The vorticity of a fluid element is found by taking the limit as $\mathbf{S}$ goes to zero. Therefore, applying this to the 2D DPIV data, we obtain:

$$(\omega_z) = \frac{1}{A}\Gamma = \frac{1}{A}\oint \mathbf{U} \cdot d\mathbf{l} \tag{2}$$

where (ω_z) is the average vorticity in the area enclosed by path $\mathbf{l}$. Computational implementing this formula involves selecting a small rectangular path of data points as shown in Fig. 4. The circulation is then calculated around this path using the trapezoidal rule of integration:

$$(\omega_z)_{i,j} = \frac{\Gamma_{i,j}}{4\Delta M \Delta N} \tag{3}$$

where

$$\Gamma_{i,j} = \frac{1}{4}\Delta M(U_{i-1,j-1} + 2U_{i,j-1} + U_{i+1,j-1}) + \frac{1}{4}\Delta N(V_{i+1,j-1} + 2V_{i+1,j} + V_{i+1,j+1}) + \frac{1}{4}\Delta M(U_{i+1,j+1} + 2U_{i,j+1} + U_{i-1,j+1}) + \frac{1}{4}\Delta N(V_{i-1,j+1} + 2V_{i-1,j} + V_{i-1,j-1})$$

Since the number of velocity points used to calculate the vorticity field with this method is more than that used with a central differencing scheme, this method performs with lower uncertainty levels of $\delta_\omega \approx 0.61(\delta_u/\Delta x)$ (albeit with poorer spatial resolution) and is therefore chosen for this work. Vorticity calculation for the points along the edges of the vector field is estimated by using either forward or backward differencing schemes.

3 Description of the Flow

Flow around surface mounted bluff bodies is strongly three dimensional. For the present case, the flow in the symmetry plane of the block starts to deflect to the sides upstream of the block. As a qualitative illustration, the flow rate along the center plane for the three Reynolds numbers investigated is calculated by integrating the velocity profiles from the surface of the flat plate ($y/a=-1$) to $y/a=1$ and normalizing by $U_{\text{inlet}}(\mathbf{y/a})$ (y defines the wall normal direction with the origin at the top of the block surface as indicated in Fig. 2). These flow rate per unit width calculations made from the mean velocity data for the flow over the top of the block are given in Fig. 5 and indicate that there is nearly a 50% reduction in the flow in the center plane: a result of more flow being directed to the sides of the block. The normalized flow rates for $Re_a=1000$ and 2500 decrease at the same rate as x/a increases; whereas, the normalized flow rate for $Re_a=500$ decreases at a higher rate for $x>a$. This corresponds to a shear layer transition that will be discussed later.

Horseshoe shaped vortices upstream of the block have been observed to be a dominant feature of surface-mounted bluff-body flows. Their size and strength affect the flow rate distribution over the top and around the sides of the block. The horseshoe vortices occur due to the adverse pressure gradient field and the subsequent flow separation upstream of the block [9]. The separated vorticity sheet from the flat plate rolls-up and wraps around the

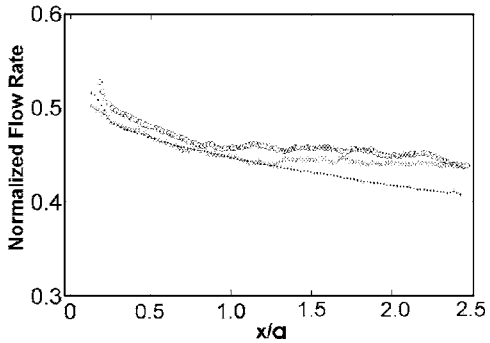

Fig. 5 Normalized flow rate for $H/a=1.825$. (…; $Re_a=500$), (ooo; $Re_a=1000$), (xxx; $Re_a=2500$).

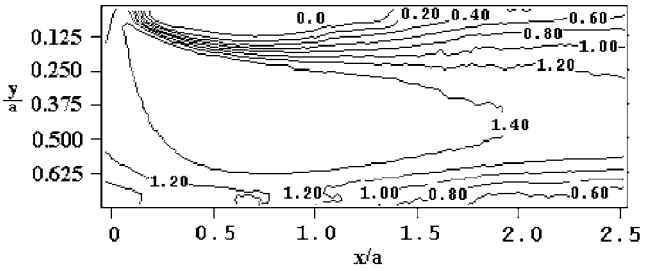

(*a*) Streamwise mean velocity, $\bar{u}$

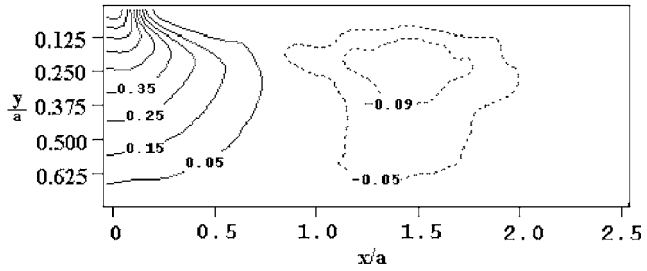

(*b*) Well-normal velocity, $\bar{v}$

Fig. 6 Mean velocity contours for the flow in the top region for Re_a=1000 at H/a=1.825. Note that the measurement region is scaled with block height (a) and block's leading and trailing edges are located at $(x/a, y/a)=(0,0)$ and $(2.5,0)$, respectively.

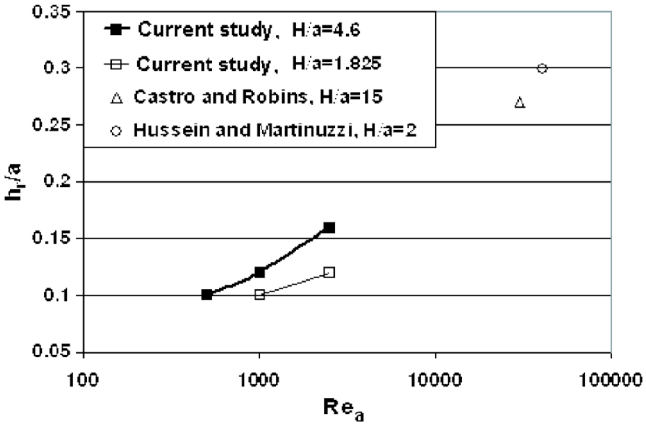

Fig. 7 Recirculation height versus Reynolds number

block. For more detail on this type of flow feature the reader is referred to the works of Baker [17], and Smith and his colleagues [10,11].

Another important feature of the flow around sharp cornered bluff bodies is the flow separation from the leading and trailing edge corners. Vorticity, at a high enough Reynolds number, in the separated shear layers rolls up into coherent vortex motions, due to a Kelvin–Helmholtz instability and eventually sheds as downstream traveling vortices [3,17]. The location of the shedding is dependent on the Reynolds number and the upstream flow features. The size of the recirculation region formed on the block's top surface is greatly influenced by the nature of the separated shear layer and the frequency and strength of the shed vortices and turbulence levels of the separated shear layer. Figure 6 shows contours of the normalized mean velocity field for Re=1000 and H/a=1.825 where the block is located on the top of the each figure and its leading edge is located at $(x/a, y/a)=(0,0)$, (see Fig. 2 for the location of the leading edge of the block). The recirculation region is defined by the contour $\bar{U}=0$. Note that the x component of the velocity vector inside this contour is negative and represents the backflow region. The length l_{rb} of this recirculation region is defined as the distance between the downstream reattachment of the $\bar{U}=0$ contour and the block's leading edge. Its height, h_r, is defined as the maximum height of the $\bar{U}=0$ contour. These mean flow length scales are functions of the block's geometry (height a, length, and width), channel height H, boundary layer thicknesses of the approaching flat plate boundary layer, δ, and of the opposite channel wall, δ_o, Reynolds number, and the upstream turbulence conditions (see Figs. 7 and 8).

The shear layer separating from the block's leading edge (see Fig. 2 for the location of the leading edge) is usually very thin because of the short development distance between the stagnation point on the upstream face of the block and its leading edge and also the favorable pressure gradient resulting from the geometrical contraction. As a result of this, the separated shear layer is usually laminar at its onset. For fixed geometry and upstream flow conditions, the Reynolds number is the sole governing parameter. It is shown that separated flow becomes unsteady with increasing Reynolds number in geometrically similar flows, (see Ref. [7]). This unsteadiness is initiated by the rolling up of this separated shear layer into coherent vortices which eventually shed from the separated shear layer. These vortices are captured by long-exposure photography and can clearly be seen in Fig. 9. Depending upon the parameters given above, the separated shear layer may remain laminar and reattach or these unsteady vortices may breakup into a turbulent motion before reattachment. The location of the first vortex formation and/or the location of the first occurrence of the turbulent state affects the recirculation region length l_{rb} and its height h_r.

The affect of l_{rb} can be summarized as follows: laminar separation/laminar reattachment results in increase of l_{rb} with increasing Reynolds number. Laminar-separation/unsteady reattachment produces a decrease in l_{rb} with increasing Reynolds number; whereas, for laminar separation/turbulent reattachment, the reattachment length changes very slowly, although Ota et al. [7] argued that no change should occur for this regime. The present study and some studies on backward facing step flow [8] indicate a small increase in l_{rb} with increasing Reynolds number.

4 Results

4.1 Mean Velocity and Vortex Shedding. Measurements of the mean streamwise and wall-normal velocities ($\bar{U}$, $\bar{V}$) indicate a recirculation region forming on the top surface of the block due to the vortex shedding events in the shear layer. The backflow component of this region is contained within the $\bar{U}=0$ contour on the top surface of the block seen in Fig. 6. The recirculating region could be considered as a further contraction to the flow passage between the block and the channel wall opposite to the flat plate and for this reason, streamwise free-stream velocities are much higher near the thickest part of the recirculation region. This is clearly seen in the shape of the $\bar{U}=1.4$ contour. Since the results in Fig. 6 were obtained for the smallest H/a case, the boundary layer on the opposite channel wall is also seen at the bottom of Fig. 6(a). The tightly packed $\bar{U}$ contours seen in this figure near the leading edge of the block, are due to the high velocity gradients of the separated shear layer. The wall normal component of the mean velocity has very high positive values near the leading edge, Fig. 6(b). The mean wall-normal velocity reaches 85% of the inlet velocity at the leading corner of the block. On the other hand, the mean wall-normal velocity component becomes very small and negative near the downstream end of the recirculation region, with a magnitute of only 10% of the inlet velocity.

Flow visualization results show no vortex formation and shedding of the separated shear layer over the top of the block for the lowest Reynolds number studied (Re_a=500). This Reynolds number is slightly larger than the first-critical Reynolds number

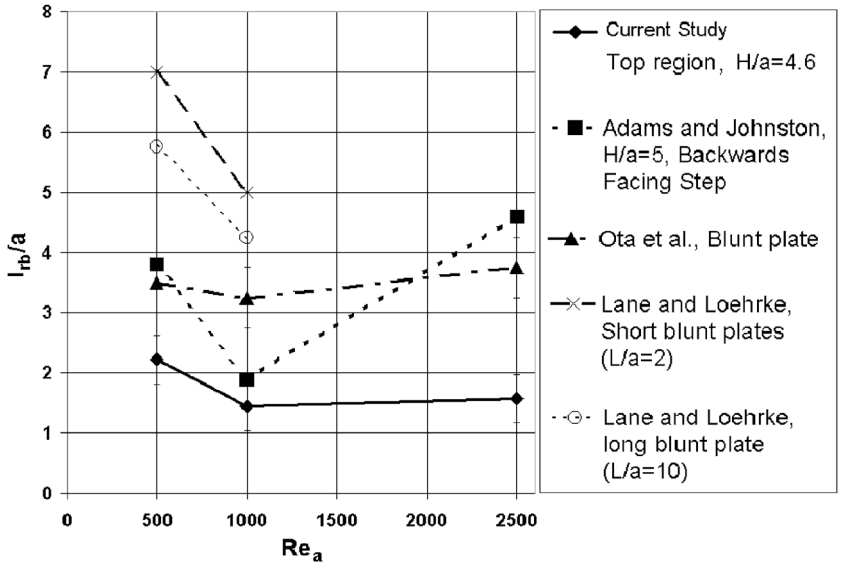

Fig. 8 Recirculation length versus Reynolds number

($Re_{crit} \approx 400$) found by Ota et al. [7] for a blunt-faced flat plate and Adams and Johnston [8] for a backward facing block. The first critical Reynolds number is defined as that for which the first signs of unsteadiness are seen to occur in the separated shear layer. However, for the larger Reynolds numbers, $Re_a = 1000$ and 2500, the shear layer rolls into shedding vortices (see Fig. 9). As this unsteadiness increases with increasing Reynolds number, the recirculation region height, h_r, also increases (see Fig. 7). Note that the smaller channel width case results in a smaller recirculation region height. The length of the recirculation region for $H/a = 4.6$ case also shows a trend consistent with results published in the literature: l_{rb} decreases considerably with increasing Reynolds number from the first Reynolds number investigated to the second Reynolds number ($Re_a \approx 1000$) and only increases slightly at the highest Reynolds number (see Fig. 8). It is theorized that a first critical transition occurs when the separated shear layer becomes unstable and generates vortices and a second transition occurs when the shear layer becomes turbulent at its onset. For a blunt leading edge, Ota et al. suggest that this second-critical Reynolds number occurs where the separated shear layer becomes turbulent just after separation. The length of the recirculation region for $H/a = 1.825$ is very close to the ones in $H/a = 4.6$ for $Re_a = 2500$ and 1000. However, the recirculation region was too small for $Re_a = 500$ to have accurate measurements for The experimental results show the impact of the generation of the shear layer vortices in reducing the length of the recirculation region. In these experiments a second transition was not seen.

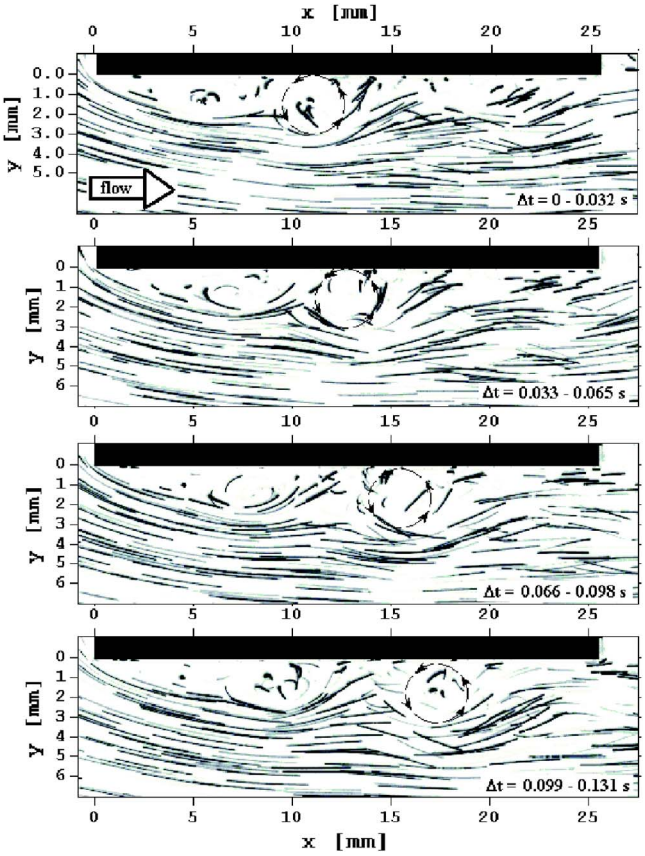

Fig. 9 Long exposure imaging of seeding particles identifying vortex shedding events over the top of the block for $Re_a = 1000$, $H/a = 4.6$. Arrows indicating the rotational motion are superimposed on the image.

4.2 Reynolds Stresses. Three components of the Reynolds stress normalized with U_{inlet}^2 are obtained for the flow over the top of the block: the streamwise and the wall-normal stresses, $\overline{u'u'}$ and $\overline{v'v'}$, and the shear stress, $\overline{u'v'}$. Hussein and Martinuzzi [5] measured the spanwise component of the normal Reynolds stress, $\overline{w'w'}$, with LDV in the symmetry plane of the flow and found it to be much smaller than the other two normal Reynolds stress components and therefore, the three measured components should be a reasonable characterization of the unsteady flow field.

DPIV measurements showed that the highest Reynolds stress magnitudes, for all three stresses measured, are contained in a small region outside of the $\bar{U} = 0$ contour for the three Reynolds numbers and the two channel width cases investigated. Figure 10 shows the streamwise Reynolds stress for $Re_a = 2500$, $H/a = 1.825$. Note that the center of the corresponding shed vortices is just outside of the $\bar{U} = 0$ contour. This might indicate a possible relation between the vortex centers and the Reynolds stress generation. It is also observed that the maximum magnitude of the streamwise normal stress, $\overline{u'u'}$, decreases downstream of the recirculation region for the first two Reynolds numbers while for the third Reynolds number there exists a region with substantial non-

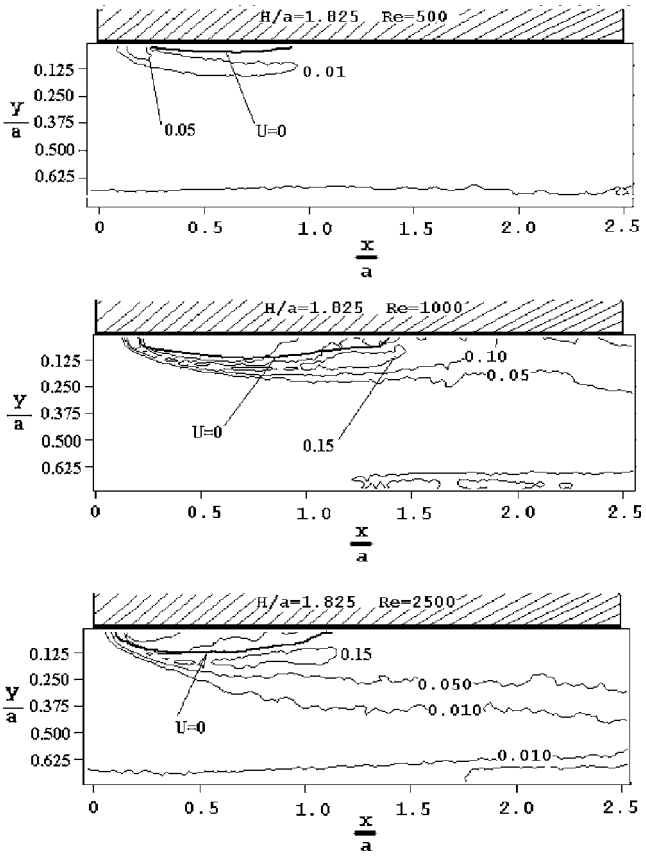

Fig. 10 Normalized streamwise Reynolds stress distributions, $\overline{u'u'}/U^2_{inlet}$, for three Reynolds numbers at H/a=1.825. The $\bar{U}$ =0 velocity contour is superimposed to indicate the size of the recirculation region.

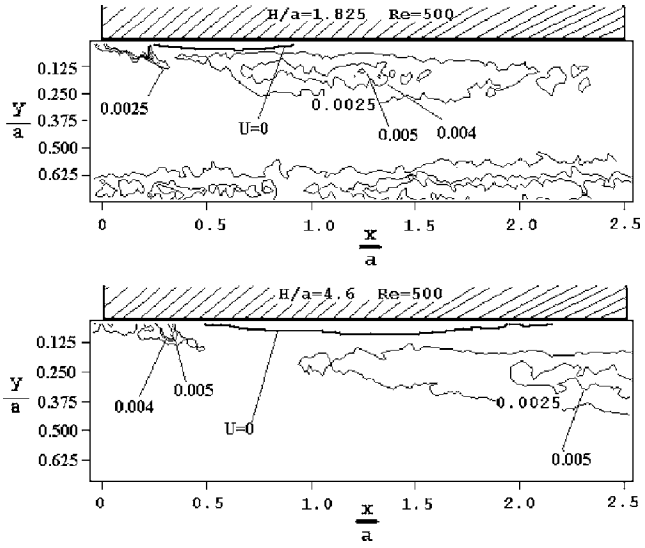

Fig. 11 Normalized wall-normal Reynolds stress distributions, $\overline{v'v'}/U^2_{inlet}$, for two different channel widths at Re_a=500

zero Reynolds stress downstream of the recirculation region. An order of magnitude increase in the maximum Reynolds stress occurs with increase of Reynolds number from Re=500 to 1000. Since the Reynolds stresses are related to the mixing process in the fluid, it could be conjectured that this increase in the stresses would lead to an increase in heat transfer as well. Increasing the Reynolds number from 1000 up to 2500 does not cause a further substantial increase in the maximum Reynolds stress magnitude. Changes in the $\overline{v'v'}$ magnitude with Reynolds number are found to be very similar to those observed for $\overline{u'u'}$, as observed for Fig. 10 [18].

Comparing the wall-normal Reynolds stresses, $\overline{v'v'}$, between the two channel widths, H/a=4.6 and 1.825, indicates that the region of the highest $\overline{v'v'}$ magnitude is related with the downstream end of the recirculation region (see Fig. 11). It is clearly evident that the proximity of the opposite channel wall has an impact on the length of the recirculation region. Note that the x-location of the approximate center of the high $v'v'$ region ($x=a$) is near the downstream end of the recirculation region. The affect of the channel width on the distribution and magnitude of $\overline{u'u'}$ is very similar to that observed for $\overline{v'v'}$ [18]. Negative mean velocity measurements indicate that the shed vortices in the separated shear layer move towards the wall in this region; however, their interaction with the wall which results in the Reynolds stress generation is not thoroughly understood [19,20].

Near the leading edge of the block there is another high $\overline{v'v'}$ region. The high stress region near the leading edge is conjectured to be due to the unsteadiness in the separation of the shear layer; whereas, the high $\overline{v'v'}$ region over the downstream end of the recirculation region is attributed to vortex formation and shedding.

The Reynolds shear stress, $\overline{u'v'}$, distribution near the leading edge of the block is observed to change its sign from positive to negative (see Fig. 12). Since this sign change is seen for all three Reynolds numbers studied, including Re_a=500 where there was no vortex shedding observed, the vortex shedding does not generate this phenomenon. As implicated by the $\overline{v'v'}$ distributions in Fig. 11, this sign change is only related to the directional change of the v' velocities and may be related to the change in direction

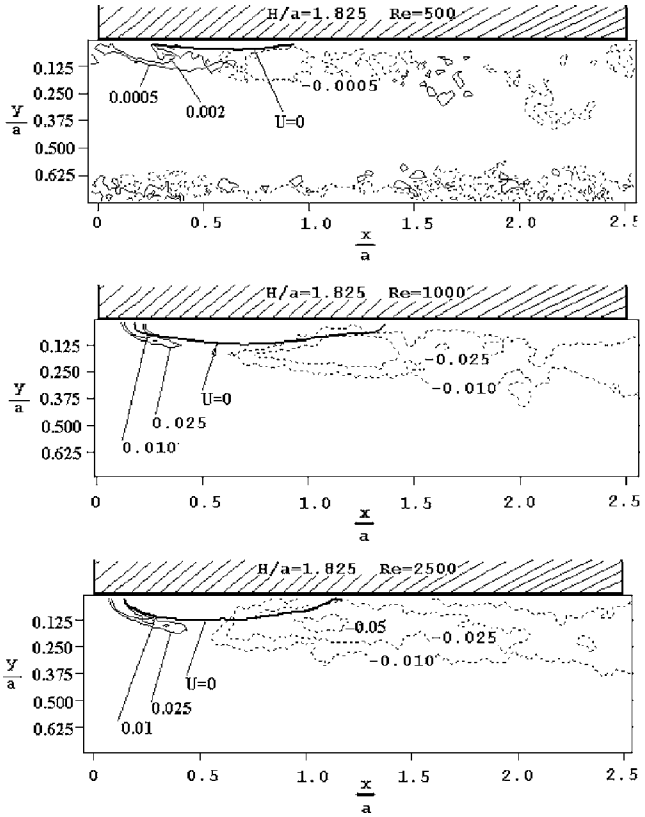

Fig. 12 Normalized Reynolds shear stress distributions, $\overline{u'v'}/U^2_{inlet}$, for three Reynolds numbers at H/a=1.825

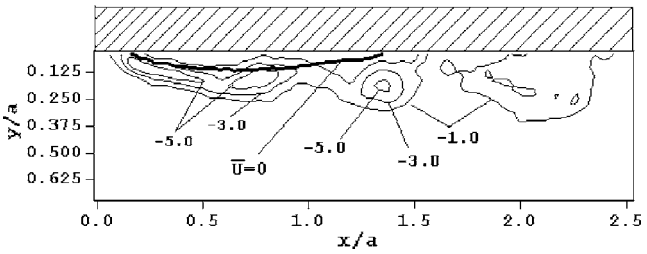

Fig. 13 Normalized instantaneous vorticity distribution, $\omega_z a/U_{inlet}$, for $Re_a=1000$, $H/a=1.825$

of the streamlines in the mean flow. A series of joint u' and v' histograms obtained from the highest Reynolds stress points in the separated shear layer shown in Fig. 3 indicate that in the positive $\overline{u'v'}$ region, the correlation between u' and v' is very strong. However, in the negative $\overline{u'v'}$ region there is more dispersion in v' due to vortex shedding; nevertheless, there is still some correlation between these two fluctuating velocity components.

4.3 Vorticity. Vorticity generated by the separated shear layer near the leading edge of the block was confined to a narrow region of high shear existing in the upstream half of the recirculation region. The vorticity layer initiates at the start of the separated shear layer and the strength of the vorticity layer is directly related to the velocity jump across the shear layer. This vorticity introduced into the fluid stream from the leading edge of the block rolls into distinct high vorticity regions due to the inviscid Kelvin–Helmholtz instability.

Figure 13 illustrates an instantaneous vorticity field for the flow over the top of the block where its leading edge is located on the upper left hand corner of the contour plot. The recirculation region is marked by the bold contour line of $\bar{U}=0$. This figure clearly illustrates an ongoing roll-up event of the vorticity layer near the middle portion of the recirculation region ($x/a \approx 0.75$) and two vortices already shed, one near the downstream end of the recirculation region ($x/a \approx 1.40$) and the other near $x/a \approx 2.0$. The distances separating each shed vortex is in the range from $0.6a$ to $0.65a$, indicating nearly periodic shedding. It is also seen from this figure that instantaneous high vorticity regions lay just outside of the $\bar{U}=0$ contour similar to the Reynolds stress regions.

Ensemble averaged vorticity fields are seen in Fig. 14 for the three Reynolds numbers at $H/a=1.825$. The data indicate that the highest vorticity magnitude occurs near the leading edge of the block. For the highest vorticity level, the magnitude doubles when the Reynolds number increases from 500 to 1000. As for the further increase in the Reynolds number to 2500, the highest vorticity magnitude only increases by 20%. Note that the largest change in the Reynolds stress magnitude also occurred between $Re_a=500$ and 1000 (see Fig. 10). The location of the highest vorticity magnitude lays in the region just outside of the $\bar{U}=0$ contour and is consistent with the instantaneous vorticity field seen in Fig. 13. Note that the regions of high vorticity magnitude and streamwise Reynolds stress are also very similar in shape and location which may indicate that behavior of the vorticity drives the Reynolds stress production.

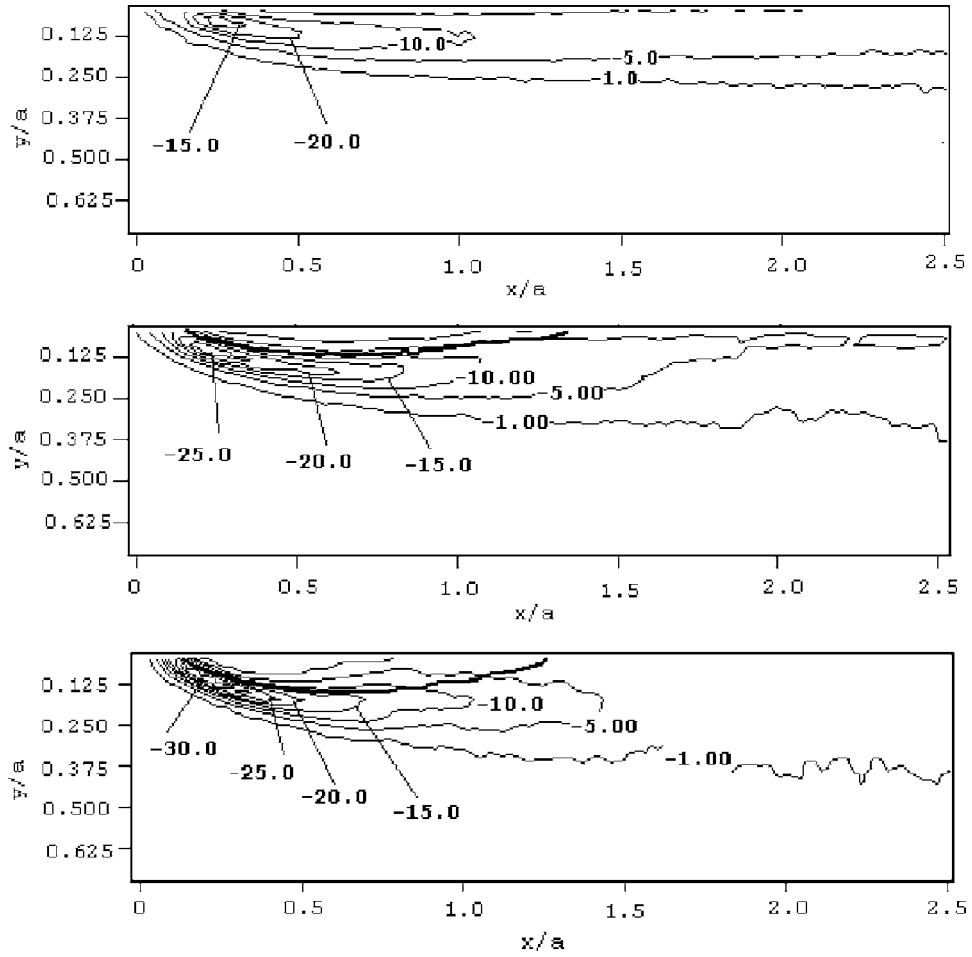

Fig. 14 Mean vorticity field for Reynolds numbers 500, 1000, and 2500 at $H/a=1.825$

5 Conclusion

A series of DPIV measurements were taken on the symmetry plane of a surface mounted block where flow separation and recirculation are important features of the flow. The experiments quantify the mean flow field, three Reynolds stress components, and the instantaneous and mean out-of-plane vorticity component. The Reynolds numbers in this study closely relate to typical electronics cooling applications.

Measured recirculation region heights and lengths show consistency with geometrically similar flows in the published literature. The experimental cases cover the first transitional behavior where the shear layer is unstable to a Kelvin–Helmholtz type of instability. The experiments reveal that vortex shedding events occur from the separated shear layer for $\mathrm{Re}_a=1000$ and 2500 but not for $\mathrm{Re}_a=500$ where the flow stays laminar. These vortex shedding events result in greatly increased Reynolds stress magnitudes. The highest Reynolds stress magnitudes are observed to be located just outside the $\bar{U}=0$ contour, indicating a relation between vortex centers and Reynolds stress generation. It was also observed that the proximity of the opposite channel wall has a strong effect on the size of the recirculation region.

A closer look at the distributions of the Reynolds stress components indicates that the magnitude of $\overline{u'u'}$ falls sharply downstream of the recirculation region, unlike the trend observed for the magnitude of $\overline{v'v'}$. Note that these differences in the levels of the components of the Reynolds stress components reveal the highly nonisotropic nature of this turbulent shear layer. The Reynolds shear stress, $\overline{u'v'}$, changes sign near the leading edge of the block from positive to negative indicating that the shear layer fluctuations change direction in this region which may be a result of the change in the streamline pattern of the mean flow field.

Instantaneous vorticity realizations more clearly show where vortex shedding initiates. These measurements are the first to relate instantaneous vorticity and the local Reynolds stress field for this type of flow. Approximate separation distances between each individual shed vortex reveal that the vortex shedding events may be periodic. The center of each shed vortex follows the path laying just outside the $\bar{U}=0$ contour. Ensemble averaged vorticity fields indicate that the highest vorticity magnitudes are located near the leading edge of the block outside of the $\bar{U}=0$ contour and that the vorticity decreases significantly downstream of the recirculation region.

Acknowledgment

The authors would like to acknowledge the generous support of Izmir Institute of Technology, Illinois Institute of Technology, and the Illinois NASA Space Grant Consortium. Communications with Professor Hassan Nagib and Professor David Williams during the design of the water flow facility are greatly appreciated.

Nomenclature

A = integration area
a = block height
H = channel width
S = integration path
l_{rb} = recirculation region length
h_r = recirculation region height
$\mathrm{Re}_a = U_{\mathrm{inlet}}a/\nu$, Reynolds number
ΔM = interrogation window size in pixels in x
ΔN = interrogation window size in pixels in y
$\bar{U}, \bar{V}$ = averaged velocity components in x and y directions
u', v' = fluctuating velocity components in x and y directions
$\overline{\omega_z}$ = mean vorticity in z
Γ = circulation

References

[1] Chu, R. C., and Simons, R. E., 1993, "Cooling Technology for High Performance Computers: Part 2.—IBM Sponsored University Research," *NATO ASI Proceedings, Cooling of Electronics Systems June 21–July 2*, Izmir, Turkey, pp. 434–459.

[2] Incropera, F. P., and Ramadhyani, S., 1993, "Application of Channel Flows to Single-Phase Liquid Cooling of Chips and Multi-Chip Modules," *NATO ASI Proceedings, Cooling of Electronics Systems June 21–July 2*, Izmir, Turkey, pp. 460–491.

[3] Castro, I. P., and Robins, A. G., 1977, "The Flow Around a Surface-Mounted Cube in Uniform and Turbulent Streams," J. Fluid Mech., **79**, pp. 307–335.

[4] Martinuzzi, R., and Tropea, C., 1993, "The Flow Around Surface Mounted Prismatic Obstacles Placed in a Fully Developed Channel Flow," J. Fluid Mech., **115**, pp. 85–92.

[5] Hussein, H. J., and Martinuzzi, R. J., 1996, "Energy Balance for Turbulent Flow Around a Surface Mounted Cube Placed in a Channel," Phys. Fluids, **8**(3), pp. 764–780.

[6] Cherry, N. J., and Hillier, R., and Latour, M. E. M. P., 1984, "Unsteady Measurements in a Separated and Reattaching Flow," J. Fluid Mech., **144**(3), pp. 13–46.

[7] Ota, T., Asano, Y., and Okawa, J., 1981, "Reattachment Length and Transition of Separated Flow Over Blunt Flat Plates," Bull. JSME, **94**(192), pp. 941–947.

[8] Adams, E. W., and Johnston, J. P., 1985, "Effects of the Upstream Boundary Layer Thickness and State on the Structure of Reattaching Flows," Symposium on Turbulent Shear Flows, 5th, Ithaca, NY, August 7-9, Proceedings (A86-30201 13-34). University Park, PA, Pennsylvania State University, pp. 5.1–5.6.

[9] Meinders, R. E., and Hanjalic, K., 1999, "Vortex Structure and Heat Transfer in the Turbulent Flow Over a Wall-Mounted Matrix of Cubes," Int. J. Heat Fluid Flow, **20**, pp. 225–267.

[10] Seal, C. V., Smith, C. R., Akin, O., and Rockwell, D., 1995, "Dynamics of the Vorticity Distribution in Endwall Junctions," J. Fluid Mech., **286**, pp. 117–135.

[11] Seal, C. V., Smith, C. R., and Rockwell, D., 1997, "Dynamics of the Vorticity Distribution in Endwall Junctions," AIAA J., **35**(6), pp. 1041–1047.

[12] Fabris, D., 1996, "Combined Experimental and Numerical Investigations of a Vortex Ring Impinging Normally on a Wall," Ph.D. thesis, University of California at Berkeley, Berkeley.

[13] Westerweel, J., 1993, "Digital Particle Image Velocimetry, Theory and Application," Ph.D. thesis, Delft University, Delft.

[14] Willert, C. E., and Gharib, M., 1991, "Digital Particle Image Velocimetry," Exp. Fluids, **10**, pp. 181–193.

[15] Weisgraber, T. H., and Liepmann, D., 1998, "Turbulent Structure During Transition to Self-Similarity in a Round Jet," Exp. Fluids, **24**, pp. 210–224.

[16] Lane, J. C., and Loehrke, R. I., 1980, "Leading Edge Separation from a Boundary Layer Plate at Low Reynolds numbers," HTD (Am. Soc. Mech. Eng.), **13**, pp. 45–48.

[17] Baker, C. J., 1977, "The Laminar Horseshoe Vortex," J. Fluid Mech., **95**(2), pp. 347–367.

[18] Özkol, Ü., 2002, "Experimental Investigation of the Flow Around a Surface Mounted Block," Ph.D. thesis, Illinois Institute of Technology, Chicago, Illinois.

[19] Eaton, J. K., and Johnston, J. P., 1985, "Turbulent Flow Reattachment: An Experimental Study of the Flow and Structure Behind a Backward-Facing Step," Rep. MD-39. Thermosciences Division, Dept. of Mech. Eng., Stanford University.

[20] Bradshaw, P., and Wong, F. Y. F., 1972, "The Reattachment and Relaxation of a Turbulent Shear Layer," J. Fluid Mech., **52**(1), pp. 113–135.

On the Use of the Squire-Long Equation to Estimate Radial Velocities in Swirling Flows

Michel J. Cervantes
e-mail: Michel.Cervantes@ltu.se

L. Håkan Gustavsson

Division of Fluid Mechanics,
Luleå University of Technology,
SE-97187 Luleå, Sweden

A method to estimate the radial velocity in swirling flows from experimental values of the axial and tangential velocities is presented. The study is motivated by the experimental difficulties to obtain this component in a draft tube model as evidenced in the Turbine-99 IAHR/ERCOFTAC Workshop. The method uses a two-dimensional nonviscous description of the flow. Such a flow is described by the Squire-Long equation for the stream function, which depends on the boundary conditions. Experimental values of the axial velocities at the inlet and outlet of the domain are used to obtain the boundary conditions on the bounded domain. The method consists of obtaining the equation related to the domain with an iterative process. The radial velocity profile is then obtained. The method may be applied to flows with a swirl number up to about Sw=0.25. *The critical value of the swirl number depends on the velocity profiles and the geometry of the domain. The applicability of the methodology is first performed on a swirling flow in a diffuser with a half angle of* 3 deg *at various swirl numbers, where three-dimensional (3D) laser Doppler velocimeter (LDV) velocity measurements are available. The method is then applied to the Turbine-99 test case, which consists in a model draft tube flow where the radial inlet velocity was undetermined. The swirl number is equal to* Sw=0.21. *The stability and the convergence of the approach is investigated in this case. The results of the pressure recovery are then compared to the experiments for validation.* [DOI: 10.1115/1.2409331]

1 Introduction

The Turbine-99 IAHR/ERCOFTAC Workshop held in 1999 in Porjus, Sweden, aimed to determine the state of the art in CFD simulations of draft tube flows. Such flows are challenging for the numerical community due to the different phenomena appearing, e.g., swirling flow in straight and curved diffusers, vortex breakdown, separation, unsteadiness, and turbulence. The organizers provided the geometry of a model draft tube and the corresponding experimental data for the inlet boundary conditions (cf. Fig. 1). Some data, such as the radial velocity, most of the Reynolds stresses, and the turbulence length scale at the inlet of the draft tube, could not be measured. As these components need to be known to perform a numerical simulation, various qualified guesses were attempted, resulting in different results [1]. The influence of the radial velocity profile was particularly striking.

Page and Giroux [1] performed calculations both with zero and nonzero radial velocity using the results of a separate Kaplan runner simulation for the latter case. The simulations produced a lower pressure recovery with zero radial velocity. Later on, they presented numerical results based on the Turbine-99 case with a more detailed investigation of the influence of the turbulence length scale and the radial velocity on the pressure recovery [2]. These calculations show clearly that the flow separates earlier on the runner cone without radial velocity at the inlet. They also get a perfect agreement with the experimental value of the pressure recovery using the radial velocity obtained with the Kaplan runner simulation. Skåre et al. [1] also performed calculations without radial velocity and obtained a low-pressure recovery compared to the experimental value.

For the second Turbine-99 IAHR/ERCOFTAC Workshop held in 2001 in Älvkarleby, Sweden, the organizers provided the geometry, a grid, and a complete set of inlet boundary conditions. The inlet radial velocity was estimated from geometrical considerations assuming the flow attached to the wall. The participants obtained values of the pressure recovery in accordance with the experimental one [3]. For the workshop, Nilsson [3] performed a numerical investigation of the corresponding runner flow and obtained a similar radial velocity profile as proposed by the organizers. Unfortunately, the runner geometry was not available for the other participants.

In order to objectively and systematically quantify the influence of the unknown parameters, Cervantes and Engström [4] applied factorial design to the Turbine-99 test case on four parameters: the radial velocity, the turbulence length scale, the surface roughness, and the grid. The radial velocity was found to have the largest influence on the pressure recovery and the loss factor.

From these results, it is obvious that the radial velocity component has a large influence on the pressure distribution and, thus, the pressure recovery. Therefore, it is essential to estimate this component before performing any numerical simulation in a draft tube. One way is to simulate the flow through the runner, as done by Page and Giroux or Nilsson [3], an approach that necessitates some hypothesis on the boundary conditions further upstream and, of course, the runner geometry. Another approach, which takes advantage of the experimental data, is to use the fact that the pressure in this system to a large extent should be governed by inertial effects and the flow is nearly axisymmetric. Therefore, the problem may be approached using inviscid rotational theory based on the Squire-Long equation. This equation has been numerically studied by Buntine and Saffman [5] for flows through a diverging pipe. Their results show that the solution ceases to be unidirectional or exist when the Squire number, ratio between the peripheral, and axial velocities, exceeds a certain value. The benefit of the approach is that the radial velocity is a part of the solution and thus can be used in computational fluid dynamics (CFD) programs to give a more reasonable radial inlet velocity.

The present work is organized into four main parts. The first is concerned with a detailed formulation of the method. Then, the applicability of the Squire-Long equation to experimental flow and the methodology are tested against 3D LDV measurements. The Turbine-99 test case is then treated. A discussion follows.

Contributed by the Fluids Engineering Division of ASME for publication in the JOURNAL OF FLUIDS ENGINEERING. Manuscript received May 31, 2005; final manuscript received August 7, 2006. Review conducted by Joseph Katz.

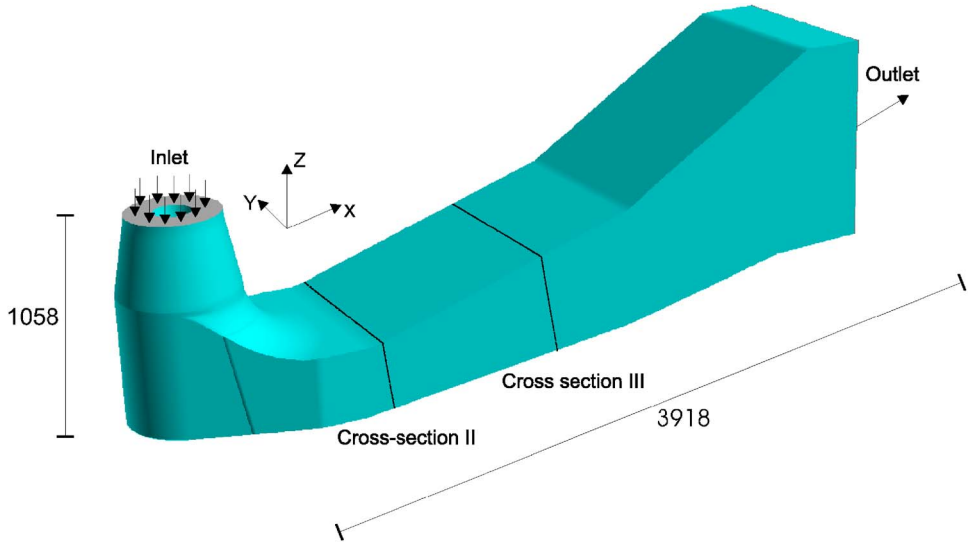

Fig. 1 CAD drawing of the Höllefors draft tube (in millimeters) [1]

2 Formulation

The flow is considered axisymmetric, nonviscous, and steady. Cylindrical polar coordinates (x,σ,ϕ) are used with velocity components (u,v,w). Since the flow is two-dimensional and incompressible, a stream function can be defined and is related to the axial and the radial velocities by

$$u = \frac{1}{\sigma}\frac{\partial \psi}{\partial \sigma} \tag{1}$$

$$v = -\frac{1}{\sigma}\frac{\partial \psi}{\partial x} \tag{2}$$

which follows from the continuity equation in cylindrical polar coordinates

$$\frac{\partial u}{\partial x} + \frac{1}{\sigma}\frac{\partial(\sigma v)}{\partial \sigma} = 0 \tag{3}$$

The axial and radial vorticity components (ω_x and ω_σ) are related to the azimuthal velocity w by

$$\omega_x = \frac{1}{\sigma}\frac{\partial(\sigma w)}{\partial \sigma} \tag{4}$$

$$\omega_\sigma = -\frac{1}{\sigma}\frac{\partial(\sigma w)}{\partial x} \tag{5}$$

and the azimuthal vorticity may be expressed through the stream function as

$$\omega_\phi = -\frac{1}{\sigma}\left(\frac{\partial^2 \psi}{\partial x^2} + \frac{\partial^2 \psi}{\partial \sigma^2} - \frac{1}{\sigma}\frac{\partial \psi}{\partial \sigma}\right) \tag{6}$$

The components of the Euler equation in this system are given by (see [6])

$$v\omega_\phi - w\omega_\sigma = \frac{\partial H}{\partial x} \tag{7}$$

$$w\omega_x - u\omega_\phi = \frac{\partial H}{\partial \sigma} \tag{8}$$

$$u\omega_\sigma - v\omega_x = 0 \tag{9}$$

where H is the Bernoulli function defined by

$$H(x,\sigma) = H(\psi) = \frac{P}{\rho} + \frac{1}{2}(u^2 + v^2 + w^2) \tag{10}$$

The azimuthal component of the Euler equation (9) may also be written

$$\vec{u} \cdot \vec{\nabla}(\sigma w) = 0 \tag{11}$$

which states that the circulation σw is constant on a stream line. Thus,

$$\sigma w = C(\psi) \tag{12}$$

Insertion of the relations (2), (5), (6), and (12) in the axial component of the Euler equation (7) gives the Squire-Long equation for the stream function (the equation was first derived by Meisel [7] according to Goldshtik and Hussain [8]).

$$\frac{\partial^2 \psi}{\partial x^2} + \frac{\partial^2 \psi}{\partial \sigma^2} - \frac{1}{\sigma}\frac{\partial \psi}{\partial \sigma} = \sigma^2 \frac{\mathrm{d}H(\psi)}{\mathrm{d}\psi} - C(\psi)\frac{\mathrm{d}C(\psi)}{\mathrm{d}\psi} \tag{13}$$

The equation is elliptic and nonlinear. Therefore, the conditions on all boundaries have to be determined. The equation may be simplified for flows without variation in the axial direction, such as flows in tubes. The variation of the radial velocity with x is then dropped from the equation, leaving a one-dimensional equation.

A relation between the velocity components and the Bernoulli function is necessary to fully determine the right-hand side of the Squire-Long equation. Such a relation is found using the definition of the Bernoulli function (10) and the radial component of the Euler equation (8). Thus, eliminating pressure gives

$$H(x,\sigma) = H(\psi) = \frac{u^2}{2} + \frac{w^2}{2} + \int \frac{w^2}{\sigma}\mathrm{d}\sigma - \int u\frac{\partial v}{\partial x}\mathrm{d}\sigma \tag{14}$$

H and C may be determined explicitly in terms of the stream function at the inlet of the domain for cylindrical flows, i.e., with no variation with x and with uniform velocity and constant angular velocity (cf. Batchelor [6]). An analytical solution of the Squire-Long equation (13) may be found for such flows.

As soon as the profiles become complicated, interpolations are required to determine H and C. It should be noted that for a certain type of inlet boundary conditions, $H(\psi)$ and $C^2(\psi)$ may be nonlinear function of ψ and, thus, multiple solutions may be found in addition to the base solution [9]. The circulation is obtained using the relation (12) and an interpolation of the experimental values of the tangential velocity at the inlet. This gives C as a

function of σ but is needed as function of ψ in (13). The Bernoulli function is obtained using the relation (14) and an interpolation of the experimental values of the axial and tangential velocities at the inlet. The x derivative of the radial velocity is set to 0 at this stage. Therefore, the correct problem is not solved using this equation. Then, H and C are plotted function of ψ for several values of σ representative of the domain. H and C are found as functions of the stream function with two interpolations.

The determination of all conditions on the boundaries, i.e., inlet, walls, outlet, and centerline is necessary to solve the Squire-Long equation. The stream function is obtained using the relation (1) and an interpolation of the experimental values of the axial velocities at the inlet and outlet of the domain. An adjustment is usually necessary to satisfy the continuity equation (cf. the Appendix). In the present work, the interpolations have been done with polynomials of different degrees. Other type of functions may also be used to interpolate the experimental values. The degrees of the polynomials used to interpolate the experimental data may be function of the complexity of the flow.

For simple geometry and inlet velocity profiles in flows varying with x, an asymptotic method may be appropriate to solve Equation (13). However, the complexity of the geometries and the velocity profiles encountered in draft tubes and the nonlinearity of Eq. (13) do not permit such an approach. A numerical method is more appropriate. For the present work, the PDE Toolbox in MATLAB is used. The core of the PDE Toolbox is a partial differential equation solver that uses the finite element method (FEM) for problems defined on bounded domains in the plane. The mesh is made of triangular elements, and regular refinement method was used in the present study, which results in a uniform mesh [10]. The equation that the solver effectively solves in the present case is

$$-\mathrm{div}\left(\frac{-1}{\sigma}\,\mathrm{grad}(\psi)\right) = \sigma\frac{\mathrm{d}H(\psi)}{\mathrm{d}\psi} - \frac{C(\psi)}{\sigma}\frac{\mathrm{d}C(\psi)}{\mathrm{d}\psi} \tag{15}$$

The Squire-Long equation has a peculiarity. It is determined with conditions on the inlet and/or outlet of the considered domain through the Bernoulli function. The method takes advantage of this coupling. It consists in obtaining the equation related to the domain through an iterative process. Symbolic calculations, to determine the equation, as well as numerical calculations, to get a solution of the equation are needed. As a first guess, the Squire-Long equation is derived with the x derivative of the radial velocity set to 0. The solution gives a nonzero x derivative of the radial velocity since the outlet boundary conditions force the streamlines to diverge. This value is used to determine the new equation, which is then solved. The solution gives a new x derivative of the radial velocity, etc. This process actually converges and thus produces a radial velocity consistent with the equation and the boundary conditions.

The iterative method described utilizes experimental values as well as an axisymmetric nonviscous description of the flow. However, experimental conditions deviate from the idealized Squire-Long description. The values are always determined with some uncertainty, which is reflected in the equation as well as the boundary conditions. The solution and the convergence may be perturbed by such a mismatch. Before we apply this scheme to the flow of the Turbine-99 test case, the method is tested to a known flow case, the flow in a straight diffuser (without inner boundary) as measured by Dahlhaug [11].

3 Dahlhaug Test Case

The diffuser used by Dahlhaug [11] has a half angle of 3 deg and measurements of the three velocity components were made before and after the diffuser at a constant Reynolds number Re $=2.8\times10^6$. The measurement sections are represented in Fig. 2. The radial velocity in such sections has an average velocity *nearly* equal to 0. Different swirl numbers were investigated; $Sw=0$, 0.1, 0.35, and 0.7. The swirl number is defined as the ratio of angular momentum flux to the axial momentum flux

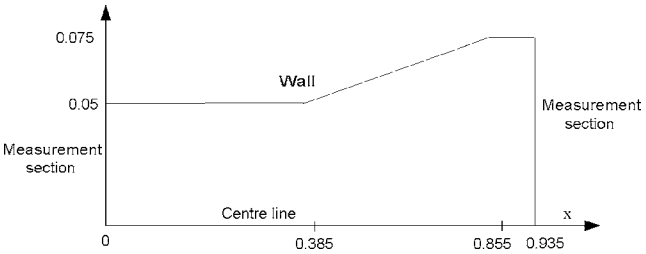

Fig. 2 Schematic of the computed area [11]

$$\mathrm{Sw} = \frac{\displaystyle\int_0^R \sigma^2 uw\,\mathrm{d}\sigma}{R\displaystyle\int_0^R \sigma u^2\,\mathrm{d}\sigma} \tag{16}$$

where R represents the pipe radius.

The interpolated dimensionless inlet axial and tangential velocities using a third order polynomial in σ and the experimental values at the inlet are represented in Figs. 3 and 4 for the different swirl numbers. The determination of the velocity on the wall is approximative. As a matter of fact, the Squire-Long equation is a two-dimensional nonviscous description of the flow, which does not take into account the effects of viscosity. Therefore, gradients in the boundary layer have to be truncated from the profiles. For example, the square ($r=0.05, U_{\mathrm{inlet}}=0.71$) in Fig. 3 represents the *natural end* of the profile on the wall for Sw=0.1. However, the calculation produces a recirculation zone, not mentioned by Dahlhaug, due to the nonviscous formulation of the equation. Therefore, the end of the profile was moved by taking the last measurement point near the wall. For swirl number Sw=0.10, a forced vortex region dominates the tangential velocity, but a Rankine-like vortex appears for higher swirl number.

Figure 5 represents the interpolated dimensionless outlet axial velocity using a third-order polynomial in σ after adjustment of the stream function to comply with continuity (cf. the Appendix)

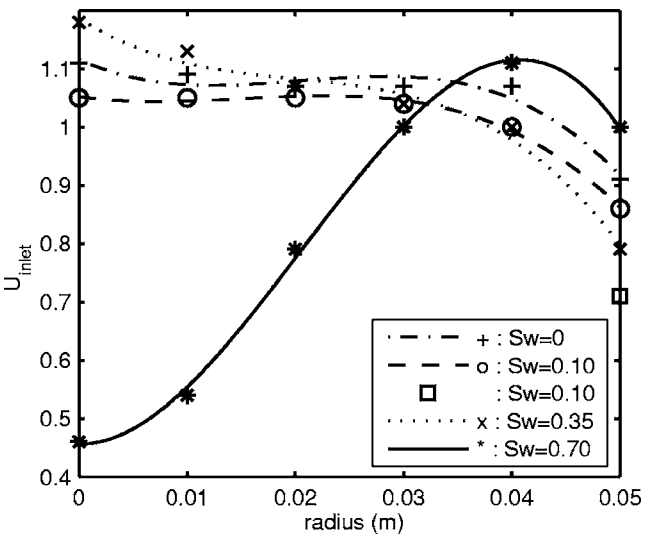

Fig. 3 Interpolated inlet axial velocity (line) and experimental values (symbol) at different swirl numbers [11]. The square ($r=0.05$, $U_{\mathrm{inlet}}=0.71$) represents the first assumption for the end of the profile on the wall for Sw=0.1.

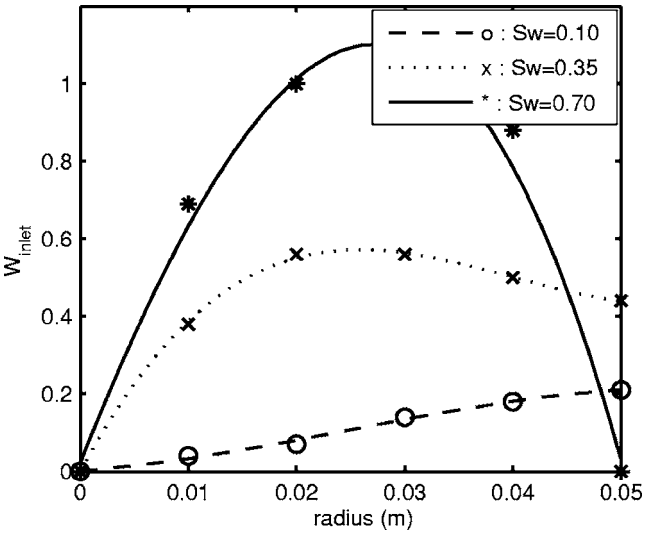

Fig. 4 Interpolated inlet tangential velocity (line) and experimental values (symbol) at different swirl numbers [11]

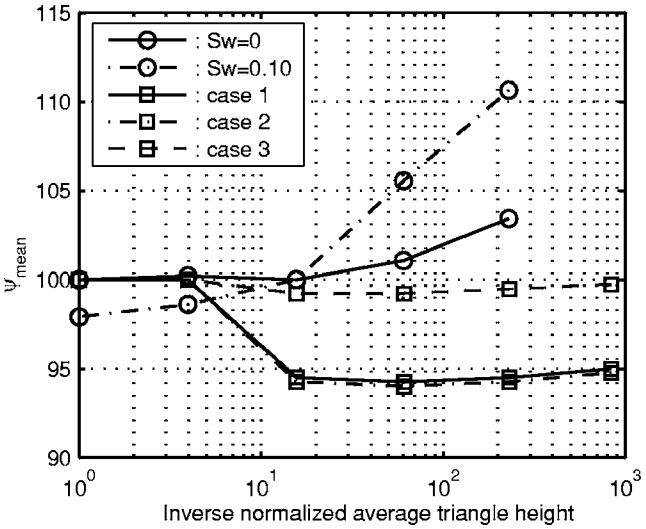

Fig. 6 Average value of the stream function over the domain function of the inverse triangle height (in percent). The average value of the stream function is normalized with the value obtained for the grid used to perform the calculation. The inverse triangle height is normalized with the minimum triangle height. Sw=0 and Sw=0.10 correspond to the test case of Sec. 3 (Dahlhaug [11]). Cases 1–3 correspond to the test case of section 4 (Turbine-99).

and the experimental values. The adjustments reflect the difficulty to get an accurate flow rate from laser Doppler anemometry measurements.

The stream functions at the inlet and the outlet of the domain are determined from the relation (1) and the interpolation of the experimental values of the axial velocities at the inlet and outlet. The adjustment necessary to satisfy the continuity equation is described in the Appendix. The stream function on the center line and pipe wall is defined by

$$\psi_{\text{center line}}(x,0) = 0 \tag{17}$$

$$\psi_{\text{wall}}(x,\sigma_{\text{wall}}) = \int_0^{\sigma} \sigma u_{\text{inlet}} \mathrm{d}\sigma = \int_0^{\sigma} \sigma u_{\text{outlet}} \mathrm{d}\sigma \tag{18}$$

The circulation is determined from the interpolation with a third-order-polynomial of the experimental values of the tangential velocity at the inlet. The circulation and the Bernoulli function are interpolated with a second- and third-order polynomial in ψ, respectively.

After a convergence study (see Fig. 6), a mesh constituted of 19,009 nodes and 36,864 triangles with an average quality of 0.837 was used for the calculation. Figure 6 presents the variation of the average value of the stream function over the domain function of the inverse average triangle height for the first iteration, i.e., $v=0$, and Sw=0 and Sw=0.10. The average values are normalized with the average value obtained with the grid chosen for the calculation.

3.1 Low Swirl Number. For Sw=0 and Sw=0.1, a weak radial velocity at the inlet of the domain is present; see, e.g., the stream function obtained after the first calculation, i.e., with the x derivative of the radial velocity set to zero, for Sw=0.1 in Fig. 7. The velocity magnitude has a maximum of 0.015 for Sw=0 and 0.045 for Sw=0.1. The magnitude of the inlet axial velocity is nearly 1. Peculiar variations of the stream function close to the

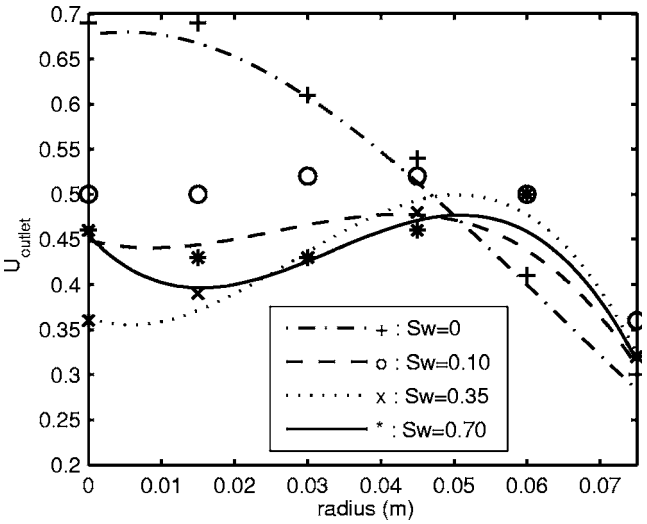

Fig. 5 Interpolated outlet axial velocity (line) and experimental values (symbol) at different swirl numbers [11]

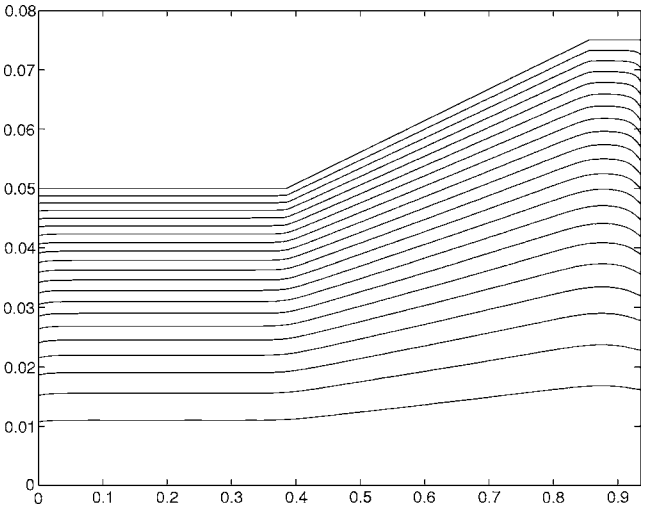

Fig. 7 Representation of the stream function for $v_{,x}=0$ and Sw=0.1

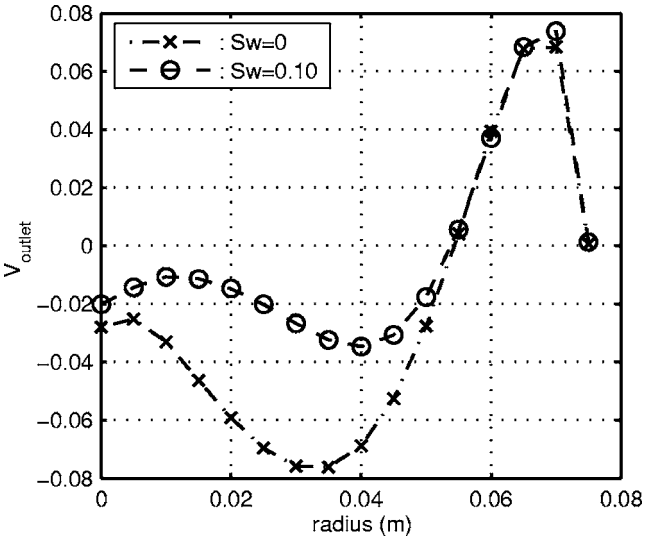

Fig. 8 Outlet radial velocity obtained after three iterations for Sw=0 and Sw=0.10

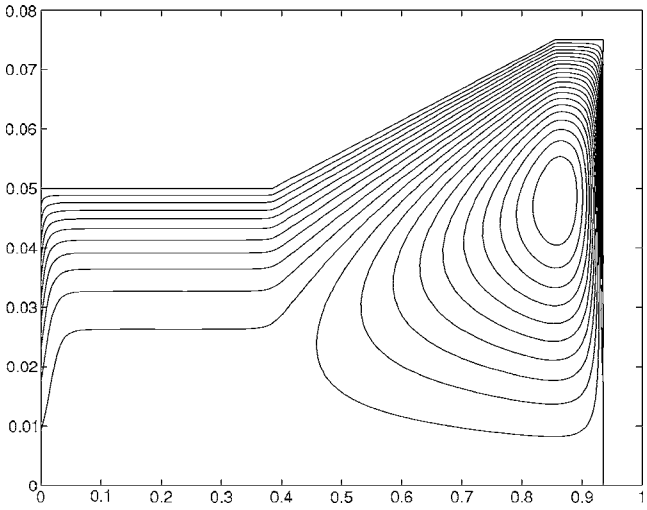

Fig. 10 Representation of the stream function for $v_{,x}=0$ and Sw=0.35

outlet boundary are obtained, leading also to a nonzero outlet radial velocity. The radial velocity has a similar shape and a maximum magnitude of ~0.08 in both cases at the outlet (see Fig. 8). The nonzero radial velocity is attributed to the outlet boundary conditions imposed by the axial velocity, which force the streamlines to specific values measured with some uncertainty and with a nearly two-dimensional viscous flow.

The nonzero radial velocity at the inlet and outlet of the domain may have several origins. Experimental values are used. The experimental data are determined with an uncertainty of 4% for the axial and radial velocities and 2% for the tangential velocity according to Dahlhaug [11]. An adjustment of the outlet profile is made to satisfy the continuity equation. Furthermore, assumptions are made on the flow, it is considered axisymmetric, laminar, and nonviscous. Thus, the present model cannot take care of the losses present in Dahlhaug experiments.

Three iterations have been performed. The convergence is straightforward with the value of the residual $R(v)$ in Fig. 9. The residual is defined by

$$R(v)=\left\{\int_a^b [v_i(\sigma)-v_{i-1}(\sigma)]^2 \mathrm{d}\sigma\right\}_{1\leqslant i\leqslant+\infty}^{1/2} \tag{19}$$

where v_i represents the radial velocity profile at the ith iteration. The initial radial velocity is $v_0=0$.

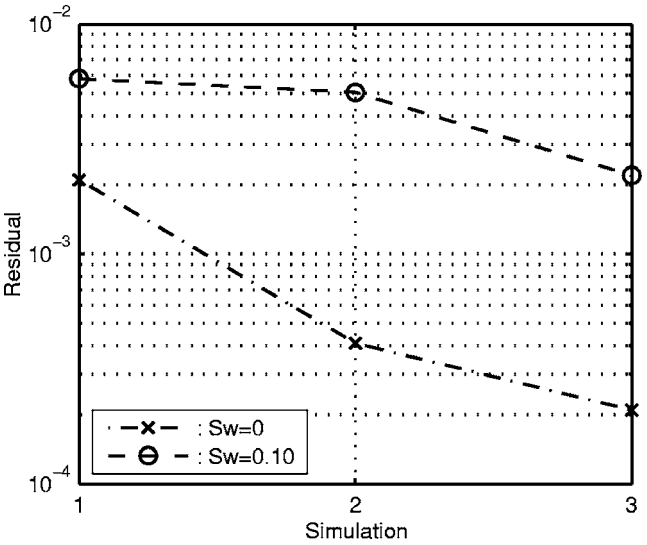

Fig. 9 Residual for Sw=0 and Sw=0.10

3.2 High Swirl Number. For Sw=0.35, the solution shows a nonunidirectional flow; see Fig. 10. Such a result is inconsistent with the visualization performed by Dahlhaug. For Sw=0.7, no solution was obtained. For such swirl numbers, the Squire-Long equation fails to describe correctly the flow. Dahlhaug's measurements may explain this behavior. They show that the root-mean-square value of the turbulence intensity for the different components of the velocity increased at the inlet and outlet of the domain with the swirl number. Furthermore, the variations in the radial direction are nonlinear, the magnitude of the turbulence intensity being greatest on the center line. The Squire-Long equation cannot take care of such a phenomenon.

Buntine and Saffman [5] studied numerically the Squire-Long equation. They found that it might fail to give a solution or give a unidirectional axial flow above a critical Squire number. This may depend on the inlet profile and the geometry considered. The Squire number in their study is defined as

$$\mathrm{Sq}=\frac{R\omega_x}{U} \tag{20}$$

where R is the radius of the inlet pipe, ω_x the vorticity, and U the axial velocity. A relation between the swirl number and the Squire number may be found for a forced vortex with a uniform axial velocity U and angular velocity Ω

$$\mathrm{Sq}=4\mathrm{Sw} \tag{21}$$

Therefore, the method cannot give a correct or any result above a critical swirl number. The exact value of the critical swirl number may vary from case to case. It should be around Sw=0.25 from the work published by Buntine and Saffman [5].

4 Turbine-99 Test Case

The test case of the Turbine-99 IAHR/ERCOFTAC Workshop is now considered. The flow between the inlet and a cross section found immediately below the cone is investigated with the method (see Fig. 11). The aim is to find a radial velocity for the inlet compatible with the axial and tangential velocities to support nu-

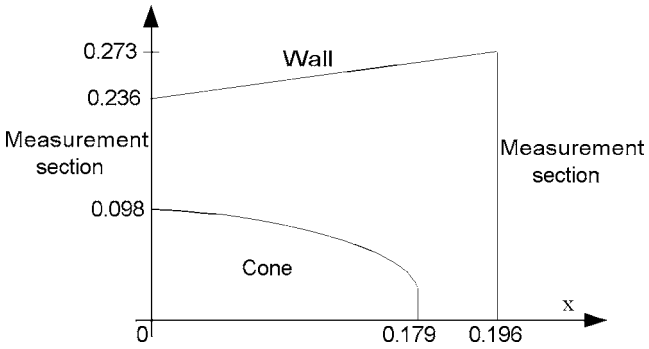

Fig. 11 Schematic of the computed area [1]

merical computation. To validate the result, the pressure recovery obtained from the calculation will be compared to the experimental one.

The boundary conditions on the bounded domain are obtained from the experimental data of the Turbine-99 test case. The data are approximated with polynomials to investigate the stability and convergence of the approach; both third- (case 1) and sixth-order (case 2) polynomials are used. In Figs. 12–14 are the two types of approximations represented. Since the stream function is related to the axial velocity via the relation (1), the stream function is represented by a fifth- and eight-degree polynomial, respectively. A shift is present between the experimental data and the interpolated curves of the axial velocity at the outlet, which is due to an adjustment. The first reason is specific to the test case, since there is a lack of experimental data in the region beneath the cone, $0 \leqslant \sigma \leqslant 0.002$. A qualified guess is therefore necessary, the consequences of which are investigated in case 3, where two points are added, leading to a stronger recirculation zone. The presence of the recirculation zone is motivated by flow visualization performed by Urban Andersson during the measurements (see Fig. 15). The second reason is the adjustment necessary to compensate for the uncertainty on the experimental data as previously mentioned (see the Appendix).

The procedure used is the following: from the relation (12), C is determined. It is a fourth- or seventh-order polynomial in σ. From the relation (14), H is determined. It is a seventh- or twelfth-order polynomial in σ with a logarithm. H is interpolated with a third-order polynomial in ψ and C with a second-order polynomial in ψ, in both cases. The equation to be computed (15) can then be determined. The iterative procedure previously described is then used to get the radial velocity profile associated with the conditions on the bounded domain and the physical description leading to the Squire-Long equation.

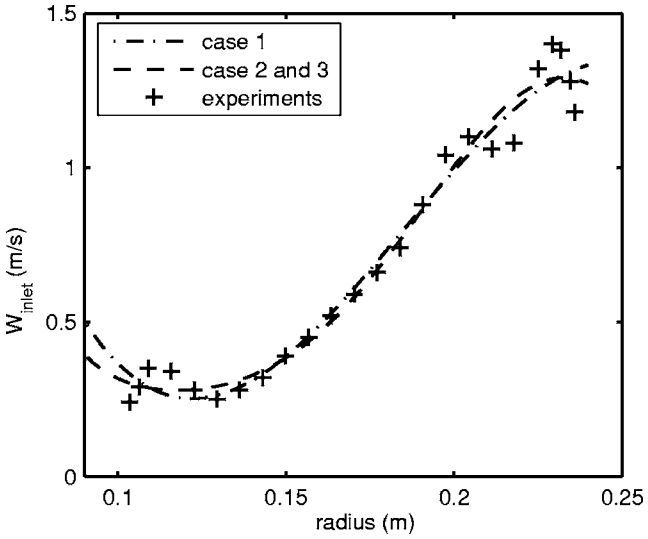

Fig. 13 Interpolated inlet tangential velocity (line) and experimental values (symbol) [1]. Case 1: third-order interpolation, cases 2 and 3: sixth-order interpolation.

Similarly to the Dahlhaug test case, a convergence study was conducted (see Fig. 6). A mesh constituted of 32,585 nodes and 64,256 triangles with an average quality of 0.947 was chosen for the calculation. The figure presents the variation of the average value of the stream function over the domain function of the inverse average triangle height for the first iteration, i.e. $\upsilon = 0$, and case 1, 2 and 3. The average values are normalized with the average value obtained with the grid used for the calculation.

4.1 Radial Velocity. The radial velocity profiles proposed by the organizers of the second Turbine-99 workshop [3], obtained

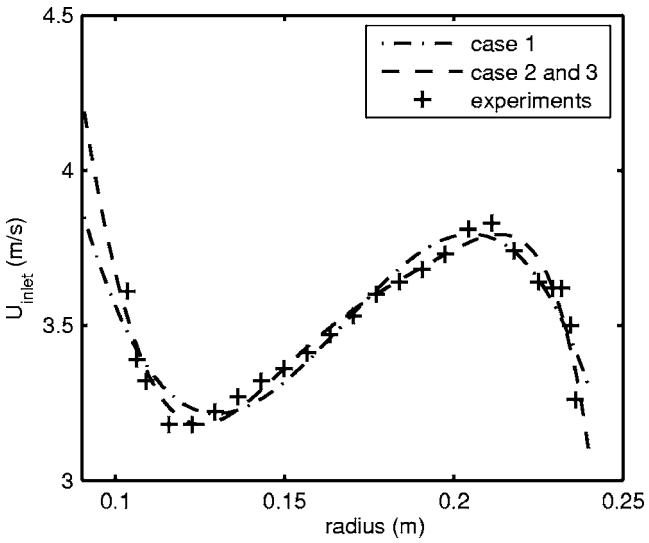

Fig. 12 Interpolated inlet axial velocity (line) and experimental values (symbol) [1]. Case 1: third-order interpolation, cases 2 and 3: sixth-order interpolation.

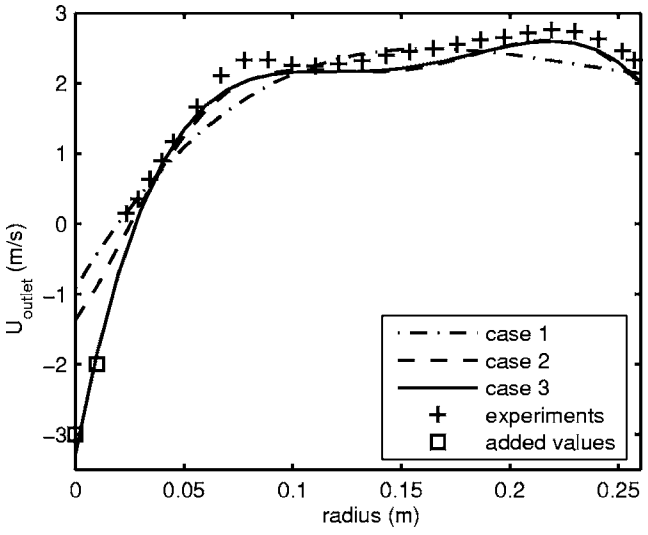

Fig. 14 Interpolated outlet axial velocity (line) and experimental values (symbol) [1]. Case 1: third-order interpolation, case 2: sixth-order interpolation, case 3: sixth-order interpolation with added values.

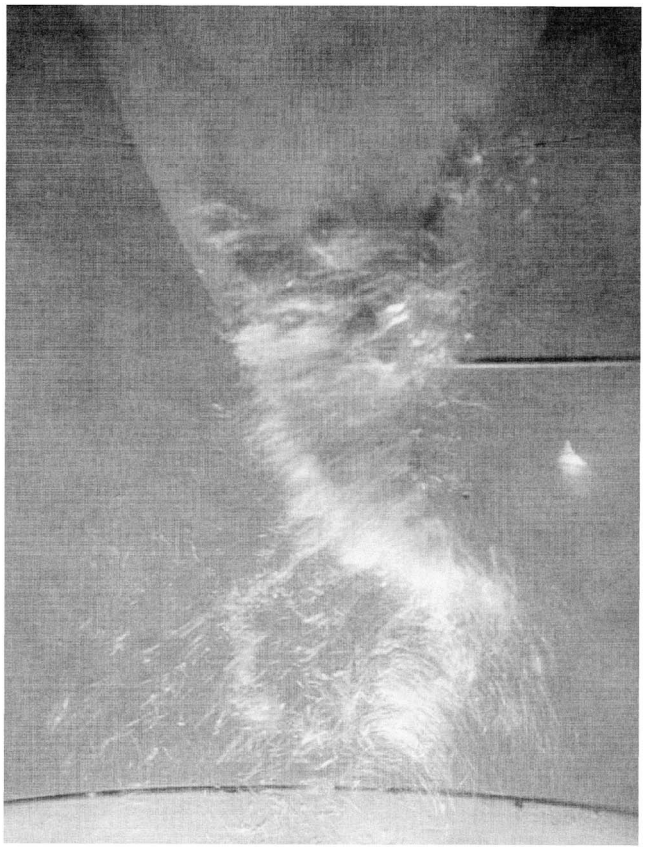

Fig. 15 Flow visualization below the cone (courtesy of Urban Andersson)

Nilsson after numerical simulation of the runner [3] and calculated with the proposed method for cases 1–3 after seven iterations are presented in Fig. 16.

The convergence is straightforward for the three cases, see the residual value $R(v)$ function of the iteration in Fig. 17, where the residual is defined by the relation (19). No conclusion may be made on the convergence even if it is better in the second and third test cases. The velocity profiles are similar in shape for the three cases. This is a sign of stability for the method.

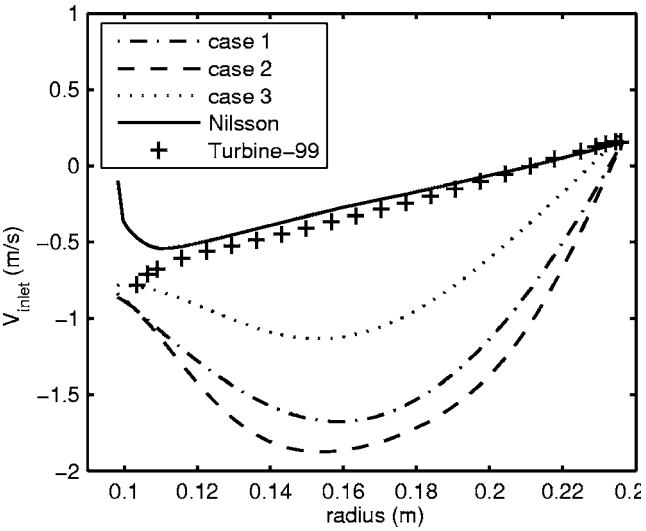

Fig. 16 Radial velocity profile proposed at the Turbine-99 workshop [3], obtained by [3] and calculated with the present method after seven iterations for cases 1–3

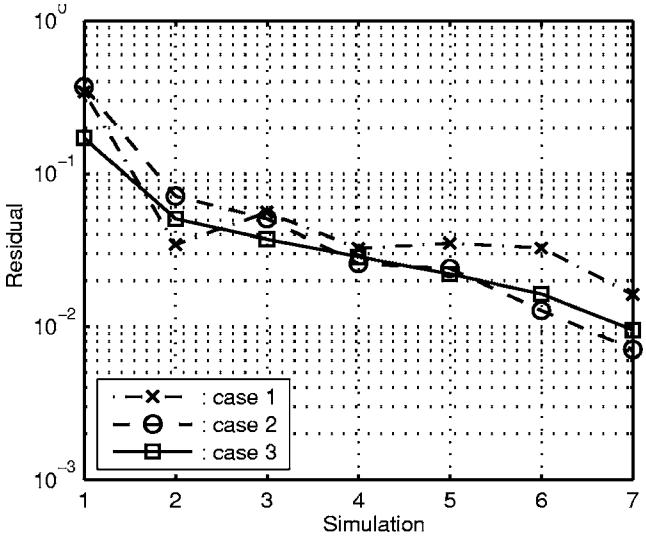

Fig. 17 Residual for test cases 1–3

The radial velocities on the cone and the wall are determined from the values of the axial velocity and the geometrical gradient, as expected. The computed profiles have significant amplitudes, especially midway between the cone and the wall. In case 3, the amplitude of the radial velocity is less important. This is expected after the addition of the outlet velocity values leading to a stronger recirculation velocity beneath the cone (see Fig. 14).

The derived profiles differ considerably from the proposed profile by the organizers of the Turbine-99 workshop. This consists of a linear profile derived from the geometrical gradient of the wall and the cone and the inlet axial velocity, such as

$$V = U \tan(\theta)$$

$$\theta = \theta_{\text{cone}} + \frac{\theta_{\text{wall}} - \theta_{\text{cone}}}{R_{\text{wall}} - R_{\text{cone}}}(r - R_{\text{cone}}) \tag{22}$$

where U is the measured axial inlet velocity, θ is the flow angle in the axial-radial direction and θ_{cone} and θ_{wall} are the angles of the runner cone and the diffuser cone wall, respectively. r is the radial coordinate from the runner axis and R_{cone} is the runner cone radius. However, simple geometrical considerations show that the volume of fluid transported toward the cone is more than twice the volume of fluid transported toward the wall. Separation occurs if such a volume of fluid is not transported toward the cone and the wall. Furthermore, many parameters work against the transfer of momentum toward the cone. The angle of the cone is important at the inlet, around 13 deg and increases downstream with 1 deg/cm, i.e., nearly 33 deg at the end of the cone. The tangential velocity creates a centrifugal force, which pulls the fluid towards the wall. Therefore, a substantial radial velocity is necessary to avoid a premature separation on the cone. The profiles calculated by Nilsson [3] and proposed by the organizers of the workshop take only into account the initial angle of the cone and the wall, the consequences of which will be later elucidated by a computation of the wall pressure recovery.

4.2 Validation. The function of a draft tube is to convert kinetic energy into static pressure. The pressure recovery is therefore a fundamental engineering quantity in the design of draft tubes. For the Turbine-99 Workshop, experimental values of the pressure recovery were available for comparison with the computed. A comparison of the pressure recovery obtained with cases

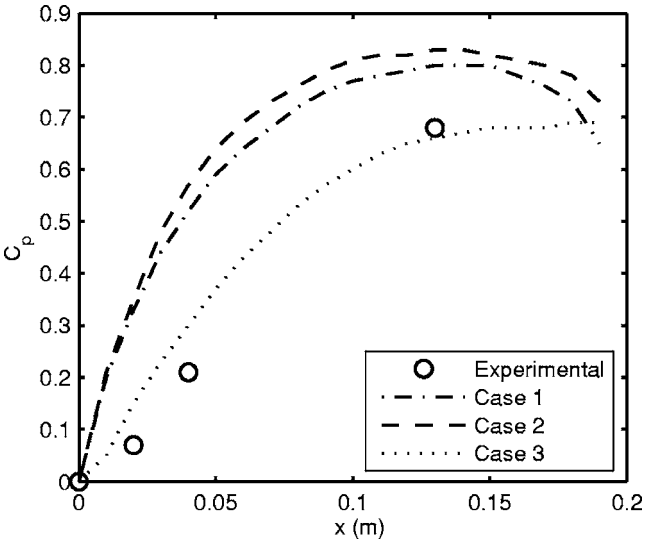

Fig. 18 Pressure recovery along the outer-wall; experimental and obtained from cases 1–3 after seven iterations

1–3 is of great interest to validate the computed results.

For the workshop, the pressure variations were normalised with the average axial flow due to the lack of information on the radial velocity. Thus, the pressure recovery on the wall is given by

$$C_p = \frac{(P_{\text{wall}} - P_{\text{wall inlet}})}{\frac{1}{2}\rho\left(\frac{Q}{A_{\text{inlet}}}\right)^2} \tag{23}$$

where Q represents the water flow rate and A_{inlet} the inlet area. The Bernoulli function being constant on the wall, the pressure recovery may be estimated from the variation of the kinetic energy

$$C_p = \frac{(u^2+v^2+w^2)_{\text{wall inlet}} - (u^2+v^2+w^2)_{\text{wall}}}{\left(\frac{Q}{A_{\text{inlet}}}\right)^2} \tag{24}$$

Figure 18 represents the pressure recovery along the wall obtained with the presented method for cases 1–3 and the experimental values available from the Turbine-99 Workshop. The numerical results correspond to the seventh iteration.

For cases 1 and 2, the pressure recovery along the wall differ slightly from each other. They are similar in shape despite the different degree of the polynomial used to interpolate the experimental data, indicating that a third-order polynomial is certainly enough to approximate the experimental data. However, the discrepancy with the experimental values is large. The assumption done on the outlet axial velocity due to the lack of data in the region, $0 \leqslant \sigma \leqslant 0.02$, beneath the cone is to a large extent responsible for it. As previously mentioned, this assumption is responsible for an important radial velocity at the inlet of the draft tube model since the recirculation region is weak. Therefore, the kinetic energy decreases quickly at the inlet along the wall accompanied by a large pressure recovery. The decrease of the pressure recovery for $x \geqslant 0.13$ is also due to the excessive inlet radial velocity. With a large inlet radial velocity, much of the fluid is directed toward the cone, allowing a large pressure recovery during the first half of the cone, as previously mentioned, since the kinetic energy decreases. However, the elliptic nature of the Squire-Long equation involve outlet experimental axial velocities, which twist back the fluid toward the wall at the end of the computed region. Thus, an increase of the kinetic energy on the wall appears decreasing the pressure recovery.

For case 3, the assumption done on the outlet axial velocity gives a wall pressure recovery in good agreement with the experimental one. For this case, the recirculation region beneath the cone is stronger (see Fig. 14). The recirculation zone decreases the amount of fluid toward the cone, and therefore, the pressure recovery on the wall compared to case 1 and 2. The decrease of pressure recovery at the end of the wall does not exist for this case, since the inlet radial velocity transport an appropriate amount of fluid toward the cone and the wall, allowing a continuous increase of the pressure recovery.

The radial velocity profile obtained with case 3 gives a pressure recovery in agreement with the experimental one. However, the profile deviates substantially from the one proposed by the organizers of the workshop, which is similar to the one calculated by Nilsson [3]. For his computation, Nilsson located the outlet after the end of the axisymmetric diffusor before the draft tube bend, with a short cylindrical section added to reduce outlet effects. Furthermore, he used fully developed Neumann boundary conditions at the outlet, which is far from the case in this region, since the boundary layer is still under development. His results show deviations from the experimental axial and tangential velocity used as inlet boundary conditions for the computed area represented in Fig. 11. At the outlet of the computed region, the results from [3] present a large discrepancy with the experimental results of the axial and tangential velocities. Good agreement with pressure recovery is obtained at the beginning of the computed area. A lower pressure recovery is obtained toward the end of the computed area, which may be partially explained by an under estimation of the radial velocity.

5 Discussion

The discrepancy in the results of the Turbine-99 Workshop points out the importance of consistent boundary conditions to perform a qualified numerical simulation, especially for critical variables such as the radial velocity in swirling flow in geometry with variable area. The utilization of inadequate boundary conditions may give convergence problems and/or odd solutions, where the implemented boundary conditions appear in the first line of cells and mysteriously change to new values afterward. The utilization of *qualified assumptions* are far from recommended as well; see the influence of the radial velocity on the pressure recovery for the Turbine-99 workshop. Therefore, the present method is particularly attractive for CFD simulations of nearly two-dimensional and nonviscous flows (e.g., draft tube and cyclone separator), where the radial velocity is delicate or impossible to measure. The calculations performed on the Dahlhaug test case point out the applicability of the method for any two-dimensional flow with swirl number ranging from 0 to ~0.25 and high Reynolds number. The work of Wang and Ruzak [9], Goldshik and Hussain [8], and Rusak et al. [12] on the analysis of inviscid vortex breakdown in semi-infinite pipe may help to determine more precisely such limits. The method may also be applied successfully to flows with zero swirl. The assumptions made on the formulation of the method and the utilization of experimental values, obtained with some uncertainty, involve a radial velocity with some uncertainty. The results obtained on the Dahlhaug test case show a fairly acceptable uncertainty.

The approach to evaluate the radial velocity from experimental values of the axial and tangential velocity components is based on the coupling between the Squire-Long equation and the considered domain. This coupling is made possible by the consistency of the Bernoulli function on streamlines for nonviscous flows, which induces the presence of boundary conditions in the equation itself. The detailed mechanism allowing the convergence to a radial velocity profile is far from clear. Speculation may be made on the exclusive presence of the tangential velocity in the equation; however, the method holds for flows with zero swirl. Further analysis seems necessary to detailed understand the process.

The Turbine-99 test case is of particular interest due to the lack of experimental value near the center line beneath the cone. This

lack of data has been investigated with the use of different polynomial and assumptions. The results point out the sensitivity of the method to the inlet and outlet boundary conditions. A good approximation of the outlet axial velocity and, thus, the radial velocity was found after comparison of the calculated and experimental pressure recovery. Comparison of the pressure recovery obtained with the present method and with CFD simulation using the same inlet radial velocity will be of great interest, since most of the participants of the second workshop found a lower pressure recovery than the experimental one in this region.

Appendix

The determination of the stream function on the domain is made with the relation (1) and an interpolation of experimental values of the axial velocity at the inlet and outlet. Such an approach induces different values of the stream function on the wall at the inlet and outlet. As a matter of fact, the experimental values are determined at certain points with some uncertainty, the flow are nearly two-dimensional and losses are present in the system. The difference in the value of the stream function at the wall is small but necessitates some modification of the inlet or outlet stream function to satisfy the continuity equation.

The interpolation of the axial velocities being performed with polynomials, the functions describing them can be written in a general form, such as

$$u_{\text{inlet}} = \sum_{i=0}^{n} a_i \sigma^i \tag{A1}$$

$$u_{\text{outlet}} = \sum_{i=0}^{n} b_i \sigma^i \tag{A2}$$

where n represents the degree of interpolation of the experimental values. The stream function is obtained using the relation (1)

$$\psi_{\text{inlet}} = \int \sigma u_{\text{inlet}} \mathrm{d}\sigma = \sum_{i=0}^{n+2} \frac{a_i}{(i+1)(i+2)} \sigma^{i+2} \tag{A3}$$

$$\psi_{\text{outlet}} = \int \sigma u_{\text{outlet}} \mathrm{d}\sigma = \sum_{i=0}^{n+2} \frac{b_i}{(i+1)(i+2)} \sigma^{i+2} \tag{A4}$$

The adjustment is performed on the coefficient attached to the lowest power in the polynomial describing the outlet stream function, such as

$$b_0 = \frac{2}{\sigma^2_{\text{wall outlet}}} \left[\psi_{\text{inlet}}(\sigma_{\text{wall inlet}}) - \sum_{i=1}^{n+2} \frac{b_i}{(i+1)(i+2)} (\sigma_{\text{wall outlet}})^{i+2} \right] \tag{A5}$$

The value of the stream function on the wall at the inlet and outlet are identical with this construction and, thus, the flow rate. The choice of b_0 is motivated by the lack of experimental value close to the center line in the Turbine-99 test case and the importance of the turbulence intensity on the center line in the Dahlhaug test case at high swirl number, b_0 represents the axial velocity on the centerline of the domain.

References

[1] Gebart, B. R., Gustavsson, L. H., and Karlsson, R. I., 2000, *Proceedings of Turbine-99 Workshop on Draft Tube Flow*, Porjus, Sweden, June 20–23, 1999, Luleå University of Technology, Technical Report.

[2] Page, M., and Giroux, A. M., 2000, "Turbulent Computation in Turbine-99 Draft Tube," CFD2K: 8th Annual Conference of the CFD Society of Canada, June 11–13, Montreal.

[3] Engström, T. F., Karlsson, R. I., and Gustavsson, L. H., 2001, "The Second ERCOFTAC Workshop on Draft Tube Flow," Älvekarleby, Sweden, June 18–20, http://www.luth.se/depts/mt/strl/turbine99/

[4] Cervantes, M. J., and Engström, T. F., 2004, "Factorial Design Applied to CFD," ASME J. Fluids Eng., **126**(5), pp. 791–798.

[5] Buntine, J. D., and Saffman, P. G., 1995, "Inviscid Swirling Flows and Vortex Breakdown," Proc. R. Soc. London, Ser. A, **449**, pp. 139–153.

[6] Batchelor, G. K., 1967, *An Introduction to Fluid Mechanics*, Cambridge University Press, Cambridge, England, pp. 543–545.

[7] Meissel, E., 1873, "Über den Aususs des Wassers aus Gefässen in zwei besonderen Fällen nach Eintritt des Beharrungszustandes," Arch. Math. Phys., Bd. 55.

[8] Goldshtik, M., and Hussain, F., 1998, "Analaysis of Inviscid Vortex Breakdownin a Semi-Infinite Pipe," Fluid Dyn. Res., **23**, pp. 189–234.

[9] Wang, S., and Rusak, A., 1997, "The Dynamics of Swirling Flow in a Pipe and Transition to Axisymmetric Vortex Breakdown," J. Fluid Mech., **340**, pp. 177–223.

[10] MathWorks, 2004, *Partial Differential Equation for Use With MATLAB Toolbox, Users Guide Version 1*, The MathWorks, Inc., Natick, MA.

[11] Dahlhaug, O. G., 1997, "A Study of Swirl Flow in Draft Tube," Ph.D. thesis, NTNU Trondheim, Norway.

[12] Rusak, Z., Wang, S., and Whiting, C. H., 1998, "The Evolution of a Perturbed Vortex in a Pipe to Axisymeetric Vortex Breakdown," J. Fluid Mech., **366**, pp. 211–237.

Finite Element and Neural Network Modeling of Viscoelastic Annular Extrusion

Han-Xiong Huang
Professor
e-mail: mmhuang@scut.edu.cn

Yan-Sheng Miao

Center for Polymer Processing Equipment and Intellectualization,
College of Industrial Equipment and Control Engineering,
South China University of Technology,
Guangzhou, P.R.C.

Plastics blow molding has grown rapidly for the past couple of decades. Annular parison extrusion is a critical stage in extrusion blow molding. In this work, numerical simulations on the parison extrusion were performed using finite element (FE) method and the Kaye-Bernstein-Kearsley-Zapas type constitutive equation. A total of 100 simulations was carried out by changing the extrusion die inclination angle, die gap, and parison length. Then a backpropagation artificial neural network (ANN) was proposed as a tool for modeling the parison extrusion using the numerical simulation results. The network architecture determination and the training process of the ANN model were discussed. The predictive ability of the ANN model was examined through several sets of FE simulation results different from those utilized in the training stage. The effects of the die inclination angle, die gap, and parison length on the parison swells can be predicted using the ANN model. The results showed that the die gap has a smaller effect on the diameter swell but a greater effect on the thickness swell. Both diameter and thickness swells increase as the die inclination angle increases. The hybrid method combining the FE and ANN can shorten the time for the predictions drastically and help search out the processing conditions and/or die geometric parameters to obtain optimal parison thickness distributions. [DOI: 10.1115/1.2409357]

Keywords: blow molding, parison extrusion, finite element simulation, neural network model

1 Introduction

Blow molding is a major polymer processing technique for manufacturing a wide variety of hollow plastic parts. It has grown rapidly for the past couple of decades. The blow molding is commonly subdivided into two main classes, i.e., the extrusion blow molding and injection stretch blow molding [1]. The former is the major blow molding category with a number of technical and economical advantages concerning the low-pressure characteristic of the process. It is traditionally used to produce packaging containers of various sizes and shapes (axisymmetric and nonaxisymmetric), but is progressively adapted to manufacture irregular complex-shaped parts for the automotive, office automation equipment, houseware, and electronic industries, etc.

The extrusion blow molding process involves the extrusion of a hollow tube, i.e., parison, through an annular die, which is pinched at the bottom end, and is then inflated inside the mold cavity. Parison extrusion is a critical stage, besides, is rather complex in that the parison dimensions, including the diameter and thickness, depend on the complex interaction of two phenomena called swell and sag. The parison swell, occurring both in diameter and thickness, is due to the molecular relaxation of the nonlinear viscoelastic deformation imposed on the polymer melt during its flow in the extrusion die. The gravity acting on the parison is the cause of the sag, where the parison is pulled down by its own weight. The swell and sag will increase and decrease the diameter and thickness of the parison, respectively. The actual swell of an annular parison under the effect of sag can be described using two swell ratios, namely, diameter swell (S_D) and thickness swell (S_H)

$$S_D = \frac{D_p}{D_0} \tag{1}$$

$$S_H = \frac{H_p}{H_0} \tag{2}$$

as shown in Fig. 1, D_0 and H_0 are the outer diameter and the lip gap of the annular die, respectively; D_p and H_p are the outer diameter and the thickness of the parison, respectively.

The actual swell determines the parison dimensions just prior to inflation, which are critical to the inflation stage, since these dimensions constitute starting point of the inflation stage and directly influence the final part dimension distribution. Since the last decade, reducing the weight becomes one of the main demands for the design of packaging containers. Therefore, process optimizing tends to produce packaging containers of minimum thickness having the best mechanical properties. So there is considerable effort in studying the annular extrusion from the parison die both experimentally and theoretically. Orbey and Dealy [2] investigated the effects of die geometry on isothermal annular swell using a modified capillary rheometer. Several research teams modeled the parison extrusion stage to predict the parison dimensions [3–8]. Early Luo and Mitsoulis [3] carried out finite element simulations of the annular swell from various types of dies using Kaye-Bernstein-Kearsley-Zapas (K-BKZ) type constitutive equation. Numerical simulations on the parison extrusion help minimize machine setup times and tooling costs as well as optimize processing parameters to yield desired final part specifications.

But numerical simulations on the swell and sag in the parison extrusion are quite time consuming [2–4]. Furthermore, swell or sag is a nonlinear behavior. This means that the dependency between parison dimensions and materials characteristics, processing conditions, and die geometry is a nonlinear one. Artificial neural networks (ANNs), as mathematical models developed to mimic certain information storing and processing capabilities of the brain of higher animals, can model highly nonlinear systems

Contributed by the Fluids Engineering Division of ASME for publication in the JOURNAL OF FLUIDS ENGINEERING. Manuscript received September 6, 2005; final manuscript received July 25, 2006. Assoc. Editor: Dennis Siginer. Paper presented at the 2005 ASME International Mechanical Engineering Congress and Exposition.

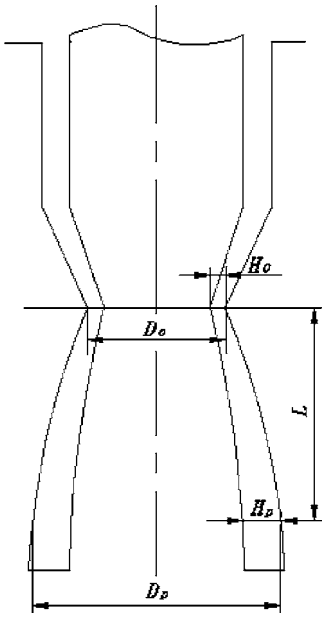

Fig. 1 Schematic of extrusion die of parison and its swells

without using complex deduction rules or large data. The ANN has been applied in many engineering applications. DiRaddo and Garcia-Rejon [9,10] utilized ANN method to predict final part dimensions from initial parison dimensions and initial parison dimensions from the specified final part thickness, respectively. Based on a series of experimental data, Huang et al. constructed the neural network models to predict the dimensions of the parison extruded from the straight die [11,12] and convergent die [13] in the extrusion blow molding and showed that the method combining the experiment and ANN can accurately predict the parison dimensions. The primary objective of the present work was to study the possibility of predicting the parison dimensions through an ANN model developed on the basis of the data taken from the finite element (FE) simulations.

2 Finite Element Simulation

The parison extrusion process can be considered as an annular extrudate swell problem of viscoelastic fluids. An isothermal, steady, and axisymmetric flow of an incompressible fluid was assumed in this work. So the equations of continuity and motion are described as

$$\nabla \cdot \mathbf{v} = 0 \tag{3}$$

$$-\nabla p + \nabla \cdot \tau + \rho g = 0 \tag{4}$$

where $\mathbf{v}$ is the velocity vector, p is the pressure, $\boldsymbol{\tau}$ is the extra stress tensor, ρ is the melt density, and g is the gravity.

The material used in the simulation was high-density polyethylene (HDPE). Its constitutive behavior was described by the K-BKZ integral model with a relaxation spectrum [14,15]

Table 1 Relaxation time spectrum for the HDPE used in simulations

i	λ_i (s)	G_i (Pa)
1	0.0054	296550
2	0.09	60220
3	1	12784
4	10	2075
5	100	735
6	500	92

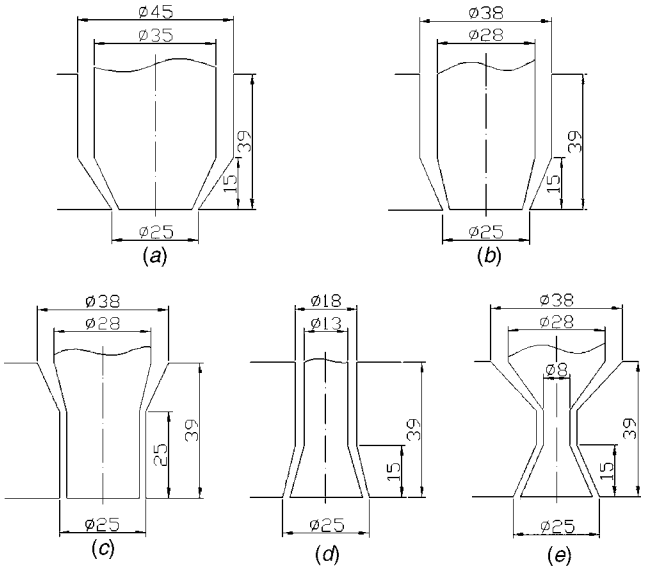

Fig. 2 Parison extrusion die geometry used in the simulations. All dimensions are in mm. (*a*) Die 1—Convergent die with a die inclination angle (Ø) of 33.7 deg; (*b*) Die 2—Convergent die with Ø of 23.4 deg; (*c*) Die 3—Straight die; (*d*) Die 4—Divergent die with Ø of −14.9 deg, and (*e*) Die 5—Divergent die with Ø of −23.4 deg.

$$\boldsymbol{\tau} = \frac{1}{1-\theta}\int_0^{\infty}\sum_{i=1}^{N}\frac{G_i}{\lambda_i}\exp\left(\frac{-s}{\lambda_i}\right)H(\mathbf{I}_{\mathbf{c}_t^{-1}},\mathbf{I}_{\mathbf{c}_t})[\mathbf{C}_t^{-1}(t-s)+\theta\mathbf{C}_t(t-s)]ds \tag{5}$$

where G_i and λ_i are the relaxation modulus and the relaxation time, respectively, $\mathbf{C}_t^{-1}$ is the Finger strain tensor, $\mathbf{C}_t$ is the Cauchy-Green strain tensor, $\mathbf{I}_{\mathbf{c}_t^{-1}}$ and $\mathbf{I}_{\mathbf{c}_t}$ are the scalar invariants of the Finger strain tensor and the Cauchy-Green strain tensor respectively, s is a time interval, θ is a material coefficient, H is the Wagner damping function and is giving by

$$H = \exp(-\alpha\sqrt{\beta I_{C_t^{-1}} + (1-\beta)I_{C_t} - 3}) \tag{6}$$

where α and β are the material constants.

The sample material was an extrusion blow molding grade HDPE (grade 5300B) manufactured by Petrochina Daqing Petrochemical Company. The relaxation time spectrum required by the K-BKZ constitutive model was obtained from dynamic storage modulus and dynamic loss modulus data measured as a function of frequency and at a temperature of 200°C using the advanced rheometric expansion system by Rheometric Science. The dynamic storage modulus and dynamic loss modulus data obtained at different frequencies were then analyzed with a linear regression method using a program developed based on the MATLAB

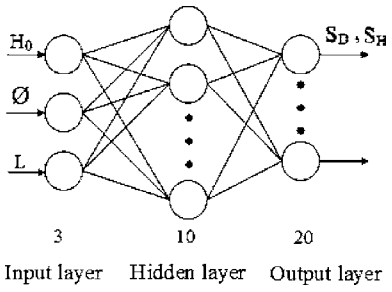

Fig. 3 Schematic of BP neural network architecture used in this work

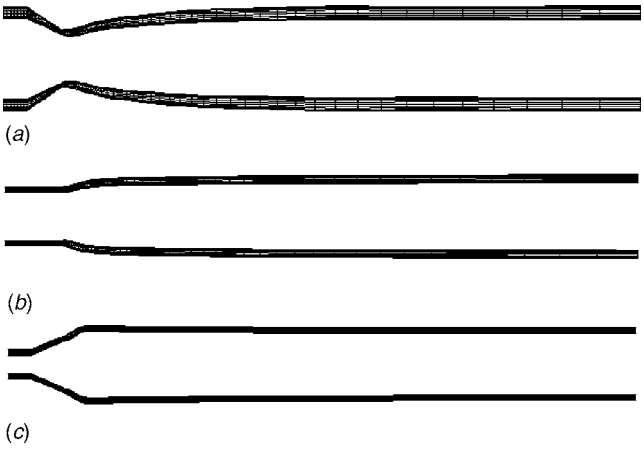

Fig. 4 Simulated profiles of the parison with a length 250 mm for (*a*) die 1, (*b*) die 3, and (*c*) die 5. The die gap is 2 mm.

software by the authors. The truncated relaxation time spectrum is listed in Table 1.

Five extrusion dies, shown in Fig. 2, were used for simulations in this work. Among them, two dies, denoted as dies 1 and 2, were convergent ones with a die inclination angle of 33.7 and 23.4 deg, respectively. One die was a straight one and denoted as die 3. The other two dies, denoted as dies 4 and 5, were divergent ones with a die inclination angle of −14.9 and −23.4 deg, respectively. All dies had an outer diameter of 25 mm. The land length for the straight die was 25 mm and the converging or diverging section length for the convergent or divergent dies was 15 mm.

The Polyflow software [16] was used to carry out the simulation works. A quadrilateral element was used during meshing. In order to assure the convergence in the minimum computer time, the meshes were refined near the die exit, near the two free surfaces (inner and outer surfaces) of the parison, and at the flow direction transition region within the die. Totally 310, 470, and 550 elements were used for the parisons with a length of 50, 150, and 250 mm, respectively. An upwinding method was used to solve the flow fields. An evolutionary scheme was used to determine the locations of the two free surfaces of the parison.

During the simulations, the melt temperature was kept at 200°C and the constant extrusion flow rate was set at 10.3 kg/h. The material constant α in the irreversible Wagner damping function was determined by comparing the shear viscosity curves obtained under different values of α and the complex viscosity curve obtained by the above-mentioned dynamic measurement. A value of α=0.28 was chosen via comparison. This value resulted in the best fit for the two viscosity curves. A small value of the material constant β in the damping function enhances extensional deformation effects [4]. In this work, the β value was determined by several trial simulations and comparing the simulation results with the corresponding experimental data. The results showed that a smaller value of β (=0.13) can better represent the occurrence of the extensional deformations within the dies shown in Fig. 2. The material coefficient θ was set as −0.1. A series of simulations were done by changing the die inclination angle (33.7, 23.4, 0, −14.9, and −23.4 deg), die gap (2.0, 2.6, 3.3, and 4.0 mm), and parison length (50, 100, 150, 200, and 250 mm).

3 Neural Network Modeling

A neural network can be considered as a collection of simple processing units, called neurons or nodes, which are mutually interconnected with variable weights. This system of units is organized to transform a set of given input signals into a set of given output signals. This transformation is organized as follows: each node of the network computes first its activation as a weighted sum of incoming signals. Then the node transforms its activation by the nonlinear transfer function and sends it to every connected node.

3.1 Determination of the Network Architecture. It was shown (e.g., Ref. [17]) that the ANNs with only one hidden layer can approximate any function, given that sufficient degrees of freedom (i.e., connection weights) are provided. So the topology of the neural network used in this work had one hidden layer.

The die gap (H_0), die inclination angle (Ø), and parison length (L) were the neural network model's inputs and the diameter swells (S_D) or thickness swells (S_H) of 20 points along the parison during its extrusion process were its outputs. That is, the neuron numbers of output and input layers were 3 and 20, respectively. However, there is not yet theoretical guidance to the determination of the number of neurons in the hidden layer. Using insufficient neurons impairs the neural network and prevents the correct mapping of input to output. Using too many neurons impedes generalization and increases training time. The number of hidden neurons can be determined through experimentation [12,13]. Here it was determined by the following equation

$$m = l - 0.618(l - n) \tag{7}$$

where l, m, and n are the neuron numbers of output, hidden, and input layers, respectively. Ten hidden neurons were finally determined for the network model. So a 3–10–20 backpropagation (BP) network was constructed and its configuration is shown in Fig. 3.

3.2 Network Training and Testing. A total of 100 simulations was carried out by changing the three input variables within the ranges as mentioned in the Sec. 2 and the outputs were recorded. And then generated inputs/outputs were used to model the process. This is a given input-known output (target) problem and forms an input pattern. After each forward transmission of the

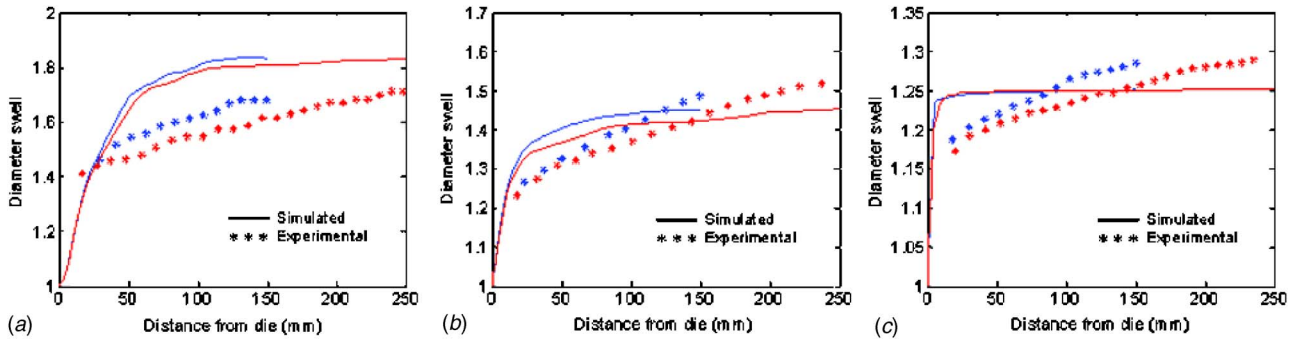

Fig. 5 Simulated and experimentally determined parison diameter swells extruded from (*a*) die 1, (*b*) die 3, and (*c*) die 5. The die gap is 2 mm.

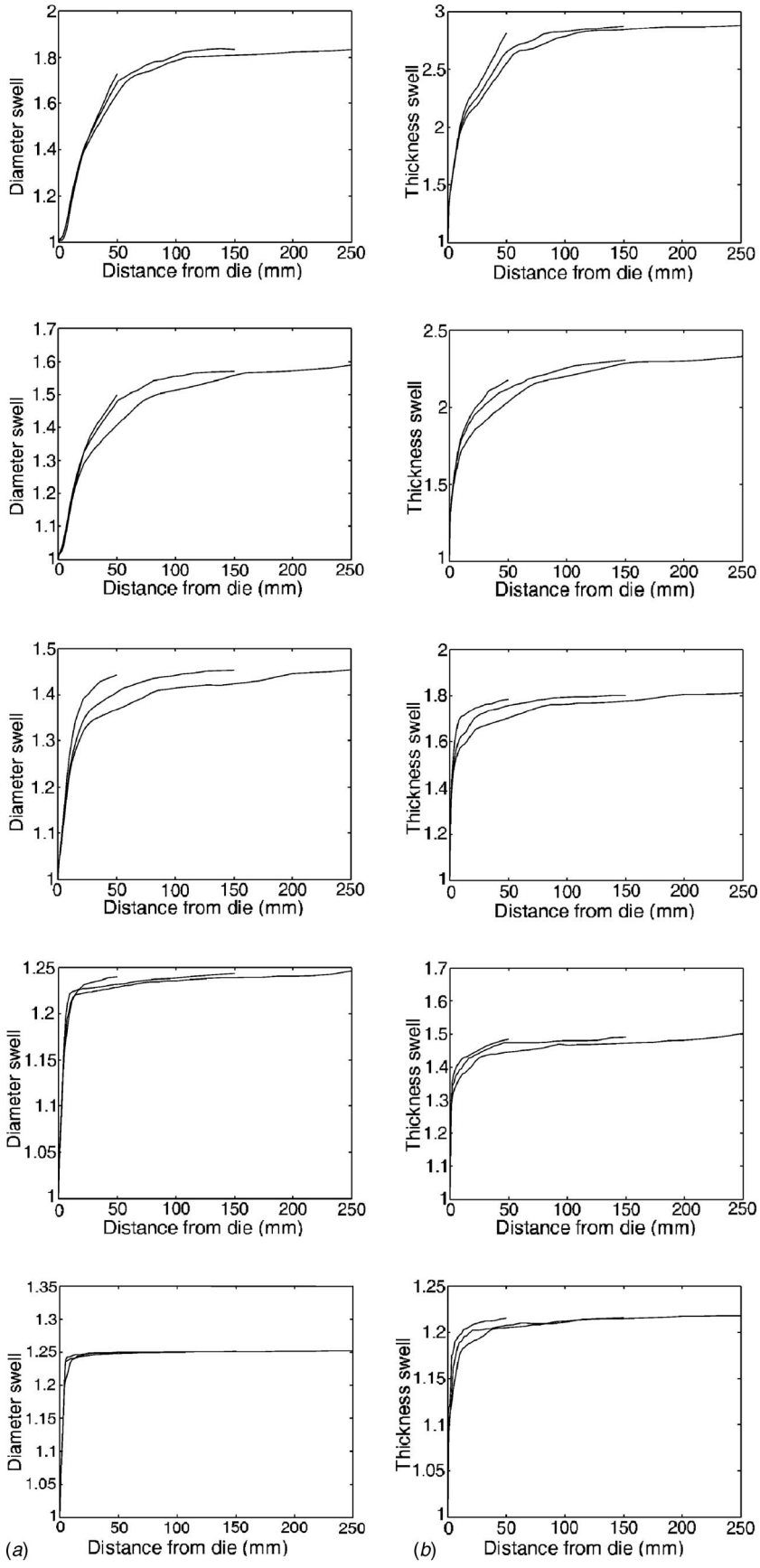

Fig. 6 Simulated (*a*) diameter and (*b*) thickness swells of the parison with a length of 50, 150, and 250 mm for (1) die 1, (2) die 2, (3) die 3, (4) die 4, and (5) die 5. The die gap is 2 mm.

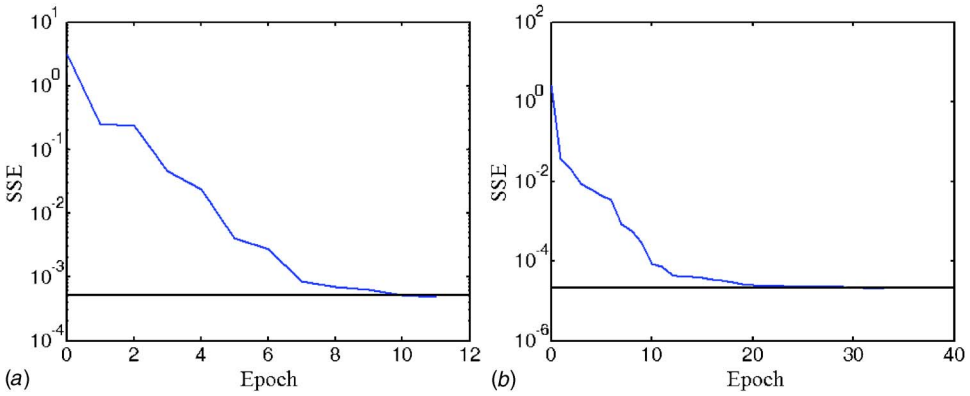

Fig. 7 SSE for the training patterns during the training of the network for (*a*) diameter and (*b*) thickness swells

input signal through the network the transformed signal was compared with the target value and the error was computed. The connection weights (strengths) between the cells were adjusted to reduce the total error between the current network response and the corresponding target. This process is called "training" or "learning." The process of weights correction was continued until the difference between the neural network output and the desired, known output was minimized for a whole set of pairs: given input-known output. Finally, the validity of the ANN model to predict the outputs was examined against several sets of finite element simulation results that not used as part of the training data. In this work, 90 data sets among 100 data sets were used as training patterns to train the neural network to ascertain its weight and threshold values. The remaining ten data sets were used as testing patterns to test the trained neural network.

It was shown that in many cases, a sigmoid activation function yields good learning results [18]. So the hyperbolic tangent sigmoid activation function shown below was used in this study

$$f(x) = \frac{1 - e^{-x}}{1 + e^{-x}} \tag{8}$$

It is usually necessary to preprocess the data before presenting the patterns to the BP network because the hyperbolic tangent sigmoid activation function modulates the output of each neuron to values between −1 and 1. Here the following normalization procedure was used

$$V' = 2\frac{V - V_{\min}}{V_{\max} - V_{\min}} - 1 \tag{9}$$

where V is the original data, $V_{\min}$ and $V_{\max}$ are the minimum and maximum values of V, respectively, and V' is the normalized data of the corresponding V. Thus, each value V is scaled to its normalized value V' between −1 and 1.

In this work, the Levenberg-Marquardt BP (LMBP) algorithm [19,20], an improved version of BP with the fastest convergence speed, was utilized during the training procedure. The LMBP algorithm is based on the Levenberg-Marquardt method, which is a variation of Newton's method. The method converges quickly in many applications because general functions can be accurately approximated by quadratic functions in a small neighborhood. Once the sum of squared error (SSE) for the training patterns reduced within a given tolerance (set at 5×10^{-4} and 2×10^{-5} for the diameter and thickness wells, respectively, in this work), or the number of training iterations reached a predetermined one (set at 100 in this work), the network training course was stopped.

4 Results and Discussion

Figure 4 shows the simulated profiles of the parison extruded from dies 1, 3, and 5 using the FE method. As can be clearly seen there is a sharp increase for the diameter and thickness of the parison near the die exit. Moreover, both diameter and thickness are largest for the convergent die and smallest for the divergent die. This is because the convergent die results in greater molecular orientation and axial and radial stresses to the polymer melt and so leads to larger parison swells. Figure 5 compares the simulated and experimentally determined parison diameter swells extruded from dies 1, 3, and 5. The experimental data were obtained online. The details on the online image acquisition and analysis technique can be found in Ref. [21]. As can be seen that some difference exists between the numerical prediction and the experimental data, but the varying trend of the two is in reasonably good agreement, especially for the straight die.

Some simulated results of the parison swells, including the diameter and thickness swells, are depicted in Fig. 6. It can be clearly seen that the swells tend to plateau values after the parison exceeds a larger length (about 100–150 mm) for the convergent and straight dies (dies 1–3), but a much smaller length (about 10–50 mm) for the divergent dies (dies 4 and 5).

The neural networks were trained by providing the data obtained from the FE simulation. Figure 7 presents the SSE for the training patterns during the training of the network. The figure shows that the SSE for the training patterns reached a predetermined one after about only 10 and 27 training iterations for the diameter and thickness swells, respectively. Upon training of the network, its performance was tested on ten sets of data different from those used in the training phase. After testing the trained network, the error between the predicted output value from the network model and numerical simulation value could be obtained. The comparison between the predicted parison swells from the trained network model and corresponding numerical simulation results is shown in Fig. 8. It can be clearly observed that quite a good agreement is obtained between the two. The SSE for the parison swells predicted from network model is very small (less than 0.002), that is, the trained neural network model shows a high degree of prediction precision.

The trained neural network model ascertains the quantitative relationships between the parison swells and the die gap, die inclination angle, and parison length. Thus, the parison swells or the dimensions including the diameter and thickness under the effect of sag can be predicted from new levels of input variables, thereby reducing the amount of numerical simulation, which might be very time consuming. Using a personal computer with Pentium III 800 CPU and 256 MB memory, about 30 min was required for every simulation by Polyflow finite element software, while only 10 s for training the ANN model and less than 1 s for every prediction from the trained ANN model in this work. So the hybrid method combining the finite element and neural network can shorten the time for the predictions drastically. The trained neural network model can be used to predict the outputs with a high

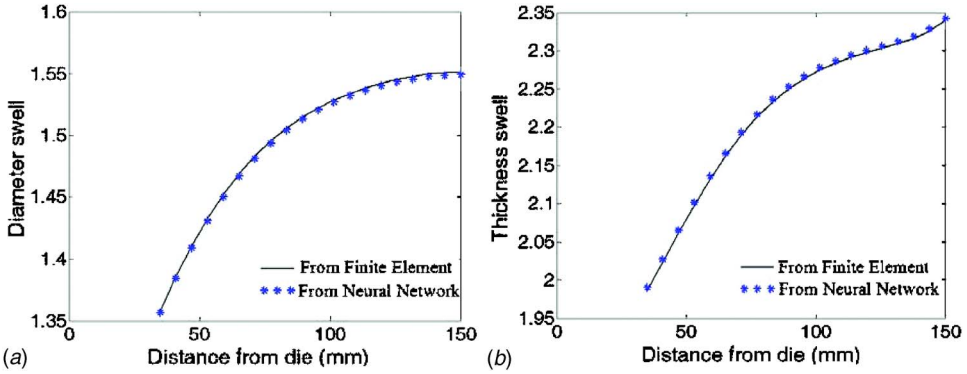

Fig. 8 Comparison of predicted (*a*) diameter and (*b*) thickness swells of parison from the network model with numerical simulation results. The die gap is 2 mm.

degree of prediction precision within the range of the FE simulations. Of course, the prediction can also be made outside the range of the FE simulations, but the degree of prediction precision will be lower.

Figure 9 illustrates the effect of the die gap on the ultimate swells, i.e., the swells at the extreme bottom of the parison, predicted by the network model at five different die inclination angles. As can be seen, the die gap has a little effect on the diameter swell. The thickness swell almost increases as the die gap decreases. This can be explained as follows. The thickness swell of the parison is primarily determined by the molecular orientation occurring due to the shear and extensional stresses imposed on the polymer melt during its flow within the extrusion die. The smaller die gap results in more rapidly converging streamlines, greater shear and extensional stresses, enhanced molecular orientation, and consequently a larger thickness swell.

Figure 10 shows the effect of the die inclination angle on the ultimate swells predicted by the network model at three different die gaps. It is seen that both diameter and thickness swells increase as the die inclination angle increases. This is because the molecular orientation and axial and radial stresses experienced by the polymer melt increase with increasing the die inclination angle.

Some results of the swell prediction of the parison with differ-

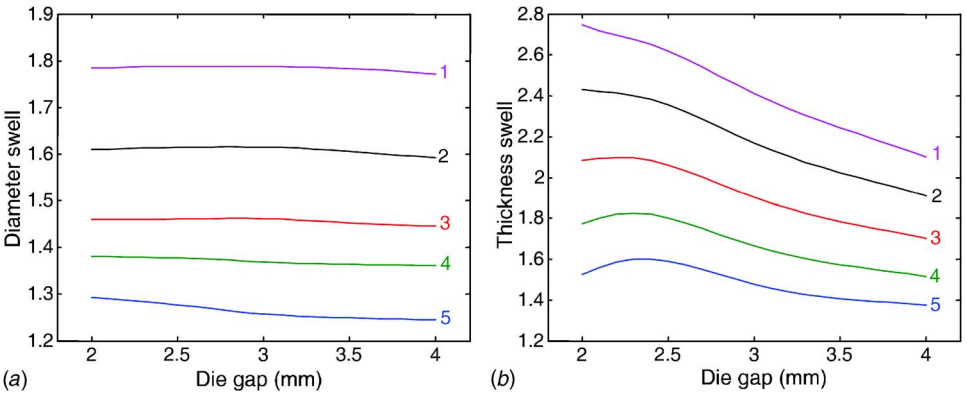

Fig. 9 Effect of the die gap on the ultimate (*a*) diameter and (*b*) thickness swells predicted from the network model for the die inclination angle of (1) 24, (2) 16, (3) 8, (4) 0, and (5) –8 deg

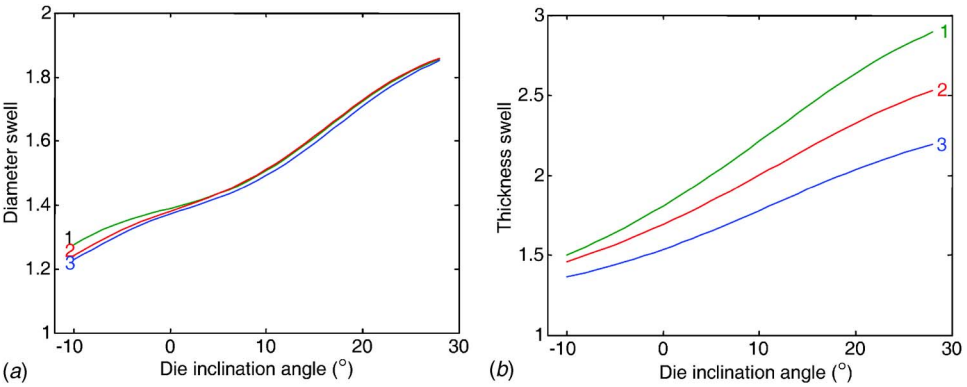

Fig. 10 Effect of the die inclination angle on the ultimate (*a*) diameter and (*b*) thickness swells predicted from the network model for die gap (mm) of (1) 2, (2) 3, and (3) 4

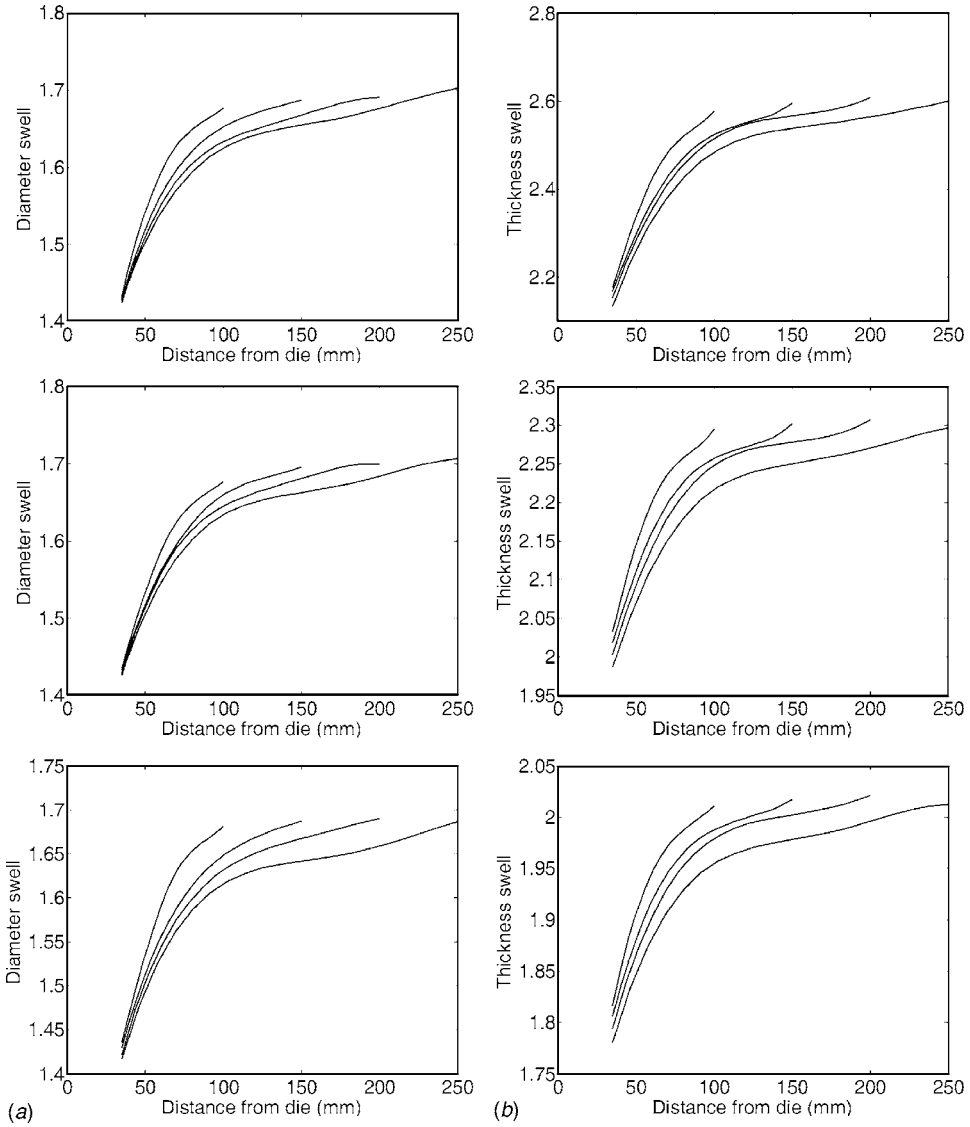

Fig. 11 Predicted parison (*a*) diameter and (*b*) thickness swells for different lengths from the network model at the die gap (mm) of (1) 2, (2) 3, and (3) 4. The die inclination angle is 20 deg.

ent lengths by the network model are shown in Fig. 11. As can be seen, the swells at the same distance from the die exit decrease gradually with increasing the parison length.

5 Conclusions

A series of simulations on the parison extrusion stage in plastics extrusion blow molding were implemented by the FE method using five extrusion die inclination angles, four die gaps, and five parison lengths. The FE simulation results showed that the parison swells tend to plateau values after the parison exceeds a larger length for the convergent and straight dies, but a much smaller length for the divergent dies. Based on the obtained inputs/outputs data, an ANN model was proposed. The ANN model can be used to predict the parison swells, including diameter and thickness swells, under the effect of sag, from different die inclination angle, die gap, and parison length. The results showed that the die gap has a smaller effect on the diameter swell but a greater effect on the thickness swell. Both diameter and thickness swells increase as the die inclination angle increases. The hybrid method combining the FE and ANN can shorten the time for the predictions drastically and help search out the processing conditions or die geometric parameters to obtain optimal parison thickness distributions.

Acknowledgment

Financial support provided by the National Natural Science Foundation of China (50390096), SRFDP (20010514002), Major Project of Key Fields in Guangdong-Hongkong (2004A10402003), and Teaching and Research Award Program for Outstanding Young Teachers in Higher Education Institutions of MOE, P.R.C. is gratefully acknowledged.

References

[1] Rosato, D. V., Rosato, A. V., and DiMattia, D. P., eds., 2004, *Blow Molding Handbook*, 2nd ed., Hanser, Munic.
[2] Orbey, N., and Dealy, J. M., 1984, "Isothermal Swell of Extrudate From Annular Dies; Effects of Die Geometry, Flow Rate, and Resin Characteristics," Polym. Eng. Sci., **24**, pp. 511–518.
[3] Luo, X. L., and Mitsoulis, E., 1989, "Memory Phenomena in Extrudate Swell Simulations for Annular Dies," J. Rheol., **33**, pp. 1307–1327.
[4] Garcia-Rejon, A., DiRaddo, R. W., and Ryan, M. E., 1995, "Effect of Die Geometry and Flow Characteristics on Viscoelastic Annular Swell," J. Non-

Newtonian Fluid Mech., **60**, pp. 107–128.
[5] Tanoue, S., Kajiwara, T., Iemoto, Y., and Funatsu, K., 1998, "High Weissenberg Number Simulation of an Annular Extrudate Swell Using the Differential Type Constitutive Equation," Polym. Eng. Sci., **38**, pp. 409–419.
[6] Laroche, D., Kabanemi, K. K., Pecora, L., and DiRaddo, R. W., 1999, "Integrated Numerical Modeling of the Blow Molding Process," Polym. Eng. Sci., **39**, pp. 1223–1233.
[7] Otsuki, Y., Kajiwara, T., and Funatsu, K., 1999, "Numerical Simulations of Annular Extrudate Swell Using Various Types of Viscoelastic Models," Polym. Eng. Sci., **39**, pp. 1969–1981.
[8] Tanifuji, S. I., Kikuchi, T., Takimoto, J. I., and Koyama, K., 2000, "Overall Numerical Simulation of Extrusion Blow Molding Process," Polym. Eng. Sci., **40**, pp. 1878–1893.
[9] DiRaddo, R. W., and Garcia-Rejon, A., 1993, "On-Line Prediction of Final Part Dimensions in Blow Molding: A Neural Network Computing Approach," Polym. Eng. Sci., **33**, pp. 653–664.
[10] DiRaddo, R. W., and Garcia-Rejon, A., 1993, "Modeling of Membrane Inflation in Blow Molding: Neural Network Prediction of Initial Dimensions From Final Part Specifications," Adv. Polym. Technol., **12**, pp. 3–24.
[11] Huang, H. X., and Liao, C. M., 2002, "Prediction of Parison Swell During Extrusion Blow Molding Using Neural Network Method," Polym. Test., **21**, pp. 745–749.
[12] Huang, H. X., and Lu, S., 2005, "Modeling Parison Formation in Extrusion Blow Molding by Neural Networks," J. Appl. Polym. Sci., **96**, pp. 2230–2239.
[13] Huang, H. X., and Lu, S., 2005, "Neural Modeling of Parison Extrusion in Extrusion Blow Molding," J. Reinf. Plast. Compos., **24**, pp. 1025–1034.
[14] Wagner, M. H., 1978, "A Constitutive Analysis of Uniaxial Elongational Flow Data of Low-Density Polyethylene Melt," J. Non-Newtonian Fluid Mech., **4**, pp. 39–55.
[15] Tanner, R. I., 2000, *Engineering Rheology*, 2nd ed., Oxford University Press, New York.
[16] Fluent Inc., 2001, Polyflow 3.9 User's Guide.
[17] Cybenko, G., 1989, "Approximation by Superpositions of a Sigmoidal Function," Math. Control, Signals, Syst., **2**, pp. 303–314.
[18] Rumelhart, D. E., McClelland, J. L., and PDP Research Group, eds., 1986, *Parallel Distributed Processing: Explorations in the Microstructure of Cognition*, MIT Press, Cambridge, MA.
[19] Hagan, M. T., and Menhaj, M. B., 1994, "Training Feedforward Networks With the Marquardt Algorithm," Neural Networks, **5**, pp. 989–993.
[20] Hagan, M. T., Demuth, H. B., and Beale, M., 1996, *Neural Network Design*, PWS, New York.
[21] Huang, H. X., and Li, J. C., 2006, "Fast Online Acquisition and Analysis for Parison Swell and Sag in Blow Molding," J. Appl. Polym. Sci., **101**, pp. 2399–2406.

Instantaneous Behavior of Streamwise Vortices for Turbulent Boundary Layer Separation Control

K. P. Angele
KTH,
Mekanik,
S-100 44 Stockholm, Sweden

F. Grewe
Hermann-Föttinger-Institut,
Strömungsmechanik Technische Universität,
10623 Berlin, Germany

The present study investigates turbulent boundary layer separation control by means of streamwise vortices with focus on the instantaneous vortex behavior. A turbulent boundary layer is exposed to a pressure gradient that generates a separation bubble with substantial backflow. The separation bubble is controlled by conventional passive vortex generators creating pairs of counterrotating vortices. Quantitative information is achieved by applying Particle Image Velocimetry (PIV) to the cross-stream plane of the vortices. The characteristics of a pair of counter-rotating vortices shed from a vortex generator is investigated in the near-field downstream of the vortex generator. The vortices were found to grow with the boundary layer in the downstream direction, and the maximum vorticity decreases as the circulation is conserved. The vortices are nonstationary, and the movements in the spanwise direction are larger than those in the wall-normal direction, due to the presence of the wall. The vortices fluctuate substantially and move over a spanwise distance, which is approximately equal to their size. The most probable instantaneous separation between the two vortices shed from one vortex generator equals the difference between their mean positions. The unsteadiness of the vortices contributes to the observed maxima in the Reynolds stresses around the mean vortex centers. The instantaneous vortex size and the instantaneous maximum vorticity are also fluctuating properties, and the instantaneous vortex is generally smaller and stronger than the mean vortex. A correlation was found between a large instantaneous vortex size and a low instantaneous maximum vorticity (and vice versa), suggesting that the vortices are subjected to vortex stretching. [DOI: 10.1115/1.2409327]

1 Introduction

Turbulent boundary layer separation is a flow phenomenon with great practical importance that has been extensively investigated; see, for example, the review by [1]. Separation is often accompanied by a decrease in lift and pressure recovery and an increase in undesirable pressure fluctuations, causing a severe reduction of the performance in many technical applications. For this reason, control of separation is desired. The aim of separation control is to manipulate the flow in such a way that the mean reverse flow can be reduced or even eliminated. This can be realized in many ways. The excitement of large-scale vortical structures for mixing enhancement is one example; see [2]. Freestream turbulence has a similar effect; see [3,4]. For extensive reviews on different techniques for separation control, see [5–7].

Whereas the trend today is to strive toward more complex flow control systems involving active feedback control, where the actuator output is based on the sensor information, the simplest and most cost-effective techniques for separation control are still old-fashioned passive devices of different kinds. An often applied technique is to introduce streamwise vortices by means of a vortex generator (VG) (see Fig. 1). Reference [8] applied the so-called vane-type VG. It consists of a pair of wings with a height of the order of the boundary layer thickness mounted normal to the surface and at an angle to the flow (see Fig. 1). Reference [9] examined different mixing devices and investigated their effect on the boundary layer development and separation in varying pressure gradients. They concluded that forced mixing had the same effect on the boundary layer, in terms of the spanwise-averaged displacement and momentum-loss thickness, as a relieved pressure gradient. Reference [10] investigated the design of VGs, which resulted in today widely used design criteria (see Table 1). Wing combinations producing both corotating and counterrotating vortices were tested. Based on inviscid theory, the vortex paths in the downstream direction were predicted. In an initially nonequidistant counterrotating setup, the vortices generated by one VG approach the wall and the spanwise distance between them is increased. The vortices eventually become equidistant and then approach each other in pairs with common outflow and move out from the surface. The best configuration was found using $D/d=4$, where D refers to the distance between two VGs and d refers to the distance between the blades of one VG (see Fig. 2). In such a case, the vortices stay within the boundary layer for a sufficient downstream distance. In a corotating setup, the whole system of vortices is displaced laterally but the vortices do not move out from the surface, which is beneficial for separation control. Model predictions for the flow field induced by triangular VGs were made by [11]. The model predicted experimental data well, and it was concluded that an increased benefit, in terms of increasing vortex strength, should be realized by an increased spanwise packing of VGs and by longer VGs. The most beneficial spanwise spacing was found to be $D/d=2.4$ (although values in the range $D/d=2-6$ were achieved). This is comparable to the value of $D/d=4$ recommended by [10].

Many studies have focused on minimizing the penalty drag caused by a VG; see the review by [12]. Reference [13] compared submerged devices (smaller than the boundary layer thickness) to large-scale VGs for separation control. None of the submerged types were larger than 60% of the local boundary layer thickness. The submerged devices showed a better pressure recovery pre-

Contributed by the Fluids Engineering Division of ASME for publication in the JOURNAL OF FLUIDS ENGINEERING. Manuscript received May 23, 2005; final manuscript received June 6, 2006. Review conducted by Joseph Katz.

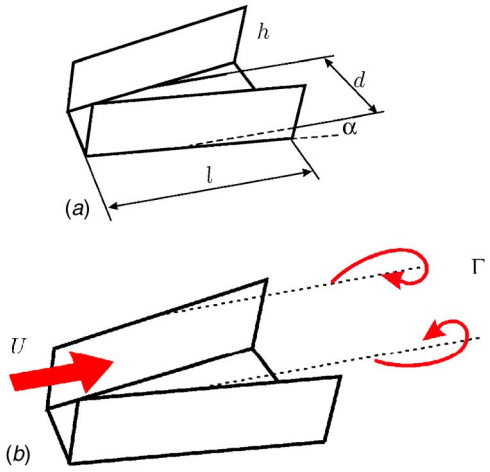

Fig. 1 Vortex generator creating counterrotating streamwise vortices in the downstream direction

sumably due to less parasite drag. Reference [14] (see also [15]) also investigated submerged VGs and compared them to conventional VGs by means of wall static-pressure measurements and flow visualization in a separated flow over a backward-facing ramp. It was found that the submerged devices were more sensitive to their relative position with respect to the mean separation line. Another way to minimize the drag associated with VGs is to apply active VGs, which can be switched off under off conditions. Reference [16] investigated wall jets introducing streamwise vortices. It was shown that skewed pairs of jets could generate the same spanwise mean wall shear stress as a VG in a zero-pressure-gradient (ZPG) turbulent boundary layer. By using thermal tufts, measuring the backflow in separated flow, it was shown that the separation could be reduced by using VG jets. The reduction of the backflow was slightly larger when using counterrotating vortices than when using corotating vortices. Reference [17] positioned micro-VGs on the rear flap of a wing profile under landing-approach conditions. The conclusion was that the drag could be reduced with a micro-VG height of 0.18% of the airfoil chord length when placed at the downstream position of 25% of the flap chord length. The relative height of the VG with respect to the boundary layer thickness, h/δ, is not clear. However, the term *micro*-VG is probably a bit misleading. Assuming δ to be on the order of 1% of the chord length, the VGs are $h/\delta=0.18$.

Table 1 VG design criteria suggested by [10]

l/h	D/d	D/h
3	4	10

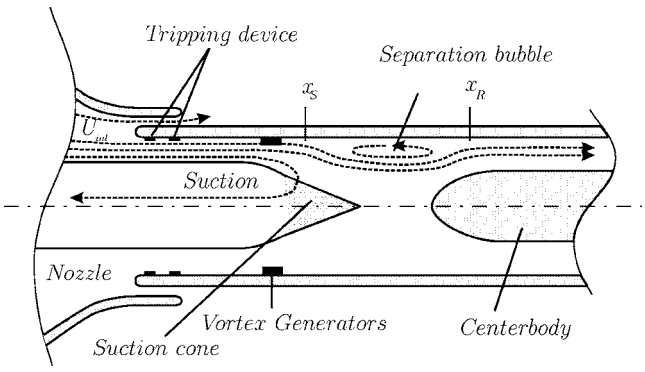

Fig. 2 Sketch of the test section

Experimental studies focused on the velocity field induced by streamwise vortices have also been carried out. Measurements of the cross-stream plane turbulence induced by a weak single streamwise vortex embedded in a ZPG turbulent boundary layer were conducted by [18]. In a companion study, [19] investigated the case of a pair of weak vortices with common outflow in the same setup. In the case of the single vortex, it was concluded that the circulation introduced by a vortex was almost conserved and that the vortex size grows with the boundary layer, in the downstream direction. Large values of the Reynolds stresses were observed around the mean vortex position. However, according to the authors, the spanwise wandering of the vortices was small. The same Reynolds stress pattern has also been observed in other studies, and it has been suggested that a wandering of the vortices might take place; see [20,21]. Large changes in the turbulence structural parameters were reported, and the general conclusion was that simple eddy-viscosity models are not likely to be able to predict such complicated Reynolds stress and turbulent diffusion patterns.

Reference [22] investigated both a vortex pair with common outflow and a vortex pair with common inflow, using Delta-wing VGs. The study was carried out in a ZPG turbulent boundary layer using a VG height of 20 mm. This corresponds to approximately 150% of the local boundary layer thickness. The length of the VG was 50 mm. The focus was on the downstream development of the vortices, in terms of vorticity and circulation. The vortex pair with common outflow was tested for three different initial distances between the vortices, 140 mm, 100 mm, and 40 mm. Only in the case where the size of the vortices was comparable to the distance between the vortices were they lifted out from the surface within the test section length (2000 mm). The peak vorticity associated with the vortices was decreased in the downstream direction by a factor of $\sim$5 and it was observed that the circulation (the integrated vorticity) was decreased by a factor of 2. For the case with common inflow, the initial VG spacing did not have any effect on the strength of the vortices but had a strong effect on the minimum boundary layer thickness downstream of a VG. The minimum boundary layer thickness was seen to decrease with decreasing initial distance between the vortices. An increase in the angle of attack did not have an effect on the minimum boundary layer thickness, but the strength of the vortices increased linearly up to an angle of attack of 18 deg.

Reference [23] observed that pairs of counterrotating vortices of the size of the boundary layer thickness, with common outflow, were lifted out from the surface. They also observed that the vortices merged into one as they developed in the downstream direction. The vortices were initially equidistant, and the distance between the vortices was approximately twice the boundary layer thickness.

As the review reveals, VGs is an old and well-established technique for separation control; however, most earlier studies have focused mainly on the change in the mean flow and, to some extent, the change in the turbulence structure. To the authors' knowledge, no studies have been made where the instantaneous vortex behavior is investigated. In order to optimize separation control based on streamwise vortices, and to be able to construct turbulence models that can capture the complicated turbulence structure, a deeper understanding of the instantaneous interaction between the vortices and a separating turbulent boundary layer can be helpful. This study is a first attempt to gain such information employing PIV. The present study was carried out in parallel to the one by [24]. The flow cases are very similar, and the same VGs were used. In the study of [24], the focus was on the change in the turbulence structure at the position of the eliminated separation bubble, and the effect of the magnitude of the circulation, the VG streamwise position, and relative height were investigated.

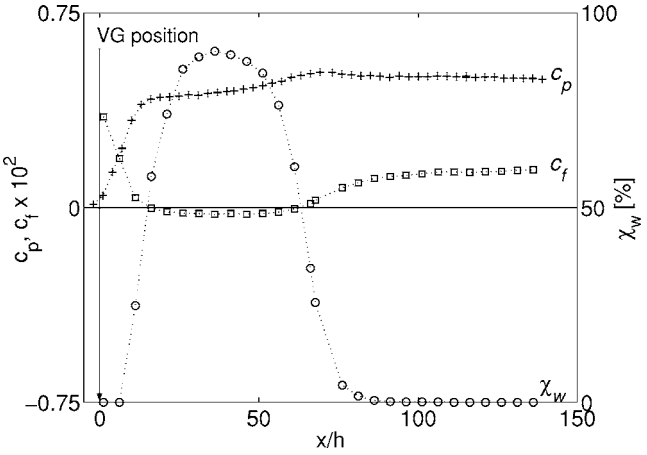

Fig. 3 Uncontrolled separated turbulent boundary layer

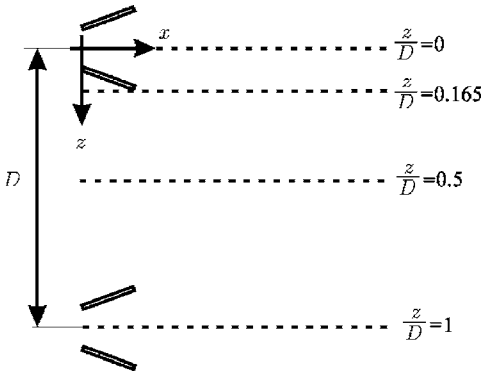

Fig. 4 VGs seen from above. The *yz* planes were captured centered around $z/D=0$, covering the region $\pm z/D=0.35$ and $y/h=4$. Spanwise positions of the *xy*-plane measurements are $z/D=0$, 0.165, and 0.5, covering $y/h=1.9$ and $\Delta x/h=2.6$.

No fundamental differences were observed for the different cases in terms of the evolution of the vortices, and therefore, the present study only investigates one standard case.

2 Method

2.1 Experimental Setup. The experiments were performed in a low-speed open-return wind tunnel at the Hermann-Föttinger-Institute (HFI). The wind tunnel is driven by a centrifugal fan located upstream of the settling chamber. To provide uniform flow conditions in the test section, the settling chamber is equipped with a nonwoven filter mat followed by a single perforated plate with an open-area ratio of 64%. Upstream of the test section, a nozzle contraction with a contraction ratio of 18.64 is accelerating the flow, damping the disturbances. For a detailed description of the wind tunnel, see [25]. The test section used here is made of Plexiglas® to allow optical access for the PIV. The test section has a circular cross section with an inner diameter of 441 mm and length of 2000 mm (see Fig. 2). This avoids end effects and eliminates problems associated with two-dimensionality, which are inherent in separation experiments. Reference [26] investigated the effect of the lateral wall curvature on the flow using a setup with a similar cross-section diameter. The shape parameter, H_{12}, differs by $<1.5\%$ compared to the planar case. Hence, the effect of the wall curvature on the velocity profiles is assumed to be negligible. The nozzle boundary layer at the end of the contraction is removed, and a new boundary layer is formed downstream of an elliptical leading edge on the inner side of the cylinder. Two rows of Dymo-tape were used as a tripping device to force transition to turbulence. Measurements were conducted at a unit Reynolds number of 9.2×10^6/m, based on $U_{\text{inl}}=14$ m/s. The level of the freestream turbulence at the inlet is $\sim0.5\%$, according to hot-wire and Laser Doppler Velocimetry (LDV) measurements. This is low enough to not have a large effect on the separation according to earlier measurements in the same setup [4]. An adverse pressure gradient (APG) was created by a concentric inner cylinder ending in a cone made of wire gauze, through which suction was applied. Downstream of the suction cone, a center body generated a favorable pressure gradient (FPG). The test section is followed by a diffuser to reduce the outflow velocity and decrease the pressure losses.

2.2 Uncontrolled Separated Turbulent Boundary Layer. The present experimental arrangement generates a streamwise pressure gradient distribution with a separation bubble (see Fig. 3). The pressure coefficient

$$c_p=\frac{p-p_\infty}{1/2\rho U_{\text{inl}}^2} \tag{1}$$

was measured using a row of 42 equally spaced static pressure taps in the streamwise direction and MKS Baratron 220C pressure transducers in the range 0–100 Pa. The accuracy is 0.15% of the full scale, giving a total error of less than ±0.4% with the present pressure range.

Also shown in Fig. 3 is the skin-friction coefficient

$$c_f=\frac{\bar{\tau}_w}{1/2\rho U_{\text{inl}}^2} \tag{2}$$

based on the mean wall shear stress, $\bar{\tau}_w$. $\bar{\tau}_w$ was measured by means of a wall pulsed-wire probe calibrated in a ZPG turbulent boundary layer against a Preston tube; see [27,28]. According to [29], the error in $\bar{\tau}_w$ using this technique is $<4\%$. The wall pulsed wire is sensitive to the direction of the flow and therefore able to measure the backflow coefficient χ_w, defined as the fraction of the total time that the flow spends in the upstream direction. This is an important quantity in a separated flow. In two-dimensional flow separation, the separation and reattachment points are defined as the locations where $c_f=0$ and $\chi_w=50\%$; see [1].

For the uncontrolled case, the mean separation, based on the VG height h, occurs at $\bar{x}_S/h=16$ and mean reattachment occurs at $\bar{x}_R/h=65$, resulting in a separation region with a length of 490 mm (see Fig. 3). The boundary layer thickness at separation is ~40 mm. The height of the mean separation bubble is only a few millimeters; however, instantaneous backflow reaches wall-normal positions in the middle of the boundary layer.

2.3 Generation of Streamwise Vortices. The streamwise vortices introduced to control the separation bubble were generated by means of fix VGs creating pairs of counterrotating vortices with common inflow. Figure 1 shows the geometry of a VG, which creates a pair of counterrotating vortices with common inflow. l is the VG side length, h the height, d is the spanwise distance between two blades (at $l/2$), and D the spanwise distance between two VGs (see Fig. 4). Table 1 shows the design criteria used here as suggested by [10]. Since $D/d=4$, the vortices are initially nonequidistant. Figure 3 shows the position of the VGs, $x/h=0$, in the early part of the pressure rise. This position was chosen based on the experiments by [24]. VGs put further upstream increase the wall shear stress too early, when it is not necessary, causing additional undesirable drag. Whereas VGs that are put further downstream, introduce vortices that might not have a sufficient distance to become equidistant, leaving pockets of backflow. The VG height was chosen as approximately equal to the local boundary layer thickness δ (see Table 2). Relatively

Table 2 Physical dimensions of the present VG

h (mm)	d (mm)	l (mm)	D (mm)
10	25	30	103

smaller VGs with $h/\delta=0.5$ and 0.3 have been shown to also work well [24]; however, in the present study it is beneficial to have large vortices to make them easier to spatially resolve. With a test section diameter of 441 mm and the present VG size, 13 VGs were used in the circumferential direction. The blade angle α was 15 deg.

2.4 Velocity Measurement Arrangements.

2.4.1 PIV Equipment. The PIV equipment used here consists of an OFS PIV system with two pulsed continuum lasers operating at 2 Hz and a PCO 12-bit digital camera with a 1024 $\times$1280 pixel CCD chip. The camera was equipped with a lens with focal length of $f=180$ mm to assure the desired image sizes. This gave a spatial resolution of 44 μm/pixel. Reference [30] showed that random errors due to poor light intensity became significant when the light intensity was below 4 bits out of 8 bit resolution. The laser, in combination with a distance between the laser sheet and the cameras, ensured that the light intensity in the images was sufficient. The particle image diameter was above two pixels, and a Gaussian peak fit was used for the subpixel interpolation, in order to minimize peak-locking effects; see [30,31]. Other PIV setup parameters were designed, according to the criteria given by [32], to minimize statistical errors introduced by peak-locking. A software system by VIDPIV was used for synchronizing and handling the measurements and for calculating the cross correlations to get the velocity vector fields. A 32 $\times$32 pixel interrogation area with 50% overlap was used for the evaluation. The validation technique was based on the peak value ratio (PVR), the ratio between the first and the second peak in the correlation plane; see [33]. The threshold value for the PVR was 1.2. An additional global filter removed vectors deviating from the overall flow field. The valid detection rate was fluctuating between approximately 90% and 95%. Removed vectors were replaced by interpolated values to be able to differentiate the instantaneous flow field and compute quantities such as the vorticity. The seeding, DEHS, was introduced in front of the fan rotor. This technique was chosen since earlier experience has shown that this is the easiest way to assure a homogeneous seeding, [34]. About ten particles are present in each interrogation area, which is above the criteria for cross-correlation PIV stated by [33,35]. The particle size was not measured in the present experiment but is estimated to be on the order of a few microns, based on the measurements by [36]. The determination of the PIV image size was done using an in-house built calibration grid with a known spatial separation. A simple statistical convergence analysis was made for the present data set. The error in the statistics was estimated as the relative difference between two successive statistical values when computed based on N and N-1 number of samples, assuming that the statistics are converging to the true value. In the present case, the error in the rms values were $\sim$4% based on 100 image pairs.

2.4.2 LDV Equipment. A two-component Dantec FiberFlow LDV system with a 300 mW argon-ion laser was used to measure the reference velocity profiles for the uncontrolled APG case. The system works on the basis of the color-separation method in backscatter mode. The resulting measurement volume was 88 μm in diameter and 1.4 mm in the spanwise direction. Between 1×10^5 and 5×10^5 bursts were collected at a data rate of up to 2 kHz.

2.4.3 Velocity Profiles in Wall-Normal Plane. Velocity and turbulence (not shown here) profiles in the xy plane were captured at the three different z positions downstream of a VG (shown in Fig. 4). The downstream positions are centered around $x/h=5.5$ and $x/h=9$. The size of the investigated area was $1.9y/h\times2.6x/h$, and the time delay between the images pairs was $\Delta t=15$ μs. Two-hundred image pairs were collected at each position.

2.4.4 Velocity Measurements in Cross-Flow Plane. Measurements capturing the vortices in the plane of rotation were made at three different positions downstream of a VG: $x/h=5.5$, 9, and 13. The size of the investigated area was $5.6y/h\times0.7z/D$ centered around $z/D=0$ (see Fig. 4). The time delay between the image pairs was $\Delta t=35$ μs. These measurements were carried out by placing a mirror close to the end of the test section at an angle of 45 deg to the wall and by placing the camera below the test section and the mirror. The distance between the measurement plane and the mirror was $\sim$1.5 m. The mirror was shown to have a negligible effect on the boundary layer in terms of c_p and c_f. Since the main flow is normal to the laser sheet, a short time delay has to be used in order to minimize loss of pairs (particles traveling out of the measurement volume between the two exposures). This puts an upper restriction on the image size, since the particles should move as far as possible in terms of pixels to minimize errors. On the other hand, a large enough image size is needed if both vortices downstream of a VG are to be captured simultaneously. This was desired to investigate the correlation between the two vortices introduced by one VG. The laser sheet was broadened to 2–3 mm in order to allow for a larger time delay between the image pairs. The displacements in the present experiment are 2–3 pixels at $x/h=5.5$. One-hundred image pairs were collected at each position; however, since each image contains two vortices, the amount of vortices for statistical evaluation is 200.

2.4.5 Vortex Identification. A proper definition of a coherent structure embedded in a turbulent flow has been debated [37]. Different techniques for characterizing a vortex have been suggested; see for example [38–40]. The quantities used here are

$$\omega_x=\frac{\partial w}{\partial y}-\frac{\partial v}{\partial z}\quad Q=-\frac{\partial w}{\partial y}\frac{\partial v}{\partial z} \tag{3}$$

the mean streamwise vorticity and the second invariant of the velocity gradient tensor, used, for example, by [41,42] for the same purpose. The latter criterion is similar to that suggested by [43], where the eigenvalues of the velocity gradient tensor were used to determine rotation. A local region of a relatively low pressure with respect to the surrounding fluid has also been used as an indication of a vortex center. A simple shear flow without a vortical structure can have vorticity. Therefore, Q is a better measure of a vortical structure than the vorticity, since a vortical flow has both a large value of Q and vorticity. Here, a local maximum in Q was taken as the center of a vortex and the maximum value was taken as its strength. The size of the vortex (A) was taken as the region around the center where the local $Q\geqslant0.05Q_{\max}$, where the latter is the maximum rotation closest to the VG. By integrating the vorticity over the vortex size, the circulation was estimated,

$$\Gamma=\sum_A \omega_x(A) \tag{4}$$

The uncertainty in the instantaneous velocity measurements is estimated to be of the order of 2%. The uncertainty in the calibration of the image size (and thereby the spatial gradient) is $\pm$0.5 mm, and the image size is 56 mm$\times$70 mm (i.e., 1%). The uncertainty in the determination of the spatial gradient of the velocity field can then estimated to be 3%. Thereby, the uncertainty in the instantaneous vorticity should be 3%, whereas the uncertainty in the instantaneous Q, which is calculated from the square of the spatial gradient of the velocity field, should have an uncertainty of 9%. The uncertainty in the determination of the vortex

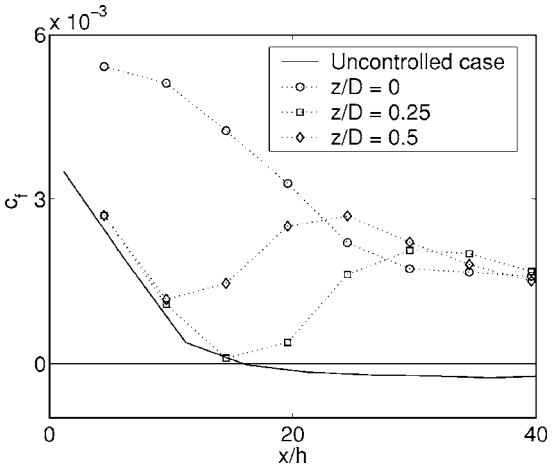

Fig. 5 Streamwise development of c_f downstream of the VGs

center, taken as a local maximum of Q, corresponds to the resolution of the PIV measurement (i.e., the size of an Interrogation Area (IA)), which is 0.875 mm).

3 Results

3.1 Wall Shear Stress. Figure 5 shows the downstream development of c_f, measured with a wall-pulsed wire, at three different spanwise positions $z/D=0$, 0.25, and 0.5, and at eight equally spaced streamwise positions downstream of the VGs (to $x/h=40$). At $x/h=40$, the backflow is strongest in the uncontrolled case (see Fig. 3). At $x/h=5$ and $z/D=0$, c_f is increased by 100% by the vortices. In the downstream direction, the pressure gradient has a similar effect on the development of c_f as in the uncontrolled case, decreasing it to a level below the initial uncontrolled value. At $z/D=0.25$ and 0.5, c_f is similar to the uncontrolled case down to $x/h=10-15$. When the uncontrolled case separates at $x/h=16$, c_f at the positions $z/D=0.25$ and 0.5 are instead increased when the high momentum fluid carried down toward the wall is spread by the vortices in the spanwise direction. However, a spanwise variation in c_f is persistent to $x/h=30$. From these measurements, it can be concluded that separation is prevented.

3.2 Velocity Field.

3.2.1 Wall-Normal Velocity Profiles Compared to the Uncontrolled Case. In this section, the effect of the vortices on the mean velocity profiles is described by a comparison with the uncontrolled APG case, measured by LDV (showed as a dashed line).

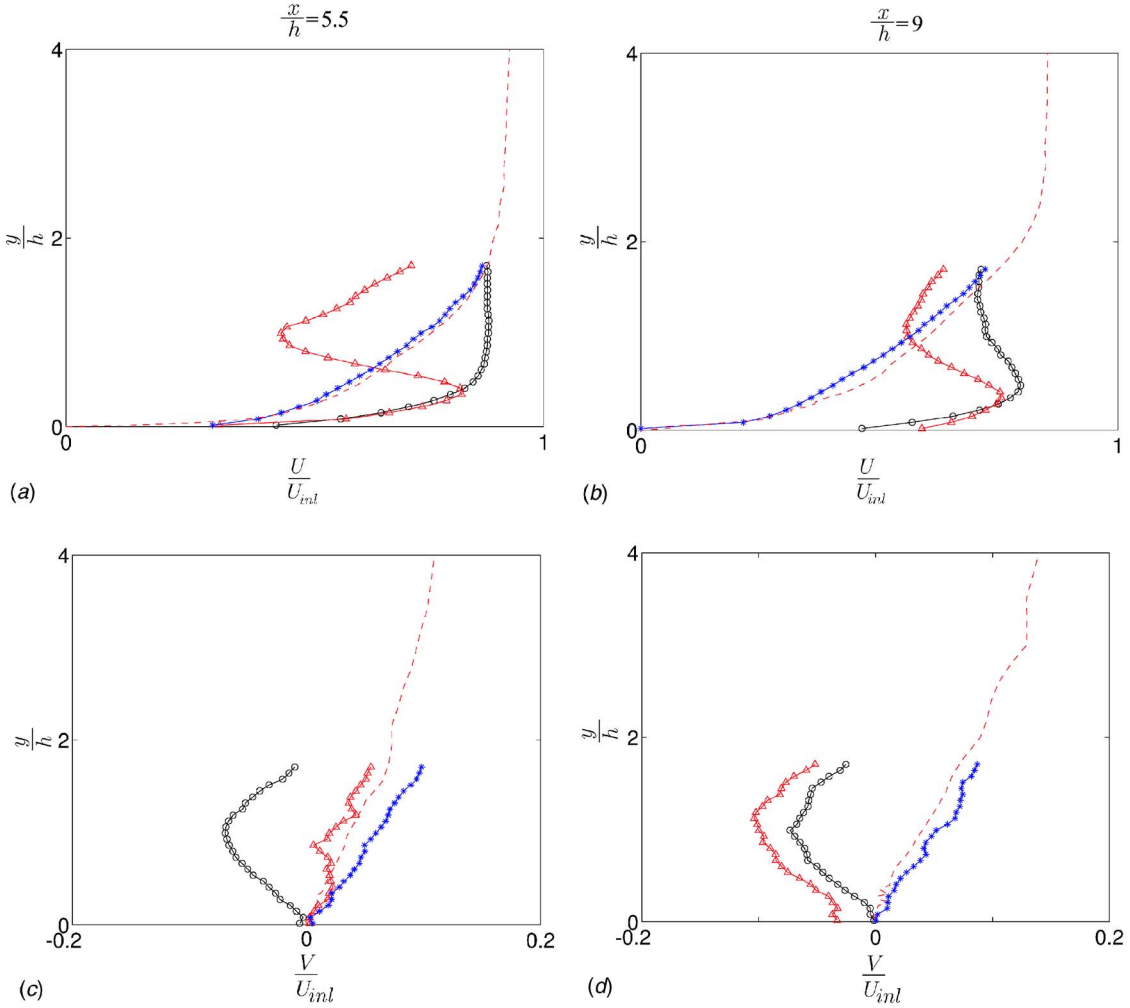

Fig. 6 Mean velocity profiles in the *xy* plane at (*a*,*c*) $x/h=5.5$ and at (*b*,*d*) $x/h=9$, compared to the uncontrolled case (LDV dashed line). Circle: $z/D=0$; triangle: $z/D=0.165$; star: $z/D=0.5$. The boundary layer thickness is $\sim 2.5h$ and $\sim 3.5h$ respectively, in the uncontrolled case.

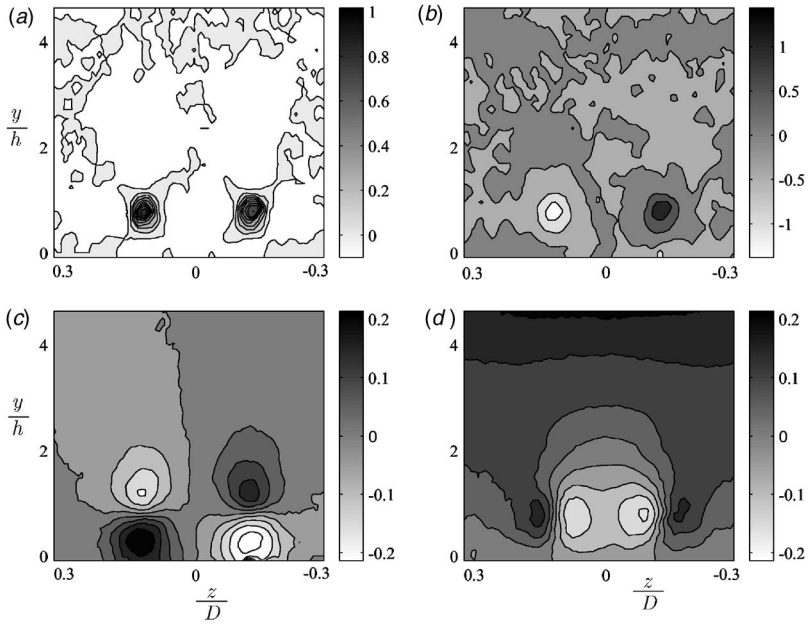

Fig. 7 (*a*) Vortex strength $Q/(U_{inl}/h)^2$, (*b*) vorticity $\omega_x/(U_{inl}/h)$ and secondary flow components, (*c*) W/U_{inl}, and (*d*) V/U_{inl} at $x/h=5.5$

Figure 6 shows the mean velocity profiles at three z positions in the xy plane at $x/h=5.5$ and 9. High-momentum fluid is carried down to the wall between the VG blades, as can be seen from the large negative V component in Fig. 6(c). This gives a fuller velocity profile and increases the wall shear stress, as was seen in Fig. 5. The streamwise velocity profile at $z/D=0.165$ has an S shape with high-velocity fluid in the near-wall region, similar in magnitude to the profile at $z/D=0$. Outside the near-wall region, a region with a lower velocity than in the uncontrolled case exists. High-momentum fluid is redistributed from the outer region where it is available to the near-wall region, where it is needed to prevent separation. At $x/h=9$, the profile at $z/D=0.165$ is less S shaped at the same time as the profile at $z/D=0$ becomes S shaped. The streamwise profile at $z/D=0.5$, where c_f was found to be virtually unchanged, is similar to the uncontrolled case since the high-momentum fluid carried by the vortices has not yet reached that far in the spanwise direction.

3.2.2 Mean Cross-Flow. Figures 7 and 8 show the nondimensional mean vorticity, $\omega_x/(U_{inl}/h)$; the nondimensional vortex strength, $Q/(U_{inl}/h)^2$; and the secondary flow components V/U_{inl} and W/U_{inl} at $x/h=5.5$ and 9. The vortices are clearly seen as regions with high values of ω_x and Q on both sides of the symmetry plane $z/D=0$. Large negative wall-normal components can

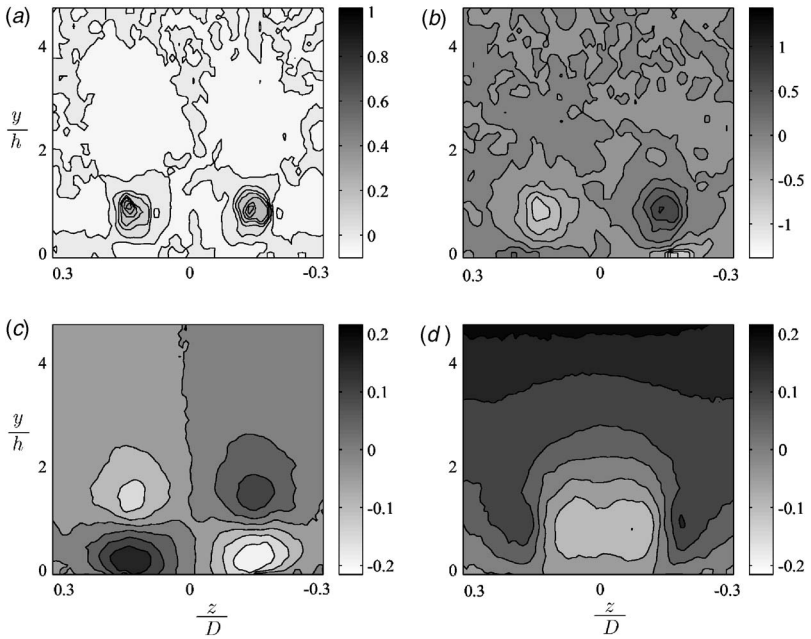

Fig. 8 (*a*) Vortex strength $Q/(U_{inl}/h)^2$, (*b*) vorticity $\omega_x/(U_{inl}/h)$ and secondary flow components, (*c*) W/U_{inl}, and (*d*) V/U_{inl} at $x/h=9$

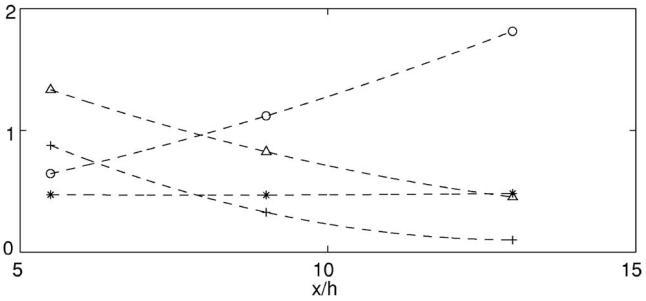

Fig. 9 Downstream development of: triangle: $\omega_{x,max}/(U_{inl}/h)$; plus: $Q_{max}/(U_{inl}h)^2$; circle: A/h^2, and star: $\Gamma/U_{inl}h$

be seen on the insides of the vortices (between the VG blades), and large positive wall-normal components can be seen on the outsides of the vortices. Large components in the spanwise velocity along the wall below and above the vortex centers can also be seen. The former is slightly larger in magnitude. The maximum magnitude of the mean cross-flow components is ~20 % of U_{inl}. The large positive wall-normal component in the upper part of Figs. 7 and 8 is due to the suction. Figure 8 shows that the vortices are weaker and cover a larger area at $x/h=9$. A region of vorticity of opposite sign is induced in the near-wall region below the vortices due to a strong shear caused by the no-slip condition in

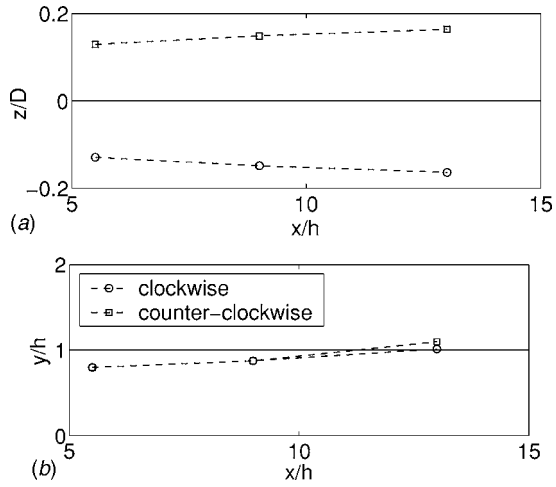

Fig. 10 Downstream development of the mean vortex centers in the (top) spanwise direction and (bottom) wall-normal direction

W. The same pattern was seen at $x/h=13$ (not shown here).

According to [44], the vortices from VGs are fairly well represented by the velocity distribution of a Lamb-Oseen vortex. The *W* component at $y/h \geq 0.7$ compares well with the velocity field generated by a row of Lamb-Oseen vortices in the spanwise direction and their images, but at $y/h \leq 0.7$, it does not, which is an effect of the no-slip condition at the wall.

Figure 9 shows that the maximum values of $Q/(U_{inl}/h)^2$ and $\omega_x/(U_{inl}/h)$ decrease in downstream direction at the same time as A/h^2 increases and the circulation is conserved. The paths of the mean vortex centers in the wall-normal and spanwise directions are displayed in Fig. 10. The vortices can be seen to move away from each other in the spanwise direction due to the mutual induction and the wall interaction (interaction with the image vortex), as indicated by [10]. The mean spanwise distance is increased from $z/D=0.26$, 0.29 to 0.34 in the downstream direction. In the wall-normal direction, the mean vortex position is moving outward from $y/h=0.77$, 0.88 to 1.0, which is contradicting the model results by [10]. The reason for this disagreement is that the model by [10] is inviscid and does not take into account that the vortices are within a developing boundary layer. The present results show that the vortices grow in size with the growing boundary layer, which is a viscous effect. This cause the vortex center to move out from the wall in terms of y/h.

3.2.3 Instantaneous Vortex Behavior. Instantaneous vector fields in the *yz* plane were investigated at $x/h=5.5$ in the same manner as in the case of the mean vortex (i.e., the maximum vorticity, the vortex center position, and the vortex size were extracted). Figure 11 shows the probability density functions (PDFs) of the instantaneous vortex positions and the instantaneous distance between them. (The mean vortex center positions (see Fig. 10), and the mean distance between the vortices have been subtracted, respectively). The vortices are clearly not stationary. The instantaneous wall-normal position is fluctuating less than the instantaneous spanwise position, presumably due to the presence of the wall. The vortices move over a spanwise distance that is approximately equal to their size. The most probable instantaneous distance between the two vortices equals the difference between the mean positions.

Figure 12 shows that the vorticity in the instantaneous vortex center, as well as the instantaneous vortex size, are also fluctuating quantities. In Fig. 12(*b*), each plus sign corresponds to one of the 200 vortex centers that were subjected to averaging. The mean value of $\omega_{x,max}$ in the instantaneous vortex center in Fig. 12(*a*) exceeds the maximum mean vorticity seen in Figs. 7(*b*) and 9. This can be explained by the movement of the vortices, which tends to smear out the vorticity. The mean value of the instantaneous vortex size in Fig. 12(*b*) is lower than the mean vortex size seen in Fig. 9, which can also be explained by the movement of the vortices. This implies that the instantaneous vortex is gener-

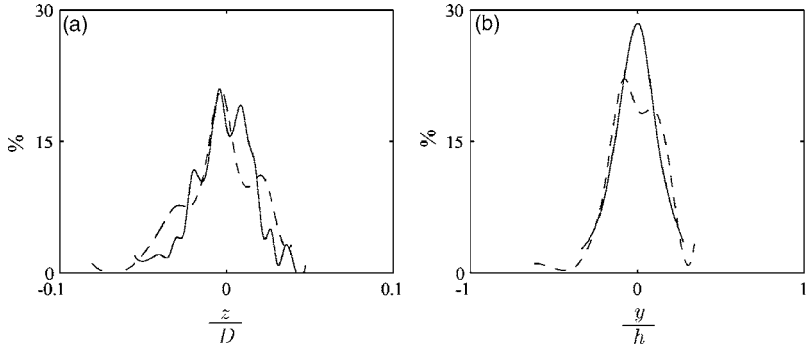

Fig. 11 (*a*) Spanwise and (*b*) wall-normal PDFs of the vortex center positions z'/D and y'/h (lines) and instantaneous distance between the vortices $\Delta z'/D$ and $\Delta y'/h$ (dashed lines) at $x/h=5.5$. Note that $D/h=10$.

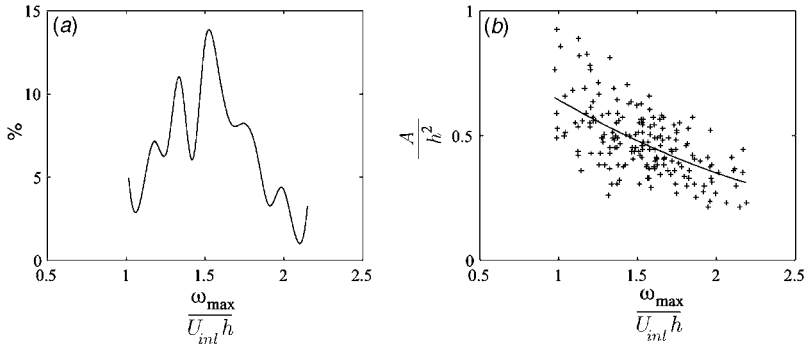

Fig. 12 (*a*) PDF of the maximum vorticity in the instantaneous vortex center and (*b*) maximum instantaneous vorticity versus instantaneous vortex size at *x*/*h*=5.5. The line is only included for visual aid.

ally smaller and stronger than the mean vortex. There is no correlation between the instantaneous $\omega_{x,\max}$ and the instantaneous vortex position; however, there is a relation to the instantaneous vortex size. Smaller vortices are stronger, and larger vortices are weaker (see Fig. 12(*b*)), suggesting that vortex stretching occurs.

Large coherent regions with a very large instantaneous wall-normal component, ranging between $\pm 0.3U_{\text{inl}}$, could be observed in virtually every instantaneous xy plane at $x/h=5.5$, at the spanwise position around the vortex center ($z/D=0.165$). This magnitude is too large to be purely random turbulent fluctuations at this position and is similar in magnitude to the cross-flow velocity induced by the vortices (see Fig. 7). Considering a fix point in space, such as the mean vortex center, spanwise vortex movements will induce large differences in wall-normal velocity (i.e., give rise to v'), whereas wall-normal vortex movements will induce large differences in the spanwise velocity (i.e., give rise to w'). Considering the spanwise distance over which the vortices were found to move at $x/h=5.5$, (see Fig. 11) and the magnitude of the instantaneous velocities, the unsteadiness of the vortices can be estimated to constitute approximately half of the value of the $\sqrt{\overline{v'^2}}/U_\infty$ in the mean vortex center seen in Fig. 13(*a*). The maximum value in the vortex center is ~500 % of the value in the uncontrolled case (not shown here). The fact that the wall-normal component $\overline{v'^2}$ has a higher magnitude than the spanwise component $\overline{w'^2}$ (see Fig. 13) is in line with the fact that the spanwise movements were found to be larger than the wall-normal ones. The fact that the maximum value of both the turbulent fluctuations shown in Fig. 13 coincides with the mean vortex center further supports the idea that the vortex unsteadiness is responsible for a large part of the fluctuations.

3.2.4 Mechanism of the Vortex Unsteadiness. The present section attempts to shed some light on the physical mechanism for the observed unsteadiness of the vortices. Its implications for separation control are discussed as is how it could be utilized for an improved efficiency in separation control.

A wing-tip vortex, which does not interact with another vortex or a boundary layer (i.e., a wall and the boundary layer turbulence) is fairly steady compared to the vortices in the present investigation. In the present study, the instantaneous vortices are affected by each other, the wall (their image vortices) and the surrounding boundary layer turbulence (which depends on the wall-normal and the spanwise position). The two former interactions cause the mean vortices to move in both the wall-normal and spanwise directions as they travel downstream, whereas the turbulence is random and has no net effect. Instantaneously though, the turbulence will also contribute to the dynamics of the vortices. The magnitude of the inviscid induced velocity can be estimated as the geometrical mean value of the velocity induced by the opposite vortex and the image vortex, $\{(\Gamma/d)^2+(\Gamma/2h)^2\}^{1/2}$. With the measured Γ at $x/h=5.5$, the magnitude becomes $0.25U_\infty$, which is naturally similar to the magnitude of the cross-flow velocities displayed in Figs. 7(*c*) and 7(*d*). The turbulent fluctuations are smaller in magnitude but should still be large enough to be important in the dynamics of the vortex movements. Because the turbulence is random and three-dimensional, the two vortices are most likely affected in different ways by the turbulence instantaneously, since the distance between them is larger than the spanwise integral length scale of the turbulence. This disturbs their "equilibrium positions" and inviscid velocities are induced, which strives to move the vortices. If, for example, one of the vortices is moved closer to the wall by the turbulence, the velocity induced by its image vortex is enhanced and causes the vortex to move away from the other vortex in the spanwise direction. If, instead, one of the vortices is moved closer to the other one by the turbulence, the magnitude of the inviscid interaction between the vor-

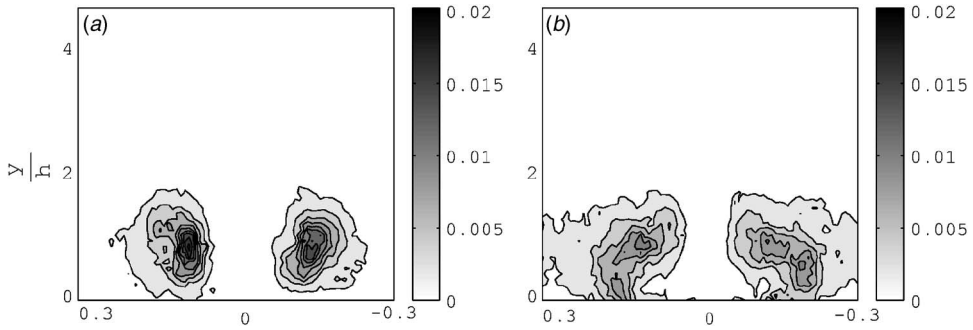

Fig. 13 The fluctuating secondary flow components (left) $\overline{v'^2}/U_{\text{inl}}^2$ and (right) $\overline{w'^2}/U_{\text{inl}}^2$ in the *yz* plane at (*a*,*b*) *x*/*h*=5.5

tices will be intensified and cause the vortices to move toward the wall. Such instantaneous interactions between the two vortices, the vortices and the wall and the vortices and the surrounding turbulence, most likely plays an important role in the dynamics that lays behind the unsteadiness of the vortices.

It was conjectured in our companion study [24], that keeping the flow locally attached at positions in the spanwise direction is optimal for separation-control purposes in the sense that the wall-shear stress is not increased more than necessary. Having pockets of instantaneous backflow at some positions in the spanwise direction is presumably possible as long as the flow is attached at other positions in the spanwise direction. The unsteady movement of the vortices in the spanwise direction acts in this sense instantaneously. Furthermore, the movement of the vortices in the spanwise direction is beneficial for separation control purposes in the sense that the effect of the vortices is distributed over a larger area than it would have been if they were steady. Perhaps active VGs, such as VG jets, can be designed so that they enhance the unsteadiness of the vortices and thereby the efficiency. Unsteady vortices might also be more efficient for breaking the elongated pockets of instantaneous backflow that constitutes the separation, as showed by [45].

4 Conclusions

Turbulent boundary layer separation control by means of streamwise vortices was investigated with focus on the mean and the instantaneous vortex behavior. A strong adverse pressure-gradient-induced separation bubble was removed by introducing pairs of initially nonequidistant counterrotating vortices by means of fix VGs positioned approximately at the position of the maximum pressure gradient. The control success was shown by measuring the downstream and spanwise development of the wall shearstress by means of wall pulsedwires. The wall shear-stress was increased initially by 100% right downstream of the VGs, but at spanwise locations between two VGs, the wall shear stress is unaffected until 15 VG heights downstream. The spanwise distribution of the wall shear-stress is three-dimensional until 30 VG heights due to the initially nonequidistant vortices. The vortices were found to grow with the growing boundary layer in the downstream direction, and the maximum vorticity decreases as the circulation (the integrated vorticity) is conserved. The vortices are nonstationary, and the movements in the spanwise direction are larger than the movements in the wall-normal direction, presumably due to the presence of the wall. The instantaneous vortices move over a spanwise distance that is approximately equal to their size. The most probable instantaneous distance between the vortices equals the difference between the mean positions. The unsteadiness of the vortices contributes to the observed maxima in the Reynolds stresses around the mean vortex centers. The instantaneous maximum vorticity and the instantaneous vortex size are also fluctuating properties. The mean value of the maximum vorticity in the instantaneous vortex center exceeds the mean value in the mean vortex center due to the movement of the vortices, which tends to smear out the vorticity. The mean value of the instantaneous vortex size is lower than the mean vortex size due to the movement of the vortices. A correlation was found between a large instantaneous vortex size and a low instantaneous maximum vorticity (and vice versa), suggesting that the vortices are subjected to vortex stretching.

Acknowledgment

The support by Prof. H.-H. Fernholz and Dr. Barbro Muhammad-Klingmann is highly acknowledged. This project was funded by TFR and DFG.

References

[1] Simpson, R., 1989, "Turbulent Boundary-Layer Separation," Annu. Rev. Fluid Mech., **21**, pp. 205–234.
[2] Kiya, M., Shimizu, M., and Mochizuki, O., 1997, "Sinusoidal Forcing of a Turbulent Separation Bubble," J. Fluid Mech., **342**, pp. 119–139.
[3] Nakamura, Y., and Ozono, S., 1987, "The Effects of Turbulence on a Separated and Reattaching Flow," J. Fluid Mech., **178**, pp. 477–490.
[4] Kalter, M., and Fernholz, H. H., 2001, "The Reduction and Elimination of a Closed Separation Region by Free-Stream Turbulence," J. Fluid Mech., **446**, pp. 271–308.
[5] Fiedler, H. E., and Fernholz, H.-H., 1990, "On Management and Control of Turbulent Shear Flows," Prog. Aerosp. Sci., **27**(4), pp. 305–387.
[6] Gad-El-Hak, M., and Bushnell, D., 1991, "Status and Outlook of Separation Control," AIAA Paper No. 91-0037.
[7] Gad-El-Hak, M., 2000, *Flow Control Passive, Active, and Reactive Flow Management*, Cambridge University Press, Cambridge, England.
[8] Taylor, H. D., 1948, "Design Criteria for and Application of the Vortex Generator Mixing Principle," United Aircraft Corp. Report No. M-15038-1.
[9] Schubauer, G., and Spangenberg, W., 1960, "Forced Mixing in Boundary Layers," J. Fluid Mech., **8**, pp. 10–32.
[10] Pearcey, H. H., 1961, "Shock-Induced Separation and Its Prevention by Design and Boundary-Layer Control," *Boundary Layer and Flow Control, Its Principle and Applications*, Vol. 2, Lachmann, G. V., ed., Pergamon Press, London.
[11] Smith, F. T., 1994, "Theoretical Prediction and Design for Vortex Generators in Turbulent Boundary Layers," J. Fluid Mech., **270**, pp. 91–131.
[12] Lin, J. C., 2000, "Review of Research on Low-Profile Vortex Generators to Control Boundary-Layer Separation," Prog. Aerosp. Sci., **38**, pp. 389–420.
[13] Rao, D., and Kariya, T., 1988, "Boundary-Layer Submerged Vortex Generators for Separation Control: An Exploratory Study," AIAA Paper No. 88-3546.
[14] Lin, J., Howard, F., and Selby, G., 1989, "Turbulent Flow Separation Control Through Passive Techniques," AIAA Paper No. 89-0976.
[15] Lin, J. C., Howard, F. G., Bushnell, D. M., and Selby, G. V., 1990, "Investigation of Several Passive and Active Methods for Turbulent Separation Control," AIAA Paper No. 90-1598.
[16] Johnston, J. P., and Nishi, M., 1990, "Vortex Generator Jets: Means for Separation Control," AIAA J., **28**(6), pp. 989–994.
[17] Lin, J., 1999, "Application of Micro-Vortex Generators for Turbulent Flow Separation Control," IUTAM Symposium on Mechanics of Passive and Active Flow Control, 81–88.
[18] Shabaka, I. M. M. A., Mehta, R. D., and Bradshaw, P., 1985, "Longitudinal Vortices Imbedded in Turbulent Boundary Layers. Part 1. Single Vortex," J. Fluid Mech., **155**, pp. 37–57.
[19] Mehta, R. D., and Bradshaw, P., 1988, "Longitudinal Vortices Imbedded in Turbulent Boundary Layers. Part 2. Vortex Pair With Common Flow Upwards," J. Fluid Mech., **188**, pp. 529–546.
[20] Mehta, R. D., 1985, "Effect of a Longitudinal Vortex on a Separated Turbulent Boundary Layer," AIAA Paper No. 85-0530. pp. 1–11.
[21] Cutler, A., and Bradshaw, P., 1989, "Vortex/Boundary Layer Interaction," AIAA Paper No. 89-0083, pp. 1–11.
[22] Pauley, W. R., and Eaton, J. K., 1988, "Experimental Study of the Development of Longitudinal Vortex Pairs Embedded in a Turbulent Boundary Layer," AIAA J., **26**(7), pp. 816–823.
[23] Zhang, H., Zhang, X., Hurst, D., and Collins, M. W., 1996, "An LDA Study of Longitudinal Vortices Embedded in a Turbulent Boundary Layer," *8th International Symposium Applications of Laser Techniques to Fluid Mechanics*.
[24] Angele, K. P., and Muhammad-Klingmann, B., 2005, "The Effect of Streamwise Vortices on the Turbulence Structure of a Separating Boundary Layer," Eur. J. Mech. B/Fluids, **24**(5), pp. 539–554.
[25] Dengel, P., and Fernholz, H., 1990, "An Experimental Investigation of an Incompressible Turbulent Boundary Layer in the Vicinity of Separation," J. Fluid Mech., **212**, pp. 615–636.
[26] Warnack, D., 1996, "Eine Experimentelle Untersuchung Beschleunigter Turbulenter Wandgrenzschichten," Dissertation, Technische Universität, Berlin.
[27] Bradbury, L. J. S., and Castro, I. P., 1971, "A Pulsed-Wire Technique for Velocity Measurements in Highly Turbulent Flow," J. Fluid Mech., **22**, pp. 679–687.
[28] Castro, I. P., 1992, "Pulsed-Wire Anemometry," Exp. Therm. Fluid Sci., **5**, pp. 770–780.
[29] Fernholz, H.-H., Janke, G., Schober, M., Wagner, P. M., and Warnack, D., 1996, "New Developments and Applications of Skin-Friction Measuring Techniques," Meas. Sci. Technol., **7**, pp. 1396–1409.
[30] Willert, C., Raffel, M., Kompenhans, J., Stasicki, B., and Kähler, C., 1996, "Recent Applications of Particle Image Velocimetry in Aerodynamic Research," Flow Meas. Instrum., **7**(3/4), pp. 247–256.
[31] Westerweel, J., 1997, "Fundamentals of Digital Particle Image Velocimetry," Meas. Sci. Technol., **8**, pp. 1379–1392.
[32] Angele, K., and Muhammad-Klingmann, B., 2005, "A Simple Model for the Effect of Peak-Locking on the Accuracy of Boundary Layer Turbulence Statistics in Digital PIV," Exp. Fluids, **38**(3), pp. 341–347.
[33] Keane, R., and Adrian, R., 1992, "Theory of Cross-Correlation in PIV," Appl. Sci. Res., **49**, pp. 191–215.
[34] Angele, K., 2003, "Experimental Studies of Turbulent Boundary Layer Separation and Control," Ph.D. thesis, Dept. of Mechanics, Royal Institute of Technology, Stockholm.
[35] Raffel, M., Willert, C., and Kompenhans, J., 1998, *Particle Image Velocimetry A Practical Guide*, Springer-Verlag, Berlin.
[36] Melling, A., 1997, "Tracer Particles and Seeding for Particle Image Velocimetry," Meas. Sci. Technol., **8**, pp. 1406–1416.
[37] Robinson, S. K., 1991, "Coherent Structures in the Turbulent Boundary Layer," Annu. Rev. Fluid Mech., **23**, pp. 601–639.

[38] Bonnet, J. P., Delville, J., Glauser, M. N., Antonia, R. A., Bisset, D. K., Cole, D. R., Fiedler, H. E., Garem, J. H., Hilberg, D., Jeong, J., Kevlahan, N. K. R., Ukeiley, L. S., and Vincendeau, E., 1998, "Collaborative Testing of Eddy Structure Identification Methods in Free Turbulent Shear Flows," Exp. Fluids, **25**, pp. 197–225.
[39] Delville, J., and Bonnet, J.-P., 2000, "Theme ERCOFTAC Bulletin No. 46: Eddy Structures Identification," Ercoftac Bull., 46.
[40] Graftieaux, L., Michard, M., and Grosejan, N., 2001, "Combining PIV, Pod and Vortex Identification Algorithms for the Study of Unsteady Turbulent Swirling Flows," Meas. Sci. Technol., **12**, pp. 1422–1429.
[41] Scarano, F., Benocci, C., and Riethmuller, M. L., 1999, "Pattern Recognition Analysis of the Turbulent Flow Past a Backward Facing Step," Phys. Fluids, **11**(12), pp. 3808–3818.
[42] Adrian, R. J., Meinhart, C. D., and Tomkins, C. D., 2000, "Vortex Organization in the Outer Region of the Turbulent Boundary Layer," J. Fluid Mech., **422**, pp. 1–54.
[43] Jeong, J., and Hussain, F., 1995, "On the Identification of a Vortex," J. Fluid Mech., **285**, pp. 66–94.
[44] Wendt, B. J., 2001, "Initial Circulation and Peak Vorticity Behavior of Vortices Shed from Airfoil Vortex Generators," NASA Glenn Technical Report No. NASA/CR-2001-211144.
[45] Angele, K. P., and Muhammad-Klingmann, B., 2006, "PIV Measurements in a Weakly Separating and Reattaching Turbulent Boundary Layer," Eur. J. Mech. B/Fluids, **25**(2), pp. 204–222.

Localized Structures in Vertically Vibrated Granular Materials

Piroz Zamankhan[1]
Laboratory of Computational Fluid and BioFluid Dynamics,
Lappeenranta University of Technology,
Lappeenranta, Finland
and
Department of Mechanical Engineering,
Shahrekord University,
P.O. Box 115,
Shahrekord, Iran
e-mail: qpz002000@yahoo.com

Jun Huang
Laboratory of Computational Fluid and BioFluid Dynamics,
Lappeenranta University of Technology,
Lappeenranta, Finland

Granular materials exhibit unusual kinds of behavior, including pattern formations during the shaking of the granular materials; the characteristics of these various patterns are not well understood. Vertically shaken granular materials undergo a transition to convective motion that can result in the formation of bubbles. A detailed overview is presented of collective processes in gas-particle flows that are useful for developing a simplified model for molecular dynamic type simulations of dense gas-particle flows. The governing equations of the gas phase are solved using large eddy simulation technique. The particle motion is predicted by a Lagrangian method. Particles are assumed to behave as viscoelastic solids during interactions with their neighboring particles. Interparticle normal and tangential contact forces are calculated using a generalized Hertzian model. The other forces that are taken into account are gravitational and drag force resulting from velocity difference with the surrounding gas. A simulation of gas-particle flow is performed for predicting the flow dynamics of dense mixtures of gas and particles in a vertical, pentagonal, prism shaped, cylindrical container. The base wall of the container is subjected to sinusoidal oscillation in the vertical direction that spans to the bottom of the container. The model predicts the formation of oscillon type structures on the free surface. In addition, the incomplete structures are observed. Interpretations are proposed for the formation of the structures, which highlights the role played by the surrounding gas in dynamics of the shaken particles. [DOI: 10.1115/1.2409358]

Keywords: localized structures, dense granular flows, vibrations, large eddy simulations, pattern formations, viscoelastic solids

1 Introduction

Vibrating heaps of fine brass balls at critical amplitude form themselves into fascinating patterns called oscillons [1]. This self-sustaining state was named by analogy to its most similar large-scale analogy, the soliton, which is a localized wave that maintains its integrity as it moves. The experimental observations suggested that oscillons may arise from cooperative behavior resulting from collisions between brass balls in an evacuated, vertically vibrated, granular layer [1]. Similar behavior has been observed in many diverse nonlinear systems having little or no dissipation [2].

The experiments detailed by Umbanhowar et al. [1] triggered a number of theoretical works in which a wide range of approaches been used [3–8]. Most notably, the molecular dynamics type simulations reported by Bizon et al. [9] have reproduced the experimental results in great detail.

The situation appears somewhat different as that reported in Umbanhowar et al. [1], when vibration is applied to thin layers of granular slurry with air above [10]. In fact, interstitial fluid, such as air or water, is known to induce convection in a granular assembly as a vibrating plate accelerates downwards [11]. Moreover, fluid particle interactions appear to produce a variety of dynamical phenomena including clustering, ordered crystalline patterns, dynamical fluctuating states, and growth (agglomeration) [12]. Recently, Zohdi [13] has proposed a fast and implicit solution scheme for agglomeration in thermochemically reacting granular flows.

In a closely related system, if a shallow bed of fine balls is shaken even at moderate amplitude with air filling the pore space, heaps develop [14]. In this case, the surrounding gas plays a key role in dynamics of vibrating particles at high amplitudes. It has been speculated that the gas trapped in the granular material is a source of the heaping [14]. Pak, Van Doorn, and Behringer [14] suggested that air heap formation in vibrating granular materials may be considered as criteria to determine when gas effects are relevant. Further understanding of the mechanism for heaping is of interest in creating ideal processing conditions and powder transport, which is of use in a number of industries including the oil industry.

Despite substantial industrial interests in processes such as food handling, mixing of building materials, and processing and handling of coal, dynamics of both dry and wet granular systems, such as those reported above, remain poorly understood. In fact, the aforementioned discoveries are motivating theorists to develop a comprehensive, hydrodynamic type description for granular materials. Hence, the objective of the current work is to develop a realistic model for a dense mixture of gas-particle flow, typical of common industrial practices. The model is validated through its application to describe the influence of periodic vertical vibrations the base of a vertical container on the dynamics of granular media for which interactions with the surrounding gas plays a role in dynamical pattern formation.

The organization of the paper is as follows. In Sec. 2, a model is developed for molecular dynamic type simulations of dense gas-particle flows. The developed model is applied to the specific example of a dense gas-particle mixture under vertical vibrations in a pentagonal, prism shaped, container. The results appear to capture salient features of observation on vertically vibrated granular materials, such as the formation of oscillon and bubbling. Concluding remarks are presented in Sec. 3, which may be useful in creating ideal processing conditions and powder transport in industrial systems.

2 Discrete Model

The sophisticated discrete model such as that outlined in a previous work [15], which contains only a few empirical parameters, may not be feasible in the future to produce detailed information,

[1]Corresponding author.

Contributed by the Fluids Engineering Division of ASME for publication in the JOURNAL OF FLUIDS ENGINEERING. Manuscript received December 15, 2005; final manuscript received August 15, 2006. Assoc. Editor: Theodore Heindel.

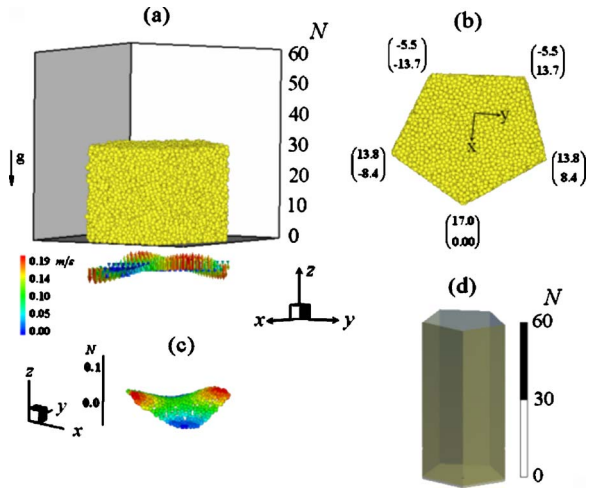

Fig. 1 (*a*) **Initial configuration of spherical particles in a vibrofluidized granular matter device. Also shown, is the typical instantaneous velocity vector field of particles located at the base of the container.** (*b*) **Top view of the initial configuration of spherical particles. All the sizes are normalized using particle diameter as a characteristic length.** (*c*) **Instantaneous configuration of particles located adjacent to the base of the container. To obtain a better visualization, the displacements of particles are rescaled.** (*d*) **Schematic of the container. The sidewalls of the container are neither moving nor deforming. The air flow in the container is resolved using 4×10^4 tetrahedral cells, nonuniformly distributed in the grid, where only one-seventh of the computational cells are used in $N\leqslant30$.**

for a vertically vibrated, granular material. Hence, a more simplified model is presented, in order to generate some useful results with a reasonable computational time.

The system, as illustrated schematically in Fig. 1(*a*), represents a virtual type, vibrofluidized, granular medium device, which will be called vibrodevice hereafter. Roughly 2×10^4 identical, slightly overlapping, spherical glass particles with a diameter of $\sigma=600$ μm are used to fill a pentagonal prism container. The initial configuration of particles in the container, more than one-half full, is illustrated in Fig. 1(*a*). The free surface, as depicted in Fig. 1(*b*), located at $N=Z_0/\sigma\approx30$, was nearly flat before vibration begins.

The base wall of the container is subjected to sinusoidal oscillation in the vertical direction given as $z=A\sin(k_v x)\sin(l_v y)\cos(\omega_v t)$, where $(\omega_v=C\sqrt{l_v^2+k_v^2})$, C is speed of wave in the base wall of the container, A is the derived amplitude, and $k_v=m_v\pi$ and $l_v=n_v\pi$. The numerical values used for the aforementioned parameters are $m_v=17$ 1/m, $n_v=13$ 1/m, and $C\approx13$ m/s. The derived amplitude is varied, and its maximum value was set to $A/\sigma=3\times10^{-1}$. The initial solid fraction ϕ_s was 0.585. The physical properties for the glass balls, the gas, and the model constants are presented in Table 1.

The system size and the values for parameters such as C (speed of wave in the bottom wall of bucket), k_v, and l_v were selected based on limitations imposed by computational resources. In addition, the complexities of granular systems such as polydispersity and the Coulomb interaction between the particles are neglected.

2.1 Numerical Models. In general, solid particles with mass m in a fluid, obey the Langevin equation given as

$$m\frac{dV_i^{(p)}}{dt}=F_i^D+F_i^g+F_i^i+F_i^b \tag{1}$$

To simplify the equation of motion for the solid particles it would be useful to define the dimensionless quantities given below

$$\mathrm{Re}_p=(1-\phi_s)\frac{\sigma|u_i-V_i^{(p)}|}{\nu_g}$$

$$\mathrm{St}=\frac{2}{9}(1-\phi_s)\left(\frac{\rho_g}{\rho_p}\right)^{-1}\frac{\sigma|u_i-V_i^{(p)}|}{\nu_g}$$

$$\mathrm{Fr}=\frac{[(1-\phi_s)|u_i-V_i^{(p)}|]^2}{gL} \tag{2}$$

Note that Fr is the ratio of the total kinetic energy of the particle to the gravitational potential energy.

Using the data presented in Table 1, the order of magnitude of the dimensionless quantities listed in Eq. (2) for the vibrodevice are estimated as $\mathrm{Re}_p\sim10$, $\mathrm{St}\sim10^3$, and $\mathrm{Fr}>1$. Since the work done by the drag force over the size of a particle is much larger

Table 1 The material properties of the particle and the continuous phase (air), which has been used in the simulation

Material	Properties	Symbol	Value
Glass	Elastic modulus	E	6.3×10^{10} Pa
	Density	ρ_p	2390 kg/m^3
	Poisson's ratio	ν	0.244
	Instantaneous shear modulus	G_0	2.53×10^{10} Pa
	Long time shear modulus	G_∞	6.1×10^9 Pa
	Relaxation time[a]	τ	9.87×10^{-6} s
	The coefficient characterizing the viscous behavior of grains[a]	K_n	143
	Tangential elastic coefficient[a] [11]	k_t	1.03×10^{15} 1/m$^{1/2}$ s^2
	Tangential damping coefficient	c_t	0
	Chemical compositions	SiO_2	66.0%
		Na_2O	16.0%
		CaO	7.0%
		Al_2O_3	5.0%
		Bi_2O_3	3.0%
	Surface friction coefficient	μ_p	0.6
Air	Density	ρ_g	1.225 kg/m^3
	Kinematic viscosity	ν_g	1.46×10^{-5} m^2/s
	Temperature	T_g	293 K

[a]See Ref. [15].

than the thermal energy [16], the random force F_i^b $(i=x,y,z)$ can be neglected. The Stokes number of the particles is large indicating that solid-body collisions play an important role in the particle velocity distribution and the effect of subgrid scale eddies on particle motion is negligible. However, the particles might be affected by the larger unsteady turbulent motions. Thus, for the case $\mathrm{Re}_p \sim 10$, and $\mathrm{St} \sim 10^3$ with nonlinear, viscoelastic, particle-particle interactions, the Langevin equation for translational motion of the jth particle in the vibrodevice may be reduced to

$$\frac{dV_i^{(j)}}{dt} = \frac{F_i^D}{m} - g\delta_{iz} + \sum_{p=1}^{N_j} F_i^{(jp)} \tag{3}$$

where $F_i^D = 3\pi\sigma\rho_g\nu_g(1-\phi_s)^{\beta}(1+0.15\,\mathrm{Re}_p^{0.687})(u_i - V_i^{(j)})$ is the drag force, δ_{ij} represents Kronecker delta, and N_j represents the number of neighboring particles in contact with the jth particle at time t. Note that the exponent β is not a constant and its value varies with the particles Reynolds number given as

$$\beta = \begin{cases} 3.7 & \mathrm{Re}_p < 5 \\ 3.689 + 2.7\times 10^{-1}\,\mathrm{Re}_p - 5.66\times 10^{-3}\,\mathrm{Re}_p^2 + 1.37\times 10^{-4}\,\mathrm{Re}_p^3 & 5 \leqslant \mathrm{Re}_p < 25 \end{cases} \tag{4}$$

The glass balls have surface roughness on many different length scales. When two glass balls are brought into contact, the area of contact will only be a fraction of the nominal contact area. The contact regions are small areas where asperities from one ball are squeezed against those of the other ball. By assuming that the asperities will deform elastically with a finite viscous relaxation time [16], τ, an expression may be obtained for the contact force per unit mass acting on the jth particle due to contacts between this particle and its neighboring pth particles at time t, given as [15,17]

$$F_i^{(jp)} = \left(\{E/[3(1-\nu_p^2)m]\}\sigma^{1/2}\delta^{(jp)^{3/2}} + \frac{K_n\tau}{m}[G_0^2/(G_0 - G_\infty)]\delta^{(jp)}\frac{d\delta^{(jp)}}{dt} \right) k_i^{(jp)} - (k_t\chi_{jp}^{3/2} + c_t V_{l,jp}^{\mathrm{imp}} e_l)e_i \tag{5}$$

The surface asperities are responsible for the tangential forces acting between the colliding pairs. The first and second terms on right hand side of Eq. (5) represent the normal and tangential components of the contact force per unit mass, respectively.

In Eq. (5), e_i is the tangential unit vector define as, $e_i = \epsilon_{imq}k_{m,jp}(\epsilon_{qst}e_{s,jp}^{V\mathrm{imp}}k_{t,jp})$. In this case, Coulomb friction law describes friction between two colliding grains with a surface friction coefficient, μ_p, when there is mutual slipping at the point of contact. The magnitude of χ_{jp} is calculated as necessary to satisfy $|F_i^{(jp)_t}| = \mu_p |F_i^{(jp)} k_i^{(jp)}|$. Otherwise, the contact surfaces are considered stuck, while $|F_i^{(jp)_t}| < \mu_p |F_i^{(jp)_n}| \cdot |F_i^{(jp)_t}|$ and $|F_i^{(jp)_n}|$ are the magnitude of the tangential and normal components of the contact force per unit mass, respectively. In addition, the rate of change of tangential displacement is given by $(d\chi^{(jp)}/dt) = V_i^{\mathrm{imp}} e_i$. The displacement, $\chi^{(jp)}$, should be set initially to zero when a new contact is established and once the contact is broken, all memory of the prior displacement will be lost.

As discussed in Zamankhan et al. [15,17], frictional forces induce torques on the particle j which is defined as $T_i^{(j)} = -\frac{1}{2}\Sigma_{p=1}^{N_j}\varepsilon_{iqr}m^{(j)}\sigma k_q^{(jp)}F_r^{(jp)}$. Hence, Eq. (3) must be augmented by a torque equation for the rotational motion of particle j which is given as

$$J^{(j)}(d\omega_i^{(j)}/dt) = T_i^{(j)} \tag{6}$$

At present, the induced flow due to particle rotational motion in the gas is neglected. This issue will be revisited in a future article [18].

Assuming that the apparent surface of contact is built up of a larger number of hierarchically ordered asperities, Brilliantov et al. [19], suggested that the friction coefficient, μ_p, may be expressed in terms of mesoscopic parameters. However, in this attempt the friction coefficient is found by comparing the geometry of a dry spill of glass particles observed experimentally and that obtained using simulations. A detailed description of the coefficient of friction is presented by Zamankhan and Huang [20].

Note that the model detailed in this section is capable of capturing chain-like contacts, which are of importance in modeling dense granular flows. To obtain an expression appropriate to spherical particle-flat wall contact from Eq. (5), $\sigma/2$ has to replace σ.

To predict the gas flow field in the vibrodevice, a generalized form of the Navier–Stokes equations for a gas interacting with a solid phase is used. That is

$$[\rho_g(1-\phi_s)u_i]_{,i} - [\rho_g(1-\phi_s)]_{,t} = 0, \tag{7}$$

$$[\rho_g(1-\phi_s)u_i]_{,t} + [\rho_g(1-\phi_s)u_iu_j]_{,j} = -[(1-\phi_s)p]_{,i} + [(1-\phi_s)\sigma_{ij}]_{,j} - (1-\phi_s)\rho_g g\delta_{iz} + f_i \tag{8}$$

The last term on the right hand side of Eq. (8) represents the particle effect on the gas, which is given as the sum of all hydrodynamic forces on the particles in a computational cell, namely $f_i = -1/[V_c(1-\phi_s)]\Sigma_{s=1}^{N_c}F_i^D$.

The governing equations of the gas phase are solved using the large eddy simulation (LES) technique. The filtered equations are similar to Eqs. (7) and (8) with the difference being that on the left hand side of Eq. (8) the gradient of the subgrid scale stress tensor must be included, given by $\tau_{ij,j}$ with $\tau_{ij} = \overline{\rho u_i u_j} - \overline{\rho u_i}\,\overline{\rho u_j}/\bar{\rho}$, where $\rho = \rho_g(1-\phi_s)$. In order to achieve closure of the LES equations for the gas phase, the subgrid model is presented in the Appendix.

The subgrid-scale model Eq. (A8) was originally proposed for compressible turbulent flow. In this attempt, without well-established subgrid-scale models (required to perform LES) for very dense solid-gas suspensions the model, Eq. (A8) is utilized, which is of use for systems in which the fluctuating fields may not be small compared with those of the mean fields.

2.2 Simulation Procedure. By performing the simulations based on the model discussed in the preceding section, an increased understanding of the dynamics of dense gas-particle flows may be obtained with the vibrodevice.

The molecular dynamic type simulation is performed to calculate the motion of the particles in the gas. The contact force, as described in the preceding section is used to capture the major features of grain interactions. A particle dynamic model is employed to account for particle contacts of finite duration, in which the viscoelastic behavior of the particles is represented using a nonlinear Hertzian type model, as presented in the preceding section. The use of a nonlinear viscoelastic model is essential for capturing granular structure formation in the vibrodevice. The flow is driven by the oscillatory movements of the base wall in the

vertical direction, given as $z=A\sin(k_v x)\sin(l_v y)\cos(\omega_v t)$. Equations (3) and (6) are integrated using fourth and fifth order embedded formulas from Dormand and Prince [21] with $\Delta t=5\times10^{-8}$ s. The calculation of drag force acting on a particle requires knowledge of the local averaged values of the fluid velocity components at the position of the particle in the Lagrangian grid. Due to the numerical solution method detailed below, these variables are only known at discrete nodes in the domain. Hence, a mass weighted averaging technique [22] has to be employed for calculating the averaged quantities in the Lagrangian grid.

The solution of the gas field requires the computational domain, as depicted in Fig. 1, to be divided into cells. The calculation of the gas is based on the numerical solution of the set of partial differential Eqs. (7), (8), and (A8). The flow is resolved using 4×10^4 tetrahedral cells, nonuniformly distributed in the grid where only one-seventh of the computational cells are used between the free surface and the base wall. The mesh spacing of this grid should be larger than the particle diameter. The discretization of the filtered equations listed above was accomplished using a fully conservative finite volume method on a staggered grid. All spatial derivatives were approximated by a second-order central differencing scheme and time advancement was handled using the second-order implicit scheme. The solution of Eqs. (7) and (8) requires specification of the solids fraction at the appropriate grid nodes. The value of the solids fraction is obtained from molecular dynamic simulations by counting the volume of particles within each computational cell divided by the volume of the cell.

Solutions of the discretized equations were obtained using the symmetric coupled Gauss Seidel method. The efficiency of this scheme was improved by introducing a multigrid method with the dynamic semi-coarsening strategy.

The time step for the calculation of fluid motion should be small enough that neither solid particles nor fluid elements can pass through a computational cell during a time step. In this light, the time step for the gas phase is set to 7×10^{-6} s. The linear interpolation routines are used to communicate the information from grid nodes to particle positions and vice-versa.

For estimating the numerical uncertainty in solutions by the LES, a posteriori method was utilized based on the Richardson extrapolation [23]. In the posteriori testing, large eddy simulations were performed with an SGS model (A8) and verified against reference solutions in terms of mean velocity, stress distributions, and spectra. As a minimum requirement for estimating solution accuracy, two grid solutions were used along with knowledge of the formal order of accuracy of the numerical scheme to produce an error estimate in the solution properties. The posteriori analysis did not demonstrate clear grid independence. As stated earlier, in this attempt the mesh spacing cannot be smaller than the particle diameter.

The required CPU time for simulation may be decreased by artificially increasing the duration of a contact between the particles as suggested by Silbert et al. [24]. However, the disadvantage of their approach is that the softer, normal interactions between the particles have to be assumed. Hence, their prediction model for the lifetime of granular clusters should be considered with caution.

2.3 Simulation Results. Deformation and flow of granular assembly in the surrounding gas of the system, as illustrated in Fig. 2, is investigated using the models described in the preceding section. To maintain motion in the glass balls, which interact with each other through energy-dissipating contact forces and interact with gas via drag forces, the energy is supplied via sinusoidal oscillations of the base wall in the vertical direction whose instantaneous configuration is illustrated in Fig. 1(*c*).

In this study, an important parameter is $\Gamma=A_{\text{eff}}\omega_v^2/g$ that measures the acceleration of the container base relative to gravity. Here, $A_{\text{eff}}=A\int\int_S|\sin(kx)\sin(ly)|dxdy/\int\int_S dxdy$, where S represents the surface of the pentagon as depicted in Fig. 1(*b*). The

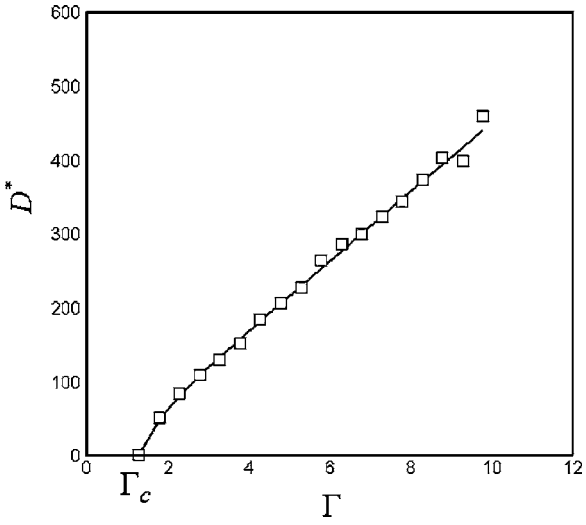

Fig. 2 Variations of the normalized coefficient of diffusivity of particles, $D^*=D/D_0$, with Γ. Note that, Γ, measures the acceleration of the container base relative to gravity. Here, D_0 is the coefficient of diffusivity at $\Gamma=1.3$. Also shown is the fitting expressed as $D^*\propto e^{-a_0/(\Gamma-\Gamma_c)}$ with $a_0=0.3$ as a solid line.

parameter Γ is varied by changing the derived amplitude. Note that $\Gamma>1$ is a necessary condition for sustained flow. As Γ exceeds a critical value Γ_c, the free surface of glass particles in the device becomes unstable. When Γ increases well above Γ_c the system undergoes transition from an initially featureless state to one with a well-defined mode with some degree of symmetry. It may be speculated that Γ behaves as the effective temperature of the environment and, therefore, the critical value Γ_c may correspond to the glass transition temperature. Figure 2 represents the normalized self diffusion coefficient [25,26] of particles, $D^*=D/D_0$, as a function of Γ, where D_0 is the diffusion coefficient at $\Gamma=1.3$.As can be seen from Fig. 2, for $\Gamma>\Gamma_c$, D^* may be given as

$$D^*\propto e^{-a_0/(\Gamma-\Gamma_c)} \tag{9}$$

where a_0 is a fitting parameter whose value is 0.3. The functional form found for the self-diffusion coefficient given in Eq. (9) appears to support conclusions made by Danna et al. [27], that the vibrofluidized granular matter can be treated (to a first approximation) with the equilibrium formalism. However, as it will be shown in the following, the granular material in the vibrodevice at Γ well above Γ_c is in a highly nonequilibrium state and there may be no reason for the existence of the fluctuation-dissipation relation, as speculated above.

When Γ increases well above Γ_c, the structures are observed with some degree of symmetry, as illustrated in Fig. 3. They are small with the typical diameter of eight particles (4% of the bucket area) and a maximum height of 20 particles. Figures 3(*a*) and 3(*b*) represent two instantaneous realizations of a descending structure each separated by roughly $1/2f$ s, where f is oscillation frequency of the base wall of the container. The base diameter of the structure in Fig. 3(*a*) is seven particle diameters and its height is 15 diameters. These are well defined localized stable structures. A few time steps later, as illustrated in Fig. 3(*c*), the structure collapses back into a bowl-shaped depression and because the structures are subharmonic, peaks and depressions can coexist. It is likely that in the vibrodevice, regular and irregular surface-wave patterns are excited subharmonically, with the frequency of the waves as a fraction of the excitation.

The structures, as shown in Fig. 3, form with nearly equal probability at all locations (except very close to the sidewalls) and are very stable. Figure 3(*d*) represents a snapshot of a single ascending structure which is very similar to the oscillons observed by

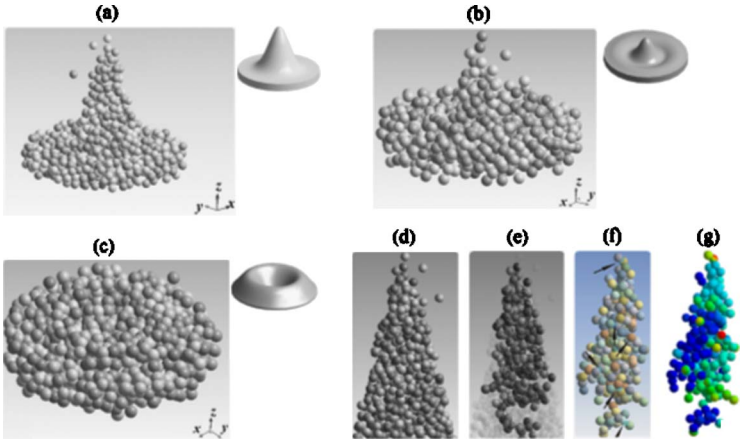

Fig. 3 (*a*) **Instantaneous configuration of glass particles in a typical perfect, descending structure. This structure was observed on the free surface of glass particles at $\Gamma \approx 10$. Here, gravity is directed in the negative *z*-direction.** (*b*) **Configuration of the glass particles in** (*a*) **after $1/2f$ s.** (*c*) **Configuration of the glass particles in** (*b*) **after roughly $1/f$ s. To obtain better visualizations, approximate shapes are presented as insets in** (*a*), (*b*), **and** (*c*). (*d*) **A typical localized ascending structure.** (*e*) **Particles within chains in** (*d*) **are highlighted.** (*f*) **The most recent contacts between the chains and single particles marked by arrows. Note that dissipations at the scale of large chains keep the structure localized.** (*g*) **Particle displacements due to chains-single particle contacts.**

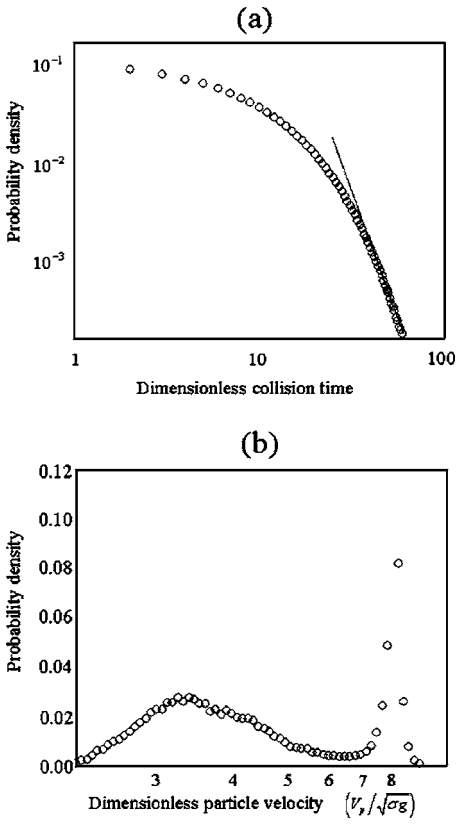

Fig. 4 (*a*) **Probability density of the normalized collision time, τ^*, for a sample data taken after 0.2 s of vibrations at $\Gamma \approx 10$. The data highlights the presence of a number of structures with long collision times. These may include active chains, whose sample is illustrated in Fig. 3(*e*). The straight line indicates the power law $(\tau^*)^{-5.2}$.** (*b*) **Probability density of the particle normalized velocity, $V^{p^*} = V^p/\sqrt{\sigma g}$, for the ascending and descending particle in the sample used in** (*a*). **The histogram illustrates a bimodal distribution.**

Umbanhowar et al. [1]. In Fig. 3(*e*) the particle chains (whose lifetimes could be an order of magnitude larger than the time of a binary collision) are highlighted within the oscillon-like structure. As can be seen from Fig. 3(*e*), the structure is a well connected, stable, network of long chains similar to those reported in Miller, O'Hern, and Behringer [28]. In Fig. 3(*f*) some of the contacts that occurred between the chains and single particles in the structure are marked using arrows. Figure 3(*g*) represents the local deformations in the structure caused by the contacts as depicted in Fig. 3(*f*). The results suggest that dissipation at the scale of large chains, which are highly dissipative, keeps the structure localized. Particles are color coded by their displacement magnitudes where the red is for the highest velocity and dark blue represents the lowest. It can be seen that there is a somewhat large displacement for some particles, while small or even no displacement for others. This observation highlights the use of a nonlinear Hertzian model such as that detailed in Sec. 2.1 which is completely different than the modified hard-sphere model used in Yamamoto et al. [29], in order to predict the chain formation accurately. An event driven scheme used in Ref. [29] might be useful for particulate systems with sufficiently low particle concentrations, for which binary collisions are overwhelmingly dominant.

More evidence of the existence of chains in a vibro-device is presented in Fig. 4(*a*) which illustrates probability density of the dimensionless collision time, τ^*, in a system whose sample results are presented in Fig. 3. The data presented in Fig. 4 has been extracted from a configuration taken after $t=0.2$ s of vibrations at $\Gamma \approx 10$. Here, the collision time is normalized using the collision time of a pair of particles with diameter $\sigma=600$ μm colliding with the characteristic impact velocity of $V_0^{imp}=1$ mm/s, which is $\tau_0 \approx 7.4 \times 10^{-5}$ s. Figure 4(*a*) excludes the results of binary collisions in the device. Figure 4(*b*) illustrates the probability density of the normalized velocity of the ascending and descending particles in the freeboard area, between the free surface and outlet of the device. Here, the particle velocity is normalized with the square root of the potential energy needed to raise a single particle by one diameter, namely $\sqrt{\sigma g}$. Given that the collision time is roughly proportional to $(V^{imp})^{-1/5}$, the results presented in Fig. 4(*a*) suggest that a large number of chains could exist in the free-

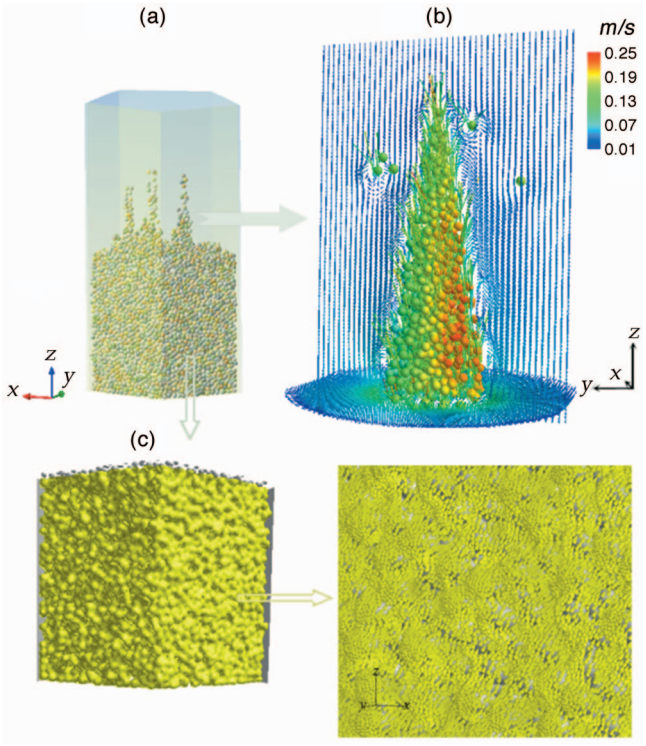

Fig. 5 (***a***) **An instantaneous configuration of glass particles in a vibrated, pentagonal, prism-shaped container at in the device at $\Gamma=10$ after $t=0.2$ s and $\Gamma=10$. Four localized structures are shown, one of which is perfect. Imperfect structures can be seen on the left side of the container. An imperfect structure consists of a number of single particles as well as thread-like chains flying over the free surface. The formation of imperfect structures may be linked to bubble burst out as they approach the free surface.** (***b***) **Computed instantaneous air velocity field around an ascending structure on two cutting *yz*-planes and *xz*-planes perpendicular to the free surface. To obtain a better visualization, the particles are also added in** (***b***). (***c***) **The cavities deep inside of the granular bed located near the sidewalls. Inset: Computed instantaneous air velocity field on a cutting *xz*-plane in the wall region. Some signatures of weak recirculation bubbles can be observed in the inset. Note that both in** (***b***) **and** (***c***) **computed velocity vectors have been interpolated onto uniform meshes.**

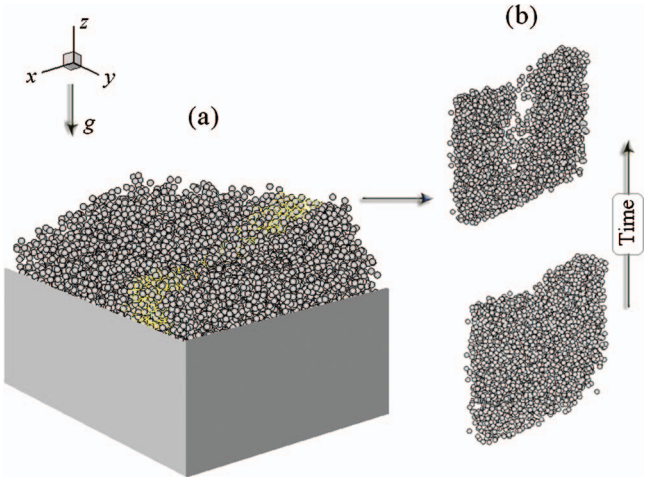

Fig. 6 (***a***) **An instantaneous configuration of glass particles in the vibrodevice at $\Gamma\approx8$ taken after $t=2$ s of shaking. Here, only a limited number of particles are shown.** (***b***) **Two instantaneous realizations in a slice as highlighted with yellow in** (***a***), **each separated by $t\approx0.2$ s.**

board area and in the upper part of the bed adjacent to the free surface. An interesting feature of probability density as depicted in Fig. 4(*b*), a bimodal (2 peak) distribution. It is very likely that, for the data presented in Fig. 4(*b*), the bimodal histogram is caused by drag force, which is resisting the movements of both ascending and descending particle. The second peak as illustrated in Fig. 4(*b*) represents the data collected for theparticles leaving the free surface for the freeboard area. Note that these ascending particles are moving against gravity.

An important question remains concerning the role played by the surrounding gas. Figure 5(*a*) shows a typical configuration of the glass balls in the device at $\Gamma=10$ after $t=0.2$ s, where t is the simulation time. The oscillon-like structure drifts around leading to a convective motion as illustrated in Fig. 5(*b*) in the gas phase. Since the gas does not slip freely at the surface of the balls, a corresponding profile of particle velocity may be induced by the drag forces exerted by the gas on the particles. As a result of gas-particle interactions, particles in the layer adjacent to the gas (which move slower) collide with the chains located in the core of the oscillon-like structure generating a random component of particle velocity characterized by a granular temperature.

An obvious question is the role the surrounding gas would play deep inside the device. Figure 5(*c*) illustrates the cavities in the wall region where small bubbles may be formed. To obtain a better visualization, the wall regions are magnified in Fig. 5(*d*) where the vector plot of the gas velocity field is depicted. The flow accelerates around windward faces and separates over the leeward faces to form weak recirculation bubbles. In fact, the overall flow is far more complicated than that illustrated in Fig. 5(*d*), with many intermediate and small-scale components.

The results presented in a previous work [15] suggest that the gas force from beneath during particle-particle collision can be collected into large cavities generated during free-flight of the particles. In fact, the effects of quantities such as local gas velocity and pressure are very important in the dynamics of bubble formation. The bubbles created in cavities, as illustrated in Fig. 5(*c*), are observed to be compressed and expanded during each cycle with the mean bubble size appearing to grow with respect to time. Figure 6(*a*) illustrates a typical configuration of particles in the vibrodevice at $\Gamma\approx8$. The growth of bubbles with respect to time can clearly be seen from Fig. 6(*b*), which depicts two instantaneous realizations in a slice of the bed, each separated by $t\approx0.2$ s. Notice the presence of at least five bubbles with different sizes in the vibro-device, as illustrated in the top part of Fig. 6(*b*). The bubbles near each other as illustrated in the top part of Fig. 6(*b*) tend to coalesce and become one large bubble.

The collapse of structures and formation of large depressions can force air into the granular assembly from the top. Figure 7 shows images of the free surface of glass particles in which peaks and depressions can be observed. This observation implies that in the vibrodevice, regular and irregular surface-wave patterns are excited subharmonically, with the frequency of the waves being a fraction of the excitation. The vector plot of velocity field of air inside of the depressions, as depicted in Figs. 7(*c*) and 7(*d*), suggests that the air flows downwards and collects into the cavities formed during the collapse. It is likely that a set of bubbles occur when the compressed air caught beneath the granular layers during the collapse can expand into neighboring cavities. It may be speculated that the aforementioned bubbles move upward due to buoyancy effects and approach the free surface. Upon reaching the free surface they burst out, creating imperfect oscillion-type structures, as illustrated in Fig. 6(*a*). The connection between bubbling and the downward convective flow induced by the collapse of structures, as well as the exact role of the gas in the development, growth and propagation of the cavities are interesting issues

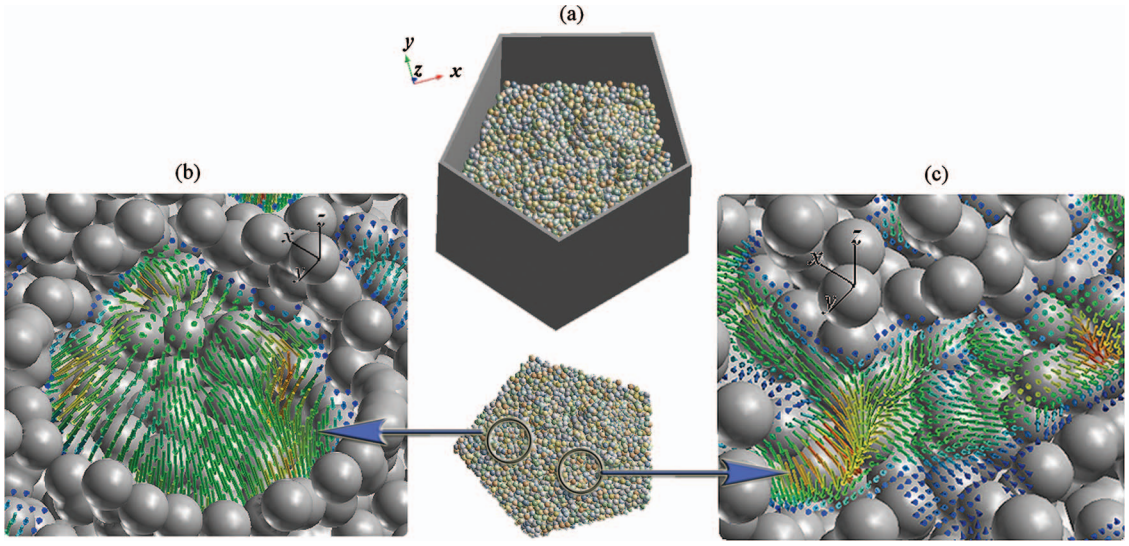

Fig. 7 (*a*) **A snapshot of the free surface of glass particles in the vertical vibrated pentagonal prism at** $\Gamma \approx 10$ **at** $t=0.4$ **s.** (*b*) **A different view of the free surface. Note that peaks and depressions can be observed.** (*c*) **and** (*d*) **Computed instantaneous velocity field on a cutting** *xy*-**plane located at** $N=35$**, above the location of the initial free surface (see Fig. 2). Computed velocity vectors have been interpolated onto a uniform mesh. To obtain a better visualization, the particles are also added in** (*c*) **and** (*d*)**.**

for further investigation.

Presently, no details such as flow dynamics of granular materials in the vibrodevice with different bucket shapes can be provided using even the simplified approach described above. Limitations in the available computational resources urge using an alternative approach such as a continuum approach, which will be proposed in the sequel paper. Indeed, the discrete model developed in this paper provides substantial insight in the physics of a shaken sandbox, which could lead to improved constitutive equations for continuum models.

3 Conclusions

Existing works on shaken sand have been largely confined to the experimental front. Indeed, the discoveries of experimentalists are spurring theorists in their search for a comprehensive, hydrodynamic type description for granular materials. Here, the development of a simplified molecular dynamics type model was considered for studying the deformation and flow of dense mixtures of gas and particles. The model is tested through its application to describe the influence of periodic vertical vibrations of the base of a pentagonal, prism shaped container on the dynamics of granular media, for which interactions with the surrounding gas plays a role in dynamical pattern deformation. The base wall of the container is subjected to sinusoidal oscillation in the vertical direction. The parameter, Γ, was defined to measure the acceleration of the container base relative to gravity. The parameter, Γ, is varied by changing the derived amplitude. As Γ is increased above a critical value Γ_c, the free surface of shaken particles became unstable. When Γ was increased well above Γ_c, the structures were observed with some degree of symmetry. The structures are subharmonic, therefore, both peaks and depressions can coexist. The incomplete structures have also been observed. The generation of incomplete structures has been linked to the formation of bubbles in the upper layers of shaken particles.

While progress on the computational and theoretical fronts has been encouraging and even oscillon-type structures similar to those observed by Umbanhowar et al. [1] have been generated, there are still many, many unsolved problems. An example of these problems includes the connection between bubbling and the downward convective flow induced by the collapse of the structures. In addition, the exact role of the gas in the development, growth and propagation of the cavities merits further investigation. Due to limitations in the available computational resources, currently no details such as flow dynamics of granular materials in containers with different bucket shapes can be provided.

Limitations in the available computational resources urged that further exploration of a shaken sandbox requires a different method along with the present approach. Because of these limitations, in the sequel to this paper as an alternative approach, a continuum approach will be proposed which retains the essential features that characterize the gas-particles flows. This attempt might help in overcoming the difficulties which lie in building a comprehensive hydrodynamic theory for the next generation of reactor models.

Nomenclature

A = derived amplitude
A_{eff} = effective amplitude
a_0 = fitting parameter
C = speed of wave in the wall of container
C_1, C_2 = dimensionless number, given in Ref. [30]
c_t = tangential damping coefficient
D = diffusion coefficient
D_0 = diffusion coefficient at $\Gamma=1.3$
D^* = normalized diffusion coefficient, $D^*=D/D_0$
E = Young's modulus
e_i = tangential unit vector, $e_i=\varepsilon_{imq}k_{m,jp}(\varepsilon_{qst}e_{s,jp}^{V\text{imp}}k_{t,jp})$
$e_s^{V_{\text{imp}}}$ = unit vector in the direction of relative impact velocity, as $e_s^{V_{\text{imp}}}=V_s^{\text{imp}}/\lvert V_s^{\text{imp}}\rvert$
F_i^b = Brownian force
F_i^D = drag force from the gas
F_i^g = gravitational force
F_i^i = particle to particle interaction
$F_i^{(jp)}$ = contact force per unit mass acting on the jth particle due to its neighboring pth particle
$F_i^{(jp)_t}$ = tangential component of the contact force per unit mass
$F_i^{(jp)_n}$ = normal component of the contact force per unit mass

Fr = Froude number
f = oscillation frequency
G = spatial filter
G_0 = instantaneous shear modulus
G_∞ = long time (glassy) shear modulus
g = acceleration of gravity
$J^{(j)}$ = moment of inertia
K_n = coefficient characterizing the viscous behavior
$k_i^{(jp)}$ = unit vector directed from the center of particle j to that of particle p at the moment of impact
k_t = tangential elastic constant
k_v = wave number $m_v = k_v/\pi$
L = linear size of the vibrodevice
l_v = wave number, $n_v = l_v/\pi$
m = mass of particle
m_v = wave number
N_c = number of particles in a computational cell
n_v = wave number
Re_p = Reynolds number
S = surface of the pentagon device
St = Stokes number
T_g = temperature of gas
$T_i^{(j)}$ = torque on the particle j
u_i = gas velocity vector ($i=x,y,z$)
$\tilde{u}_i$ = Favre filer
$V_i^{(p)}$ = particle velocity vector ($i=x,y,z$)
V_c = volume of a computational cell
V^{imp} = magnitude of impact velocity
V_o^{imp} = reference impact velocity
V_i^{imp} = impact velocity vector ($i=x,y,z$)
v_g = kinematic viscosity
Z_0 = vertical distances

Greek Symbols

β = coefficient, given by Eq. (4)
Γ = dimensionless number, $\Gamma = A_{\mathrm{eff}}\omega_v^2/g$
Γ_c = critical value of Γ
$\bar{\gamma}$ = constant, whose value usually chosen to be 6
$\bar{\Delta}$ = cutoff length
Δt = time step
$\varepsilon_{\mathrm{ijk}}$ = alternating tensor
μ_p = surface friction
δ_{ij} = Kronecker delta
$\delta^{(jp)}$ = overlapping between the pth and jth particles
ν_p = Poisson's ratio
ρ = apparent density
ρ_g = gas density
ρ_p = material density
σ = particle diameter
τ = relaxation time
τ_{ij} = stress tensor
τ^* = collision time
ϕ_s = solid fraction
$\chi^{(jp)}$ = tangential displacement
$\omega_i^{(j)}$ = angular velocity vector ($i=x,y,z$) of the jth particle
ω_v = frequency

Subscript

$,t$ = derivatives with respect to time
$,i$ = derivatives with respect to space, ($i=x,y,z$)

Appendix

By applying the Gaussian filter

$$G(x_i-\xi_i) = (\bar{\gamma}/\pi\bar{\Delta}^2)^{1/2}\exp(-\bar{\gamma}|x_i-\xi_i|^2/\bar{\Delta}^2) \tag{A1}$$

with filter width $\Delta_i (i=x,y,z)$ equates the grid spacing to the Eqs. (7) and (8), the filtered equations are obtained as

$$[\overline{\rho_g(1-\phi_s)u_i}]_{,i} - \overline{\rho_g(1-\phi_s)}_{,t} = 0 \tag{A2}$$

$$[\overline{\rho_g(1-\phi_s)u_i}]_{,t} + [\overline{\rho_g(1-\phi_s)u_iu_j}]_{,j} = -[\overline{(1-\phi_s)p}]_{,i} + [\overline{(1-\phi_s)\sigma_{ij}}]_{,j} - \overline{(1-\phi_s)}g\rho_g\delta_{iz} + \bar{f}_i \tag{A3}$$

where an overbar represents the spatial filter. Note that any quantity such as u_i in the flow domain can be decomposed as $u_i=\bar{u}_i+u_i'$, where u_i' is the subgrid-scale part that accounts for the scales not resolved by the computational grid.

Equations (7) and (8) look like the equation of motion for a fluid of variable density $\rho=\rho_g(1-\phi_s)$. Hence, as an alternative to the aforementioned approach discussed in the preceding section, a Favre filter can be defined as

$$\tilde{u}_i = \frac{\overline{\rho u_i}}{\bar{\rho}} \tag{A4}$$

This gives rise to the alternative decomposition $u_i=\tilde{u}_i+u_i''$, where u_i'' represents the subgrid-scale part of u_i based on Favre filtering. The Favre filtered governing equations are given as

$$(\bar{\rho}\tilde{u}_i)_{,i} - \bar{\rho}_{,t} = 0 \tag{A5}$$

$$(\bar{\rho}\tilde{u}_i)_{,t} + (\bar{\rho}\tilde{u}_i\tilde{u}_j)_{,j} = -[\overline{(1-\phi_s)}\bar{p}]_{,i} + [\overline{(1-\phi_s)}\bar{\sigma}_{ij}]_{,j} + \tau_{ij,j} - \bar{\rho}g\delta_{iz} + \bar{f}_i \tag{A6}$$

In Eq. (A6), the molecular stress tensor, and the subgrid scale stress tensor are given as

$$\sigma_{ij} = -\frac{2}{3}\mu_g u_{p,p}\delta_{ij} + \mu_g(u_{i,j}+u_{j,i}) \tag{A7}$$

$$\tau_{ij} = -\bar{\rho}(\widetilde{\tilde{u}_i\tilde{u}_j} - \tilde{u}_i\tilde{u}_j + \widetilde{u_i''\tilde{u}_j} + \widetilde{\tilde{u}_iu_j''} + \widetilde{u_i''u_j''}) \tag{A8}$$

As a tentative first attempt at closure, the LES equations Eqs. (A5) and (A6) may be closed with a subgrid-scale model for, τ_{ij}, given as [29]

$$\tau_{ij} = -\bar{\rho}(\widetilde{\tilde{u}_i\tilde{u}_j} - \tilde{\tilde{u}}_i\tilde{\tilde{u}}_j) + 2C_1\bar{\rho}\Delta_i^2(\tilde{S}_{mn}\tilde{S}_{mn})^{1/2}\left(\tilde{S}_{ij} - \frac{1}{3}\tilde{S}_{pp}\delta_{ij}\right) - \frac{2}{3}C_2\bar{\rho}\Delta_i^2(\tilde{S}_{mn}\tilde{S}_{mn})^{1/2}\delta_{ij} \tag{A9}$$

where C_1 and C_2 are dimensionless constants whose values may be determined by correlating the results of analysis, such as that detailed in Ref. [15]. However, a highly resolved flow field is required to estimate the aforementioned constants accurately. Note that Speziale et al. [30] found that the values of constants C_1 and C_2 for compressible turbulence are 0.012 and 0.0066, respectively.

Generally speaking, the gas can be assumed as an ideal gas whose material density, pressure and temperature are related to each other by the equation of state, defined as $P/\rho_g = RT_g$, where $R=0.286$ kJ/kg K. Note that the gas compressibility might play a role in solid contact breaking processes during propagation of the cavities. However, it is not quite clear how to modify the simplified model detailed in Sec. 2 in order to take into account contact breaking processes.

References

[1] Umbanhowar, P., Melo, F., and Swinney, H., 1996, "Localized Excitations in Vertically Vibrated Granular Layer," Nature (London), **382**, pp. 739–796.
[2] Fineberg, J., 1996, "Physics in a Jumping Sandbox," Nature (London), **382**, pp. 763–764.
[3] Aoki, K. M., and Akiyama, T., 1996, "Spontaneous Wave Pattern Formation in Vibrated Granular Materials," Phys. Rev. Lett., **77**, pp. 4166–4169.
[4] Shinbrot, T., 1997, "Competition Between Randomizing Impact and Inelastic

Collision in Granular Pattern Formation," Nature (London), **389**, pp. 574–576.
[5] Cerda, E., Melo, F., and Rica, S., 1997, "Model for Subharmonic Waves in Granular Materials," Phys. Rev. Lett., **79**, pp. 4570–4573.
[6] Tsimring, L., and Aranson, I., 1997, "Model for Subharmonic Waves in Granular Materials," Phys. Rev. Lett., **79**, pp. 213–216.
[7] Venkataramani, S., and Ott, E., 1998, "Spatiotemporal Bifurcation Phenomena With Temporal Period Doubling: Patterns in Vibrated Sand," Phys. Rev. Lett., **80**, pp. 3495–3498.
[8] Rothman, D., 1998, "Oscillons, Spiral Waves, and Stripes in a Model of Vibrated Sand," Phys. Rev. E, **57**, pp. R1239–R1242.
[9] Bizon, C., Shattuck, M. D., Swift, J. B., McCormick, W. D., and Swinney, H. L., 1998, "Patterns in 3D Vertically Oscillated Granular Layers: Simulation and Experiment," Phys. Rev. Lett., **80**, pp. 57–60.
[10] Schleier-Smith, J. M., and Stone, H. A., 2001, "Convection, Heaping, and Cracking in Vertically Vibrated Granular Slurries," Phys. Rev. Lett., **86**, pp. 3016–3019.
[11] Faraday, M., 1831, "Acoustic Streaming Over Vibrating Plates," Philos. Trans. R. Soc. London, **121**, pp. 299–318.
[12] Voth, G. A., Bigger, B., Buckley, M. R., Losert, W., Brenner, M. P., Stone, H. A., and Gollub, J. P., 2002, "Ordered Clusters and Dynamical States of Particles in a Vibrated Fluid," Phys. Rev. Lett., **88**, pp. 234–301.
[13] Zohdi, T. I., 2004, "A Computational Framework for Agglomeration in Thermochemically Reacting Granular Flows," Proc. R. Soc. A: Math. Phys. Eng. Sci., 460, pp. 3421–3445.
[14] Pak, H. K., Van Doorn, E., and Behringer, R. P., 1995, "Effects of Ambient Gases on Granular Materials Under Vertical Vibration," Phys. Rev. Lett., **74**, pp. 4643–4646.
[15] Zamankhan, P., and Bordbar, M. H., 2006, "Complex Flow Dynamics in Dense Granular Flows—Part I: Experimentation," ASME J. Appl. Mech., **73**, pp. 648–657.
[16] Phan-Thien, N., 2002, *Understanding Viscoelasticity*, Springer, Heidelberg.
[17] Zamankhan, P., Soleymani, A., Polashenski, W., Jr., and Zamankhan, P., 2004, "Flow Dynamics of Grains in Spinning Bucket at High Frequencies," Chem. Eng. Sci., **59**, pp. 235–246.
[18] Zamankhan, P., and Bordbar, M. H., "Dynamical Simulations of Vibrated Rough Spherical Glass Beads," Phys. Rev. E (submitted).
[19] Brilliantov, N. V., Spahn, F., Hertzsch, J.-M., and Pöschel, T., 1996, "Model for Collisions in Granular Gases," Phys. Rev. E, **53**, pp. 5382–5392.
[20] Zamankhan, P., and Huang, J., "Complex Flow Dynamics in Dense Granular Flows, Part II: Simulations," ASME J. Appl. Mech., submitted.
[21] Dormand, J. R., and Prince, P. J., 1980, "A Family of Embedded Runge–Kutta Formulae," J. Comput. Appl. Math., **6**, pp. 19–26.
[22] Zamankhan, P., 1995, "Kinetic Theory of Multicomponent Dense Mixtures of Slightly Inelastic Spherical Particles," Phys. Rev. E, **52**, pp. 4877–4891.
[23] Roache, P. J., 1998, *Verification and Validation in Computational Science and Engineering*, Hermosa, Albuquerque, NM.
[24] Silbert, L. E., Ertas, D, Grest, G. S., Hasley, T. S., Levin, D., and Plimpton, S. J., 2001, "Granular Flow Down an Inclined Plane: Bagnold Scaling and Rheology," Phys. Rev. E, **64**, p. 051302.
[25] Einstein, A., 1905, "Über die von der Molekularkinetischen Theorie der Wärme Geforderte Bewegung von in Ruhenden Flüssigkeiten Suspendierten Teilchen," Ann. Phys., **17**, pp. 549–560.
[26] Zamankhan, P., Polashenski, W., Jr., Vahedi Tafreshi, H., Shakib Manesh, A., and Sarkomaa, P., 1998, "Shear-Induced Particle Diffusion in Inelastic Hard Sphere Fluids," Phys. Rev. E, **58**, pp. R5237–R5240.
[27] D'Anna, G., Mayor, P., Barrat, A., Loreto, V., and Nori, F., 2003, "Observing Brownian Motion in Vibration-Fluidized Granular Matter," Nature (London), **424**, pp. 909–912.
[28] Miller, B., O'Hern, C., and Behringer, R. P., 1996, "Stress Fluctuations for Continuously Sheared Granular Materials," Phys. Rev. Lett., **77**, pp. 3110–3113.
[29] Yamamoto, Y., Potthoff, M., Tannka, T., Kajlshima, T., and Tsuji, Y., 2001, "Large-Eddy Simulation of Turbulent Gas-Particle Flow in a Vertical Channel: Effect of Considering Inter-Particle Collisions," J. Fluid Mech., **442**, pp. 303–334.
[30] Speziale, C. G., Erlebacher, G., Zang, T. A., and Hussaini, M. Y., 1988, "The Subgrid-Scale Modeling of Compressible Turbulence," Phys. Fluids, **31**, pp. 940–942.

Journal of Fluids Engineering

Technical Brief

Variation of the Recirculation Length of Newtonian and Non-Newtonian Power-Law Fluids in Laminar Flow Through a Suddenly Expanded Axisymmetric Geometry

Debabrata Nag
Department of Mechanical Engineering,
Jadavpur University,
Kolkata 700 032, India

Amitava Datta
Department of Power Engineering,
Jadavpur University,
Salt Lake Campus,
Kolkata 700 098, India
e-mail: amdatta_ju@yahoo.com

A numerical study has been carried out for the laminar flow of Newtonian and non-Newtonian power-law fluids through a suddenly expanded axisymmetric geometry. Mathematical correlations are proposed for the prediction of the length of the recirculating eddy in terms of Reynolds number, expansion ratio and rheological parameters. A wide range of expansion ratios ($1.25 \leqslant \mathrm{ER} \leqslant 8.0$) *has been covered for the Newtonian fluid and both the shear-thinning and shear-thickening flow characteristic fluids have been considered for the non-Newtonian fluids.*
[DOI: 10.1115/1.2409361]

1 Introduction

Flow through a confined axisymmetric geometry with a sudden expansion occurs frequently in important industrial applications. In this geometry, a recirculating vortex is generated because of the separation of flow from the solid wall at the expansion plane followed by its subsequent reattachment. The length of the recirculating eddy in sudden expansion flow is dependent on the geometrical characteristic of the flow passage, such as the expansion ratio ($\mathrm{ER}=D/d$) and on the flow characteristic represented by the Reynolds number (Re). For the non-Newtonian power-law fluids, fluid rheology, i.e., flow behavior and consistency indices, plays a major role in controlling the size of the recirculating eddy.

Contributed by the Fluids Engineering Division of ASME for publication in the JOURNAL OF FLUIDS ENGINEERING. Manuscript received March 17, 2006; final manuscript received September 5, 2006. Assoc. Editor: Dimitris Drikakis.

Following the work of Macagno and Hung [1], many researchers (e.g., Fletcher et al. [2], Back and Roschke [3], Badekas and Knight [4], etc.) performed studies of laminar flow through suddenly expanded pipes. The fundamental observation of all the studies on the recirculation length is the linear variation of its nondimensional value (normalized against d) with the Reynolds number in the laminar regime. Badekas and Knight [4] proposed a linear correlation between the nondimensional reattachment length (L_r/d) and Reynolds number, where the slope of the line varies linearly with the expansion ratio for $1.5 \leqslant \mathrm{ER} \leqslant 6.0$ and $50 \leqslant \mathrm{Re} \leqslant 200$. However, the model correlation was so formed that it cannot be extended below an expansion ratio of 1.24 and near expansion ratio of 1.0 it gives physically unrealistic negative lengths of the recirculating eddies.

In many realistic industrial flow situations through suddenly expanded geometries, non-Newtonian models can best represent the rheological properties of the fluid. Halmos et al. [5,6] carried out both numerical and experimental work with shear-thinning power law liquids (with flow behaviour index "n" ranging from 0.65 to 1.0) in geometries with various ER. They found that the length of the separated shear layer is a linear function of $\mathrm{Re}_{\mathrm{mod}} = \rho d^n \bar{u}^{(2-n)}/K$, where K is the consistency index of the fluid. Kahine et al. [7] and Nguyen et al. [8] proposed a mathematical correlation of the reattachment length with $\mathrm{Re}_{\mathrm{gen}} = (\rho d^n \bar{u}^{(2-n)}/K) \times (3+1/n)^{-n}(2^{-(n-3)})$ for the shear-thinning liquids (with n from 0.3 to 1.0). However, their correlation overestimated the recirculation length for the Newtonian fluids ($n=1$) by as much as 150% in comparison to the published results. Their results further indicate that the recirculation length increases for a given value of expansion ratio and Reynolds number as the flow index is increased. Similar trends had also been reported by Pinho et al. [9]. Results of Kahine et al. [7] further confirmed that at a given flow index and generalized Reynolds number, longer eddy length is produced as ER is increased. In their studies with generalized Newtonian fluids, Neofytou and Drikakis [10] and Neofytou [11] showed that a bifurcation in flow takes place beyond a critical Reynolds number in a suddenly expanded plane symmetric geometry and asymmetry in the recirculating eddies is observed after the expansion plane.

In the present work, numerical studies have been carried out for the laminar flow of both the Newtonian and non-Newtonian power-law fluids in an axisymmetric suddenly expanded geometry, as shown in Fig. 1, under conditions where no bifurcation in the flow takes place. Both the shear-thinning ($n<1$) and shear-thickening ($n>1$) variations of the power-law fluids are considered for the analysis, noting that very little data are available on the flow of shear-thickening fluids across an abrupt expansion in spite of their practical importance in food processing, suspensions, and slurries. The recirculation length, in its nondimensional form, has been predicted for Newtonian and non-Newtonian fluids and its variations with the geometrical and flow parameters as well as with the flow behavior index are studied. Suitable mathematical correlations are proposed separately for the Newtonian and non-

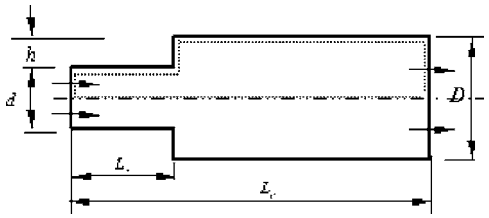

Fig. 1 Physical geometry of flow path. Dotted line shows the computational domain of the geometry.

Newtonian fluids for the prediction of the length of the recirculating eddy in the range of parameters considered in the present study.

2 Methodology

2.1 Governing Equations. The axisymmetric Navier–Stokes equations and the continuity equation for incompressible non-Newtonian fluid, considered for the solution, are as follows:

Axial Momentum

$$\frac{\partial u}{\partial t}+\frac{1}{r}\frac{\partial}{\partial r}(ruv)+\frac{\partial u^2}{\partial z}=-\frac{1}{\rho}\frac{\partial p}{\partial z}+\frac{1}{r}\frac{\partial}{\partial r}\left[\frac{\mu_{\text{app}}}{\rho}r\left(\frac{\partial u}{\partial r}+\frac{\partial v}{\partial z}\right)\right]+\frac{\partial}{\partial z}\left(\frac{2\mu_{\text{app}}}{\rho}\frac{\partial u}{\partial z}\right) \tag{1a}$$

Radial Momentum

$$\frac{\partial v}{\partial t}+\frac{1}{r}\frac{\partial}{\partial r}(rv^2)+\frac{\partial}{\partial z}(uv)=-\frac{1}{\rho}\frac{\partial p}{\partial r}+\frac{1}{r}\frac{\partial}{\partial r}\left(\frac{2\mu_{\text{app}}}{\rho}r\frac{\partial v}{\partial r}\right)-\frac{2\mu_{\text{app}}}{\rho}\frac{v}{r^2}+\frac{\partial}{\partial z}\left[\frac{\mu_{\text{app}}}{\rho}\left(\frac{\partial u}{\partial r}+\frac{\partial v}{\partial z}\right)\right] \tag{1b}$$

Continuity

$$\frac{1}{r}\frac{\partial(rv)}{\partial r}+\frac{\partial u}{\partial z}=0 \tag{2}$$

In the above equations (1*a*) and (1*b*), the non-Newtonian constitutive equation for Ostwald–de-Waele's "power-law" model is

$$\mu_{\text{app}}=K\left(\sqrt{\left|\frac{1}{2}\text{tr}\Delta^2\right|}\right)^{(n-1)} \tag{3a}$$

where Δ is the rate of strain tensor and

$$\frac{1}{2}\text{tr}(\Delta^2)=2\left[\left(\frac{\partial v}{\partial r}\right)^2+\left(\frac{v}{r}\right)^2+\left(\frac{\partial u}{\partial z}\right)^2\right]+\left(\frac{\partial u}{\partial r}+\frac{\partial v}{\partial z}\right)^2 \tag{3b}$$

For $n=1$, the above equations take the corresponding Newtonian forms, with K representing the coefficient of dynamic viscosity (μ) and Re_{gen} taking the conventional form of Reynolds number defined for a Newtonian fluid ($\text{Re}=\rho\bar{u}d/\mu$).

2.2 Numerical Solution. The numerical solutions are obtained for the above equations using an explicit finite difference based numerical approach, following a modified version of the SOLA scheme originally proposed by Hirt and Cook [12]. The variables in the domain have been defined following a staggered grid arrangement. The convective terms of the conservation equations are discretized using a quadratic upstream biased interpolation, while the diffusion terms are discretized following central differencing, as was recommended in the QUICK scheme by Leonard [13]. The solution is advanced in a time marching technique over suitably evaluated time steps, limited by the stability and Courant–Friedrich–Lewy criteria, until a steady state convergence is achieved. At this condition, the dimensional values of the temporal velocity gradients in both radial and stream-wise directions fall below a preassigned small number ($\varepsilon=0.0001$). During each time step, the pressure and velocity corrections are done by an iterative technique to keep the velocity divergence in each control volume within a prescribed limit (<0.0001). The numerical code is first developed for the Newtonian fluid and then is extended for the non-Newtonian fluid.

Table 1 Comparison of the present work and grid sensitivity studies of Newtonian fluids with the results of Macagno and Hung (see Ref. [1]) and Fletcher et al. (see Ref. [2]) for ER =2.0

	L_r/h				
			Present prediction		
Re	Macagno and Hung[a]	Fletcher et al.[b]	150×60	200×90	250×90
50	4.68	4.56	4.67	4.50	4.50
100	9.00	9.06	9.43	9.00	9.02
150	13.34	13.52	13.61	13.50	13.48
200	17.74	17.90	18.32	18.00	17.98

[a]See Ref. [1].
[b]See Ref. [2].

At the inlet boundary of the smaller pipe preceding the expansion plane (refer to Fig. 1) fully developed velocity profiles are specified for each case of Newtonian and non-Newtonian fluids. For the Newtonian fluid, the inlet velocity is represented by the parabolic distribution, while for the non-Newtonian fluid it is expressed using the following expression (Bird et al. [14])

$$u(r)=\bar{u}\left(\frac{3n+1}{n+1}\right)\left[1-\left(\frac{r}{R}\right)^{n+1/n}\right] \tag{4}$$

On the solid walls a "no slip" condition has been imposed. An axisymmetric condition is assumed at the axis and linearised convective outflow boundary condition (Nataf [15]) is assumed at the outlet plane in each case. The outflow boundary condition finally leads to the zero axial gradient condition for the stream-wise velocity under the steady state condition. Some numerical problems have been encountered while considering shear-thinning fluids because of the high viscosity values as the shear-rate becomes small. In such cases, a biviscosity rheological model [16] has been considered, where a high value of viscosity is assumed for the values of the strain rate lower than a threshold limit. This essentially assumes a very high value of viscosity as the shear rate falls below a critical level. A grid sensitivity study, as shown in Tables 1 and 2, has been done and based on it 200×90 (z,r) sized grid has been adopted.

Table 2 Comparison of the present work of non-Newtonian fluid with the experimental results of Halmos et al. (see Ref. [6]) with ER=2.0 and *n*=0.8

	L_r/h			
		Present prediction		
Re_{gen}	Halmos et al.[a]	150×60	200×90	250×90
57.76	4.00	3.35	3.00	3.00
115.52	8.00	7.91	7.80	7.80
144.40	10.02	9.87	9.80	9.79
173.28	12.20	11.72	11.60	11.59
202.16	14.40	13.00	12.94	12.92

[a]See Ref. [6].

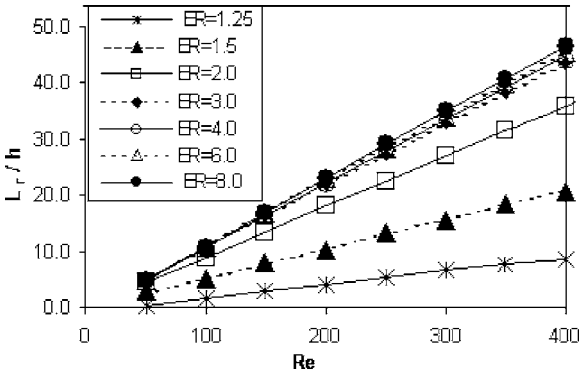

Fig. 2 Variation of nondimensional corner recirculation length with Reynolds number for various ER of a Newtonian fluid ($n=1.0$)

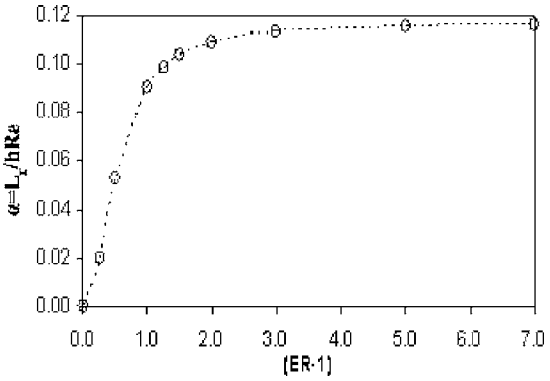

Fig. 3 Variation of coefficient $\alpha = L_r/h\,\mathrm{Re}$ with expansion ratio

3 Results and Discussions

As a part of the validation of the Newtonian version of the present code, the results of reattachment length (L_r) normalized by the step height (h) are validated with the experimental data of Macagno and Hung [1] and the numerical results of Fletcher et al. [2] for $50 \leqslant \mathrm{Re} \leqslant 200$. The results are compared in the Table 1 for ER=2.0. For the non-Newtonian flow, similar validation is done with the experimental data of Halmos et al. [6] for a fluid with $n=0.8$ through a circular duct with ER=2.0 and the comparison results are presented in Table 2. It is seen from the comparisons that the grid-independent results of the present code (both Newtonian and non-Newtonian cases) have very good agreement with the existing experimental and numerical results published in the literature. A detailed study of the recirculation length for the different flow situations is subsequently undertaken. For this study, the diameter of the pipe after expansion (D) is kept constant at 60 mm, while the inlet diameter (d) has been varied to get different expansion ratios. The length of the smaller pipe (L_i) is chosen so as to produce no influence on the predicted results past the expansion plane (Biswas et al. [17]).

3.1 Newtonian Fluid Flow. We have considered wider ranges of expansion ratio ($1.25 \leqslant \mathrm{ER} \leqslant 8.0$) and Reynolds number ($50 \leqslant \mathrm{Re} \leqslant 400$), compared to the previous works (e.g., Ref. [3,4] for the study of the recirculation length for Newtonian fluid flow. Figure 2 shows a comprehensive plot for the nondimensional recirculation length (L_r/h) against Re for different ER values. It is observed from the figure that, for a fixed ER, the recirculating eddy increases linearly as Re increases. It is also observed that for a fixed Reynolds number, the increase in the nondimensional recirculation length with ER is more for lower values of the expansion ratio. For example, at Re=100, the L_r/h value increases from 5.0 to 9.0 as ER increases from 1.5 to 2.0, while, the increase in L_r/h is from 10.5 to 10.7 as ER increases from 4.0 to 6.0. Therefore, the major impact of the expansion ratio on the nondimensional length of the recirculating zone can be observed at the lower values of the expansion ratio. The correlation of Badekas and Knight [4] for the prediction of recirculation length fails in the lower expansion ratio region and thus calls for a better correlation covering a wider range of expansion ratios. The predictions of the nondimensional recirculation length at all ER values satisfy a linear relation of the form

$$\frac{L_r}{h} = \alpha\,\mathrm{Re} \tag{5}$$

where α is a parameter that depends on the expansion ratio. Figure 3 shows a plot of α versus. (ER-1) showing a sigmoidal variation, where a curve-fitting exercise gives

$$\alpha = \frac{ab + c(\mathrm{ER}-1)^k}{b + (\mathrm{ER}-1)^k} \tag{6}$$

where $a=0.000258$, $b=0.295221$, $c=0.116905$, and $k=2.02686$. Chi-square goodness of fit has been adopted for this numerical exercise showing 99.98% goodness of fit with 0.12% residual error.

The present sigmoidal model is better than the correlation in Ref. [4], as it overcomes the limitations of the earlier correlation and extends up to the low values of expansion ratios with small margin of error. For example, with ER=1.25 and at Re=50, the present model predicts a recirculation length within 5% of that computed by the present numerical calculation, while the correlation of Ref. [4] gives an error of 65%, if extrapolated to this expansion ratio. This establishes the importance of the present model.

3.2 Non-Newtonian Fluid Flow. The present study in non-Newtonian fluids is based on the range of Re_{gen} between 50 and 200 (laminar flow) and ER of 2.0–6.0 for power-law fluids with $n=0.7$, 0.8, 1.0, 1.2, and 1.3. Figures 4(a)–4(c) present the variations of the nondimensional reattachment length (L_r/h) against Re_{gen} over different expansion ratios for $n=0.7$, 1.0 (Newtonian case), and 1.3, respectively. Additionally, Fig. 4(d) shows the variation of (L_r/h) with Re_{gen} at ER=3.0 for different flow behavior indices, n. Similar figures exist for all the cases studied but they could not be presented here for space limitations.

The figures confirm that L_r/h is a linear function of Re_{gen} over the entire range of study. For the shear-thinning fluid (Fig. 4(a)), the nondimensional reattachment length decreases with the increase in ER at a given Re_{gen}, while the opposite phenomenon is true for shear-thickening fluid (Fig. 4(c)) and the Newtonian one (Fig. 4(b)). The reason may be attributed to the local variation in the apparent viscosity of the fluid following the expansion plane, due to the variation in the local strain rate, at different expansion ratios. It has been observed that with the increase in ER, the apparent viscosity of the shear-thinning fluids after the expansion increases, while for the shear-thickening fluids the apparent viscosity following the expansion decreases. The variation in the apparent viscosity following the expansion is the cause of the variation in their recirculating length characteristics. Figure 4(d) further shows that for the same ER and Re_{gen}, L_r/h increases with flow behavior index n. The slope of the line α ($=L_r/h\,\mathrm{Re}_{gen}$) is now a function of ER and n. The variations of α with (ER-1) are shown in Fig. 5(a) for various flow behavior indices, while Fig. 5(b) shows the parabolic variation of α with n for various expansion ratios. Figure 5(a) clearly shows a drooping characteristic of α at high ER for shear-thinning fluids and a rising characteristic for shear-thickening fluid. Therefore, a new numerical curve-

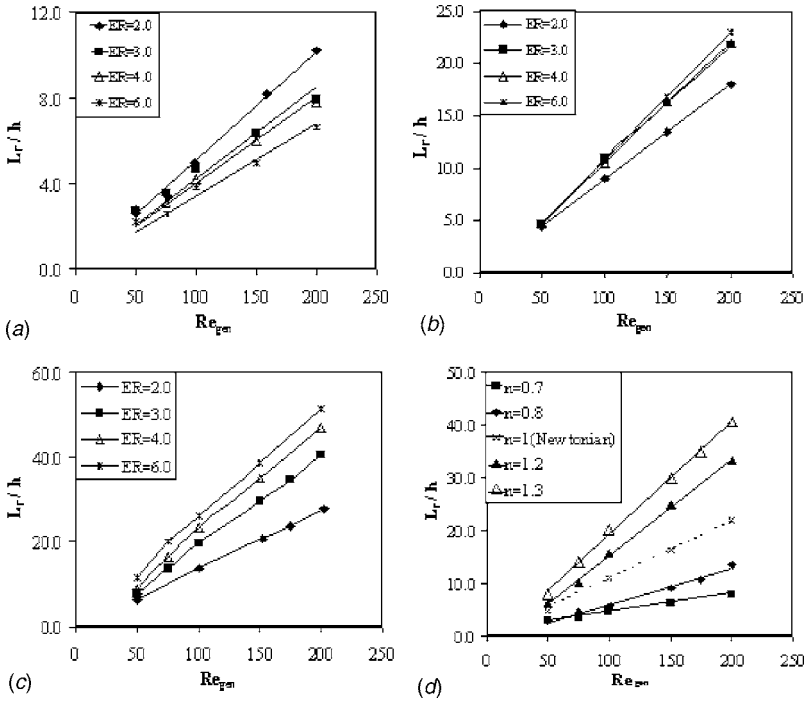

Fig. 4 (*a*) **Variation of recirculation length of $n=0.7$ for different expansion ratios.** (*b*) **Variation of recirculation length of $n=1.0$ for different expansion ratios.** (*c*) **Variation of recirculation length of $n=1.3$ for different expansion ratios.** (*d*) **Variation of recirculation length as a function of flow index for ER =3.0.**

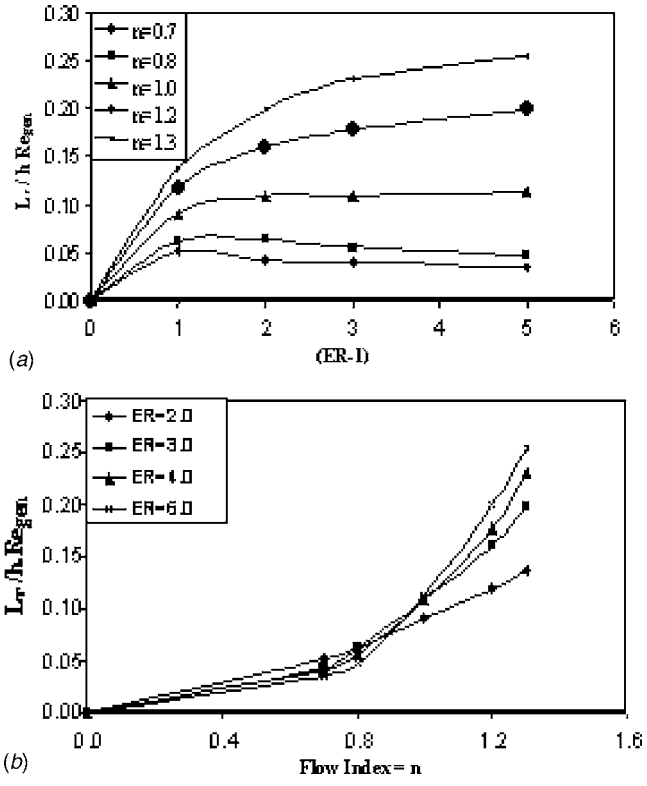

Fig. 5 (*a*) **Variation of $\alpha = L_r/h\,\mathrm{Re}_{gen}$ as function of expansion ratio for different flow indices of non-Newtonian fluids.** (*b*) **Variation of $\alpha = L_r/h\,\mathrm{Re}_{gen}$ as a function of flow index for different expansion ratios of non-Newtonian fluids.**

fitting exercise involving all the related parameters has been carried out, which gives the following model from the data obtained with non-Newtonian power-law fluids

$$\frac{L_r}{h} = [a(\mathrm{ER})n + b(\mathrm{ER})n^2]\mathrm{Re}_{gen} \tag{7}$$

The constants "*a*" and "*b*" are functions of the expansion ratio. Another numerical curve fitting reveals that

$$a = 0.144001 - 0.16485\ln(\mathrm{ER})$$

$$b = -0.06755 + 0.188134\ln(\mathrm{ER}) \tag{8}$$

The proposed relationships expressed by Eqs. (7) and (8) require that $2.0 \leqslant \mathrm{ER} \leqslant 6.0$ and $50 \leqslant \mathrm{Re}_{gen} \leqslant 200$ and they encompass both the shear-thinning and shear-thickening fluids.

Nguyen et al. [8] proposed a mathematical correlation for the recirculation length in case of shear-thinning power-law fluids, which after simplification, is given by

$$\frac{L_r}{h} = \frac{\mathrm{Re}_{gen}}{25}(5.1n + 3.5n^2)\frac{\ln(\mathrm{ER})}{(\mathrm{ER}-1)} \tag{9}$$

The present correlation gives more realistic comparison against the experimental data of Halmos et al. [6] than the correlation data of Nguyen et al. as shown in Fig. 6. Moreover, for $n=1.0$ and $\mathrm{ER}=2.0$, Eq. (9) predicts that $L_r/h = 0.238\,\mathrm{Re}_{gen}$, while our prediction from Eq. (7) gives $L_r/h = 0.093\,\mathrm{Re}_{gen}$. For such a condition, $\mathrm{Re}_{gen}=\mathrm{Re}$ and the values of $L_r/h\,\mathrm{Re}_{gen}$ from the experimental data of earlier researchers such as Ref. [1,4] are 0.0887 and 0.0912, respectively. Clearly, the correlation proposed by Nguyen et al. [8] fails to predict the Newtonian reattachment length completely.

The correlation for Newtonian fluid obtained from Eq. (7) is somewhat different from that of Eq. (5). Therefore, a comparison of the predicted values from the two correlations is tried in Fig. 7. It is to be noted that the correlation expressed by Eq. (5) is appli-

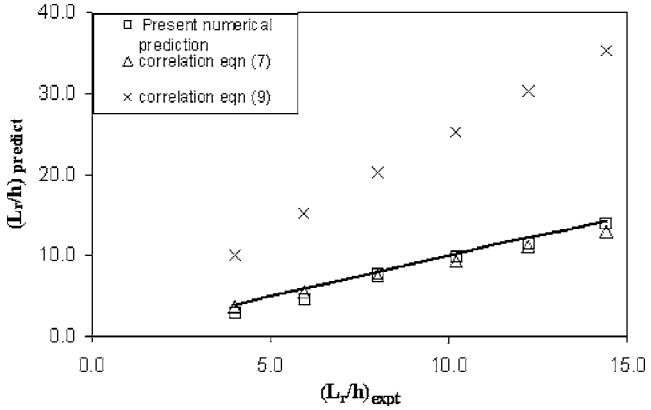

Fig. 6 Comparison of experimental L_r/h (Halmos et al. (see Ref. [6])) against predicted L_r/h from present numerical prediction, present correlation (Eq. (7)) and correlation of Eq. (9) (Nguyen et al. (see Ref. [8])) for $50 \leqslant Re \leqslant 200$, ER=2.0, and $n=0.8$

cable over wider ranges of expansion ratio ($1.25 \leqslant ER \leqslant 8.0$) and Reynolds number ($50 \leqslant Re \leqslant 400$) than the correlation expressed by Eq. (7), where the corresponding ranges are $2.0 \leqslant ER \leqslant 6.0$ and $50 \leqslant Re_{gen} \leqslant 200$, respectively. Figure 7 reveals that for ER and Re valid in the range of both the correlations (i.e., $2.0 \leqslant ER \leqslant 6.0$ and $50 \leqslant Re \leqslant 200$), the predictions from the two correlations agree excellently. The variations in the predictions from the two correlations, as shown in the figure (using hollow and solid square legends), are all for values outside the range where Eq. (7) is defined. The variations are particularly evident for low expansion ratios ($1.25 \leqslant ER < 2.0$) represented by hollow squares in Fig. 7. While for ER=8.0, the variations in the predictions from the two equations are prominently observed at higher Re, where the lengths of recirculating eddies are more (solid squares in Fig. 7). Interestingly, it is further noted that, for ($2.0 \leqslant ER \leqslant 6.0$), Eq. (7) is able to predict the (L_r/h) values corresponding to $200 \leqslant Re \leqslant 400$ closely as to the values predicted by Eq. (5), although the above range of Reynolds number is not within the purview of the range over which Eq. (7) is defined. We, however, propose correlation (5) for the Newtonian flow to predict the values of L_r/h as it is based on a much wider expansion ratio and Reynolds number.

4 Conclusion

The variations in the length of the recirculation eddy in case of laminar axisymmetric geometry with a sudden expansion have been studied numerically for Newtonian and non-Newtonian power-law fluids having both shear-thinning and shear-thickening features to study the effects of the geometric and hydrodynamic parameters. Suitable correlations for the predictions of the recirculation lengths in terms of geometrical and flow parameters and flow behavior index are proposed, which are applicable over wider ranges and with better accuracy than similar correlations previously existing in the literature. The following points are further observed:

- In Newtonian flow, the nondimensional recirculation length (L_r/h) varies linearly with Re at a fixed ER over the entire range of $1.25 \leqslant ER \leqslant 8.0$ and $50 \leqslant Re \leqslant 400$.
- In the case of non-Newtonian flow, the nondimensional recirculation length is also observed to be a linear function of Reynolds number for a given flow behavior index and expansion ratio, both for shear-thinning and shear-thickening power-law fluids. The study has been conducted with $50 \leqslant Re_{gen} \leqslant 200$ and for $2.0 \leqslant ER \leqslant 6.0$. It is observed that at a given expansion ratio and Re_{gen}, longer nondimensional recirculation length (L_r/h) has been obtained with the increase in flow behavior index. It is further noted that, the effect of increasing the expansion ratio at constant Re_{gen} is to shorten the nondimensional recirculation length (L_r/h) for the shear-thinning fluids, while, it is the opposite in case of shear-thickening and Newtonian fluids.

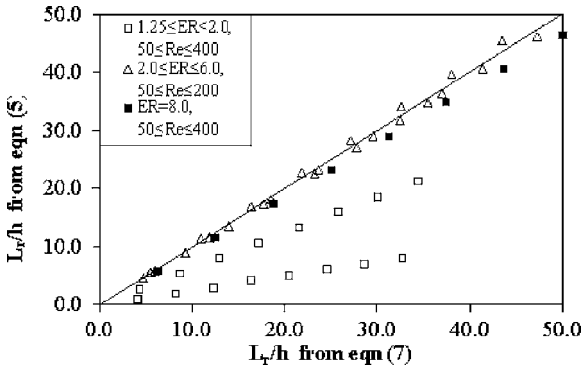

Fig. 7 Comparison of the prediction of L_r/h values from correlation Eqs. (5) and (7) for Newtonian flow ($n=1$)

Nomenclature

D = diameter of outlet pipe
d = diameter of inlet pipe
h = step height $(=(D-d)/2)$
L_r = length of corner recirculation measured from expansion plane
n = flow behavior index
Re_{gen} = genralized Reynolds number of non-Newtonian fluid
Re_{mod} = modified Reynolds number of non-Newtonian fluid
$\bar{u}$ = mean bulk axial velocity
ρ = density of fluid

References

[1] Macagno, O. E., and Hung, T. K., 1967, "Computational and Experimental Study of Captive Annular Eddy," J. Fluid Mech., **28**(1), pp. 43–64.
[2] Fletcher, D., Maskel, S., and Patrick, M., 1985, "Heat and Mass Transfer Computations for Laminar Flow in an Axisymmetric Sudden Expansion," Comput. Fluids, **13**, pp. 207–221.
[3] Back, L., and Roshke, E., 1972, "Shear Layer Regimes and Wave Instabilities and Reattachment Lengths Downstream of an Abrupt Circular Channel Expansion," ASME J. Appl. Mech., **94**, pp. 677–681.
[4] Badekas, D., and Knight, D. D., 1992, "Eddy Correlations for Laminar Axisymmetric Sudden Expansion Flows," ASME Trans. J. Fluids Eng., **114**, pp. 119–121.
[5] Halmos, A. L., Boger, D. V., and Cabelli, A., 1975, "The Behaviour of a Power-law Fluid Flowing Through a Sudden Expansion, Part I: A Numerical Solution," AIChE J., **21**, pp. 540–549.
[6] Halmos, A. L., Boger, D. V., and Cabelli, A., 1975, "The Behaviour of a Power-law Fluid Flowing Through a Sudden Expansion, Part II: Experimental Verification," AIChE J., **21**, pp. 550–553.
[7] Kahine, K., Nguyen, V. T., and Lebouché, M., 1997, "Ecoulment de Fluides Non-Newtonians a Travers des Elargissements Brusques," Int. Commun. Heat Mass Transfer, **24**, pp. 1103–1112.
[8] Nguyen, V. T., Kahine, K., and Lebouché, M., 1999, "Étude Numérique de l'Écoulement de Fluides Non Newtoniens à Travers un Élargissement Brusque," Mécanique des Fluides/Fluid Mechanics, **327** série II b, 91–94.
[9] Pinho, F. T., Oliveira, P. J., and Miranda, J. P., 2003, "Pressure Losses in the Laminar Flow of Shear-Thinning Power-law Fluids Across a Sudden Axisymmetric Expansion," Int. J. Heat Fluid Flow, **24**, pp. 747–761.
[10] Neofytou, P., and Drikakis, D., 2003, "Non-Newtonian Flow Instability in a Channel With a Sudden Expansion," J. Non-Newtonian Fluid Mech., **111**, pp. 127–150.

[11] Neofytou, P., 2006, "Transition to Asymmetry of Generalized Newtonian Fluid Flows Through a Symmetric Sudden Expansion," J. Non-Newtonian Fluid Mech., **133**, pp. 132–140.
[12] Hirt, C. W., and Cook, J. L., 1972, "Calculating Three-Dimensional Flows Around Structures and Over Rough Terrain," J. Comput. Phys., **10**, pp. 324–341.
[13] Leonard, B. P., 1976, "A Stable and Accurate Convective Modeling Procedure Based on Quadratic Upstream Interpolation," Comput. Methods Appl. Mech. Eng., **19**, pp. 59–98.
[14] Bird, R. B., Stewart, W. E., and Lightfoot, E. N., 1960, *Transport Phenomena*, Wiley, New York.
[15] Nataf, F., 1989, "An Open Boundary Condition for the Computation of the Steady Incompressible Navier–Stokes Equations," J. Comput. Phys., **85**, pp. 104–129.
[16] Hammad, K. J., Vradis, G. C., and Ötügen, M. V., 2001, "Laminar Flow of a Herschel–Bulkeley Fluid Over an Axisymmetric Sudden Expansion," ASME Trans. J. Fluids Eng., **123**, pp. 588–594.
[17] Biswas, G., Breuer, M., and Durst, F., 2004, "Backward-Facing Step Flows for Various Expansion Ratios at Low and Moderate Reynolds Numbers," ASME Trans. J. Fluids Eng., **126**, pp. 362–374.